



LUND UNIVERSITY

Laser-Driven Plasma Waves for Particle Acceleration and X-ray Production

Genoud, Guillaume

2011

[Link to publication](#)

Citation for published version (APA):

Genoud, G. (2011). *Laser-Driven Plasma Waves for Particle Acceleration and X-ray Production*. [Doctoral Thesis (compilation), Atomic Physics].

Total number of authors:

1

General rights

Unless other specific re-use rights are stated the following general rights apply:

Copyright and moral rights for the publications made accessible in the public portal are retained by the authors and/or other copyright owners and it is a condition of accessing publications that users recognise and abide by the legal requirements associated with these rights.

- Users may download and print one copy of any publication from the public portal for the purpose of private study or research.
- You may not further distribute the material or use it for any profit-making activity or commercial gain
- You may freely distribute the URL identifying the publication in the public portal

Read more about Creative commons licenses: <https://creativecommons.org/licenses/>

Take down policy

If you believe that this document breaches copyright please contact us providing details, and we will remove access to the work immediately and investigate your claim.

LUND UNIVERSITY

PO Box 117
221 00 Lund
+46 46-222 00 00

LASER-DRIVEN PLASMA WAVES FOR PARTICLE ACCELERATION AND X-RAY PRODUCTION

Guillaume Genoud

Doctoral Thesis
2011



LUND UNIVERSITY

LASER-DRIVEN PLASMA WAVES FOR PARTICLE ACCELERATION AND
X-RAY PRODUCTION

© 2011 Guillaume Genoud
All rights reserved
Printed in Sweden by Media-Tryck, Lund, 2011

Division of Atomic Physics
Department of Physics
Faculty of Engineering, LTH
Lund University
P.O. Box 118
SE-221 00 Lund
Sweden

<http://www.atomic.physics.lu.se>

ISSN 0281-2762
Lund Reports on Atomic Physics, LRAP-443

ISBN 978-91-7473-164-4

*Le savant n'est pas l'homme qui fournit les vraies réponses,
c'est celui qui pose les vraies questions.*
Le Cru et le cuit

Claude Lévi-Strauss

ABSTRACT

This thesis presents experimental results related to laser plasma accelerators. These rely on very different principles from conventional particle accelerators. They are able to accelerate particles over a very short distance and produce synchrotron x-rays at the same time, potentially providing a compact particle accelerator and x-ray source for many future applications.

The laser pulses used in the experiments reported in this thesis were extremely powerful (TW) and when focused, intensities as high as 10^{20} W/cm² were achieved. When matter is exposed to such high intensities, it becomes a plasma, and collective motion of electrons is possible. The laser pulse “ploughs” through the plasma creating a plasma wave behind it, very much like a boat at sea. The perturbation in electron density caused by the wave produces strong longitudinal electric fields, travelling at the same speed as the laser pulse. These fields can then be used to accelerate electrons to hundreds of MeV in only a few mm. In addition to longitudinal electric fields, transverse fields are also produced, which can make the electrons “wiggle” transversely and emit x-rays. In a related process, heavy ions can also be accelerated by high-intensity lasers, when interacting with a solid target.

In the experimental work reported in this thesis, the use of dielectric capillary tubes was explored in order to increase the accelerating length by externally guiding the laser pulse and counteracting diffraction. Linear plasma waves over several centimetres were produced and characterised. Electron beams and x-rays produced in dielectric capillary tubes were also studied, where it was found that it was possible to trap electrons even at a low initial laser intensity. An active stabilisation system was developed in parallel to improve the pointing of the laser system, as the dielectric capillaries are very sensitive to pointing fluctuation. The laser focal spot was modified in a controlled way using adaptive optics. By adding coma aberration, the focal spot could be made asymmetric and the x-ray emission enhanced, as the electrons oscillate with a greater amplitude. Adding spherical aberration allowed the effect of the quality of the focal spot on the wavebreaking threshold to be studied. A simple model predicting whether or

not the plasma wave breaks was developed by varying the laser energy and pulse duration.

Two ways of increasing or modifying the proton energy distribution without increasing the laser power are also presented in this thesis. The absorption of the main laser pulse was improved and the proton energy increased by using a 100 fs long laser prepulse. Finally, hollow microspheres were used as targets, which allowed for “recycling” of the laterally spreading electrons to establish a new accelerating field that could accelerate the protons once more.

POPULÄRVETENSKAPLIG SAMMANFATTNING

Denna avhandling ger en introduktion till laser-plasma acceleratorer, vilket även utgör ämnet för de vetenskapliga artiklar som ingår i avhandlingen. Det är en ny typ av acceleratorer som utnyttjar mycket kraftfulla lasrar för att accelerera elektroner och protoner. Partikelacceleratorer används för att ge partiklar hög rörelseenergi, vilket kan utnyttjas för många olika tillämpningar, t.ex. inom medicin, och för att generera intensiv röntgenstrålning. Vanliga partikelacceleratorer är baserade på elektriska fält i kaviteter av metall, som endast tål begränsade fältstyrkor. De måste därför göras väldigt långa för att riktigt höga partikelenergor ska kunna uppnås. Av den anledningen är antalet acceleratorer som kan accelerera partiklar till de mycket höga energier som behövs för studier av elementarpartikelfysik och för att producera intensiv röntgenstrålning, av kostnadsskäl begränsat. Acceleratorer som baseras på laserproducerade plasmer fungerar helt annorlunda. Med dessa kan elektroner accelereras på betydligt kortare sträckor, och dessutom producera röntgenstrålning på samma gång. Det innebär att man eventuellt kommer att kunna bygga mycket kompakta acceleratorer och röntgenkällor för olika tillämpningar i framtiden.

De laserpulser som utnyttjas för experimenten som beskrivs i denna avhandling har mycket hög toppeffekt. Varje ljuspuls har ca en joule energi, men varar endast i ca 30 femtosekunder ($1 \text{ fs} = 10^{-15} \text{ s}$). Toppeffekten i varje puls blir på så vis mycket hög, av storleksordningen tiotals terawatt (10^{12} W). När dessa ljuspulser fokuseras till en liten fläck, eller strålmidja, med en diameter om endast några få mikrometer, blirer ljusintensiteten där *extremt* hög. Materia som utsätts för så starkt ljus joniseras redan under ljuspulses stiftid, så att ett plasma bildas. Ett plasma är ungefär som en gas av positivt laddade joner och negativt laddade elektroner som rör sig fritt relativt varandra. Toppen av ljuspulsen växelverkar alltså med fria laddningar. Den kan driva kollektiva rörelser hos de lätta elektronerna, medan de betydligt

tyngre jonerna kan betraktas som opåverkade under den korta tid laserpulsen växelverkar med plasmat. Det visar sig att en intensiv laserpuls som passerar genom ett tunt plasma trycker undan elektroner och skapar en våg bakom sig, ungefär på samma vis som en båt på en sjö. Den variation i elektronräntet som vågen utgör leder till starka elektriska fält, riktade i vågens utbredningsriktning. Ljuspulsens elektromagnetiska fält, som svänger vinkelrätt mot utbredningsriktningen, har alltså i plasmat omvandlats till ett longitudinellt fält som följer vågen, med ljuspulsen hastighet. Fältstyrkor av storleksordningen 100 gigavolt per meter (GV/m) kan skapas, vilket är många storleksordningar högre än vad som kan åstadkommas med konventionell teknik. Där är styrkan på de elektriska fälten begränsad på grund av risken för elektriska överslag i kaviteterna. I vårt fall existerar inte denna risk, eftersom vi redan är i ett joniserat medium. De longitudinella fälten i plasmat lämpar sig för att accelerera laddade partiklar. Speciellt elektroner kan fångas av vågen och accelereras till hundratals mega-elektronvolt (MeV) på bara några få mm, ungefär som en surfare på en våg på havet. Som en konsekvens av den extrema styrkan i det elektriska fältet kan accelerationssträckan vara mycket kort.

Förutom de longitudinella elektriska fälten förekommer även transversella fält, vilket gör att elektroner som accelereras i framåtriktingen samtidigt svänger vinkelrätt mot denna. De svängande elektronerna skickar då ut elektromagnetisk strålning i framåtriktingen, på samma vis som elektronerna i en undulator eller wiggler vid en konventionell synkrotronljusanläggning. Strålningen som har studerats och diskuteras i denna avhandling ligger inom energiområdet 1–10 kiloelektronvolt (keV). Denna, i framtiden ännu hårdare röntgenstrålning, kan komma att visa sig användbar för en rad intressanta tillämpningar. Såväl elektron- som röntgenpulserna har speciella egenskaper på grund av att de inblandade processerna sker på så extremt liten skala. Pulserna blir mycket korta (av storleksordningen 10 fs) och strålkällan får ytterst liten utbredning, endast ett fåtal mikrometer. Denna nya strålningskälla har därför stor potential för tidsupplösta studier.

Bland de experiment som beskrivs i denna avhandling har användningen av kapillärrör av glas undersökts som en metod för att förlänga accelerationssträckan genom att leda laserpulserna genom röret och på så vis motverka diffraction. Plasmavågor som utbredder sig över flera cm inne i dylika rör kunde produceras och karakteriseras. Dessutom studerades elektroner som accelererats och röntgenstrålning som genererats inne i rören. Vi fann då att det är möjligt att fånga och accelerera elektroner med lägre laserintensitet än utan kapillärrör. Parallelt med dessa studier utvecklades och installerades ett aktivt reglersystem för att förbättra laserstrålens riktningsstabilitet, vilket visade sig vara väsentligt för experiment med kapillärer. I andra studier modifier-

ades fokusfläckens form på ett kontrollerat sätt med hjälp av adaptiv optik. Genom att lägga till aberrationen koma kunde fläcken göras asymmetrisk på ett systematiskt och välbestämt sätt. Detta visade sig leda till mer divergenta elektronpulser, men samtidigt hårdare röntgenstrålning. Detta följer av att elektronerna på grund av asymmetrin i fokus får att svänga med större amplitud kring utbredningsriktningen. Genom att i stället lägga till sfärisk aberration kunde inverkan av strålmidjans form på vågens förmåga att fånga och accelerera elektroner studeras.

Joner kan också accelereras med lasrar med hög intensitet. Då utnyttjas ett fast strålmål, vanligtvis en tunn metallfolie med endast några mikrometers tjocklek. När laserpulsen växelverkar med det tätta plasma som bildas på strålmålet, trycks elektroner genom folien till baksidan där de expanderar ut i vakuум, varvid ett extremt starkt elektrostatiskt fält skapas. Detta fält är riktat vinkelrätt mot ytan och kan nå en styrka av storleksordningen teravolt per meter (TV/m). Protoner och andra joner, till exempel från vattenmolekyler eller föroreningar på foliens baksida, kan accelereras i dessa fält till flera MeV på bara några få mikrometers accelerationssträcka. Två olika sätt att öka, eller modifiera, energifördelningen hos laseraccelererade protoner utan att öka laser-effekten presenteras i denna avhandling. Först visade vi hur 100 fs långa förpulser, vid rätt vald tid, kunde förbättra absorptionen av huvudpulsen och därmed öka effektiviteten. Sedan visade vi att ihåliga mikrosfärer kan vara intressanta som strålmål vid protonacceleration. Dessa möjliggör nämligen att elektroner som inte direkt bidrar till acceleration, utan sprids transversellt på ytan, kan bidra till acceleration när de möts på sfärens motsatta sida och där etablerar ett annat accelerationsfält.

LIST OF PUBLICATIONS

This thesis is based on the following papers, which will be referred to by their Roman numerals in the text.

I Active control of the pointing of a multi-terawatt laser

G. Genoud, F. Wojda, M. Burza, A. Persson, and C.-G. Wahlström.

Rev. Sci. Instrum. **82**, 033102 (2011).

II Laser-driven plasma waves in capillary tubes

F. Wojda, K. Cassou, G. Genoud, M. Burza, Y. Glinec, O. Lundh, A. Persson, G. Vieux, E. Brunetti, R.P. Shanks, D. Jaroszynski, N. E. Andreev, C.-G. Wahlström and B. Cros. *Phys. Rev. E* **80**, 066403 (2009).

III Analysis of laser wakefield dynamics in capillary tubes

N. E. Andreev, K. Cassou, F. Wojda, G. Genoud, M. Burza, O. Lundh, A. Persson, B. Cros, V. E. Fortov and C-G Wahlström.

New J. Phys. **12**, 045024 (2010).

IV Laser-plasma electron acceleration in dielectric capillary tubes

G. Genoud, K. Cassou, F. Wojda, H. E. Ferrari, C. Kamperidis, M. Burza, A. Persson, J. Uhlig, S. Kneip, S.P.D. Mangles, A. Lifschitz, B. Cros and C.-G. Wahlström.

Appl. Phys. B, in Press, DOI: 10.1007/s00340-011-4639-4 (2011).

V Controlling the spectrum of x-rays generated in a laser-plasma accelerator by tailoring the laser wavefront

S. P. D. Mangles, G. Genoud, S. Kneip, M. Burza, K. Cassou, B. Cros, N. P. Dover, C. Kamperidis, Z. Najmudin, A. Persson, J. Schreiber, F. Wojda and C.-G. Wahlström.
Appl. Phys. Lett. **95**, 181106 (2009).

VI Experimental study of the wavebreaking threshold in a laser wakefield accelerator

S. P. D. Mangles, G. Genoud, M. S. Bloom, M. Burza, Z. Najmudin, A. Persson, K. Svensson, A. G. R. Thomas and C.-G. Wahlström.

Manuscript.

VII Evolution of energy spectrum from laser-accelerated protons with a 100 fs intense prepulse

Y. Glinec, G. Genoud, O. Lundh, A. Persson and C.-G. Wahlström.

Appl. Phys. B **93**, 317 (2008).

VIII Hollow microspheres as targets for staged laser-driven proton acceleration

M. Burza, A. Gonoskov, G. Genoud, A. Persson, K. Svensson, M. Quinn, P. McKenna, M. Marklund and C.-G. Wahlström.

New J. Phys. **13**, 013030 (2011).

CONTENTS

1	Introduction	1
2	Laser wakefield acceleration of electrons	5
2.1	Introduction	5
2.2	Laser parameters	6
2.3	Ionisation	8
2.4	Plasma waves	9
2.4.1	The ponderomotive force	11
2.4.2	Plasma wave generation	12
	The linear case	13
	The nonlinear case	15
2.4.3	Wavebreaking	17
2.5	The bubble regime	17
2.6	Acceleration and dephasing	19
2.6.1	Beam loading	22
2.7	Injection	23
2.7.1	Self-injection	24
2.7.2	Alternative injection schemes	24
	External injection	25
2.8	Laser propagation in underdense plasma	26
2.8.1	Ionisation defocusing	27
2.8.2	Self-focusing	27
2.8.3	Frequency shift and pulse compression	29
2.8.4	Pump depletion	30
2.9	Limit on energy gain and scaling laws	30
3	The plasma wiggler x-ray source	33
3.1	Introduction	33
3.2	Electron trajectories	35
3.3	Emitted radiation	36
3.3.1	Spatial distribution of the radiation	38
3.3.2	Spectral features	39
3.4	Effect of acceleration	41
3.5	Emission from many electrons	42
4	Experimental methods	45
4.1	The multi-terawatt laser of the Lund Laser Centre	45
4.1.1	Pointing	46
4.1.2	Adaptive optics	50
4.2	Typical experimental arrangement and diagnostics	52
4.2.1	Gas medium	53
	Capillary tubes	53
4.2.2	Electron diagnostics	56
4.2.3	Optical diagnostics	56

Thomson side scattering	56
Transmitted light	57
4.3 X-ray detection	58
4.3.1 Filter arrays	59
4.3.2 Single-hit counting	60
4.4 Radiation safety	63
5 Experimental results	67
5.1 Laser plasma interaction in dielectric capillary tubes	67
5.1.1 Linear plasma waves in capillary tubes	67
Guiding	68
Characterisation of linear plasma waves	68
Outlook	70
5.1.2 Electrons and x-rays from capillary tubes	70
X-rays	71
5.2 Influence of the quality of the focal spot	73
5.2.1 Asymmetric focal spot	73
Increasing the critical energy of the x-ray spectrum	75
5.2.2 Varying the fraction of energy inside the central part of the focal spot	76
Influence on the transmitted light	76
5.3 The self-injection threshold	78
5.3.1 Influence of the pulse duration on self-injection	79
5.3.2 A self-injection threshold model	80
6 Proton acceleration	83
6.1 Introduction	83
6.2 Intense laser-matter interactions with solids	84
6.2.1 Electron heating	84
6.2.2 Target normal sheath acceleration	85
6.2.3 Electron transport	86
6.3 Experimental methods	86
6.3.1 Contrast	87
6.3.2 Detection	88
6.4 Use of a prepulse	89
6.4.1 Results and discussion	90
6.5 Hollow microspheres	91
6.5.1 Results and discussion	92
7 Summary and Outlook	95
Role of the Author	97
Acknowledgments	101
References	103

Papers

I	Active control of the pointing of a multi-terawatt laser	119
II	Laser-driven plasma waves in capillary tubes	127
III	Analysis of laser wakefield dynamics in capillary tubes	133
IV	Laser-plasma electron acceleration in dielectric capillary tubes	153
V	Controlling the spectrum of x-rays generated in a laser-plasma accelerator by tailoring the laser wavefront	163
VI	Experimental study of the wavebreaking threshold in a laser wakefield accelerator	169
VII	Evolution of energy spectrum from laser-accelerated protons with a 100 fs intense prepulse	175
VIII	Hollow microspheres as targets for staged laser-driven proton acceleration	183

INTRODUCTION

Since its invention in 1960, the laser has become part of everyday life. At the same time, it is a very important tool for research in physics and other scientific fields. Various types of pulsed lasers have been developed over the years, from very energetic ones, used for laboratory astrophysics or inertial confinement fusion, to ultra-short pulsed lasers, with pulse durations of only a few femtoseconds, for time-resolved studies. Extremely high peak powers of the order of terawatts can be achieved by combining high pulse energy and short pulse duration. Thanks to the introduction of the chirped pulse amplification technique [1], high peak power can be achieved in university-scale laboratories and exciting new physics can be investigated. In the work presented in this thesis, focused laser intensities with values as high as 10^{20} W/cm², corresponding to a peak transverse electric field exceeding 10^{13} V/m, have been used. When exposed to such extreme conditions, matter is instantaneously ionised and the laser interacts with the plasma formed. The electric field generated by the laser causes the free electrons to oscillate with velocities approaching the speed of light, hence the term “relativistic laser intensities”. In particular, laser plasma interactions at these intensities can be used to accelerate electrons to relativistic energies. This is the main subject of this thesis.

Although the laser field itself drives the electrons to relativistic velocities, its oscillating and transverse nature prevents it from efficiently accelerating particles in a given direction. In a plasma, high-amplitude longitudinal waves with relativistic velocities can be driven by a laser pulse, thus transforming the transverse fields into longitudinal ones, as illustrated in Fig. 1.1. As we will see in Chapter 2, this wave can break, trap and generate acceleration forces more than a thousand times stronger than those achieved in accelerators based on conventional technology. Large transverse fields are also produced in the plasma by the laser pulse. They can make the forward accelerated electrons “wiggle” and emit x-rays,

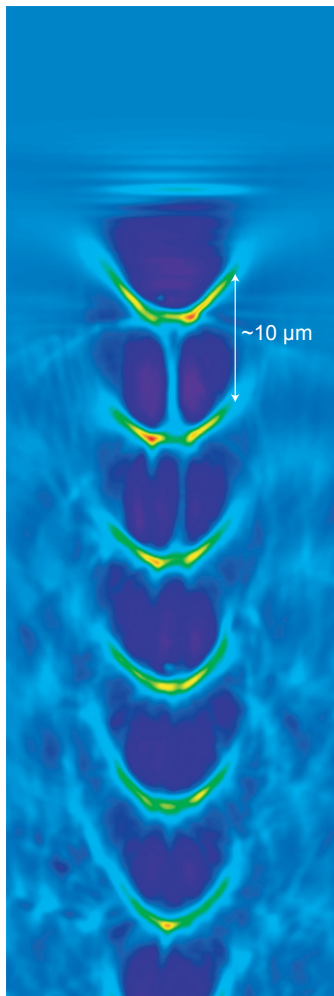


Figure 1.1. Electron density variation in the wake of an intense laser pulse, simulated using the 2D particle-in-cell code OSIRIS. The longitudinal electric fields produced by this density modulation can be used to accelerate electrons to relativistic energies. The laser pulse propagates towards the top of the image (courtesy of S. P. D. Mangles).

as discussed in Chapter 3. The laser plasma can thus play the role of both accelerator and wiggler, providing a compact ultra-fast x-ray source, of great interest for many applications in various fields of science [2]. The experimental methods and results are presented in Chapter 4 and Chapter 5. In a related process, ions can also be accelerated using high-power lasers by establishing a quasi-static electric field at the boundary of thin foils. This is described in Chapter 6. The novelty of these accelerators resides in the scale of the processes involved. For example, electrons are accelerated to hundreds of MeV in only a few millimetres, and protons to several MeV in a few micrometres.

Particle accelerators are at the forefront of modern science. Their applications vary from fundamental research in high-energy physics, to medical applications and x-ray production. While accelerators delivering particle beams of moderate energy are widespread, the challenge in accelerator technology has been to provide high-energy particles, required for many applications. For example, such accelerators have been used at synchrotron facilities to produce intense x-ray beams, contributing to many discoveries in different scientific fields. Some of these accelerators are today among the most advanced scientific tools available. The Large Hadron Collider at CERN, for example, is the most advanced accelerator on earth, and is being used to study the building blocks of matter. Extraordinary discoveries will certainly be made. Based on a 3 km long linear accelerator, the Linac Coherent Light Source at SLAC is another facility which recently came into operation. Designed to produce the most intense x-ray beams ever, this free-electron laser is the first of its kind. Experiments have already been successfully carried out [3, 4] and more exciting ones are yet to come. While pushing the frontier of science, these extraordinary machines are limited in number due to their large size and cost. Even with their small number, they have already proven their use and revolutionised research in physics, chemistry, biology, medicine and materials science.

In a conventional accelerator, the accelerating fields are created by radio-frequency cavities. The electric field strength is limited by electrical breakdown, which will occur above a certain field strength. In order to accelerate particles to high energies, many cavities must be combined in series, thus making the accelerator very large. In order to limit the size, the cavities are usually configured in a ring. However, a large radius of curvature is needed in order to prevent the particles from radiating too much energy. Also, a linear accelerator is more suitable to preserve a short pulse duration. There is no such limit in plasma accelerators: as the medium is already ionised, electrical breakdown is not possible. The accelerating field achievable in this type of accelerator can be many orders of magnitude higher than in conventional accelerators, and the accelerating length can therefore

be reduced, decreasing the size of the accelerator. Laser-based accelerators might therefore, in the future, bridge the gap between the small number of advanced machines and the large number of potential users, as more compact and affordable particle and x-ray sources become available in university-scale laboratories. In addition, the particular characteristics of these sources could lead to new applications not previously envisioned. The femtosecond pulse duration of both the electron beam and the x-rays provides a time resolution from which many applications may benefit.

As high-power lasers have become more available, many groups have started to work on this subject. The field has greatly benefited from this, as more advanced experiments have been carried out and more subtle physical effects investigated. In addition to improving the stability of the beams, the challenges of fully understanding the interactions taking place and making measurements of some of the key characteristics of the particle beams more precisely still remain. Due to the novelty of the process, many techniques used at conventional accelerators can not be used here, or must be adapted, e.g. for single-shot operation. The true potential of this new kind of accelerator is therefore not yet fully known.

The work described in this thesis was performed within the framework of the European MAXLAS project, the aim of which was to combine laser and accelerator physics, by stimulating collaboration between the Lund Laser Centre and the MAX-lab synchrotron laboratory in Lund. This work can therefore be considered a contribution to bridging the gap between these two fields, as lasers are used to accelerate particles. It is also a sign that this rapidly growing field of research is attracting more and more attention from the accelerator community, as a possible alternative to conventional technology. The quality, stability and repetition rate of the beams produced are however, still a long way from that achieved with conventional accelerator technology. If these issues are not addressed, laser-driven particle acceleration will never reach users in the accelerator community or other fields.

When I started my PhD studies, electrons and protons were already being accelerated at the Lund High-Power Laser Facility using the multi-terawatt laser. During my time, more systematic investigations were carried out. The laser system was upgraded allowing for new types of experiments, and investigations on the laser plasma wiggler started and are presented here. Most of my time has been devoted to laser-driven electron acceleration and x-ray production, which is the biggest part of this thesis. I have also participated in proton acceleration experiments, which are summarised in the last chapter. While many other laboratories around the world are focusing on producing beams with higher and higher energies with increasing laser power, the issues that have been and will be pursued in Lund are to find means of in-

creasing the energy of the particles, by using advanced targets, for example, and improving stability.

Being at the crossroads of many fields such as optics, accelerator physics, plasma physics and x-ray science, this work is truly multidisciplinary. This is reflected in this thesis, where many different subjects are dealt with. The whole process has been studied, from laser development in Paper **I**, to the production of linear plasma waves in Papers **II** and **III**, via electron beams in Papers **IV**, **V** and **VI**, to their application as x-ray sources in Papers **IV** and **V**. Proton acceleration has also been studied and ways of improving the beams, using novel techniques, are discussed in Papers **VII** and **VIII**.

LASER WAKEFIELD ACCELERATION OF ELECTRONS

This chapter presents the theoretical background behind laser wakefield acceleration. The concept of a plasma accelerator is introduced, starting from the laser, including the generation of plasma waves, and finally the trapping and acceleration of electrons. The pulse evolution of the laser due to relativistic nonlinear plasma optics is also discussed. In the last section, scaling and limits on energy gain are discussed.

2.1 Introduction

In laser wakefield acceleration (LWFA), electrons reach relativistic energies over a very short distance. When interacting with a plasma, the ponderomotive force of an intense femtosecond laser pulse “pushes” electrons away from their equilibrium position while the ions remain at rest. The restoring force due to space charge, makes the electrons oscillate, generating a high-amplitude plasma wave. This wave produces strong longitudinal fields that can be used to accelerate electrons. These propagate close to the speed of light behind the laser pulse. Trapped electrons are in phase with the accelerating structure and can “surf the wave”, similarly to a surfer catching a wave in the sea. Acceleration forces are a thousand times stronger than those achieved in accelerators based on conventional technology. These beams have a small angular divergence and a significant charge (about 10–1000 pC).

The theoretical work behind nonlinear wave propagation in plasmas is more than 50 years old [5]. However, it was not until 1979 that Tajima and Dawson proposed the use of these waves to accelerate electrons to high energies [6]. In their pioneering

¹Emittance is an important concept for any particle accelerator. It describes the area occupied by the particles in the momentum phase space. In a low-emittance beam all the particles are confined in a small space and have nearly the same momentum.

work, they already saw the potential of using short-pulse lasers to efficiently generate plasma waves and accelerate electrons, thus converting the transverse oscillation field of a laser beam into longitudinal fields, suitable for accelerating particles. The emergence of increasingly powerful lasers allowed the efficient acceleration of electrons, but they exhibited thermal spectral distributions [7, 8]. A milestone in this research was the production of quasi-monoenergetic beams in 2004, using lasers whose pulse duration was shorter than the plasma wavelength [9–11]. Acceleration of electrons up to a GeV was soon demonstrated by increasing the acceleration length to a few centimetres [12]. Using colliding pulses, beams of high quality both in terms of stability and energy spread, were also achieved [13]. In addition to providing a compact accelerator, laser wakefields have unique properties due to the small scale of the process. Recent measurements have shown that the pulse duration of the electron bunch is only a few femtoseconds [14, 15], and the transverse emittance¹ only $\sim 1\pi$ mm mrad [16, 17]. Note that plasma waves can also be driven by an electron beam instead of a laser pulse [18], and in the future it might even be possible to use a proton beam as a driver [19]. This chapter gives an overview of the main principles of laser plasma wakefield acceleration of electrons. A more extensive description of this subject can be found in Ref. [20]. Papers **II** and **III** present experimental work on the production of linear plasma waves and their characterisation. In the experiments presented in Papers **IV** to **VI**, electrons were accelerated by nonlinear plasma waves, and some of their characteristics were studied.

2.2 Laser parameters

A laser beam is described by an electromagnetic wave. Its propagation in a medium is governed by Maxwell's equations and the wave equation. A laser beam is confined in space and the electric and magnetic fields, **E** and **B**, are represented mathematically by a gaussian function in space. A laser pulse can also, in most cases, be described by a gaussian function in the spectral and time domains. For a linearly polarised pulse in vacuum, the electric field of the laser pulse is then:

$$\begin{aligned} \mathbf{E}(r, z, t) &= \frac{E_0}{2} \frac{w_0}{w(z)} \exp\left(-\frac{r^2}{w^2(z)}\right) f(t, z) \\ &\times \Re\left(\exp\left(-ik_0z - i\frac{k_0r^2}{2R(z)} + i\phi(z)\right)\right) \mathbf{e}_x, \end{aligned} \quad (2.1)$$

where w_0 is the waist of the pulse (radius of the beam at $1/e$ of the electric field in the focal plane $z = 0$) and $k_0 = \omega_0/c$ is the wavenumber corresponding to a light frequency of ω_0 and

wavelength λ_0 . $R(z)$ is the radius of curvature of the wavefront and $\phi(z)$ the Gouy phase shift. The time evolution of \mathbf{E} is given by $f(t, z)$, where τ is the pulse duration at full width half maximum (FWHM):

$$f(t, z) = \exp \left[-2\ln(2) \left(\frac{t-z/c}{\tau} \right)^2 + i\omega_0 t \right]. \quad (2.2)$$

The Rayleigh length, $z_r = \pi w_0^2 / \lambda_0$, represents the position at which the intensity is half the intensity in the focal plane. The intensity is defined as the average over one optical cycle of the Poynting vector:

$$I = c^2 \epsilon_0 \langle \mathbf{E} \times \mathbf{B} \rangle = \frac{c\epsilon_0}{2} |E|^2, \quad (2.3)$$

where ϵ_0 is the vacuum permittivity and c the speed of light in vacuum. The peak intensity, I_0 , in the focal plane, the peak power, P_0 , and the total energy, U , in the pulse are related through:

$$\begin{aligned} U &= \iiint_{-\infty}^{\infty} I(x, y, t) dx dy dt = \pi c \epsilon_0 \int_{-\infty}^{\infty} \int_0^{\infty} |\mathbf{E}(r, 0, t)|^2 r dr dt \\ \Rightarrow I_0 &= \frac{2P_0}{\pi w_0^2} \\ \Rightarrow P_0 &= 2\sqrt{\frac{\ln(2)}{\pi}} \frac{U}{\tau} \simeq \frac{U}{\tau}, \end{aligned} \quad (2.4)$$

The electric and magnetic fields can be conveniently related to the electromagnetic potentials \mathbf{A} and Φ through:

$$\begin{aligned} \mathbf{E} &= -\nabla\Phi - \frac{\partial\mathbf{A}}{\partial t}, \\ \mathbf{B} &= \nabla \times \mathbf{A}. \end{aligned} \quad (2.5)$$

These potentials are not uniquely defined and other solutions can be found using a gauge transformation. We will use the normalised vector potential, \mathbf{a} :

$$\mathbf{a} = \frac{e\mathbf{A}}{m_e c}, \quad (2.6)$$

where m_e is the electron rest mass and e the elementary charge. The maximum value of a is often used to characterise the pulse intensity and is given by:

$$a_0 = \sqrt{\frac{e^2}{2\pi^2 \epsilon_0 m_e^2 c^5} \lambda_0^2 I_0} \simeq 0.86 \lambda [\mu\text{m}] \sqrt{I [10^{18} \text{W/cm}^2]}. \quad (2.7)$$

Table 2.1. Laser parameters (w_0 in μm and z_r in mm) for the different focusing optics used in the experiments. The waist of the beam before the optics is 35 mm (the real beam profile is actually closer to a super-gaussian beam than a gaussian beam). The peak intensity ($[10^{18}] \text{ W/cm}^2$), electric field E_0 ($[\text{TV/m}]$) and normalised vector potential are calculated for a pulse energy of 0.7 J and a pulse duration of 40 fs, which were typically used in the experiments.

f	0.15	0.45	1.5
w_0	4.4	13.1	43.7
z_r	0.075	0.67	7.5
I_0	54.9	6.1	0.55
E_0	20.3	6.8	2
a_0	5.1	1.7	0.5

In our experiments, a parallel beam is focused onto the interaction point to reach high intensities. In order to apply the equations given above, one must first know the focal spot waist, w_0 . This can be calculated using gaussian optics, where the focal spot profile is also described by a gaussian function, as a gaussian beam remains gaussian when focused. For a focusing optics of focal length f and a beam radius W , the spot size is given by :

$$w_0 = \frac{\lambda_0}{\pi W} f. \quad (2.8)$$

Table 2.1 summarises these different parameters for the different focusing optics used in the experiments described in this thesis.

Finally, an electron in the laser field moves according to the Lorentz equation:

$$\frac{d\mathbf{p}}{dt} = -e(\mathbf{E} + \mathbf{v} \times \mathbf{B}), \quad (2.9)$$

and an energy equation

$$\frac{d}{dt}(\gamma mc^2) = -e(\mathbf{v}\mathbf{E}), \quad (2.10)$$

where the momentum, \mathbf{p} , and the relativistic factor, γ , are given by:

$$\mathbf{p} = \gamma m_e \mathbf{v},$$

$$\gamma = \sqrt{1 + \frac{p^2}{m_e^2 c^2}} = \frac{1}{\sqrt{1 - \frac{v^2}{c^2}}}. \quad (2.11)$$

2.3 Ionisation

The laser pulse interacts first with neutral atoms, in which the electrons are bound to the atoms. Because of the strong electric field at the leading edge of the laser pulse, the medium becomes ionised, as the electric field of the laser is of the same order of magnitude as the field experienced by the electrons in the Coulomb potential of the atom. Depending on the strength and wavelength of the laser, different models are used to explain the ionisation process. If the field is weak, the Coulomb potential remains almost unperturbed. Ionisation can still occur either by multi-photon absorption (see Fig. 2.1 (a)) or by absorbing one energetic photon, e. g. an XUV photon. For strong fields the Coulomb potential is strongly perturbed by the laser field, as illustrated in Fig. 2.1 (b). When the laser field approaches the field strength of the Coulomb potential, the electrons have a certain probability of tunnelling through the potential barrier and ionisation takes place. This

process is used to produce high-order harmonics of the fundamental laser wavelength. When the intensity is very strong, the potential barrier decreases even more, and the electrons are no longer bound to the atom. This process is called over-the-barrier ionisation (OTBI). The limit between these different regimes depends on which electron of which atom is considered, as a valence electron is much easier to ionise than a core electron.

In the case of a hydrogen atom, the binding electric field strength is $E_a = e/(4\pi\epsilon_0 a_B^2) \simeq 5.1 \times 10^{11} \text{ V/m}$, where a_B is the Bohr radius. The corresponding intensity, $I_a = 3.5 \times 10^{16} \text{ W/cm}^2$, is found using Eq. 2.3. In this case, a laser intensity of $I_0 > I_a$ guarantees ionisation, although ionisation can occur below this limit as seen previously, through multi-photon absorption or tunnelling. OTBI occurs if the barrier modified by the laser field falls below the ionisation energy of the ion, ε_{ion} . The Coulomb potential modified by a stationary homogeneous electric field, E , is given by: $V(x) = -Ze^2/(4\pi\epsilon_0 x) - eEx$, and illustrated in Fig. 2.1 (b). In the case of an oscillating laser field, E is the electric field at a given time. By determining the position of the barrier, x_{max} , we find the threshold field strength for which OTBI occurs and the corresponding intensity using Eq. 2.3, called the appearance intensity:

$$I_{app} = \frac{\pi^2 c \epsilon_0^3 \varepsilon_{ion}^4}{2 Z^2 e^6}, \quad (2.12)$$

where Z is the charge of the created ions [21]. The appearance intensity of some ions of interest for the experiments described in this thesis are given in Table 2.2. We see immediately that, for $I > 10 \times 10^{18} \text{ W/cm}^2$ and for the typical gases used in the experiments, such as helium and hydrogen, the leading edge of the focused pulse fully ionises the medium. The most intense part of the pulse therefore interacts with a plasma and from now on it will be assumed that the laser is interacting with free charges. As we will see later, ionisation can, however, not be completely ignored as effects such as ionisation defocusing can influence the interaction. In this case, more advanced models must be used to correctly account for effects such as tunnelling and multi-photon ionisation, in order to correctly calculate the ionisation rates.

2.4 Plasma waves

As seen in the previous section, when interacting with hydrogen or helium, the leading edge of an ultra-intense laser pulse ($I_0 > 10^{18} \text{ W/cm}^2$) fully ionises the medium. Most of the laser pulse therefore interacts with free charges, i.e. a plasma. Ions are much heavier than electrons and are considered to be stationary on the timescale we are interested in. If some electrons are displaced

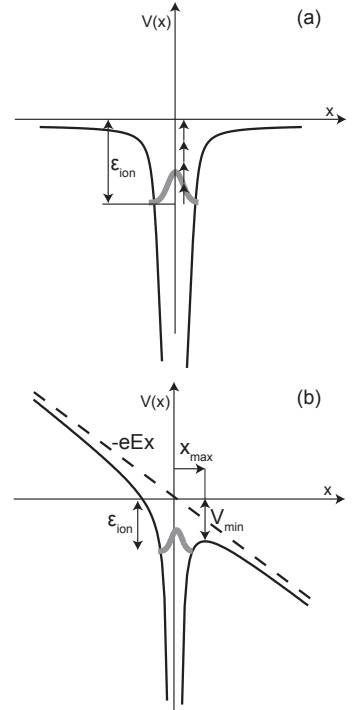


Figure 2.1. Illustration of the ionisation process by a laser field. For a weak electric field, the Coulomb potential of the atom is not perturbed as shown in (a). Ionisation can still occur through multi-photon absorption. In (b), a strong electric field perturbs the Coulomb potential and electrons are no longer bound to the atom.

Table 2.2. Ionisation energy in [eV] and corresponding appearance intensity in [Wcm^{-2}] for some ions for the over-the-barrier ionisation model.

Ion	ε_{ion}	I_{app}
H ⁺	13.61	1.4×10^{14}
He ⁺	24.59	1.4×10^{15}
He ²⁺	54.42	8.8×10^{15}
N ⁵⁺	97.9	1.5×10^{16}
N ⁷⁺	667.1	1.6×10^{19}
Ar ⁸⁺	143.5	2.6×10^{16}
Ar ¹⁰⁺	478.7	2.1×10^{18}
Ar ¹⁶⁺	918	1.1×10^{19}
Ar ¹⁸⁺	4426.4	4.7×10^{21}

from their equilibrium, they will feel a restoring force due to space charge, and will oscillate around an equilibrium position. The motion of the electrons can be described by Maxwell's equations. In a homogeneous medium, the solutions are the sum of the Fourier mode: $\mathbf{E}(\mathbf{r}, t) = \int \mathbf{E}_k e^{i(\mathbf{k}\mathbf{r}-\omega t)} d\mathbf{k}$ and $\mathbf{B}(\mathbf{r}, t) = \int \mathbf{B}_k e^{i(\mathbf{k}\mathbf{r}-\omega t)} d\mathbf{k}$. In the same way, the electron velocity in the plasma can be written: $\mathbf{v}(\mathbf{r}, t) = \int \mathbf{v}_k e^{i(\mathbf{k}\mathbf{r}-\omega t)} d\mathbf{k}$. Finally, using $-e\mathbf{E} = m_e \dot{\mathbf{v}}$ and $\mathbf{J} = -en_e \mathbf{v}$, we can also write the electron current density as the sum of Fourier modes: $\mathbf{J}_k = in_e e^2 \mathbf{E}_k / (\omega m_e)$. Maxwell's equations for the Fourier mode then become:

$$\begin{aligned}\mathbf{k} \times \mathbf{E}_k &= \omega \mathbf{B}_k, \\ \mathbf{k} \times \mathbf{B}_k &= \mu_0 n_e \frac{e^2 \mathbf{E}_k}{\omega m_e} - \mu_0 \epsilon_0 \omega \mathbf{E}_k.\end{aligned}\quad (2.13)$$

For $\mathbf{k} \parallel \mathbf{E}_k$, it follows that $\mathbf{B}_k = 0$, and the electron density oscillates at the plasma frequency, ω_p :

$$\omega_p [\text{s}^{-1}] = \sqrt{\frac{e^2 n_e}{\epsilon_0 m_e}} \simeq 56400 \sqrt{n_e [\text{cm}^{-3}]}, \quad (2.14)$$

where n_e is the electron density.

For $\mathbf{k} \perp \mathbf{E}_k$, Eq. 2.13 gives solutions for the propagation of electromagnetic waves in the plasma. We find the following dispersion relation, where ω_0 is the frequency of the laser:

$$\omega_0 = \sqrt{\omega_p^2 + k^2 c^2}. \quad (2.15)$$

For $\omega_0 > \omega_p$, the solution is real and the wave propagates through the plasma. The medium is called underdense, and is typically an ionised gas. For $\omega_0 < \omega_p$, the solution is imaginary and the wave is described as being evanescent. When the medium is overdense, typically an ionised solid, the wave does not propagate, and the laser is absorbed or reflected. The critical density defines the boundary between these two regions, and is given by:

$$n_c [10^{21} \text{cm}^{-3}] = \frac{\omega_0^2 \epsilon_0 m_e}{e^2} \simeq \frac{1.12}{\lambda^2 [\mu\text{m}]}.\quad (2.16)$$

We can then find the corresponding phase and group velocity:

$$\begin{aligned}v_{ph} &= \frac{\omega_0}{k} = \sqrt{c^2 + \frac{\omega_p^2}{k^2}}, \\ v_g &= \frac{d\omega_0}{dk} = \frac{c^2 k}{\sqrt{\omega_p^2 + k^2 c^2}}.\end{aligned}\quad (2.17)$$

The plasma wave travels behind the driving laser pulse with a phase velocity equal to the group velocity of the laser. We can then define the normalised phase velocity, β_p , and relativistic factor, γ_p , associated with the plasma wave as:

$$\begin{aligned}\beta_p &= \frac{v_g}{c} = \sqrt{1 - \frac{n_e}{n_c}}, \\ \gamma_p &= \frac{1}{\sqrt{1 - \beta_p^2}} = \sqrt{\frac{n_c}{n_e}}.\end{aligned}\tag{2.18}$$

Of course, it is impossible to track the motion of each particle in the plasma. The electrons are therefore treated as a fluid. In this case, we rewrite the Lorentz equation (Eq. 2.9) for the plasma fluid momentum motion:

$$\frac{d\mathbf{p}}{dt} = \left(\frac{\partial}{\partial t} + \mathbf{v} \cdot \nabla \right) \mathbf{p} = -e [\mathbf{E} + \mathbf{v} \times \mathbf{B}],\tag{2.19}$$

where \mathbf{p} is given by Eq. 2.11. Together with the continuity equation:

$$\frac{\partial n_e}{\partial t} + \nabla \cdot (n_e \mathbf{v}) = 0,\tag{2.20}$$

and Poisson's equation:

$$\nabla \cdot \mathbf{E} = -\nabla^2 \Phi = \frac{\rho}{\epsilon_0} = -e \frac{n_e - n_{e0}}{\epsilon_0} = -e \frac{\delta n_e}{\epsilon_0},\tag{2.21}$$

we obtain a set of equations that can be used to describe the motion of the electrons due to their interaction with the intense laser field. δn_e describes the density perturbation associated with the plasma wave.

Let us first consider the case of a small sinusoidal perturbation of the electron density, $\delta n_e = \delta n_{e0} \sin [\omega_p(z/c - t)]$. With Poisson's equation, we see that this density modulation produces a longitudinal electric field that can be used to accelerate particles:

$$\nabla \cdot \mathbf{E} = -\frac{e\delta n_e}{\epsilon_0} \Rightarrow \mathbf{E}(z, t) = \frac{\delta n_{e0} e}{k_p \epsilon_0} \cos [\omega_p(z/c - t)] \mathbf{e}_z.\tag{2.22}$$

We observe that the electric field is out of phase by $-\pi/4$ relative to the electron density.

2.4.1 The ponderomotive force

Although collective motion of electrons is possible in a plasma, we will first consider the case of the interaction with a single electron. At high intensity, both the electric and the magnetic fields are capable of moving particles. In the case of a plane wave, an electron will not gain any energy from the laser field, as the time-average of the field is zero. For linearly polarised light, the electron oscillates in the plane of polarisation due to the

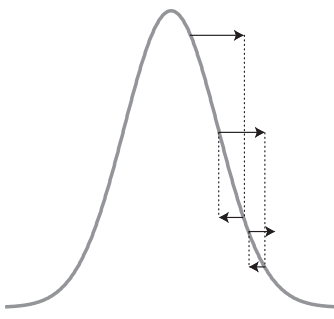


Figure 2.2. Schematic explanation of the ponderomotive force. Because of the intensity gradient, electrons are pushed away from high-intensity regions.

force produced by the electric field component of the wave. At relativistic laser intensities, the strength of the electric field will drive the electron to velocities approaching c , and the $\mathbf{v} \times \mathbf{B}$ term in Eq. 2.9 becomes important. It pushes the electron in the direction of propagation of the wave. The net effect is therefore just a forward translation of the electron, and it will remain at rest once the laser pulse has passed. We see that the laser field is able to move electrons, but is not suitable for producing the high longitudinal electric field required for particle acceleration. As we will see later, a plasma medium produces collective motion of electrons, which makes it possible to translate the laser energy into longitudinal momentum.

Under the experimental conditions used in the present work, the wave is far from a plane wave, as the laser beam is focused, creating strong radial intensity gradients. The so-called ponderomotive force pushes electrons away from regions of high intensity and they will gain velocity in this process, as illustrated in Fig. 2.2. In the linear limit, i.e. $a_0 \ll 1$, the first-order motion of an electron exposed to the laser field is the quiver velocity:

$$\mathbf{v}_q = c\mathbf{a}, \quad (2.23)$$

as $m_e \partial \mathbf{v}_q / \partial t = -e\mathbf{E} = e\partial\mathbf{A}/\partial t$. Assuming a small perturbation of the velocity, $\mathbf{v} = \mathbf{v}_q + \delta\mathbf{v}$, the second-order motion becomes (using Eq. 2.19):

$$\begin{aligned} \frac{d\delta\mathbf{p}}{dt} &= -m_e [(\mathbf{v}_q \cdot \nabla) \mathbf{v}_q + c\mathbf{v}_q \times (\nabla \times \mathbf{a})] \\ &= -m_e c^2 [(\mathbf{a} \cdot \nabla) \mathbf{a} + \mathbf{a} \times (\nabla \times \mathbf{a})] \\ &= -m_e c^2 \nabla \frac{a^2}{2} = \mathbf{F}_p, \end{aligned} \quad (2.24)$$

where $\mathbf{F}_p \propto -\nabla(I\lambda_0^2)$ is the ponderomotive force [22]. The vector potential is averaged over one laser cycle and from now on, only the envelope of the laser pulse is considered: $a(t) = \langle a \rangle = a_0 \exp[-2\ln(2)(t/\tau)^2]$.

For $a_0 > 1$, relativistic effects come into play, and these must be taken into account when calculating the ponderomotive force. As we will see in the next section, it arises naturally in the calculation of plasma wave generation. It is found [23, 24], that the nonlinear ponderomotive force can be written as:

$$\mathbf{F}_{pn} = -m_e c^2 \nabla \langle \gamma \rangle, \quad (2.25)$$

where $\langle \gamma \rangle$ is the relativistic factor of an electron in the laser field, given by Eq. 2.11 and averaged over one laser cycle.

2.4.2 Plasma wave generation

So far, we have seen that longitudinal waves can propagate in a plasma, and we will now investigate how they can be created.

One way to bring about the displacement of electrons is to use an intense laser pulse. The electrons are pushed away from their equilibrium position by the ponderomotive force introduced in Section 2.4.1. A general equation for the production of plasma waves is given here. We will assume a cold plasma, i.e. the thermal motion of the electrons is negligible compared to the typical oscillation energy due to the laser field.

The electromagnetic fields of the laser are described by the electromagnetic potentials given in Eq. 2.5, and the fluid equation (Eq. 2.19) can be written in the Coulomb gauge ($\nabla \cdot \mathbf{A} = 0$) as:

$$\left(\frac{\partial}{\partial t} + \mathbf{v} \cdot \nabla \right) \mathbf{p} = e \left(\nabla \Phi + \frac{\partial \mathbf{A}}{\partial t} - \mathbf{v} \times \nabla \times \mathbf{A} \right). \quad (2.26)$$

Using Eq. 2.11 and the identity $\nabla p^2 = 2[(\mathbf{p} \cdot \nabla) \mathbf{p} + \mathbf{p} \times (\nabla \times \mathbf{p})]$, we find that:

$$(\mathbf{v} \cdot \nabla) \mathbf{p} = m_e c^2 \nabla \gamma - \mathbf{v} \times (\nabla \times \mathbf{p}). \quad (2.27)$$

Inserting this into Eq. 2.26, we finally obtain:

$$\frac{\partial}{\partial t} \mathbf{p} = e \nabla \Phi + e \frac{\partial \mathbf{A}}{\partial t} - m_e c^2 \nabla \gamma, \quad (2.28)$$

where $\mathbf{v} \times \nabla \times (\mathbf{p} - e\mathbf{A}) = 0$ is due to the initial condition that there is no perturbation before the laser pulse arrives. We identify here the term $-m_e c^2 \nabla \gamma$ as the relativistic ponderomotive force mentioned previously. This equation, together with Eqs. 2.20 and 2.21 describe the generation of a plasma wave by a laser pulse. We will now explore some solutions and properties of these equations in different cases relevant to the work described in this thesis. Linear plasma waves were generated and used in the experiments described in Papers II and III, and the results from the next section are applicable. In the experiments presented in Papers IV to VI, the nonlinear case should be considered, and will be treated later.

The linear case

To obtain some physical insight, we start with the simple case of a small pump strength where the density perturbation is small, $\delta n_e \ll n_e$. Eq. 2.20 becomes:

$$\frac{\partial \delta n_e}{\partial t} + n_{e0} \nabla \cdot \mathbf{v} = 0. \quad (2.29)$$

Using Eqs. 2.21 and 2.28, we finally obtain :

$$\left(\frac{\partial^2}{\partial t^2} + \omega_p^2 \right) \frac{\delta n_e}{n_{e0}} = c^2 \nabla^2 \frac{a^2}{2}. \quad (2.30)$$

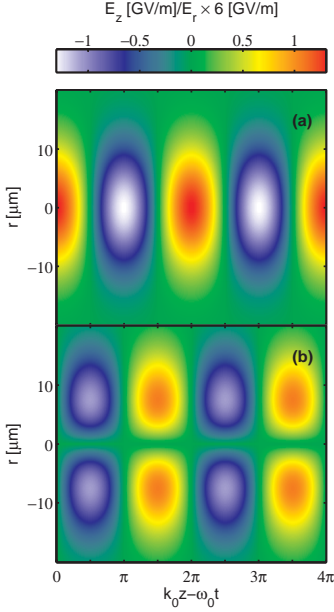


Figure 2.3. Longitudinal (a), and radial (b) electric fields for $n_e = 1 \times 10^{19} \text{ cm}^{-3}$ generated by a laser pulse with $a_0 = 0.2$, $w_0 = 15 \mu\text{m}$ and $\tau = 30 \text{ fs}$.

This equation describes a forced oscillator, where the restoring force is represented by space charge ($\omega_p^2 \delta n e / n_{e0}$) and the driving force by the ponderomotive force of the laser ($c^2 \nabla^2 a^2 / 2$). The solution of Eq. 2.30 for the longitudinal and radial electric fields, for a gaussian laser pulse with $a_0 \ll 1$ is [25]:

$$\begin{aligned} E_z(r, z, t) &= f(r) \cos(k_0 z - \omega_0 t), \\ E_r(r, z, t) &= -f(r) \frac{4c}{\omega_p} \frac{r}{w_0^2} \sin(k_0 z - \omega_0 t), \end{aligned} \quad (2.31)$$

where

$$f(r) = E_p \sqrt{\frac{\pi}{2}} a_0^2 \frac{\omega_p \tau}{4\sqrt{2 \ln 2}} \exp\left(-\frac{\omega_p^2 \tau^2}{16 \ln 2}\right) \exp\left(-\frac{2r^2}{w_0^2}\right), \quad (2.32)$$

and $E_p = m_e c \omega_p / e$. The first noticeable feature is that both fields are oscillating, and that they are out of phase, as can be seen in Fig. 2.3 where the longitudinal (a), and radial (b), electric fields are shown. There are regions where the longitudinal field is either accelerating or decelerating and the radial field is either focusing or defocusing. The longitudinal field is maximum on-axis, where the radial field is zero. The region of interest is where we find an accelerating and focusing field for electrons, i.e. for $\pi/2 \leq k_0 z - \omega_0 t \leq \pi$ modulo 2π . Finally, we also notice that the field strength scales with $I_0 \lambda^2 = a_0^2$.

The pulse duration, τ , also influences the amplitude of the fields. At a fixed electron density, $f(\tau)$ is maximum for:

$$c\tau = \frac{\sqrt{2 \ln 2}}{\pi} \lambda_p \approx 0.37 \lambda_p. \quad (2.33)$$

This resonance condition is illustrated in Fig. 2.4, and can be understood as follows. When the laser pulse arrives, the electrons are “kicked” forward by the ponderomotive force (a). They will then experience a restoring force due to space charge and oscillate at the plasma frequency, ω_p , given by Eq. 2.14 (b). Halfway through, the electrons experience a ponderomotive “kick” in the other direction, as the sign of the gradient has changed (c). Clearly, if the pulse duration corresponds to roughly half a plasma period, this effect will increase the oscillation due to resonance.

At the electron densities required to produce high-amplitude plasma waves, the plasma wavelength is short (only $\sim 10 \mu\text{m}$ for $n_e = 10^{19} \text{ cm}^{-3}$). The advent of short-pulse lasers, i.e. laser with pulses that are of the order of the plasma wavelength, allowed the production of much larger amplitude plasma waves, as the resonance condition could be fulfilled. Before that, it was necessary to use other configurations to generate plasma waves, as the pulse duration of the laser was not matched to the plasma wavelength.

First, the beat wave schemes used two long-pulse laser beams that interfered to create short-pulse interference [26, 27]. Later, pulses a couple of plasma wavelengths long were used. They generated a small-amplitude plasma wave that modulated the refractive index (see Section 2.8). In return, this modulated the laser pulse envelope and amplified the plasma wave. This feedback mechanism ultimately separated the laser pulse into many shorter pulses separated by the plasma wavelength. This process, known as self-modulation wakefield, can produce high-amplitude waves [28, 29].

The nonlinear case

The experiments reported in Papers IV to VI were performed in regimes where $a_0 > 1$. The assumption of a small pump strength is no longer valid, and Eq. 2.30 can not be used. The more general case of an arbitrary pump strength in one dimension, where analytical solutions can be found, will be explored. The three-dimensional (3D) problem is not solvable analytically, and complex numerical tools are necessary to deal with it. Most of the physics can, however, be extracted from a 1D model [30–32].

We start by making a coordinate transformation to a frame moving with the laser pulse, $t \rightarrow \tau$, $z - v_g t \rightarrow \xi$, where v_g is the group velocity of the pulse. We further use the quasi-static approximation $\partial/\partial\tau = 0$. Poisson's equation then becomes:

$$\frac{\partial^2 \phi}{\partial \xi^2} = k_p^2 \left(\frac{n_e}{n_{e0}} - 1 \right), \quad (2.34)$$

where $\phi = e\Phi/(m_e c^2)$ is the normalised electrostatic potential. As we are considering the 1D problem, we can decompose the electron motion into the direction of propagation, $v_z = c\beta_z$, and in the transverse direction. The relativistic factor then becomes:

$$\gamma^2 = \frac{\gamma_\perp^2}{1 - \beta_z^2}, \quad (2.35)$$

where $\gamma_\perp^2 = 1 + a^2/2$ is the relativistic Lorentz factor associated with the electron quiver velocity introduced in Eq. 2.23. For the longitudinal motion, Eq. 2.28 becomes:

$$\frac{\partial p_z}{\partial t} = m_e c \frac{\partial(\gamma\beta_z)}{\partial t} = m_e c^2 \frac{\partial(\phi - \gamma)}{\partial z}, \quad (2.36)$$

where the contribution from the term $\partial A/\partial t$ is not relevant because it oscillates only in the transverse direction. Writing this equation and Eq. 2.20 in the quasi-static approximation gives $(1 - \beta_z) = n_{e0}/n_e$, which can be inserted into Eq. 2.34, and we finally obtain a differential equation for ϕ :

$$\frac{\partial^2 \phi}{\partial \xi^2} = k_p^2 \gamma_p^2 \left[\beta_p \left(1 - \frac{\gamma_\perp^2}{\gamma_p^2(1 + \phi)^2} \right)^{-1/2} - 1 \right]. \quad (2.37)$$

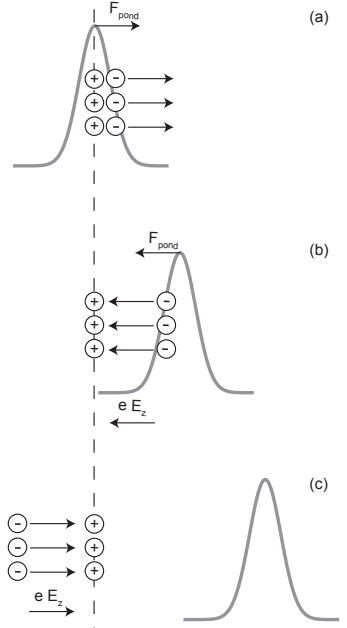


Figure 2.4. Schematic illustration of the resonance condition for plasma wave generation. Two ponderomotive “kicks” occur, one on each side of the pulse.

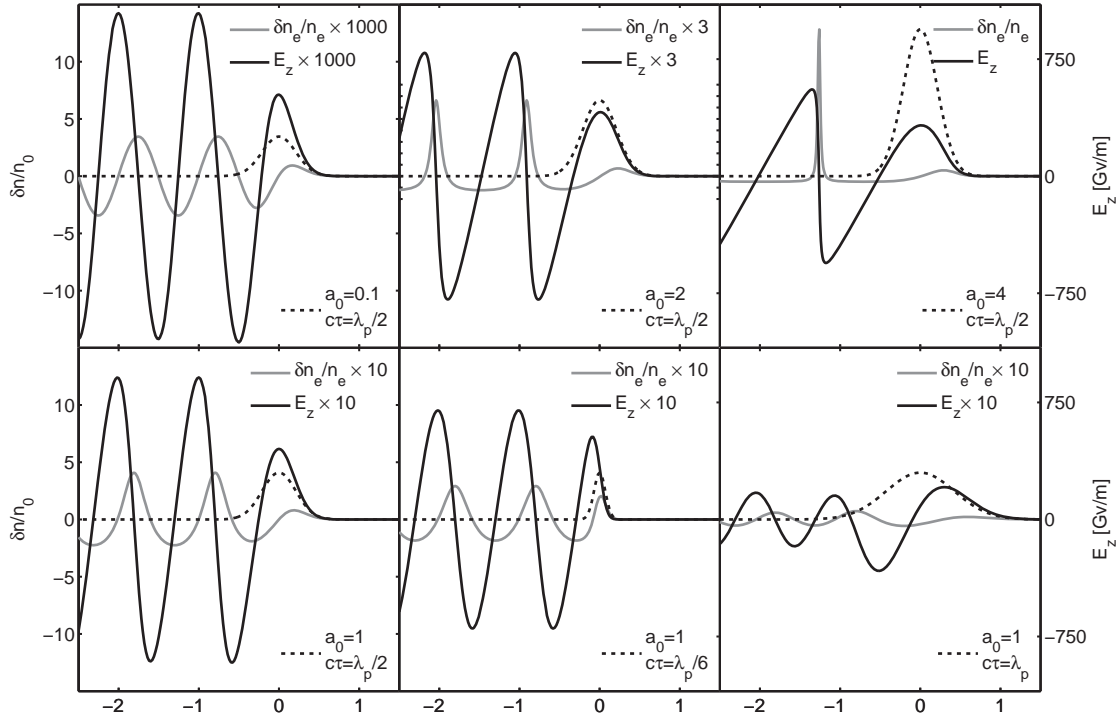


Figure 2.5. Waves generated by different pump strengths and pulse durations at an electron density of $n_e = 1 \times 10^{19} \text{ cm}^{-3}$. The solid black lines represent the longitudinal electric field, the solid grey lines the electron density perturbation, and the dashed lines the laser pulse envelope.

This equation can be solved for ϕ , and the electric field can be inferred through $E = -E_p \partial \phi / \partial \xi$. The density perturbation, $\delta n_e = n_e - n_{e0}$, is then obtained using Eq. 2.34.

This equation was solved for different laser parameters and the results are shown in Fig. 2.5. On the first row, a_0 increases while the pulse duration remains constant. Several features can be noted. First, as expected, the plasma wave becomes more and more nonlinear as a_0 increases. For $a_0 = 0.1$, the wave is sinusoidal, but for $a_0 = 4$ the electric field has a sawtooth shape with very steep gradients. The field strength is 3 orders of magnitude greater than in the linear case. We further notice that the nonlinear plasma wavelength, λ_{np} , increases for large values of a_0 : $\lambda_p < \lambda_{np} \propto \lambda_p E_{max} / E_p \propto \lambda_p a_0$ for $a_0^2 \gg 1$. In two dimensions, the gaussian profile of the laser pulse produces higher amplitude waves at the centre than further away from the optical axis. The plasma wavelength will therefore be larger at the centre and decrease with distance from the optical axis. The wavefront of the plasma wave is thus curved and exhibits a horseshoe structure.

The second row in Fig. 2.5 shows the effect of varying the

pulse duration while keeping a_0 fixed. As was seen in the previous section, the pulse duration should be roughly half a plasma period long in order to generate plasma waves efficiently. Longer or shorter pulses will still drive a wake, but not as efficiently. In fact, as long as the pulse is kept short ($c\tau \lesssim \lambda_p$), changes in pulse duration do not produce very different plasma waves. Figure 2.6 shows the maximum electric field as a function of pulse duration calculated with Eq. 2.37 for different values of a_0 . We see that the optimal pulse duration is the same for all values of a_0 and approximately at $0.37\lambda_p$. The curves are broader at high values of a_0 due to the increase in λ_{np} .

2.4.3 Wavebreaking

A natural question is how high the density perturbation can be and ultimately, thus what is the maximum electric field achievable. This is important because, for a fixed acceleration length, this will define the maximum energy to which the electrons can be accelerated. In the linear case, the maximum density perturbation is $\delta n_e/n_{e0} = 1$. As a matter of fact, this point will never be reached as the wave will break before this. This is a very important concept because, as we will see later, it can be used to self-inject electrons into the wakefield.

Wavebreaking occurs when the speed of the electrons producing the wave reaches the velocity of the wave itself. When this happens, the wave structure loses coherence. The maximum achievable electric field is then given by:

$$E_{wb0} = E_p = \frac{m_e c \omega_p}{e}. \quad (2.38)$$

In a fully relativistic 1D case, an analytical solution for a cold plasma can be found using Eq. 2.37. The equation breaks down when the electron density becomes singular, i.e. when $\partial^2 \phi / \partial \xi^2 \rightarrow \infty$. This occurs when $\gamma_\perp = \gamma_p(1 + \phi)$ and, as shown in Ref. [32], it corresponds to a maximum electric field given by:

$$E_{wb} = E_{wb0} \sqrt{2(\gamma_p - 1)}. \quad (2.39)$$

Thus, in the nonlinear case, the maximum electric field can be greater than E_{wb0} .² Thermal effects in the plasma reduce the wavebreaking threshold [33, 34]. The wave structure can still be maintained above the wavebreaking threshold if the driver remains constant long enough, which is the case when the laser pulse is propagating in the plasma.

2.5 The bubble regime

While the 3D linear case was presented in Section 2.4.2, the nonlinear regime has only been considered in the 1D case. This ap-

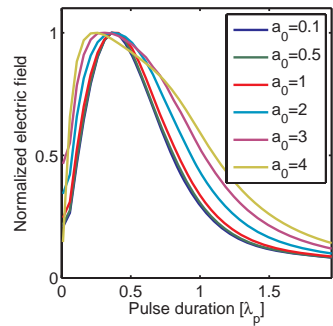


Figure 2.6. Maximum electric field as a function of pulse duration in a 1D nonlinear model for different laser pulse intensities.

²For a plasma of electron density $n_e = 1 \times 10^{19} \text{ cm}^{-3}$, $E_{wb0} = 304 \text{ GV/m}$. In the nonlinear case, $E_{wb} = 5E_{wb0} = 1502 \text{ GV/m}$.

proach gives a very good understanding of the physics involved, but a 3D model is necessary to obtain a full picture of the process. Different models have been developed in this 3D nonlinear regime, giving a good understanding of the process [35, 36]. However, it requires laborious numerical calculations, known as particle-in-cell (PIC) simulations, which are beyond the scope of this thesis.

For $a_0 \gg 1$ electrons are completely expelled from the focal spot region by the ponderomotive force of the laser, while the ions remain approximately stationary because of their inertia. This produces an electron-free region behind the laser pulse, called a bubble. A schematic view of the bubble regime is shown in Fig. 2.7. Electrons from the background plasma stream around the bubble and, depending on their initial position, their transverse deflection will be more or less important. In the so-called matched condition, the ponderomotive force of the laser and the restoring force due to the charge separation of the ion cavity balance each other, thus defining the radius of the bubble, r_b . Under these conditions, only a thin layer of electrons streams around the bubble, and the most ideal wake is produced. It has been found that the waist of the laser pulse, w_0 , has the appropriate value when:

$$k_p w_0 = k_p r_b = 2\sqrt{a_0}. \quad (2.40)$$

This means that if we increase a_0 , the size of the laser focal spot should be increased accordingly. For sufficiently intense and ultra-short lasers, $a_0 > 4$, the bubble resembles a spherical cavity [36]. For $2 < a_0 < 4$ electron blow-out still occurs, but the cavity deviates slightly from a spherical shape. It should be noted here that for most experiments the initial waist does not have the appropriate size and the pulse duration is not resonant, but through pulse evolution in the plasma, it reaches the matched size in both space and time, as will be discussed in Section 2.8.

The fields inside the bubble can be represented by the fields of a sphere, uniformly charged, propagating at a relativistic velocity. The longitudinal field inside the bubble is independent of the radius, allowing for uniform acceleration, and increases almost linearly, $\partial E_z / \partial \xi \simeq 1/2$ [37]. The radial fields are linearly focusing preserving the transverse emittance. The bubble regime is, therefore, particularly interesting for electron acceleration.

Electrons streaming around the bubble will be trapped if they reach a velocity close to the bubble phase velocity by the time they reach the back of the bubble; this is comparable to wavebreaking. The electrons are then attracted by the fields inside the bubble, enter the bubble and are accelerated. This regime produces high-quality beams with quasi-monoenergetic features, thanks to the effect of beam loading which will be introduced in Section 2.6.1. In addition, an important part of the laser pulse is in the electron-free zone, and propagates as in vacuum, unaffected by the interaction, which might also be an advantage.

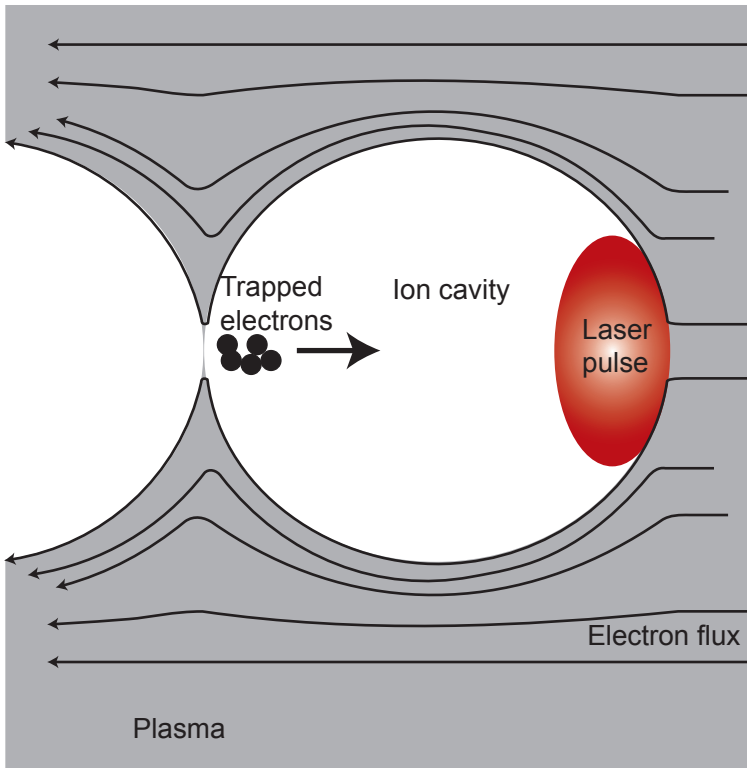


Figure 2.7. Schematic illustration of the bubble regime in the co-moving frame. Electrons follow different trajectories around the bubble depending on their initial position. Some electrons can be trapped by the fields inside the bubble and be accelerated.

2.6 Acceleration and dephasing

The longitudinal dynamics of a test electron injected into the potential of the wave can be described using the results presented in Section 2.4.2. This electron has a momentum of $p_z = \gamma m_e v_z = m_e c u_z$, where u_z is the normalised momentum. Its motion can be described using the hamiltonian formalism [31] and Eq. 2.36:

$$\begin{aligned} \frac{d\xi}{dt} &= c \frac{u_z}{\gamma} - c \beta_p &= \frac{\partial \mathcal{H}}{\partial u_z}, \\ \frac{du_z}{dt} &= c \left[\frac{\partial \phi}{\partial \xi} - \frac{\partial \gamma}{\partial \xi} \right] &= -\frac{\partial \mathcal{H}}{\partial \xi}. \end{aligned} \quad (2.41)$$

where $\gamma^2 = \gamma_{\perp}^2 + u_z^2$ and:

$$\mathcal{H}(u_z, \xi) = \sqrt{\gamma_{\perp}^2 + u_z^2} - \beta_p u_z - \phi(\xi). \quad (2.42)$$

\mathcal{H} is the hamiltonian describing the motion of a test electron in the plasma wave in a given electron orbit $\mathcal{H}(u_z, \xi) = H_c = \text{const.}$ The momentum of a test electron in the potential of the wave is then given by:

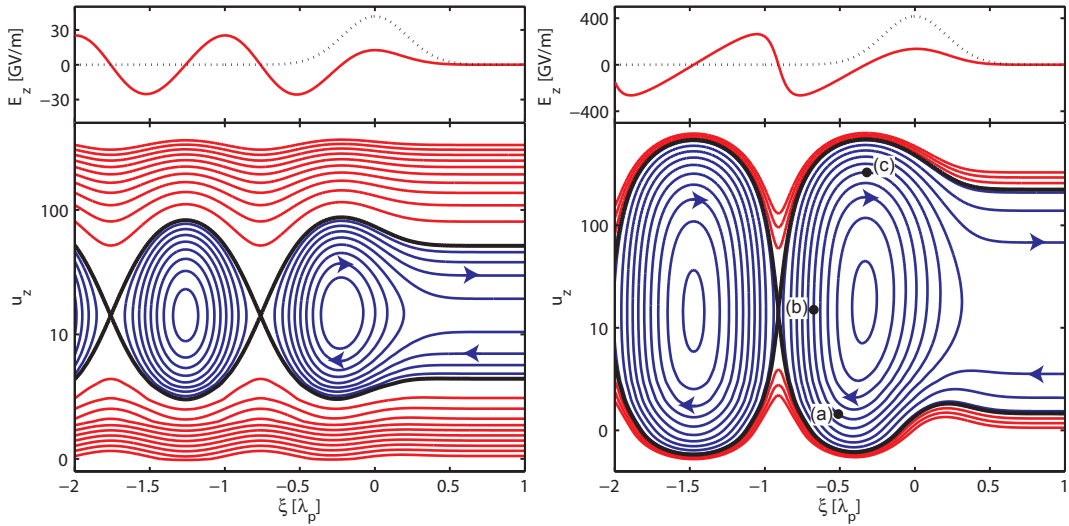


Figure 2.8. Orbits of electrons injected into the wakefield for $a_0 = 0.5$ (on the left) and $a_0 = 2$ (on the right), and $c\tau = \lambda_p/2$. The trace at the top of the figures shows the corresponding longitudinal electric field. The electron density is $n_e = 1 \times 10^{19} \text{ cm}^{-3}$, which corresponds to $\gamma_p \approx 13$.

$$u_z(\xi) = \beta_p \gamma_p^2 (H_c + \phi(\xi)) \pm \gamma_p \sqrt{\gamma_p^2 (H_c + \phi(\xi))^2 - \gamma_{\perp}^2}. \quad (2.43)$$

where $\gamma_{\perp} = 1 + a^2/2$.

Several of these orbits are drawn in Fig. 2.8 for $a_0 = 0.5$ and $a_0 = 2$, and $c\tau = \lambda_p/2$. The first feature of interest is that there are two types of orbit. Electrons in an orbit drawn in blue are trapped by the wake. They are then accelerated by the wakefield, reach maximum energy and are eventually decelerated. Electrons following an orbit drawn in red are not trapped and do not gain any net momentum from the plasma wave. Different “buckets” can also be seen in Fig. 2.8, where electrons can be trapped and accelerated. In the first bucket (on the right of the figure), some orbits are open, which means that trapped electrons will not remain inside the bucket after reaching their maximum energy. When injection relies on wavebreaking, the electrons are mostly trapped in this bucket, because this is where the wave amplitude is greatest [38]. Electrons trapped in the second bucket can follow closed orbits and can be accelerated and decelerated many times, as they can not escape the potential of the wake.

The wave propagates at a phase velocity corresponding to $\gamma_p \approx 13$. If the test electron has the right momentum and phase, it will be trapped at the point (a) and be accelerated by the wake. If it is trapped with a momentum smaller than γ_p , the electron is

slower than the wake and moves backwards in the wave frame. At (b) the electron reaches the phase velocity of the wave and turns around in the wave frame, as its velocity is now slightly greater than the phase velocity of the plasma wave. Finally, at (c), the electron reaches its maximum energy and should be extracted (the interaction should stop). If it is not, it will be decelerated again as the electron outruns the plasma wave. The point at which the electron reaches its maximum energy is called the dephasing point.

The separatrix (black line) divides the two regions between trapped and untrapped electrons. Electrons outside the separatrix have a momentum that is either too low or too high to be trapped by the wake. The lowest orbit is the fluid orbit corresponding to electrons initially at rest, and is followed by the background plasma electrons. These electrons are not trapped and therefore background electrons are not accelerated by the wake. It is therefore necessary to inject electrons by other means (see Section 2.7). The separatrix can be found at the point where the upper and lower orbits meet, which is at $\gamma_p^2(H_c + \min(\phi(\xi)))^2 - \gamma_\perp^2 = 0$, which corresponds to the hamiltonian $H_s = \gamma_\perp/\gamma_p - \min(\phi(\xi))$. An electron will gain maximum energy when following the separatrix.

Figure 2.9 (a) shows the separatrix of the second bucket in phase space for different values of a_0 . First, we observe that the separatrix becomes wider as a_0 increases, due to the increase in nonlinear plasma wavelength, λ_{np} , discussed previously. For small a_0 , the separatrix is symmetric. For large values of a_0 , it becomes asymmetric and a lower momentum is required for an electron to be trapped. For the largest values of a_0 , even an electron moving backwards in the laboratory frame (negative values of u_z) would be trapped. Note that, even in this case, the background electrons would not be trapped as the fluid orbit is always lower than the separatrix. Further increasing a_0 causes $\gamma_{\min} = \gamma_p$ and corresponds to the wavebreaking limit.

Figure 2.9 (b) shows the separatrix of the first bucket plotted in the laboratory frame. We see the dephasing of the test electron trapped at the minimum energy possible, which then follows the separatrix. This particular orbit gives the electron the maximum energy gain. The distance after which the maximum energy is reached is the dephasing length, and it can be seen that it increases as a_0 increases. In the linear case the dephasing length is given by:

$$L_d = \frac{n_c}{n_e} \lambda_p. \quad (2.44)$$

and does not depend on a_0 . In the nonlinear case, however, as the plasma wavelength increases with increasing a_0 , so does the dephasing length. In the 3D nonlinear case, the dephasing length

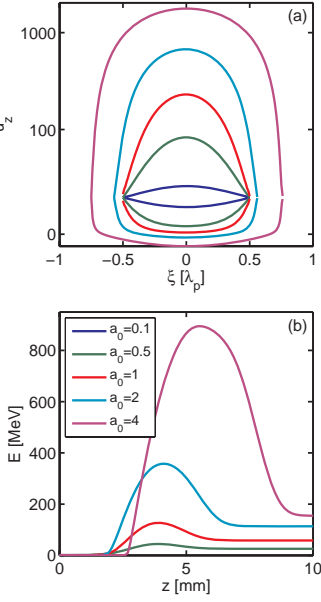


Figure 2.9. The separatrix is plotted for different values of a_0 in the phase space in (a) and in the laboratory frame in (b). In (a) the separatrix of the second bucket is shown, while (b) shows the separatrix of the first bucket.

is given by [39]:

$$L_d^{3D} = \frac{4}{3} \sqrt{a_0} \frac{c\omega_0^2}{\omega_p^3}. \quad (2.45)$$

Finally, the maximum value reached in each orbit in Fig. 2.9 (b) corresponds to the maximum energy that can be achieved during acceleration. Ideally, the interaction should therefore stop at this point. Figure 2.9 corresponds to a 1D nonlinear model and the different quantities (such as length and energy) scale differently in three dimensions, as will be discussed in Section 2.9.

2.6.1 Beam loading

So far, we have assumed that the electrons trapped by the wake do not participate in the interaction. However, these electrons will also produce an electric field and drive their own wake, and thus modify the shape of the plasma wave and the acceleration process [40]. The electron bunch is shorter than half the plasma wavelength and the electric field generated by the electrons is decelerating, as the field is positive in the first half of the plasma wavelength. This can be seen in Fig. 2.10 (b), which shows a simulation of the field generated by an electron bunch. However, as we will see later, in some cases beam loading is beneficial for the quality of the electron beam. Although it was not studied directly during the course of this work, it is an important concept and is in fact responsible for the production of quasi-monoenergetic electron beams in the bubble regime.

Let us consider the 1D case presented in Section 2.4.2, which will provide some insight into the physics. We add a term representing the electron beam in Poisson's equation (2.34):

$$\frac{\partial^2 \phi}{\partial \xi^2} = k_p^2 \left(\frac{n_e}{n_{e0}} + \frac{n_b(\xi)}{n_{e0}} - 1 \right), \quad (2.46)$$

where $n_b(\xi) = n_{b0} f(\xi)$ represents the electron beam distribution in the co-moving coordinate system. Eq. 2.37 becomes then:

$$\frac{\partial^2 \phi}{\partial \xi^2} = k_p^2 \gamma_p^2 \left[\beta_p \left(1 - \frac{\gamma_\perp^2}{\gamma_p^2 (1 + \phi)^2} \right)^{-1/2} - 1 \right] + k_p^2 \frac{n_b(\xi)}{n_{e0}}. \quad (2.47)$$

Figure 2.10 shows the longitudinal electric field calculated using this equation at an electron density of $n_{e0} = 1 \times 10^{19} \text{ cm}^{-3}$ for different parameters. The electron bunch is represented by a gaussian distribution, $f(\xi)$, in time with a FWHM pulse duration of 10 fs and different peak electron densities n_{b0} . The electric field produced by a laser pulse with $\tau = 30$ fs and $a_0 = 1$ and an electron bunch with $n_{b0} = 0.09 n_{e0}$ are shown separately in (a) and (b). In (c) both effects are taken into account and different features can be observed. First, the electric field decreases, in particular,

the back of the electron bunch experiences a lower electric field than without beam loading, and some electrons therefore gain less energy. Beam loading effects will therefore decrease the energy of the electron beam. Secondly, for an optimal charge, the electric field is flattened by beam loading, and the entire electron bunch experiences the same electric field. This reduces the energy dispersion of the electron beam, thus improving the quality of the beam. For a smaller charge density of $n_{b0} = 0.04n_{e0}$, the effect of beam loading is small, as shown in (d). Finally, for a large charge, the electric field is strongly influenced by beam loading effects, as can be seen in (e) for $n_{b0} = 0.17n_{e0}$. The plasma waves generated by the laser and the electron beam interfere negatively and some electrons are decelerated, giving energy back to the plasma wave. This limits the amount of charge (it is actually a current limit) that can be accelerated [41].

In the 3D nonlinear regime, the trapped electron beam influences the trajectory of the electrons around the bubble, which in turn influences the longitudinal field. The scalings are different in the 3D geometry, but a similar effect is observed [42]. As can be seen in Fig. 2.10, the flattening of the electric field is possible only with an increasing electric field ($dE_z/d\xi > 0$). If the electron is trapped in the region $-\lambda_p < \xi < -\lambda_p/2$, the field is decreasing in the linear regime, and the electrons at the front of the bunch experience a stronger accelerating field than the electrons at the back of the bunch. In the case of self-injection, the electrons are trapped in this region and in this 1D model, it would not possible to achieve monoenergetic beams. However, in the bubble regime it was discussed in Section 2.5, that the fields are increasing linearly, and beam loading effects are able to flatten the electric field for self-injected electrons. When the wave starts to break, electrons are trapped due to self-injection. As seen previously, this reduces the amplitude of the wave and therefore self-injection stops. This limits the self-injection process to a very short time and, together with the flattening of the electric field, allows for the production of quasi-monoenergetic electron beams.

2.7 Injection

Up to this point, we have discussed the generation of plasma waves by a laser pulse. It was also shown in the previous section that if a test electron has enough initial momentum, it is trapped in this accelerating structure and accelerated to high energies. However we have also seen that if the initial energy of the electron is too low, it will not be trapped by the wakefield. A good injection scheme is therefore important for wakefield accelerators. Electrons must be injected into the wakefield with the right energy and at the right moment.

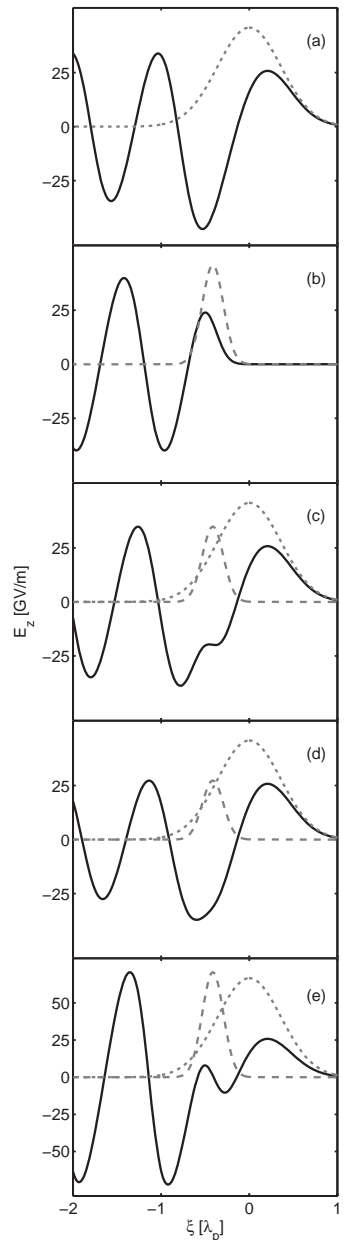


Figure 2.10. Effect of beam loading on the plasma wave generated by a 30 fs laser pulse with $a_0 = 1$. In (a), the plasma wave is generated only by the laser pulse and in (b) only by the electron beam. In (c)-(e), both effects are taken into account for a electron beam charge of $n_{b0} = 0.09n_{e0}$ in (c), $n_{b0} = 0.04n_{e0}$ in (d) and $n_{b0} = 0.17n_{e0}$ in (e).

2.7.1 Self-injection

As shown in Section 2.4.3, at high laser intensity, highly nonlinear plasma waves are created, which eventually break. Electrons from the background can be trapped in the wakefield and accelerated. Usually, the wave does not break immediately, because the laser pulse has to evolve sufficiently in space and time to reach the matched condition and produce high-amplitude waves. If the electron density or the laser energy is too low, wavebreaking will not occur, no electrons are self-injected, and no beam is observed. This is the self-injection threshold, which is a crucial parameter for laser plasma accelerators. A study of self-injection using experimental data is reported in Paper VI and discussed in Section 5.3. By operating just above the self-injection threshold, it is possible to limit the injection time and improve the quality of the beam in terms of the energy spread, for example, as seen in Section 2.6.1. This mechanism was responsible for the observation of electron beams described in Papers IV to VI. In the experiments presented in Papers II and III, no electron beams were observed. As the laser intensity was relatively low, the plasma waves did not break and self-injection did not occur.

2.7.2 Alternative injection schemes

Although self-injection has the advantage of automatically trapping electrons in the wave, it relies on the production of very nonlinear plasma waves and on wavebreaking, which are by nature unstable processes. The resulting electron beams are therefore highly unstable, with low shot-to-shot reproducibility. Therefore, it is an advantage to work in the linear or moderately nonlinear regime. In this case, electrons must be injected into the accelerating structure by some other means. By limiting the injection time of the electrons, beams with narrow energy spread could be achieved. The type of linear plasma waves characterised in Papers II and III would be suitable for accelerating injected electrons over long distances.

Injection can be controlled by using two colliding laser pulses. One pulse drives the plasma wave without self-injecting electrons, while the second pulse injects electrons by stochastically heating some electrons that can be trapped and accelerated further. This allows very localised injection and produces stable beams with a narrow energy spread [13]. The different beam parameters can be further controlled by varying the point of injection in the gas jet, or by varying the energy of the injection pulse [43]. It has been suggested that an even smaller energy spread could be achieved by colliding circularly polarised pulses in a cold injection scheme [44].

A gradient in density also allows for localised injection, which occurs at a lower density than in the case of self-injection. In this scheme, the wavelength of the plasma wave rapidly expands and allows electrons from the background to be trapped. The density gradient can be produced by inserting a razor blade into the gas flow [45], or by firing another laser pulse which will locally remove electrons by the ponderomotive force [46]. Beams with better stability and/or better energy spread can be achieved with this relatively simple method [47].

Finally, adding a small amount of a different gas to the main gas also produces more stable beams [48, 49]. All the electrons in the dominant gas (helium or hydrogen) are liberated through ionisation by the leading edge of the laser pulse. They stream around the bubble and when trapped have a certain momentum. As can be seen from Table 2.2, the ionisation energy of multiply ionised atoms of the contaminant gas (argon or nitrogen, for example) is very high and these electrons are released only at the maximum intensity. Created on-axis with almost no momentum, these electrons are directly trapped by the wakefield, allowing for more stable acceleration. Injection also occurs at lower electron density than with pure hydrogen or helium, and higher electron energies can be thus achieved, due to the longer dephasing length. For example, electrons have been accelerated up to an energy of 1.4 GeV using this method [50]. This method was investigated in connection with the experiment reported in Paper VI, and electron beams of good quality were indeed observed at a lower density than with pure helium.

These schemes rely on operating below the self-injection threshold. It is therefore important to know when self-injection occurs, and the model presented in Paper VI is therefore important in these cases.

External injection

External injection was not studied in the current work, but it is relevant to present it briefly here, as it could be the most suitable method of accelerating electrons with the linear plasma waves produced in the experiments reported in Papers II and III. Historically, the first acceleration of electrons by a wakefield structure was performed by external injection of electrons into the plasma [26, 28, 29]. As seen in the previous section, if electrons are introduced into the accelerating structure with the appropriate energy, they will be trapped and accelerated. In order to be trapped by the wave, their energy should be typically a few MeV. This method has the advantage of making it possible to operate at moderate laser intensities, where the plasma wave will still be linear and therefore more stable, and more tunable beams are expected. The accelerating fields are also weaker, but the electrons

can be accelerated over a longer distance. However, this method requires very good timing between the injected electron bunch and the plasma wave. One scheme is to inject a sub-picosecond electron bunch just before the laser pulse [51]. The electron bunch is then overtaken by the laser pulse, compressed, and accelerated by the wakefield.

The source of the externally injected electrons could be a traditional RF injector, which has the advantage of delivering a well-controlled beam. However, they are difficult to operate. All-optical injection is also possible, by generating low-energy electrons with a gas jet, and then injecting them in the wakefield by either guiding them into the wake with magnets or positioning the gas jet very close to the second acceleration stage. This has been demonstrated recently using a single laser pulse in two different gas cells [52, 53]. By using two different pulses, it might be possible to adjust the timing between the two accelerating structures and inject the electrons in the right phase of the second accelerating wave. The advantage of this scheme is that it can be repeated several times, creating a multi-stage accelerator and possibly reaching very high electron energies.

2.8 Laser propagation in underdense plasma

When considering the plasma wave dynamics, it was assumed that the laser pulse propagates like a rigid photon bullet, which is far from reality. First of all, a real laser pulse is focused to achieve high intensity and it experiences diffraction. Then the interaction itself modifies the laser pulse. A density gradient in the plasma produces refraction and diffraction. Nonlinear relativistic plasma optics influences the pulse further, as the refractive index of a plasma depends on the electron density, electron density gradients and relativistic effects. The propagation of the laser pulse in a plasma is strongly affected by this changing refractive index as it, among other things, transversally focuses the beam, compresses the pulse and shifts its frequency [54].

The refractive index of the plasma, η , can be obtained from the dispersion relation (Eq. 2.15):

$$\eta = \frac{ck}{\omega_0} = \sqrt{1 - \frac{\omega_p^2}{\gamma_{\perp}\omega_0^2}} \approx 1 - \frac{1}{2} \frac{n_e}{\gamma_{\perp}n_c}, \quad (2.48)$$

for an underdense plasma, i.e. $\omega_p^2/(\gamma\omega_0^2) \ll 1$. The gamma factor, $\gamma_{\perp} = 1 + a^2/2$, is due to the increase in the relativistic mass of the electron, mainly due to its wiggling motion in the strong laser field. If we consider the weakly relativistic case, i.e. small density modulations, we obtain:

$$\eta \simeq 1 - \frac{1}{2} \frac{\omega_p^2}{\omega_0} \left(1 + \frac{\delta n_e}{n_{e0}} - \frac{a^2}{2} - \frac{2\delta\omega_0}{\omega_0} \right) \quad (2.49)$$

It is clear that the refractive index can be modulated through changes in either electron density, laser intensity or laser frequency. Only particular cases of transverse and longitudinal modulations of η for various values of electron density and laser intensity ($\delta\omega_0 = 0$) will be considered below.

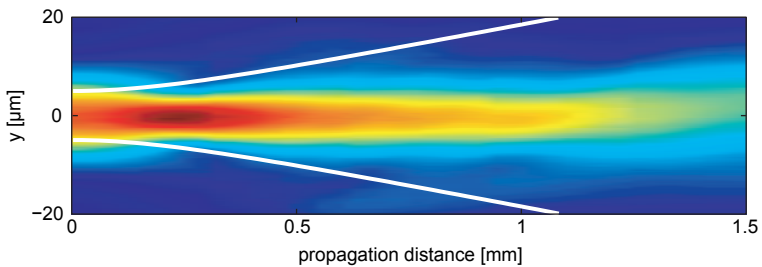
2.8.1 Ionisation defocusing

The first term in Eq. 2.49 shows that the refractive index depends on the number of free electron as $\eta \simeq 1 - \omega_p^2/2\omega_0^2 = 1 - n_e(r, t)/2n_c$, with n_c given by Eq. 2.16. When focusing a gaussian pulse into the plasma, the centre of the beam is much more intense than its wings. Thus, there will be more ionisation at the centre, producing a gradient in refractive index acting as a negative lens. As shown in Section 2.3, ionisation occurs at relatively low laser intensities, and this effect is especially important at the leading edge of the pulse, where the intensity is close to the appearance intensity of the corresponding ion. For moderately intense pulses, ionisation defocusing actually prevents the medium from being fully ionised as the pulse becomes more and more defocused as it propagates through the gas, and its intensity decreases. One way to circumvent this is to focus the laser pulse on the edge of the gas medium. The maximum intensity will therefore reach the medium and directly ionise it completely. This is done by using gas media with a sharp density gradient, such as the supersonic gas jets used in the experiments reported in Papers V and VI. In addition, the intensity of the pulses used in the experiments reported here are several orders of magnitude above the intensity required for ionisation. In the case of hydrogen or helium, the apparent intensity is low (see Table 2.2) and at the peak intensity of the pulse, the medium is fully ionised and ionisation defocusing disappears. It might, however, still be present away from the centre of the beam where the intensity in the wings is around the ionisation intensity. For other gases such as argon, the multiple ionisation stages produce a long density gradient, and most of the laser pulse experience defocusing. For this reason, hydrogen or helium was used in the experiments reported in Papers II to VI.

2.8.2 Self-focusing

Relativistic effects also affect the refractive index according to the term $a(r, t)^2/2$ in Eq. 2.49. Because of the transverse intensity gradient of the gaussian beam, the refractive index has a curved transverse profile, according to the transverse profile of a^2 . The

Figure 2.11. 2D OSIRIS (PIC) simulation [55] of self-focusing for a laser beam focused by an $f/9$ focusing optics for $n_e = 7 \times 10^{18} \text{ cm}^{-3}$. Colour indicates the laser intensity. The white line shows the natural diffraction of the laser beam (courtesy of S. P. D. Mangles).



refractive index is greater at the centre, where a is at its maximum, producing a focusing effect called relativistic self-focusing. This effect balances diffraction and allows the beam to be guided over many Rayleigh lengths. Diffraction is counteracted when the power of the beam is above the critical power for self-focusing P_c , given by [56, 57]:

$$P_c[\text{GW}] = \frac{8\pi\epsilon_0 m_e^2 c^5}{e^2} \frac{n_c}{n_e} \simeq 17.3 \frac{n_c}{n_e}. \quad (2.50)$$

It should be noted here that although the threshold for self-focusing is a power threshold, the intensity must be sufficiently high to fully ionised the medium first.

Other effects due to variation of the electron density must also be taken into account, which makes the dynamics of self-focusing highly complex [58]. In the case of ultra-short pulses, the ponderomotive force of the laser ploughs through the plasma and strongly perturbs the electron density. There is an increase in density in front of the pulse, which defocuses the leading part of the pulse and cancels the relativistic effects [30]. This part of the pulse is, however, depleted as it drives the plasma wave (as will be shown in Section 2.8.4), and it does not have time to diffract. Cavitation occurs behind the pulse, and the trailing part of the pulse is still well guided. This allows ultra-short laser pulses to be guided [59]. Guiding due to relativistic effects is, however, more efficient and long pulses are more efficiently guided over long distances [60, 61]. A simulation of self-focusing using the same parameters as in the experiment presented in Paper V is shown in Fig. 2.11, where it can be seen that the pulse can be guided over a distance longer than the Rayleigh length.

In the bubble regime, the pulse will evolve due to self-focusing until it reaches the appropriate size given by Eq. 2.40. The peak intensity can then be written as $I_0 = k_p P_0 / (2\pi a_0)$ using Eq. 2.4. Eq. 2.7 gives then the value of the vector potential, once the matched size is reached by self-focusing: $a_{0m} = 2 \sqrt[3]{P_0/P_c}$, which depends on the peak power of the laser pulse and the electron density.

2.8.3 Frequency shift and pulse compression

So far, we have studied the effect of transverse variations of the refractive index on the laser pulse. We will now consider the longitudinal changes in refractive index. The main contribution to the refractive index are the perturbations in electron density and the longitudinal variation of a . As η varies, the group and phase velocity of the laser also vary, according to:

$$v_{ph} = \frac{c}{\eta} = c \left[1 + \frac{1}{2} \frac{\omega_p^2}{\omega_0^2} \left(1 + \frac{\delta n_e}{n_{e0}} - \frac{a^2}{2} - \frac{2\delta\omega_L}{\omega_0} \right) \right], \quad (2.51)$$

$$v_g = \frac{\partial\omega}{\partial k} = c \left[1 - \frac{1}{2} \frac{\omega_p^2}{\omega_0^2} \left(1 + \frac{\delta n_e}{n_{e0}} - \frac{a^2}{2} - \frac{2\delta\omega_L}{\omega_0} \right) \right]. \quad (2.52)$$

Figure 2.12 shows the effect of the density perturbation due the plasma wave and the relativistic factor on the group and phase velocity. In (a) the density perturbation generated by a laser pulse (dashed line) with $a_0 = 0.1$ and $c\tau = \lambda_p/2$ is shown. It can be seen in Fig. 2.12 (b) that different parts of the pulse experience different group velocities. The group velocity at the back of the laser pulse is higher than at the front of the pulse. As a result of this, the laser pulse is compressed by the plasma. Note that in the bubble regime the back of the pulse is in vacuum and, therefore, also travels faster than the leading part of the pulse.

The variation in phase velocity observed in Fig. 2.12 (c) leads to frequency shifts. The wavefronts bunch together and spread apart with decreasing and increasing phase velocities, respectively. The frequency will therefore increase (also known as photon acceleration), or decrease (also known as photon deceleration). The introduced frequency shift can be calculated using:

$$\delta\omega = \omega_0 \int_0^L \frac{\partial\eta}{\partial\xi} dz, \quad (2.53)$$

and is illustrated in Fig. 2.12 (d) for $L = 2$ mm. It is clear that the spectral content of the pulse is modified, as different values of $\delta\omega$ are found at the position of the laser pulse. The intense part of the laser pulse is found where $\delta\omega < 0$ and therefore a red shift will be observed, which is proportional to the plasma wave amplitude and the interaction length. As the length is usually known, the amplitude of the plasma wave can be inferred from the amount of red shift. This was the main diagnostic used to determined the amplitude of the linear plasma waves produced in the experiments discussed in Papers II and III.

Note that frequency shifts and pulse compression, do not occur independently of each other. The laser spectrum is therefore

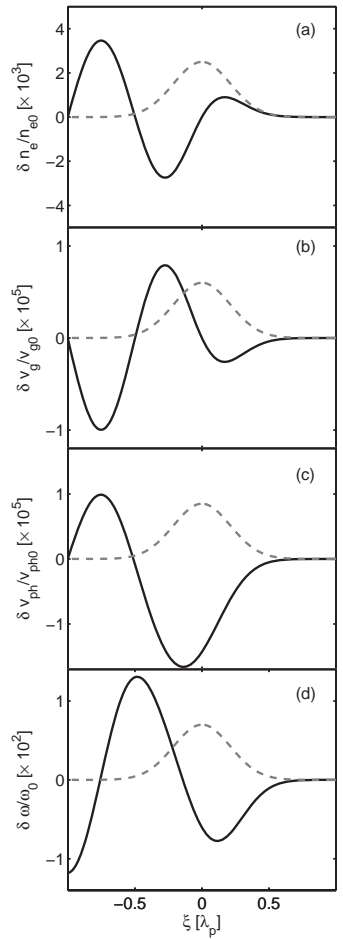


Figure 2.12. Effect of the density modulation and relativistic effects on the group and phase velocities in (b) and (c) and on the spectrum in (d) for $a_0 = 0.1$ and $c\tau = \lambda_p/2$. In (a) the density modulation is shown in black. The laser pulse is shown by the dashed lines.

broadened by the plasma wave, while the pulse is simultaneously compressed in time. It has been found experimentally that a pulse with an initial duration of 38 fs could be compressed to 10–14 fs [62, 63]. As shown in Section 2.4.2, the plasma wave generation is optimal for pulse durations shorter than the plasma wavelength, which is often not the case for the initial pulse duration. The pulse duration can, however, be shortened by the compression in the plasma wave, and a plasma wave can still be efficiently excited, as pulse evolution allows the pulse to be resonant.

2.8.4 Pump depletion

As it drives the plasma wave, the laser pulse loses energy, a process known as pump depletion. The laser energy is transferred to the plasma wakefield, and will eventually be transformed into heat. The depletion length is therefore defined as the length of the plasma wave at which the laser energy is completely depleted. The energy density associated with the plasma wave can be written as $U = 1/2\epsilon_0 E_z^2$, and is contained in a volume $V = \pi w_0^2 L_{pd}$. In the 1D linear regime $E_z = a_0^2 \omega_p$, and by comparing it with the energy contained in the laser pulse, the depletion length in the linear regime can be expressed as:

$$L_{pd}^L = \frac{c\omega_0^2 \tau}{\omega_p^2 a_0^2}. \quad (2.54)$$

In the nonlinear case, an alternative has been proposed in which the laser pulse loses energy from the front of the pulse [64]. The leading edge of the pulse is gradually etched backwards with a velocity given by:

$$v_{etch} \simeq \frac{c\omega_p^2}{\omega_0^2} \quad (2.55)$$

This model is based on nonlinear 1D effects, and it has been found that it is also valid in the 3D case [39]. The laser will be fully depleted after the depletion length:

$$L_{pd}^{NL} = \frac{c}{v_{etch}} c\tau \simeq \frac{\omega_0^2}{\omega_p^2} c\tau. \quad (2.56)$$

2.9 Limit on energy gain and scaling laws

The maximum energy gain achievable in a laser plasma accelerator depends on the product of the electric field strength and the acceleration length. While the electric field is ultimately limited by wavebreaking, the acceleration length is limited by the diffraction of the laser pulse, the dephasing length or the pump depletion length. All these quantities scale differently in the 1D

Table 2.3. Summary of the different scaling laws from the linear theory and the 3D nonlinear theory. The value of a_0 determines when each theory should be applied and w_0 is the appropriate value of the laser waist. The dephasing length, L_d , the pump depletion length, L_{pd} , the plasma wavelength, λ_p , the associated relativistic factor, γ_p , and the average electric field normalised to $E_p = m_e c \omega_p / e$, E_z , have different dependence on the electron density and the normalised vector potential in the linear and nonlinear cases. ΔW is the energy gain of an electron accelerated over the dephasing length.

Model	a_0	w_0	L_d	L_{pd}	λ_p	γ_p	E_z	$\Delta W/m_e c^2$
Linear	< 1	$2\pi/k_p$	$\frac{\lambda_p \omega_0^2}{\omega_p^2}$	$\frac{c\omega_0^2 \tau}{\omega_p^2 a_0^2}$	$\frac{2\pi c}{\omega_p}$	$\frac{\omega_0}{\omega_p}$	a_0^2	$\frac{\omega_0^2}{\omega_p^2} a_0^2$
3D nonlinear	> 2	$2\sqrt{a_0}/k_p$	$\frac{4}{3} \frac{c\omega_0^2}{\omega_p^3} \sqrt{a_0}$	$\frac{c\omega_0^2 \tau}{\omega_p^2}$	$\sqrt{a_0} \frac{2\pi c}{\omega_p}$	$\frac{\omega_0}{\sqrt{3}\omega_p}$	$\frac{1}{2} \sqrt{a_0}$	$\frac{2\omega_0^2}{3\omega_p^2} a_0$

linear and the 3D nonlinear regimes, as can be seen from Table 2.3 (we have already encountered some of these values in the previous sections). In the linear case, analytical expressions can be derived, whereas in the nonlinear case, 3D PIC simulations are required. Ref. [39] gives a good overview of how the different quantities scale in the highly nonlinear regime ($a_0 > 2$). These two regimes were encountered during the work presented in this thesis. In the experiments reported in Papers II and III, the value of a_0 was 0.2, i.e. the linear regime. In the experiments described in Papers V and VI, the 3D nonlinear regime was reached ($a_0 > 2$) through pulse evolution, in particular self-focusing as $P > P_c$. In the experiment presented in Paper IV, pulse evolution also occurred. From the simulations, it could be seen that the intensity barely reached $a_0 = 2$, i.e. an intermediate regime. Note that some values have been derived previously in the 1D nonlinear regime. They can, however, not be used for realistic scaling as a 3D model is required in the nonlinear regime.

The energy gain of an electron accelerated by the wakefield is determined by:

$$\Delta W = -e \int_0^L E_z(z) dt, \quad (2.57)$$

where E_z is the longitudinal electric field experienced by the electron at a distance z from the point of injection. L is the acceleration distance, which is limited by diffraction of the laser pulse, the dephasing length or the pump depletion length. In order to assess which of them limits the acceleration length, it is necessary to determine which value is smallest in the different regimes.

Diffraction occurs over the Rayleigh length $z_r = \pi w_0^2 / \lambda_0$ (given in Section 2.2) and at the matched conditions, we can replace the waist by $w_0 = \lambda_p$ in the linear regime and $w_0 = 2\sqrt{a_0}/k_p$ in the 3D nonlinear regime. The dephasing and depletion length in the different regimes can be found in Table 2.3. Figure 2.13 shows these different values as a function of electron density in

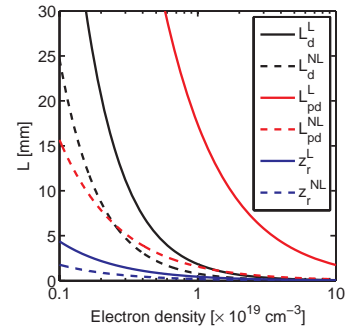


Figure 2.13. Electron density dependence of the dephasing, pump depletion and diffraction length, L_d , L_{pd} and z_r , respectively. The dashed lines represent the 3D nonlinear regime, while the solid lines represent the linear regime.

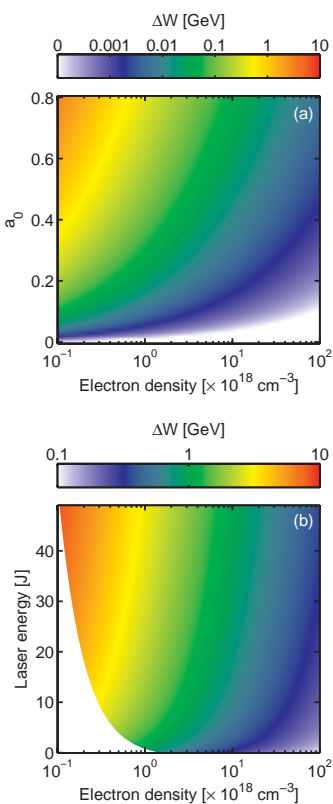


Figure 2.14. Maximum energy gain of an electron as a function of electron density and normalised vector potential, a_0 , in the linear case (a) and as function of the laser energy in the 3D nonlinear case (b). The white area in (b) corresponds to $a_0 < 2$, where the 3D nonlinear theory does not apply.

the linear (for $a_0 = 0.3$) and the nonlinear (for $a_0 = 4$) case. The pulse duration was 30 fs in both cases.

It can be seen that the acceleration length is fundamentally limited by diffraction. Without a mechanism to counteract it, the plasma wave would be sustained only for a short distance. If the laser power is above the critical power for self-focusing (see Section 2.8.2), the laser beam will be automatically guided over several millimetres as self-focusing balances diffraction. As discussed in Paper IV, this process can extend over several millimetres and finally allows for electron trapping. For $P < P_{crit}$, the laser beam must be externally guided. The laser can be guided over tens of centimetres using, for example, plasma discharge channels [65] or dielectric capillary tubes, which will be presented in Section 4.2.1. In Papers II and III, it was demonstrated that the laser pulse could be guided up to 8 cm.

Comparing the dephasing and the depletion lengths, shows that in the linear case, the pump depletion is much larger than the dephasing length. Pump depletion is therefore not an issue, as the particle dephases before it occurs. The interaction length is therefore limited by dephasing in the linear regime (assuming that diffraction has been prevented). In the 3D nonlinear case, the dephasing and pump depletion length are of the same order, and it can be seen in Fig. 2.13 that at low density the interaction is actually limited by pump depletion and not dephasing.

If we assume that the accelerating length is only limited by dephasing, the electrons reach their maximum energy at the dephasing point. The dephasing length should then match the gas medium length, otherwise the electrons are not extracted at their maximum energy and the acceleration process is not optimal. When limited by dephasing, the maximum energy gain of electrons in LWFA can be calculated using Eq. 2.57 with $L = L_d$. Figure 2.14 (a) shows the dependence of ΔW on the electron density and a_0 for the linear case. It can be observed that the most energetic electrons are obtained at low electron density.

It is important to keep in mind the matched conditions. When n_e is decreased the plasma wavelength increases, and the pulse duration should be increased in order to resonantly excite the plasma wave. In the bubble regime, when increasing a_0 , the spot size should increase, as discussed in Section 2.5. When increasing the pulse duration or the spot size, the energy in the pulse should therefore be increased in order to maintain the same vector potential. This is illustrated in Fig. 2.14 (b) in the nonlinear case ($a_0 > 2$). The energy gain has been plotted as a function of the laser energy in the matched condition ($w_0 = 2\sqrt{a_0}/k_p$) for a pulse duration $\tau = \lambda_p/(2c)$. We observe that the energy gain does not depend strongly on the laser energy due to the matched conditions. The dependence on the electron density is much stronger.

THE PLASMA WIGGLER X-RAY SOURCE

This chapter describes how a laser plasma accelerator also acts as a plasma wiggler. Due to the transverse electric field in the ion channel, the electrons wiggle along the ion channel and emit x-rays with a synchrotron-like spectrum. A basic theoretical description of the source is given, illustrated by numerical calculations of the main features of the source.

3.1 Introduction

As seen in the previous chapter, when an intense laser pulse interacts with a plasma, electrons are expelled from the region of high intensity by the ponderomotive force, while the ions are almost unperturbed. The resulting positively charged ion channel produces a focusing effect on the accelerated electrons due to space charge. Thus, in addition to the strong forward acceleration produced in the wake of the laser pulse, electrons launched off-axis relative to the ion channel or on-axis but with a transverse momentum will oscillate around the axis in a sinusoidal-like motion, as illustrated

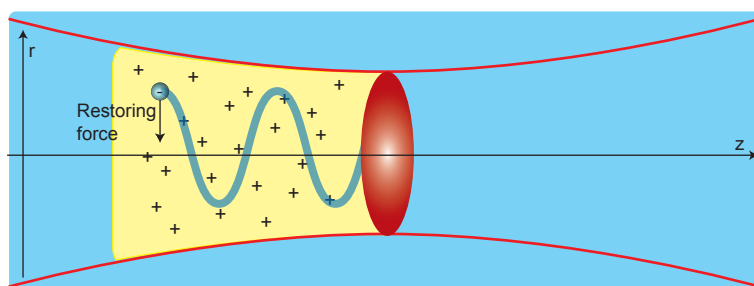


Figure 3.1. Schematic view of the plasma wiggler. Electrons off-axis relative to the ion channel experience a restoring force, which makes them oscillate in a sinusoidal-like motion.

¹The brightness (also sometimes called brilliance) defines how the radiation is confined in time and space. It is defined as the flux per mrad^2 per mm^2 and the flux is defined as the number of photons per 0.1% bandwidth per second.

in Fig. 3.1. Like any accelerated charged particles, these electrons emit radiation. This is similar to the motion of electrons in insertion devices such as wigglers or undulators in conventional synchrotron facilities. This chapter presents the main concepts of the plasma wiggler, and a more thorough theoretical description can be found in Ref. [66].

Historically, this wiggler motion and subsequent x-ray emission was first observed in a beam-driven plasma accelerator [67]. It was therefore expected that the same phenomenon would also be observed in laser plasma accelerators [68]. Indeed, the first study of the source in a laser plasma accelerator was presented in 2004 [69] when x-rays up to 10 keV were observed. At that time, its potential as a compact ultra-fast x-ray source was already clear. The characteristics of the source, such as the number of photons produced, spectrum, source size and pulse duration, were investigated later in detail [70–73]. The source has also been studied with more powerful lasers, where it was shown that this radiation has properties, in particular peak brightness, similar to those achievable with third generation light sources [74, 75].

As for the electrons, this x-ray source has special properties due to the small scale of the process. The wavelength of the wiggling motion is only $\sim 100 \mu\text{m}$. Because the amplitude of the oscillations is only a few micrometres the source size is very small [70, 75, 76]. Due to the difficulty of the task, no experimental measurement of the x-ray pulse duration has yet been performed. It is, however, believed that it will be similar to the electron bunch duration, i.e. a few fs [14, 15]. The source therefore has the advantage of being partially spatially coherent and intrinsically ultra-fast. These two features of the beam makes this source very bright.¹ While the average brightness is rather low due to the low repetition rate of the source, peak brightness as high as 1×10^{22} photons per second per mrad^2 per mm^2 per 0.1% bandwidth has been reported recently [75]. Compared with conventional synchrotron sources, this source has the advantage of being more compact and more affordable, and could possibly be used as a table-top source in university-scale laboratories. In contrary to other laser-based sources, such as high-order harmonic generation, $K\alpha$ x-ray sources or soft x-ray lasers, it provides photons of high energies in a collimated beam. In the future, many scientists may benefit from this source as it allows a range of advanced applications to be explored.

Studies of the plasma wiggler are included in this thesis work. Ways of increasing the energy of the radiation were investigated (Paper V), and the radiation was used as a diagnostic of the electron acceleration process (Paper IV). The plasma wiggler was therefore studied from the point of view of the radiation source, and the point of view of the electron accelerator.

3.2 Electron trajectories

In the blow-out regime, i.e. when all the electrons have been dispersed by the ponderomotive force of the laser, the ion channel can be considered to be cylindrically symmetric along the z -axis (see Fig. 3.1). Gauss's law,

$$\nabla \cdot \mathbf{E} = \frac{\rho}{\epsilon_0} = \frac{-en_e}{\epsilon_0}, \quad (3.1)$$

can be used to find the electric field at a distance r from the centre of the channel. Using cylindrical symmetry and integrating (with $E_r(r=0) = 0$), gives:

$$\nabla \cdot \mathbf{E} = \frac{1}{r} \frac{d}{dr}(rE_r) = \frac{-en_e}{\epsilon_0} \Rightarrow E_r = \frac{-en_e r}{\epsilon_0 2}. \quad (3.2)$$

An electron at a distance r from the axis of the ion channel experiences a force given by:

$$\mathbf{F}_{\text{res}} = -e\mathbf{E} = \frac{e^2 n_e \mathbf{r}}{2\epsilon_0} \quad (3.3)$$

The equation of motion of the electron is then:

$$\frac{d\mathbf{p}}{dt} = \mathbf{F}_{\text{res}} = \frac{m_e \omega_p \mathbf{r}}{2}, \quad (3.4)$$

where ω_p is the plasma frequency in the ambient plasma, and is given by Eq. 2.14. As a zeroth-order approximation, it can be assumed that the transverse motion is small and does not change the total energy of the particle ($\gamma \simeq \gamma_{z0} \simeq \text{constant}$; γ_{z0} the initial relativistic factor). Writing the relativistic momentum as $\mathbf{p} = \gamma m_e \dot{\mathbf{r}}$ and considering only the radial component, we obtain:

$$\ddot{r} - \frac{\omega_p^2}{2\gamma} r = 0. \quad (3.5)$$

which is the equation of motion of a harmonic oscillator with frequency:

$$\omega_\beta = \frac{\omega_p}{\sqrt{2\gamma}}, \quad (3.6)$$

where ω_β is the so-called betatron frequency.² Physically, the betatron frequency is just the plasma frequency modified by $\sqrt{\gamma}$ due to the relativistic mass increase and $\sqrt{2}$ due to the cylindrical geometry.

This simple model allows us to calculate the trajectories of any electron launched into the ion channel by solving Eq. 3.5 for different initial conditions: the initial momentum $\mathbf{p}_0(p_{x0}, p_{y0}, p_{z0})$ with $p_{z0} \gg p_{x0}, p_{y0}$, and the initial transverse position $\mathbf{r}_0(x_0, y_0)$.

²In the publication reporting the first experiments on this type of motion and radiation, the term betatron was introduced. As this word is somehow misleading (it has other uses in other fields), we prefer to use the term plasma wiggler instead. However, some quantities or symbols may be labelled as betatron for convenience.

We now assume that the energy of the particle is no longer constant, but the transverse momentum does not significantly affect the total energy of the electron: $\gamma(t = 0) = \gamma_{z0} \gg \gamma_\perp$. For example, the motion of an electron in the (x, z) plane launched at $r_0 = r_\beta$ is given by:

$$\begin{aligned} x &\simeq r_\beta \sin(k_\beta ct), \\ \beta_x &\simeq k_\beta r_\beta \cos(k_\beta ct), \end{aligned} \quad (3.7)$$

where β_x is the normalised velocity of the electron in the transverse direction. r_β describes the maximum amplitude of the oscillation and $k_\beta = k_p/\sqrt{2\gamma_{z0}}$ the betatron wave number. For a relativistic particle, $\beta(t = 0) = \beta_{z0} \rightarrow 1$, but if it acquires some momentum in the transverse direction, the longitudinal momentum will be affected: $\beta_z^2 = \beta_{z0}^2 - \beta_x^2$. For $|\beta_x| \ll |\beta| = 1$, we obtain:

$$\begin{aligned} z &\simeq z_0 + \beta_{z0}(1 - k_\beta^2 r_\beta^2/4)ct - \beta_{z0}(k_\beta^2 r_\beta^2/8) \sin(2k_\beta ct), \\ \beta_z &\simeq \beta_{z0}(1 - k_\beta^2 r_\beta^2/4) - \beta_{z0}(k_\beta^2 r_\beta^2/4) \cos(2k_\beta ct). \end{aligned} \quad (3.8)$$

More complicated trajectories are calculated numerically. Examples of such trajectories are shown in the first row of Fig. 3.2. For $\mathbf{p}_{\perp 0} = 0$ and $r_0 \neq 0$, the electron oscillates in a plane, as shown in Fig. 3.2 (a). Similar motion would be obtained for $r_0 = 0$ and $\mathbf{p}_{\perp 0} \neq 0$. If the electron has some initial transverse momentum it will spiral around the axis of the channel, as seen in Fig. 3.2 (b). With other initial conditions elliptical trajectories can be obtained, such as the one shown in Fig. 3.2 (c).

It can therefore be seen that the plasma channel allows a wide range of trajectories depending on the initial conditions of the electrons. In a conventional magnetic insertion device the trajectory of the electron is fixed by the direction of the magnetic field and all the electrons oscillate in the same fashion, which is of advantage for the realisation of a free-electron laser (FEL), for example.

3.3 Emitted radiation

For a given trajectory, the total power radiated by an accelerated charge is given by the relativistic generalisation of Larmor's formula [77], derived from the Liénart-Wiechert potentials in Ref. [78]:

$$P = \frac{e^2}{6\pi\epsilon_0 c^3} \gamma^6 \left[(\dot{\beta})^2 - (\beta \times \dot{\beta})^2 \right]. \quad (3.9)$$

The energy radiated per unit solid angle, $d\Omega$, per unit frequency, $d\omega$, can then be calculated as:

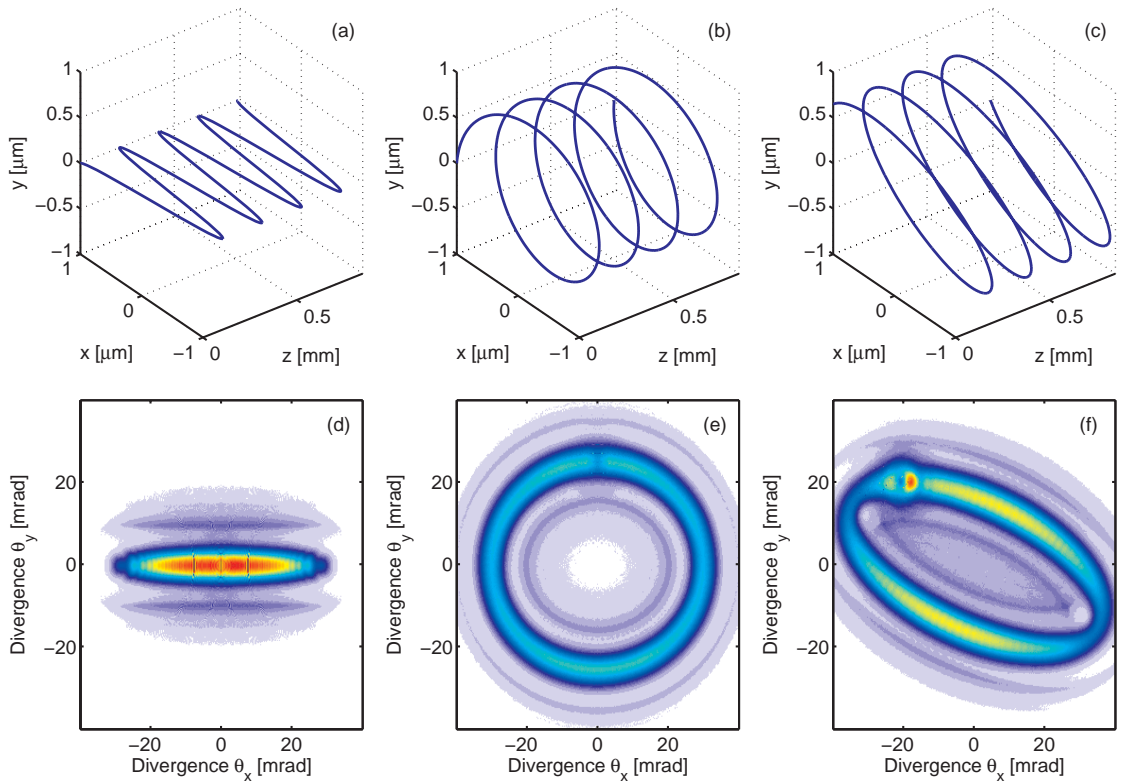


Figure 3.2. Different trajectories of an electron with energy 100 MeV in a plasma channel with density $n_e = 1 \times 10^{19} \text{ cm}^{-3}$. The electron was launched with different initial conditions: (a) $r_0 = 1 \mu\text{m}$ and $p_{x0} = p_{y0} = 0$; (b) $r_0 = 1 \mu\text{m}$, $p_{x0} = 0$ and $p_{y0} = 5m_ec$; (c) $r_0 = 1 \mu\text{m}$ and $p_{x0} = p_{y0} = 4m_ec$. The lower row (d-f) shows the corresponding emitted radiation for photon energies between 2 and 10 keV. The searchlight beam can be seen to sweep across the observation plane.

$$\frac{d^2I}{d\omega d\Omega} = \frac{e^2}{16\pi^3\epsilon_0 c^3} \left| \int_{-\infty}^{+\infty} e^{i\omega(t-\mathbf{n}\cdot\mathbf{r}/c)} \frac{\mathbf{n} \times [(\mathbf{n} - \beta) \times \dot{\beta}]}{(1 - \beta \cdot \mathbf{n})^2} dt \right|^2, \quad (3.10)$$

where $\mathbf{r}(t)$, $\beta(t)$ and $\dot{\beta}(t)$ are the position, the normalized velocity, and the acceleration of the electron as function of time, respectively. \mathbf{n} is the observation direction as defined in Fig. 3.3. Analytical solutions of Eq. 3.10 can be found for simple cases of periodic orbits, otherwise, the equation must be solved numerically to obtain spectral and spatial information about the emitted radiation. It is possible to obtain the most important features of the x-ray radiation by solving Eq. 3.10 approximately [66, 78].

Using the orbit given in Eqs. 3.7 and 3.8, Eq. 3.9 gives the total power radiated by a single electron, averaged over one oscil-

lation period:

$$\bar{P}_s \simeq \frac{e^2 c}{12\pi\epsilon_0} \gamma_{z0}^4 k_\beta^4 r_\beta^2 \propto \gamma_{z0}^2 r_\beta^2. \quad (3.11)$$

It can be noted that the radiated power is a strong function of both γ and r_β . The total energy radiated by a single electron is the product of P_s and the interaction time $N_\beta \lambda_\beta / c$:

$$W_s = \frac{e^2 c}{6\epsilon_0} \gamma_{z0}^4 k_\beta^3 r_\beta^2 N_\beta \propto \gamma_{z0}^{5/2} r_\beta^2. \quad (3.12)$$

where N_β is the number of electron oscillation periods.

3.3.1 Spatial distribution of the radiation

In the previous section, it was described how a charged particle oscillates around the plasma channel due to the force produced by the electric field. Inversely, the Lorentz equation also shows that when a charged particle experiences a force, it generates an electric field, as $\mathbf{F} = m\mathbf{a} = q\mathbf{E}$. The radiation propagates in space in the direction of the Poynting vector $\mathbf{S} \propto \mathbf{E} \times \mathbf{B}$ perpendicularly to the acceleration in a donut shape, whose axis is the acceleration vector. This is true in the rest frame of the electron. In the relativistic case, the shape of the radiation in the laboratory frame is quite different. The field lines are Doppler shifted and the radiation is emitted within a narrow cone with an opening angle $\Theta_0 = 1/\gamma \simeq 1/\gamma_{z0}$, tangentially to the particle's trajectory. The radiation can be likened to a searchlight beam sweeping across the point of observation. This can be seen in the second row of Fig. 3.2, where the far-field profile of the x-ray beam of the trajectory shown on the first row is calculated using Eq. 3.10. It can clearly be seen that the spatial profile of the x-ray beam is correlated to the electron trajectories, as discussed in Ref. [76, 79].

The “searchlight” beam of radiation is emitted in the forward direction of the tangent of the trajectory. One can distinguish two regimes, defined by the angle at which the electron trajectory crosses the ion channel axis, Θ . If $\Theta > \Theta_0$, the amplitude of the electron motion is large, and an observer placed far away sees a series of flicks of the searchlight beam, as seen in Fig. 3.4 (a). This is known as the wiggler regime. On the other hand, if $\Theta < \Theta_0$, the amplitude of the motion is small and the radiation moves negligibly compared to its own angular width, as shown in Fig. 3.4 (b). The main contribution to the divergence of the beam itself. In this case, the radiation becomes a superposition of the radiation emitted during each oscillation. This is called the undulator regime.

In the wiggler regime, the divergence is given by the angle at which the trajectory crosses the optical axis:

$$\Theta = \left(\frac{dx}{dz} \right)_{z=0} = \beta k_\beta r_\beta \simeq \frac{\omega_\beta}{c} r_\beta = \frac{K}{\gamma_{z0}}, \quad (3.13)$$

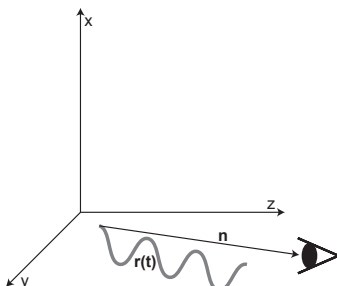


Figure 3.3. Coordinate system for the calculation of the radiation emitted by a particle following a trajectory $\mathbf{r}(t)$. \mathbf{n} defines the observation direction.

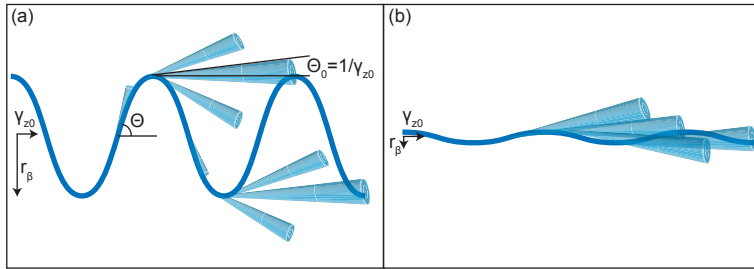


Figure 3.4. Schematic illustration of the radiation emitted from an oscillating relativistic electron. The radiation is emitted within a narrow cone with an opening angle $1/\gamma$. In (a), the amplitude of the oscillation is large and the deviation in the radiation direction is mostly due to the electron motion. This is the wiggler regime. In (b), the transverse electron motion is small compared to the intrinsic divergence of the radiation, allowing for interferences effects between the radiation emitted from the different parts of the trajectory. This is the undulator regime.

where

$$K = \gamma_{z0} r_\beta \frac{\omega_\beta}{c}, \quad (3.14)$$

is the strength parameter of the plasma wiggler.³ Figure 3.5 shows the dependence of K on r_β and γ_{z0} . The black line is drawn at $K = 1$, and indicates the border between the wiggler and the undulator regimes. In the experiment described in Paper V, typical values for the K parameter were 5–15, as presented in Section 5.2.1. In the wiggler regime, the divergence of the x-ray beam is therefore proportional to the strength parameter K . In the undulator regime, the divergence will be even smaller than the intrinsic divergence of the beam, Θ_0 , due to interference effects and $\Theta = \gamma/\sqrt{N_\beta}$, where N_β is the number of oscillation periods.

3.3.2 Spectral features

In the case of large amplitudes, an observer sees the searchlight turning on and off. These pulses of radiation can be expanded by Fourier transform, and since they are short, they correspond to a broad spectrum. For small oscillation amplitudes, an observer always sees the light, and the radiation is a coherent superposition of the radiation emitted at each oscillation, as shown in Fig. 3.4 (b). In the case of an infinitely long undulator, the radiation would be monochromatic. In reality, the undulator spectrum consists of the fundamental and its harmonics.

Spectrally, the different regimes of radiation are also conveniently described by the strength parameter. For $K \ll 1$, the transverse amplitude of the electron trajectories is small compared to its wavelength, and the radiation is mainly emitted around a fundamental frequency given by:

$$\omega_f = \frac{2\gamma_{z0}^2 \omega_\beta \left(1 + \frac{K^2}{2}\right)}{\left(1 + \frac{K^2}{2}\right)^2 + 2\gamma_{z0}^4 \theta^2}, \quad (3.15)$$

³In synchrotron facilities, a similar parameter is used, $K = (eB_0\lambda_u)/(2\pi m_0 c)$, which depends on the strength of the magnetic field, B_0 , and the undulator period, λ_u .

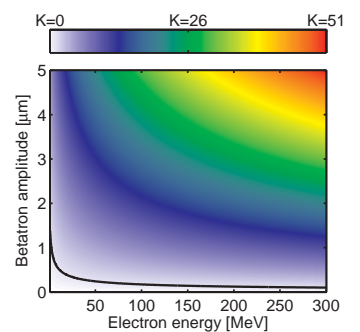


Figure 3.5. Dependence of the parameter K on the oscillation amplitude, r_β , and the electron energy for $n_e = 1 \times 10^{19} \text{ cm}^{-3}$.

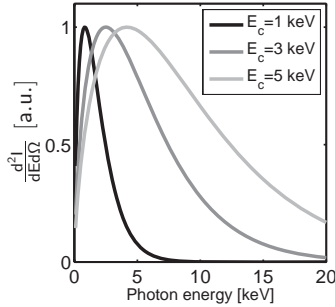


Figure 3.6. Normalised synchrotron spectra for different critical energies.

⁴Other definitions of E_c are in use. This one corresponds to the 3rd edition of Ref. [78] and is generally used. In some publications, an older definition is used which gives a critical energy that is twice this.

where θ the angle of observation relative to the z-axis. For $K \sim 1$, harmonics of the fundamental frequency appear. Finally, for $K \gg 1$, the oscillation amplitude is large and high harmonics are radiated. The emitted spectrum is broadband, consisting of unresolved, closely spaced harmonic peaks. The radiation emitted follows a spectrum described by [66]:

$$\frac{d^2I}{d\omega d\Omega} \simeq N_\beta \frac{3e^2}{2\pi^3 \epsilon_0 c^3} \frac{\gamma_{z0}^2 \zeta^2}{1 + \gamma_{z0}^2 \theta^2} \left[\frac{\gamma_{z0}^2 \theta^2}{1 + \gamma_{z0} \theta^2} \mathcal{K}_{1/3}^2(\zeta) + \mathcal{K}_{2/3}^2(\zeta) \right], \quad (3.16)$$

where \mathcal{K}_n the modified Bessel function of order n of the second kind, and

$$\zeta = \frac{E}{2E_c} (1 + \gamma_{z0}^2 \theta^2)^{3/2}. \quad (3.17)$$

$$E_c = \frac{3}{2} \hbar \gamma_{z0}^3 \omega_\beta^2 r_\beta / c \quad (3.18)$$

is the critical energy⁴ of the spectrum. This simplified description of the spectrum is referred to as the synchrotron asymptotic limit. In most cases, we are interested in radiation close to the axis, and the radiation follows a spectrum described by:

$$\frac{d^2I}{(dEd\Omega)_{\theta=0}} \propto \gamma_{z0}^2 \xi^2 \mathcal{K}_{2/3}^2(\xi/2), \quad (3.19)$$

where $\xi = E/E_c$. Note that this spectrum is defined solely by E_c . Figure 3.6 shows such spectra for different values of E_c . They are peaked close to the critical energy and are considered to be synchrotron-like. For an ensemble of electrons it has been shown that the spectrum is also synchrotron-like [66], as will be discussed in Section 3.5. This has also been recently confirmed experimentally [80] using a method described in Section 4.3.2.

The parameter K can be varied by varying the oscillation amplitude r_β . The spectrum varies accordingly, as can be seen in Fig. 3.7, where Eq. 3.10 was solved numerically for trajectories corresponding to different injection radii and no initial transverse momentum, as a result of which, $r_\beta = r_0$. In (a), $K=0.4$ and only the fundamental is observed. For $K=1.3$, harmonics of the fundamental appear, as can be seen in Fig. 3.7 (b). In Fig. 3.7 (c) $K=4.2$, and the spectrum is broad. The energy of the emitted x-rays increases for larger values of K . In (b) and (c) synchrotron spectra with critical energies of 0.16 keV and 0.5 keV, respectively, can be fitted (black line). Note that these calculations were performed for the radiation emitted on-axis. The off-axis radiation spectrum will be different. In the wiggler regime, the off-axis spectrum is not very different from the on-axis spectrum, and it remains broadband. In the undulator regime, the position of the peaks will vary as the fundamental is a strong function of θ , as can

be seen from Eq. 3.15. This angle dependence must therefore be taken into account when measuring the radiation. As we will see later in Section 4.3, the methods of detection used record x-rays at different angles. However, as the angles are small and we are in the wiggler regime, it was assumed in Papers IV and V, that the radiation was on-axis.

3.4 Effect of acceleration

So far, we have assumed that the electrons have a constant energy. However, as seen in Section 2.6, in a laser plasma accelerator the electrons are accelerated, possibly reach dephasing, and are decelerated again if the medium is long enough. The trajectory of the oscillating electron will be affected. This is illustrated in Fig. 3.8 (a), where the trajectory of an electron launched off-axis with different injection radii, has been calculated while it follows the orbit corresponding to $a_0 = 1$ in Fig. 2.9 (b), and shown by the dashed line in Fig. 3.8 (a). The oscillation amplitude decreases due the increase in the relativistic mass of the electron. The oscillation frequency $\omega_\beta = \omega_p/\sqrt{2\gamma}$ follows the same behaviour. The emitted radiation will in turn be influenced by the varying γ . However, the main contribution arises from the part of the trajectory where the electrons are most energetic, as γ varies much more than r_β and the emitted power is a strong function of γ (see Eq. 3.11). This can be seen in Fig. 3.8 (b), where the radiation emitted on-axis during acceleration was calculated for a trajectory in the wiggler regime (black line in Fig. 3.8 (a)). It can be seen that the spectrum remains synchrotron-like. It can be fitted with a synchrotron spectrum with $E_c = 2.7$ keV (black line in (b)). This is close to the radiation spectrum corresponding to the maximum energy of the electron ($E_c = 3.2$ keV).

On the other hand, for a smaller injection radius, we are in the undulator regime and one might expect that the harmonic peaks will be washed out by the acceleration process, as the fundamental frequency given by Eq. 3.15 depends on the electron energy. Nevertheless, as shown in Fig. 3.8 (c) in grey, the peaks are still visible and at the same positions as the radiation peaks emitted by an electron with constant energy (black line). Around the dephasing point, i.e. where the electron reaches its maximum energy, the electron energy remains relatively constant over several oscillations and the oscillation amplitude remains constant. The emitted power is maximum in this region, and the undulator peaks are still observed in this one-electron calculation. However, as will be discussed below, when considering many electrons, the peaks may disappear.

In an experiment, the electron energy is often measured at the same time as the energy of the x-rays, which can then be

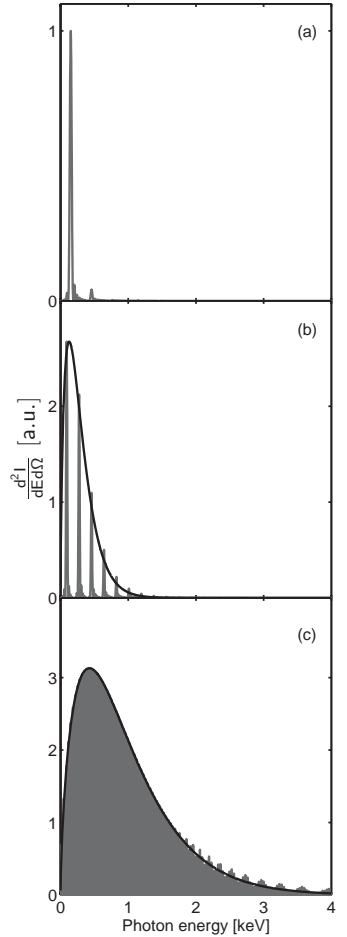


Figure 3.7. Simulated spectra for a 50 MeV electron oscillating 4 times around a plasma channel of density $n_e = 1 \times 10^{19} \text{ cm}^{-3}$. As the injection radius varies, different regimes are reached. In (a) with $r_\beta = 0.1 \mu\text{m}$, only the fundamental is visible. In (b) with $r_\beta = 0.3 \mu\text{m}$, the undulator regime is reached as harmonics of the fundamental appear. Finally, in (c) with $r_\beta = 1 \mu\text{m}$, the harmonics are closely spaced constituting a broadband spectrum typical of the wiggler regime and a synchrotron spectrum can be fitted (black line).

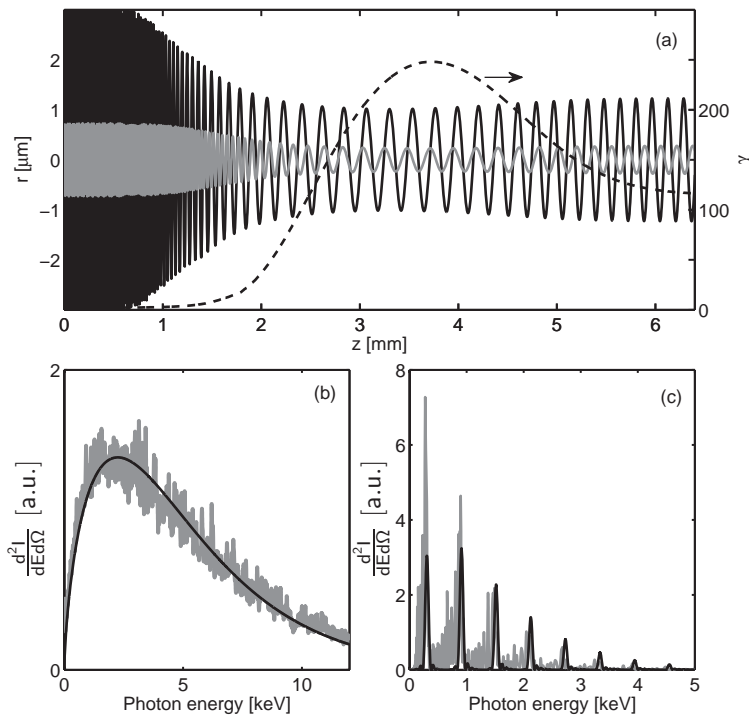


Figure 3.8. The effect of acceleration on the electron trajectory and emitted radiation. The electron is accelerated according to the dashed curve shown in (a) and corresponding to the orbit in Fig. 2.9 (b) for $a_0 = 1$. At the maximum electron energy, $r_\beta = 1 \mu\text{m}$ for the black line in (a) and the corresponding spectrum in (b), while $r_\beta = 0.2 \mu\text{m}$ for the grey line in (a) and the corresponding spectrum in (c). A synchrotron spectrum with $E_c = 2.7 \text{ keV}$ can still be fitted in (b), while in (c) the black line corresponds to the radiation emitted by an electron with constant energy.

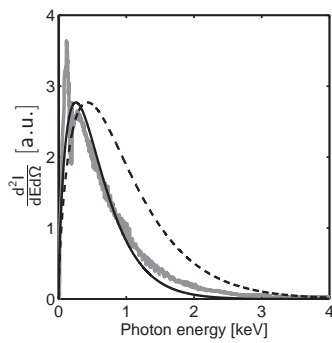


Figure 3.9. Simulated spectrum, in grey, for 46 electrons of energy 50 MeV injected at different radii ranging from 0.1 to 1 μm at an electron density of $n_e = 1 \times 10^{19} \text{ cm}^{-3}$. The solid black line shows the fitted synchrotron spectrum, while the dashed line is the spectrum expected for an electron injected at 1 μm .

used to determine, for example, the injection radius as described in Paper V. When doing this, it is important to ensure that the electrons have not yet reached dephasing when exiting the plasma, otherwise the measured electron energy will not correspond to the electron energy when most of the x-rays were emitted.

3.5 Emission from many electrons

The previous calculations and simulations were performed for a single electron. In reality, many electrons are accelerated and oscillate simultaneously in the plasma channel. Each electron is expected to have a different trajectory defined by different initial conditions, \mathbf{r}_0 and \mathbf{p}_0 . The amplitude of oscillation differs, as well as the plane and type (circular, planar, elliptical,...) of oscillation. The emitted radiation is affected both spectrally and spatially, and instead of observing radiation corresponding to a well-defined trajectory, the sum of the radiation from each trajectory is observed. We can, however, define a maximum oscillation amplitude. As the radiated power is proportional to r_β^2 , the radiation emitted by electrons with maximum amplitude will dominate the emission. This is illustrated in Fig. 3.9, where the radiation was calculated for 46 electrons injected at different radii ranging from 0.1 to 1 μm . The black line shows a fit to the spectrum with

$E_c = 0.35$ keV. As seen in Fig. 3.7 (c), the radiation emitted by an electron oscillating with $r_\beta = 1 \mu\text{m}$ would have a critical energy, E_c , of 0.5 keV, which is also shown by the dashed line in Fig. 3.9. This spectrum is close to the calculated spectrum emitted by the ensemble of electrons. The radiation emitted by the electrons with the maximum oscillation amplitude therefore dominates, while the electrons injected at smaller radii tend to shift the spectrum towards lower photon energies.

The electron beam is often spectrally broad. Of course, quasi-monoenergetic electron beams can be obtained in a laser plasma accelerator. However, electron beams with higher charge, which produce more radiation, exhibit a broad electron spectrum. Electrons with different energies will have different trajectories. The spectrum and strength of the emitted radiation from different electrons differ considerably, as they are a strong function of γ . Figure 3.10 shows the x-ray spectrum obtained for different electron beam spectra shown in the inset. As expected in (a), a quasi-monoenergetic electron spectrum gives a well-defined synchrotron spectrum that can be fitted with the expected critical energy according to Eq. 3.18. The same fit is shown by the dashed line in Fig. 3.10 (b) and (c). In Fig. 3.10 (b), the x-ray spectrum still has a synchrotron-like shape, but lower critical energy (fitted with the black line), corresponding to the spectrum that would be obtained for an electron with an energy of 60 MeV. This shows that the most energetic electrons contribute most to the radiation. Finally, in Fig. 3.10 (c), the fitted spectrum corresponds to the spectrum of an electron of an even lower energy, of 56 MeV.

A one-electron model may, therefore, not give the best description of x-ray emission. Any features produced by the individual electrons (for example, undulator peaks) would be washed out. In particular, the realisation of an x-ray FEL or ion-channel laser [81] based on this scheme would be extremely difficult [82]. However in the wiggler regime, the one-electron model still provides a good understanding of the physics. Together with the effect of acceleration seen in Section 3.4, the varying K , due to different r_β and γ , smoothes the spectrum, which becomes a sum of synchrotron spectra [83]. The radiation emitted by the most energetic electrons around the dephasing region and/or the electrons with the largest oscillation amplitude dominate the spectrum.

Spatially, instead of observing well-defined trajectories a circular beam is observed with a divergence given by $\theta = \max(K/\gamma) \propto \max(r_\beta/\sqrt{\gamma})$. Nevertheless, under some conditions, which are not clear at the moment, collective motion of electrons has been experimentally observed, and spatial profiles similar to those shown in Fig. 3.2 were observed. This is discussed in Paper IV and Ref. [76].

The main conclusion from the calculations presented in the previous sections on the effect of acceleration and many electrons

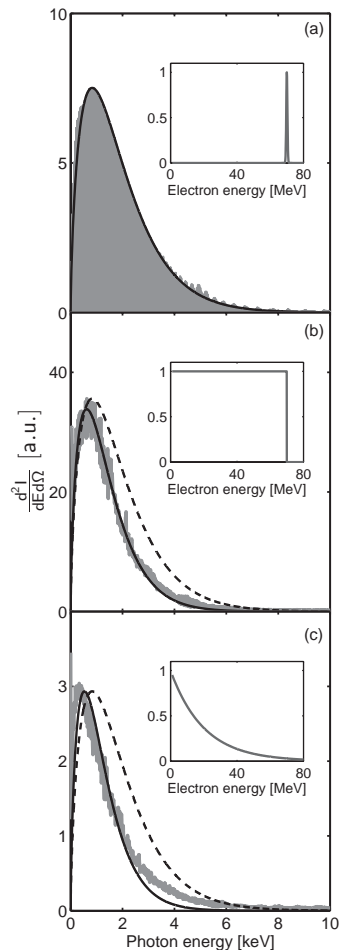


Figure 3.10. X-ray spectra, in grey, generated for $r_\beta = 1 \mu\text{m}$ for the different electron spectra shown in the inset. The black line is a fit using Eq. 3.19. In (a) $E_c = 1$ keV, in (b) $E_c = 0.74$ keV and in (c) $E_c = 0.64$ keV. The dashed lines in (b) and (c) show the spectrum of a single electron of energy 70 MeV.

with different injection radii and/or energy distribution, is that in the wiggler regime, the spectrum can still be described by a synchrotron spectrum. In the plasma wiggler, the injection radius is rather large, as is the electron energy. We are therefore mostly in the wiggler regime. As will be seen below, in the experimental investigations reported in Papers **IV** and **V**, it was assumed that the x-ray spectrum was synchrotron-like in order to determine its critical energy with the method described in Section 4.3.1. One must be more cautious when obtaining information about the electron beam from the measured x-rays, e.g. the oscillation amplitude, as the critical energy will depend on the electron energy and its spectral distribution. In Paper **V**, for example, the injection radius was inferred by measuring the critical energy of the x-rays and the electron spectrum. As the mean energy of the electrons was approximately constant, the change in critical energy was attributed to changes in the oscillation amplitude.

EXPERIMENTAL METHODS

This chapter introduces the experimental methods used during the different experiments on electron acceleration and x-ray production. An overview of the main components of the experiments is given: from the laser system, together with some of the developments made to improve some of its characteristics, to the gas medium, concentrating on laser propagation in gas-filled dielectric capillary tubes. The electron and optical diagnostics are described, as well as the x-ray detection. Finally, radiation safety issues are discussed.

4.1 The multi-terawatt laser of the Lund Laser Centre

The experiments described in this thesis were performed using the multi-terawatt laser of the Lund Laser Centre. This laser is a chirped pulse amplification system [1, 84], using titanium-doped sapphire as amplifying medium, which allows for ultra-short pulses due to its spectrally large bandwidth. A schematic of the laser system is shown in Fig. 4.1. A Kerr lens mode-locked oscillator [85] provides pulses at 80 MHz, of which 10 per second are selected, stretched in time to 300 ps and amplified in three stages. Finally, the pulses are compressed to ~ 35 fs in vacuum and delivered to the experiment. The laser beam diameter is expanded as the energy in the pulse increases in order to prevent damage to the optical components. Frequency-doubled Q-switched Nd:YAG lasers, delivering in total ~ 8 J at 532 nm, are used to pump the different stages of amplification. Various components are used to clean and shape the pulse in space (spatial filter), in time (Pockels cells) and spectrally (a Dazzler). A preamplifier was also used before the stretcher to improve the temporal contrast of the pulse, which is crucial for ion acceleration, as discussed in Section 6.3.1.

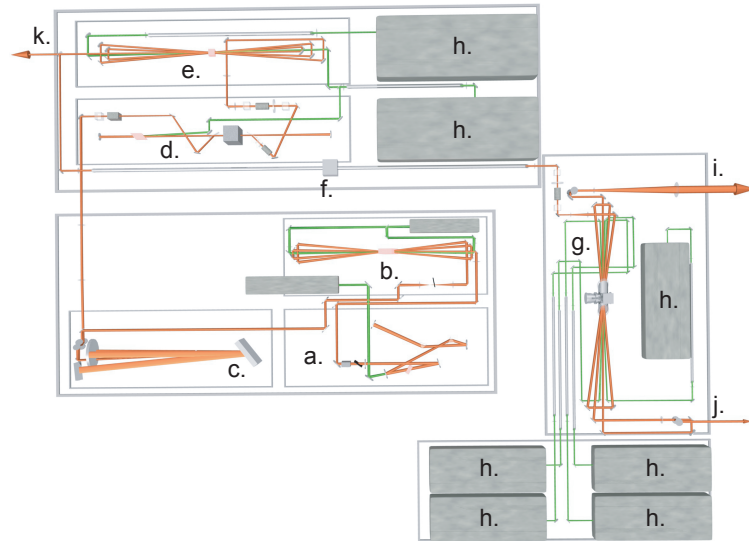


Figure 4.1. Schematic view of the Lund multi-TW laser used for the different experiments. a. Mode-locked oscillator with the Dazzler. b. Pre-amplifier. c. Stretcher. d. Regenerative amplifier with Pockels cells. e. Multipass amplifier with a Pockels cell. f. Spatial filter. g. Cryogenically cooled multipass amplifier with a Pockels cell. h. Nd:YAG pump lasers. i. Main beam. j. Secondary beam. In k. part of the beam is sent to another experiment. The different beams are then sent to different compressors not shown here.

A second beam can also be extracted from the third amplification stage and sent to a separate air compressor to provide an additional beam, as in the experiment presented in Paper **VII**. The different laser parameters are summarized in Table 4.1.

While still being a highly complex machine, the Lund multi-terawatt laser is a standard laser system. Therefore, instead of describing it in detail, work carried out in the scope of this thesis to improve its quality will be described. In particular, the experiments reported in Papers **II**, **III** and **IV** required stable laser beam pointing and a good wavefront, to avoid damaging the dielectric capillary tubes used in these experiments. An active pointing stabilisation system was designed and implemented, which is the subject of Paper **I**. Adaptive optics has also been implemented to obtain the most symmetric pulses, critical for the experiment with dielectric capillaries. It also allowed for very interesting experiments, where the wavefront was modified in a controlled way. This is reported in Papers **V** and **VI**.

4.1.1 Pointing

The general trend in high-power laser development is to obtain higher and higher peak powers, by increasing the energy or decreasing the pulse duration [86]. However, it is also important to improve the quality of these laser systems; the stability of the laser parameters being one of the major issues. One of the main themes of my thesis was to improve the pointing stability of the Lund multi-TW laser. Paper **I** reports on this work, where the system is described in details. Therefore, after a brief overview of

the system, this section will focus on issues only briefly mentioned in the paper, such as feedback theory and signal processing.

The targets used in the experiments reported in Papers **II**, **III** and **IV**, were dielectric capillary tubes of only 100–200 μm diameter, while the laser spot radius was 40 μm (first zero of an Airy pattern). If the laser beam did not remain well-centred along the capillary axis, the capillaries would have been destroyed after only a few shots. Good pointing stability was therefore crucial in order for these experiments to be successful.

As illustrated in Fig. 4.2, the position of the laser beam is detected, and if it deviates from the set position, a piezo-mirror compensates for this deviation. A feedback loop is thus established between a position-sensitive detector (PSD) and the piezo-mirror. Feedback allows very good control of the system as it makes the system insensitive to disturbances and component variation [87]. The drawbacks are that the system can become unstable and sensor noise is fed into the system. Filtering of the input signal is therefore crucial.

The complete stabilisation set-up is shown schematically in Fig. 4.3. Two feedback loops each consisting of a piezo-mirror and a PSD were used to correct for both the near and far field. Part of the oscillator beam is used as a reference beam. With its 80 MHz repetition rate, it is considered continuous on the time scale considered here. This allows the main beam to be operated in single-shot mode. The reference beam is injected through a polariser as shown in the inset (a) in Fig. 4.3. The beams are made collinear by using irises and sending them through the same spatial filter. The reference beam is imaged on the detectors using different sets of lenses. These detectors would be destroyed if the main laser beam were to hit them. In order to protect them, fast shutters are used, which close just before the shot arrives, and the voltages transmitted to the piezo-mirrors are kept constant during this time, as illustrated in the inset (b).

Finally, because high-frequency components in the signal would be amplified by the feedback loop, it is necessary to avoid them as far as possible. Even after filtering the signal, some of these components remain. One source of these high-frequency components is the cryogenic cooler of the final amplifier. Its compressor produces bursts of vibrations at 2 Hz which last about 100 ms. During this time the stabilisation system does not work well, and the pointing of the laser deteriorates. As the experiments were carried out in single-shot mode, these bursts of vibration could be avoided. The main shutter of the laser system only delivered shots during the period between the bursts, as described in the inset (c) in Fig. 4.3.

In order for the active stabilisation system to work efficiently, the controller must be chosen carefully and optimised for speed. Suitable software must also be used. LabView FPGA (Field-

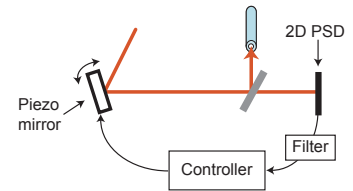


Figure 4.2. Basic principle of the pointing stabilisation system. The offset compared to the desired position is recorded using a 2D position-sensitive detector (PSD). The piezo-mirror moves to compensate for this offset according to the value computed by the controller. Filtering is also necessary in order to avoid noise being fed to the piezo-mirror.

4.1.1 Pointing

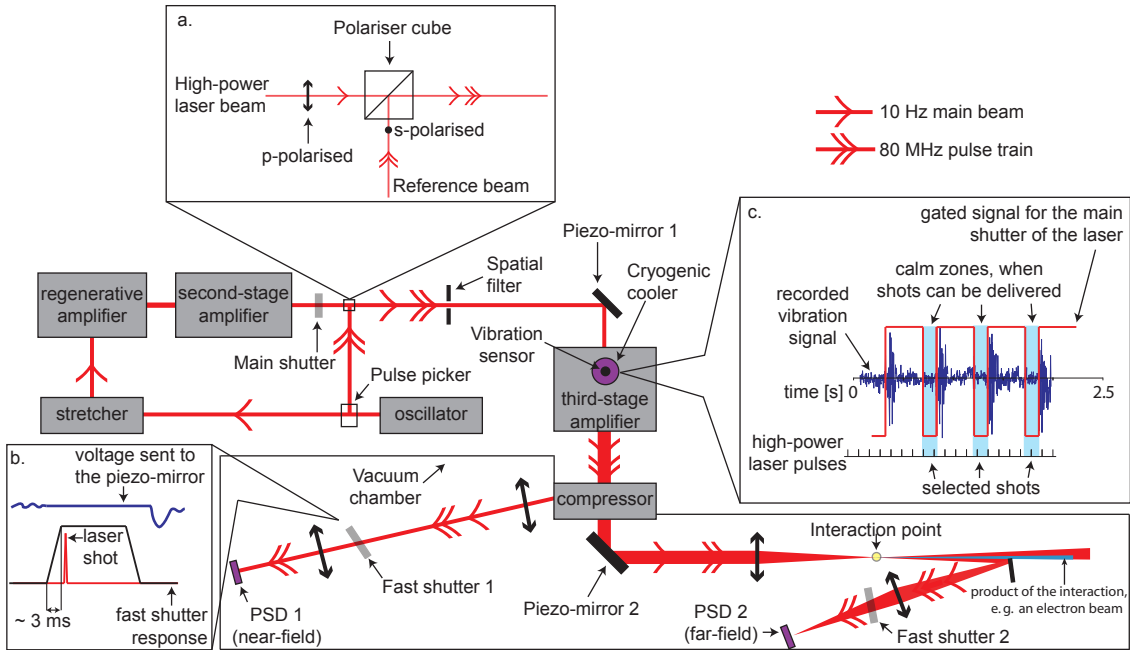


Figure 4.3. Experimental arrangement of the pointing stabilisation system, adopted from Paper I.

Programmable Gate Array) was chosen for its reliability, determinism and parallelism. In addition, proportional-integral-derivative (PID) controllers were implemented in the code, which allow for faster corrections than simple proportional controllers.¹ The output signal is calculated in order to minimise the error, which is the difference between a measured process variable and a desired setpoint. The operation of the PID controller is optimised by adjusting the so-called PID parameters, which depend on the nature of the system to be regulated. The proportional term changes the output proportionally to the current error value. The integral term (when added to the proportional term) accelerates the movement of the process towards the setpoint, and eliminates the residual steady-state error that occurs with a simple proportional controller. The derivative term slows the rate of change of the controller output and can be used to reduce the amount of overshoot. It must, however, be used with care as it can easily cause the system to become unstable [88]. The response of a PID controller to an error, $e(t)$, is described by the following equation:

$$u(t) = k_p e(t) + k_i \int_0^t e(\tau) d\tau + k_d \frac{de(t)}{dt}, \quad (4.1)$$

where k_p , k_i and k_d are the proportional, integral and derivative PID parameters, respectively. The best parameters can be determined using a Ziegler–Nichols frequency response method. In

practise, the derivative term is often set to zero as non-zero values make the system very sensitive to noise. The controller is then referred to as a proportional-integral (PI) controller.

Feedback control has many advantages, but one of its main disadvantages is that it can be very sensitive to noise. High-frequency noise can be amplified by the feedback loop and impeding the stabilisation. It is therefore crucial to filter the detector signals in order to avoid noise being fed into the feedback loop. Low-pass filters can be inserted after the detector, however, standard low-pass filters introduce a phase delay in the signal² and this will reduce the speed at which the system will be able to stabilise the pointing. Advanced digital filters were therefore used. These finite impulse response (FIR) filters have the advantage of producing a smaller phase delay than conventional filters [89]. While infinite impulse response (IIR) filters, such as Butterworth filters, might also have good performance, FIR filters have the advantage of introducing the same delay for all frequencies. Figure 4.4 compares the magnitude and phase response of IIR and FIR filters.³

Frequency analysis provides information on how well the stabilisation system performs. For example, the signal from PSD 2 was recorded and its Fourier components analysed, from which a power spectrum was extracted. Figure 4.5 shows the sensitivity functions for different PI parameters. The sensitivity function is defined as the error signal with the feedback loop closed, divided by the error signal without feedback:

$$S = \frac{y_{\text{closed loop}}}{y_{\text{open loop}}} \quad (4.2)$$

For $S < 1$, frequencies are attenuated by the feedback loop, while when $S > 1$ some frequencies are actually amplified by the feedback loop. In Fig. 4.5, it can be seen that the fluctuations at low frequencies can be attenuated by increasing the PI parameters, but at the expense of the high frequencies. This is known as the waterbed effect, where the areas below and above $S = 1$ remain equal. A feedback loop can, therefore, never attenuate all frequencies. Using filters, it is possible to spread the high-frequency part to higher frequencies and to avoid the creation of a peak at a certain frequency, while still attenuating the low frequency part. This way, good performance of the feedback loop can be obtained. For example, as mentioned in Paper I, it takes about 5 ms for the implemented system to react to a disturbance.

The pointing fluctuations originate from different sources. Thermal drifts occurring over hours and air flows over seconds are easily dealt with by the stabilisation system. Mechanical vibrations (> 10 Hz) are more difficult to compensate for, but are partly attenuated by the system. Of course, there is still room for improvement, and more advanced feedback controllers could improve the pointing even more. One should not forget that even if

²A passive RC low-pass filter with a cut-off frequency of 100 Hz introduces a delay of 1.5 ms at 30 Hz.

³While IIR filters can be implemented as either analogue or digital filters, FIR filters can be constructed only digitally. These filters were therefore implemented directly in the LabView program.

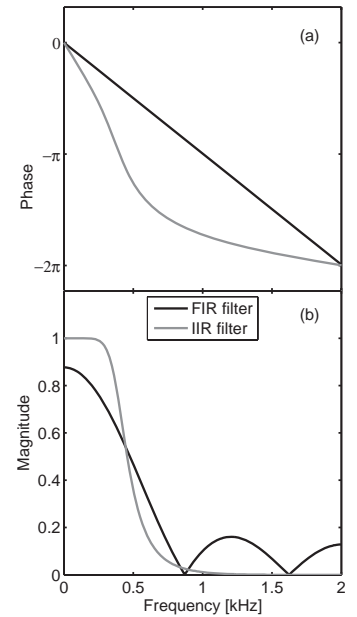


Figure 4.4. Phase (a) and magnitude (b) response of FIR and IIR filters. It can be seen that the FIR filters introduce a smaller phase delay ($d\phi/df$) than IIR filters. However, IIR filters attenuate the high frequencies better.

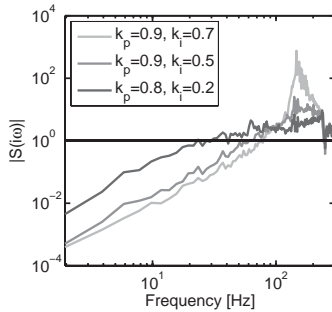


Figure 4.5. Sensitivity function plotted against frequency for increasing PI parameters k_p and k_i (given in arbitrary units). A waterbed effect is observed, where high-frequency components increase while the low-frequency components are attenuated more.

the reference beam is perfectly stabilised, this does not guarantee that the main laser beam pointing will be stable. This may place some limitations on the ultimate performance of such a stabilisation system. Nevertheless, all this work greatly improved the feasibility of the experiments with dielectric capillaries reported in Papers **II** to **IV**, as the lifetime of each capillary tube was increased from a few shots to more than 100 shots.

4.1.2 Adaptive optics

A deformable mirror was also implemented in the laser system during my studies. Adaptive optics is a powerful tool, allowing the wavefront to be shaped, and thus the focal spot when the beam is focused. As in astronomy, where adaptive optics is used to compensate for perturbations caused by the atmosphere, a deformable mirror is used to compensate for aberrations produced by the different optical components of the laser and for errors in the shape and alignment of the focusing optics. The goal is to obtain a full control of the wavefront and, in most cases, obtain a beam as close to the diffraction limit as possible. For the experiments discussed in Papers **II** to **IV**, a circular focal spot was needed to achieve the best coupling inside the capillary tubes, and for those in Papers **V** and **VI**, we wanted to add aberrations in a controlled way.

The deformable mirror is composed of piezoelectric ceramics, glued to a thin substrate. An actuator pattern is printed on the other side of the ceramic disc. When a high voltage is applied to the actuators, it locally deforms the ceramic and the substrate. This mirror was placed in the beam path, directly after the compressor.

The wavefront must be measured in order to determine which voltages to apply to the deformable mirror. Our wavefront sensor is based on a 4-wave shearing interferometry technique [90], and placed after the focusing optics. In this way, any effects due to the focusing optics are also measured. A feedback loop is established between the wavefront sensor and the deformable mirror, and a software computes which voltages to apply to the deformable mirror in order to reach the desired wavefront. The desired wavefront is obtained, with a typical error of 4% rms, after a few iterations.

Mathematically, the laser wavefront can be conveniently written as a linear combination of Zernike polynomials :

$$W(\rho, \theta) = \sum_n \sum_{m=-n}^k W_n^m Z_n^m(\rho, \phi), \quad (4.3)$$

where W_n^m are the Zernike coefficients, and ρ and ϕ are the radial distance and the azimuthal angle, respectively. The Zernike polynomials, $Z_n^m(\rho, \phi)$, are given by:

Table 4.2. List of the first Zernike polynomials and their expression corresponding to the most common laser beam aberrations.

Name	n	m	Polar form (rms)
Defocus	2	0	$\sqrt{3}(2\rho^2 - 1)$
Astigmatism 0°	2	2	$\sqrt{6}\rho^2 \cos(2\theta)$
Astigmatism 45°	2	-2	$\sqrt{6}\rho^2 \sin(2\theta)$
Coma X	3	1	$\sqrt{8}(3\rho^3 - 2\rho) \cos(\theta)$
Coma Y	3	-1	$\sqrt{8}(3\rho^3 - 2\rho) \sin(\theta)$
Spherical aberration	4	0	$\sqrt{5}(6\rho^4 - 6\rho^2 + 1)$

$$\begin{aligned} Z_n^m(\rho, \theta) &= R_n^m(\rho) \cos(m\theta) \\ Z_n^{-m}(\rho, \theta) &= R_n^m(\rho) \sin(m\theta), \end{aligned} \quad (4.4)$$

where R_n^m are the radial polynomials. $R_n^m = 0$ for odd values of $n - m$ and otherwise:

$$R_n^m(\rho) = \sum_{k=0}^{(n-m)/2} \frac{(-1)^k (n-k)!}{k!((n+m)/2-k)!((n-m)/2-k)!} \rho^{n-2k}. \quad (4.5)$$

The low-order Zernike polynomials describe the most common aberrations of a laser beam, as can be seen in Table 4.2. These 6 polynomials are sufficient to interpret most laser beam aberrations, as they are linked to optical misalignment or thermal effects. This description of the wavefront is thus very useful as it identifies the main aberrations present in the beam. When this description is used in the adaptive optics loop, it is also easy to add or remove a particular aberration.

The deformable mirror is imaged onto the wavefront sensor, in order to discriminate between intensity and phase errors. As the laser beam must be smaller than the wavefront sensor (~ 3 mm), additional optics is usually required to reduce the beam.⁴ First, the system is calibrated by applying known voltages to the mirror actuators and measuring the effect on the wavefront phase. After calibration, the relation between the voltages applied to the actuators and the phase is obtained and represented by a matrix, $\Phi_m = M_{mn}V_n$, where Φ_m is the wavefront distortion induced by a set of voltages V_n . The matrix M_{mn} is then inverted using singular-value decomposition, where the pseudo-eigenmodes of the mirror are extracted. Some of these modes correspond to the first Zernike polynomials and therefore compensate for particular kind of aberration. Once the matrix is inverted, it converges quickly towards any desired wavefront using an iterative process.⁵

⁴It was, however, found during the different experiments that it is not crucial to be in the image plane of the deformable mirror. This provides more flexibility in the set-up, as no optics, apart from the focusing optics, was necessary in front of the wavefront sensor.

⁵It is also possible to measure the focal spot intensity distribution and use an iteration process (based on a genetic algorithm, for example) to achieve a circular focal spot. However, this process takes longer to converge.

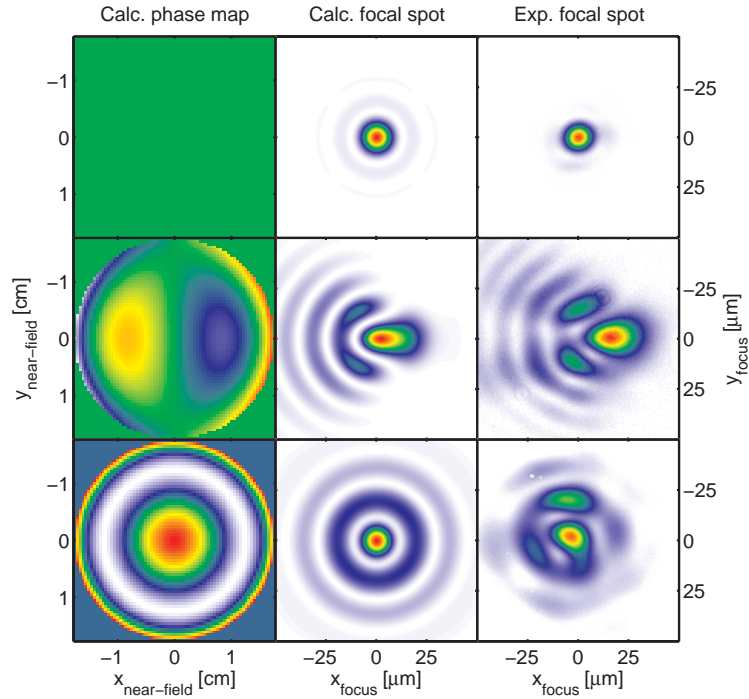


Figure 4.6. Examples of calculated phase maps and the corresponding focal spots for a top-hat beam with a 35 mm diameter. This is compared with experimental focal spots obtained with a focusing optics of 45 cm focal length. In the first row, the wavefront is flat, i.e. the beam is close to the diffraction limit. In the second row, the Zernike polynomial corresponding to the coma X aberration $W(\rho, \theta) = CZ_3^1(\rho, \phi) = C\sqrt{8}(3\rho^3 - 2\rho)\cos\theta$ is added to the wavefront, where $C = 0.14 \mu\text{m}$ is the rms amplitude of the aberration. In the third row, spherical aberration is added: $W(\rho, \theta) = SZ_4^0(\rho, \phi) = S\sqrt{5}(6\rho^4 - 6\rho^2 + 1)$, where $S = 0.15 \mu\text{m}$.

Figure 4.6 presents the theoretical and experimental results of using the adaptive optics. The far-field intensity is computed with a Fourier transform from the theoretical phase map calculated using Eq. 4.3, and then compared with the experimental measurements for different wavefronts. It can be seen that the adaptive optics works well, and that aberrations can be added to the wavefront in a controlled way. Although the last amplification stage is cryogenically cooled, the thermal conditions still vary slightly with different amounts of pumping of the final amplifier. Figure 4.7 shows two experimental focal spots recorded without amplification in the last amplifier (a), and with full amplification (b). In addition to the focal plane movement due to thermal lensing, the quality of the focal spot is different. It is therefore important to optimise the beam under the actual experimental conditions, i.e. at full power. However, the beam must be properly attenuated in order to run the adaptive optics loop. This was done using reflective attenuators.

4.2 Typical experimental arrangement and diagnostics

In a typical experimental set-up, such as that shown in Fig. 4.8, the laser beam is focused onto a gas medium, where it drives

plasma waves and accelerates electrons. The electrons are then detected using a scintillator or a phosphor screen. A dipole magnet can be placed between the source and the screen to record electron spectra. Additional diagnostics can be implemented to gain better insight into the interaction. The laser light after the interaction can be collected and its spatial and spectral content analysed. Side- and top-view images of the interaction in the plasma are obtained by collecting the light produced in the interaction through Thomson scattering, using optical imaging systems. Finally, x-rays produced in the plasma wiggler can be detected using an x-ray camera, placed on the laser axis. In this case, the dipole magnet should be in the beam to prevent electrons from hitting the camera.

4.2.1 Gas medium

The gas medium is typically a few mm long and has an electron density, n_e , of 10^{18} – 10^{20} cm $^{-3}$. In order to avoid ionisation defocusing, helium or hydrogen is used, which are easily ionised, as discussed in Section 2.3. As hydrogen is a diatomic molecule, when ionised both hydrogen and helium produce two electrons per molecule/atom. Helium has the advantage of being safer than hydrogen and is used most of the time. However, recent experimental findings seem to indicate that hydrogen has some interesting features and, in particular, produces more stable electron beams. The gas medium is characterised using interferometric methods which allow the density and profile of the gas distribution to be determined.

A supersonic gas jet is often used as a gas medium. High-pressure gas is pulsed through a conically shaped nozzle, which produces a supersonic flow with sharp gradients at the edges of the jet. This is done to avoid ionisation defocusing before the most intense part of the pulse arrives. A large range of pressures can be attained with such a device by varying the backing pressure in the range 0–100 bar. Depending on the laser energy, focusing conditions, and experimental requirements, different nozzle sizes are used, typically with a diameter of a couple of millimetres. For example, in the experiments described in Papers V and VI, the nozzle had a diameter of 2 mm.

Capillary tubes

As was shown in Section 2.8.2, the laser can be guided over several millimetres when self-focusing counteracts diffraction. However, as the laser will lose energy to the wake, self-focusing will eventually stop, and the laser pulse will no longer be guided. In addition, as discussed in Section 2.9, the final electron energy scales as $1/n_e$, and lowering the electron density allows higher energies

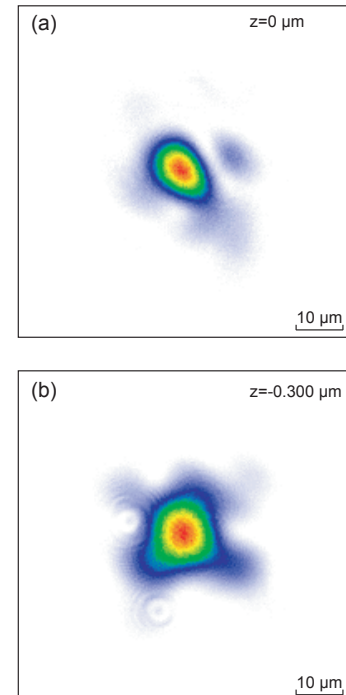


Figure 4.7. Experimental focal spots without pumping of the final amplifier (a), and with full amplification (b). Between the two cases, the focal plane has moved by approximately 300 μm due to thermal lensing. The wavefront is also affected by thermal effects. The focusing optics had a focal length of 45 cm.

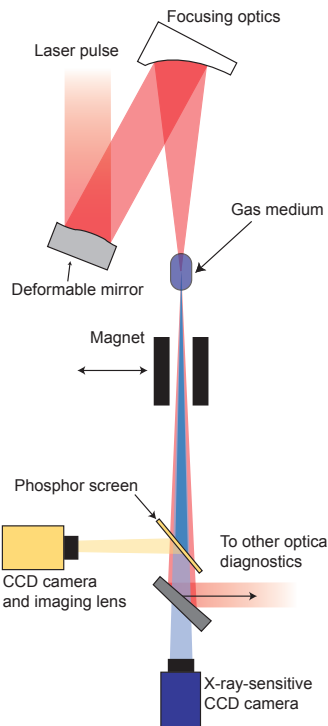


Figure 4.8. Typical experimental set-up. Most of the components are in a vacuum chamber where the pressure is of the order of 10^{-5} mbar. Windows in the vacuum chamber allow some components, such as the optical diagnostics or the camera imaging the phosphor screen, to be located outside.

to be reached. However, the critical power for self-focusing increases and guiding due to self-focusing does not occur at all. In both cases, the laser pulse must be guided externally in order to counteract diffraction. As electrons reach their maximum energy at the dephasing point, the guiding length should ideally be the dephasing length, which also scales as $1/n_e$. When guided, the laser pulse interacts with the medium over long distances, of the order of centimetres.

Several groups are using plasma discharge capillaries, where an electrical discharge is used to ionise the medium before the arrival of the laser pulse, producing a parabolic, transverse refractive index profile suitable for guiding [65]. Electrons have been accelerated over 30 mm, up to 1 GeV in some cases [12, 91, 92]. Another alternative is presented in Papers **II**, **III** and **IV**, where dielectric capillary tubes were used to guide the laser pulse. The inside walls are smooth and the laser pulse is guided by Fresnel reflections from the wall. This method has the advantage that an arbitrary low density can be achieved inside the capillary tube, while the discharge capillaries require a minimum density (of the order of 10^{18} cm^{-3}) in order for the discharge to be possible. Lowering the electron density allows higher energies to be reached, however, the laser pulse must be guided over very long distances. One drawback is that these capillary tubes are made of glass, which makes them very sensitive to pointing instabilities, which may cause breakage. For good coupling, the quality of the focal spot is also crucial. The beam pointing system and the adaptive optics described in Sections 4.1.1 and 4.1.2 were therefore critical in the success of the experiments described, for example, in Papers **II**, **III** and **IV**.

Depending on the ratio between the focal spot and the capillary tube diameter, different modes propagate inside the tube. To achieve a long, linear plasma wave, the laser pulse should be guided in the monomode regime. High transmission can then be achieved over several centimetres. Paper **II** reports, for example, guiding over 8 cm. The experimental investigations described in Papers **II** and **III** also showed that a linear plasma wave was excited over this length. As seen previously, in Section 2.7, electrons would have to be injected externally in this accelerating structure in order to be accelerated. If the focal spot is small compared with the capillary diameter, higher-order modes are also excited and propagation becomes multi-mode. This is less desirable from the point of view of guiding, but as higher intensities are achieved, electrons can be self-injected and accelerated. This is presented in Paper **IV**.

In the paraxial approximation, the electric field inside the capillary can be written as a superposition of the eigenmodes of the tube [93]. The energy in each mode varies as $\exp(-2k_a z)$, where $L_a = 1/k_a$ is the attenuation length. Table 4.3 gives the values of

L_a for the different modes. It is clear that the first mode is only weakly attenuated while the attenuation is much greater for the higher-order modes. The proportion of each mode propagating in the capillary tube depends on the projection of the incident beam onto the mode. Therefore, the coupling of the incident beam to the capillary is important as different modes show different propagation behaviour. The proportion of energy coupled to mode m is a function of the ratio between the capillary radius, R_{cap} , and the beam waist, w_0 .

Figure 4.9 shows the coupling to the different modes as a function of $\alpha = R_{cap}/w_0$. It can be seen that for $\alpha = 1.55$, the propagation is quasi-monomode. In this case, 98% of the incident energy is coupled to the first mode, while the rest of the energy is coupled to higher-order modes or lost in the capillary walls. If $\alpha > 1.55$, energy is also coupled to the other modes and the propagation becomes multi-mode. If the incident beam is not gaussian, the coupling is not as efficient for monomode guiding. For example, for an Airy distribution (which is closer to the experimental conditions), monomode coupling is achieved for $R_{cap}/r_0 = 1$ (where r_0 is the radius to the first minimum of the Airy pattern), and 83% of the incident energy is coupled while 17% is lost in the capillary walls. In the experiments discussed in Papers II and III, the propagation was close to monomode, while in the experiment described in Paper IV, capillaries with larger diameters were used and the propagation was multi-mode.

The dashed line in Fig. 4.9 shows the sum of the coupling of all the modes up to $m = 10$. It can be seen that even in multi-mode propagation, the total coupled energy remains high. However, as the attenuation length is very different for the different modes, the transmission after propagation in the tube decreases for large α , as only the first mode has a very long propagation length. This is illustrated in Fig. 4.10, where a 2D plot shows the transmission as a function of α and the propagation distance, z . Only monomode propagation (dashed line) allows good transmission over a long distance.

In the different calculations presented above, it was assumed that the incident beam remained aligned with the capillary axis. However, this is not the case experimentally, as there are fluctuations in the pointing of the laser beam. A detailed investigation of the effect of an offset between the centre of the beam and the centre of tube and/or an angle between the axis of the beam and the axis of the tube on guiding is presented in Ref. [94]. The transmission is affected by these displacements, as well as the beam profiles after propagation in the tubes. An asymmetric beam profile is obtained if the centring in the tube is not perfect. This further motivated the development and use of the beam pointing system described in Section 4.1.1.

Table 4.3. Attenuation length, L_a , as a function of the mode, m , for a capillary tube of radius 50 μm and a laser wavelength of 800 nm.

m	L_a [cm]
1	91.7
2	17.4
3	7.1
4	3.8
5	2.4
6	1.6
7	1.2
8	0.9
9	0.7

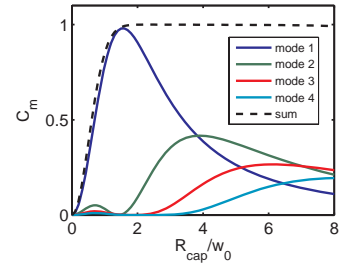


Figure 4.9. Coupling of a gaussian beam to the different capillary tube modes.

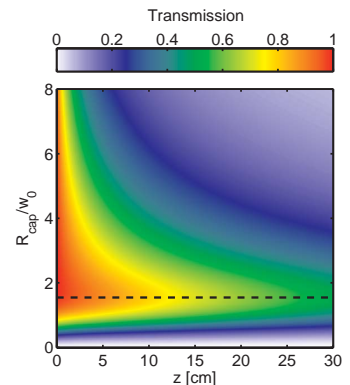


Figure 4.10. Total transmission of a gaussian beam after a distance z for different ratios between the beam waist and the capillary tube diameter. The dashed line represents monomode propagation.

4.2.2 Electron diagnostics

In the electron acceleration experiments presented in this thesis, the electrons were detected using a Kodak Lanex phosphor screen. Electrons hitting the screen cause fluorescence at 545 nm, which can be recorded in a CCD camera. A metallic sheet is placed in front of the screen to prevent laser light and low-energy electrons from reaching the screen. The emission efficiency of the Lanex screen peaks for electrons with kinetic energy of 450 keV, and becomes flat above 1 MeV [95]. It is therefore necessary to block electrons with energies below 1 MeV. By blocking all electrons with energies below this value, the amount of light detected depends only on the number of electrons, i.e. the charge.

At the same time as electrons are accelerated, a high number of infrared photons are present in the chamber. To avoid saturation of the camera, an interference filter is placed in front of the CCD, in order to detect only the green light emitted by the screen. Appropriate shielding is also necessary to prevent any laser light from reaching the camera. Alternatively, as the emission lifetime of Lanex is $660 \mu\text{s}$ [96], the camera can be triggered a few μs after the laser shot. The laser light will have disappeared, but most of the Lanex emission is still collected by the camera. The amount of light collected by the camera is given by: $\int_{\Delta t}^{\infty} \exp(-t/\tau) dt / \int_0^{\infty} \exp(-t/\tau) dt$, where Δt is the time at which the camera was triggered after the laser shot. For $\Delta t = 5 \mu\text{s}$, 99.2% of the light emitted by the screen is collected. This method was used successfully in the study discussed in Paper VI.

The electron spectrum is obtained by inserting a dipole magnet between the source and the Lanex screen. Using permanent magnets, the dipole can be small and placed very close to the interaction, keeping the set-up very compact. The magnet used in this work had a length of 100 mm, a height of 50 mm, a gap of 10 mm and a maximum magnetic field of 0.8 T. The magnetic field inside the magnet is non-uniform and in order to track electrons precisely, it was mapped using a Hall probe. Finally, in order to reduce the fringe fields, the permanent magnets were embedded in iron yokes.

4.2.3 Optical diagnostics

Thomson side scattering

Top- and side-view imaging are important diagnostic techniques in experiments using underdense plasma. When propagating in the plasma, the laser pulse experiences Thomson scattering. This is the elastic scattering of the electromagnetic radiation by a free charged particle and occurs at the laser wavelength $\lambda_s = \lambda_0$, and offers a means of visualising how the laser pulse is guided. The measured signal depends on the laser intensity and the electron

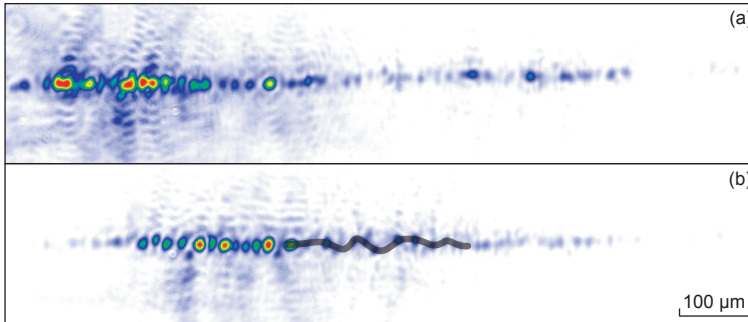


Figure 4.11. Examples of top views of plasma channels. The laser enters from the left. Hosing modulation of the plasma channel is observed in (b).

density along the viewing axis, y :

$$S \propto \int I(y)n_e(y)dy. \quad (4.6)$$

For a weak intensity, when the electron density is not too perturbed, this measurement gives an indication of the laser intensity. However in the nonlinear case, the electron density is strongly perturbed by the laser field, and it is more difficult to extract information about either the intensity or the electron density [97]. Figure 4.11 (a) shows a typical image recorded using this type of diagnostic technique during the experiment reported in Paper V. As the laser pulse becomes self-focused, a strong signal can be observed at the beginning of the channel, according to Eq. 4.6. The signal then decreases, despite the fact that the laser intensity remains the same. This is due to cavitation, i.e. electrons are forced away from the region of high intensity by the ponderomotive force of the laser and there is much less scattering, as the electron density is decreased.

While most of the channels are single and straight, split or kinked channels can be observed from time to time. For example, Fig. 4.11 (b) displays the so-called hosing modulation of the plasma channel, i.e. a transverse oscillation of the pulse during its propagation through the plasma. This was observed while modifying the spatial profile of the laser to produce asymmetric focal spots, as will be discussed below in Section 5.2.1, and also reported in Ref. [98].

Transmitted light

As seen in Section 2.8, a laser pulse undergoes many changes during its propagation in the plasma, such as focusing, compression and frequency shifts. It is, therefore, very interesting to collect the laser light after the interaction in order to analyse it and extract information about the interaction. In the experiments reported in Papers II, III and VI, wedges were inserted after the gas medium in order to attenuate the beam, which is then made parallel by

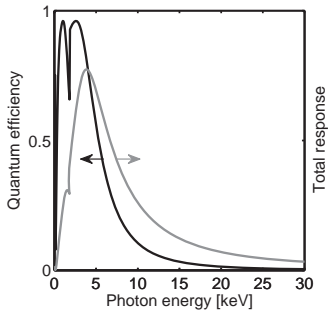


Figure 4.12. Typical quantum efficiency of an x-ray CCD camera and total response taking into account that the number of electrons produced in the chip depends on the energy of the x-ray photons.

passing it through a lens. The beam is sent outside the vacuum chamber, and focused by a second lens onto the different optical diagnostic equipments. Having a parallel beam after the lens is advantageous as the distance between the two lenses can be chosen arbitrarily and the beam experiences minimum aberration while passing through the chamber window.

By varying the position of the lenses it is possible to image any plane along the interaction. The exit of the beam from the gas medium is usually imaged with a magnification of 1. A CCD camera equipped with a microscope objective is used to obtain spatial information. Part of the light can also be sent to a spectrometer, where frequency shifts can be detected. This was the main diagnostic technique used in the experiments reported in Papers [II](#) and [III](#). A photo-diode can also be used to measure the total transmission of the laser pulse through the plasma. This experimental arrangement was, for example, used in the experiment discussed in Paper [VI](#) and is shown in Fig. 5.11.

4.3 X-ray detection

As discussed in Chapter 3, x-rays can also be produced during the laser plasma interaction. Their investigation is important in order to determine the characteristics of this new x-ray source. It also provides great insight into the interaction itself. The detection and characterisation of these x-ray pulses is a challenge for many reasons. The source is not reproducible, therefore the detection method should work on a single-shot basis in order to extract meaningful information. Thus, some x-ray detectors used, e.g., in nuclear physics, are not suitable, as they are designed for long-term acquisition with low photon rates. In the present case, a high photon flux is delivered in a very short time. The electron beam is deflected by a dipole magnet (see Section 4.2.2), and the laser light is blocked by a metallic filter to avoid the detector from being saturated by infrared photons. Other x-ray photons, such as Bremsstrahlung should also be taken into account.

A convenient way to detect these x-rays is to use an x-ray CCD camera. Such devices can detect well into the hard x-ray region (see Fig. 4.12). It can simply be inserted into the beam to investigate the spatial features of the beam. However, as the sensitivity of the camera depends strongly on the energy of the photons, spectral information must also be obtained in order not to misinterpret the images. Obtaining a higher signal in the camera may mean either more photons or photons of different energy. The sensitivity of the camera can be extended towards harder x-rays by using a chip with a deeper depletion region, i.e. a thicker sensitive silicon layer. During my PhD studies, two methods, described in more detail below, were investigated in order to study

the spectral content of the source: placing a matrix of metallic filters in front of the CCD chip, and using the CCD in direct detection mode. Bragg diffraction from a crystal can also be used [73], but this gives information only in one narrow spectral range, and many shots are necessary to acquire a full spectrum in a range limited to about 1–3 keV.

It is also crucial to ensure that the measured signal is indeed coming from the plasma wiggler. For example, when the electron beam is dumped, or hits a metallic object, such as the magnet, it produces a large amount of Bremsstrahlung which may be detected by the camera. By placing an object (for example thin wires) between the source and the detector, it is possible to discriminate between the different sources of radiation, as the shadow of the wires will only be visible if the source is in the line of view between the wires and the camera. In addition, the source is smaller than the smallest visible wire diameter. In the case of Bremsstrahlung created by electrons hitting objects in the chamber, the emission is isotropic and the source large. The wires would therefore not be visible. Figure 4.13 was acquired during the experiment reported in Paper V. The shadow of the wires is clearly visible, showing that the source size is smaller than 50 μm , confirming that we are indeed detecting x-rays produced by the plasma wiggler.

4.3.1 Filter arrays

Information on the x-ray spectrum can be obtained using Ross filters, i.e. an array of different filters [99–101]. Assuming a synchrotron-like spectral distribution, described by Eq. 3.19, the only free parameter is the critical energy, E_c . It is then possible to calculate the transmission through each filter as function of E_c . As can be seen in Fig. 4.14, the transmission of x-rays through different materials depends strongly on the photon energy. This is therefore an energy-sensitive method. Using a least-squares method, it is then possible to determine the energy that best fits the experimental data [74, 75].

This method is illustrated in Fig. 4.15, with an experimental image from Paper V. The signal shown is the average of the different filters (labelled 1–6). The background is obtained by blocking part of the CCD with a thick sheet of metal (labelled 7). This signal is normalised and compared with the signal from synchrotron spectra of different critical energies, as shown in Fig. 4.15 (b). In this case, the best fit is obtained for $E_c = 1.4$ keV. In (c), the difference between the measured signal, s_m , and the fitted signal, s_f , is shown, where $\chi^2 = \sum(s_m - s_f)^2$ is plotted as a function of the critical energy. A clear minimum can be observed at $E_c = 1.4$ keV.

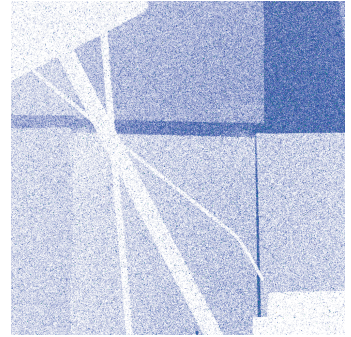


Figure 4.13. Far-field profile of the x-ray beam recorded with an x-ray CCD camera with different metallic filters in front of the chip. Metallic wires of various thicknesses (50, 100 and 250 μm) were placed between the source and the detector. Their visible shadows on the image, confirm that the x-ray source is smaller than the wire diameter, and is placed on the optical axis.

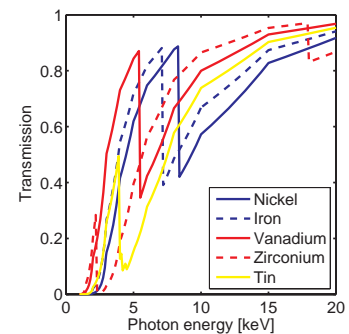


Figure 4.14. Transmission of photons through different metallic filters with a thickness of 3 μm .

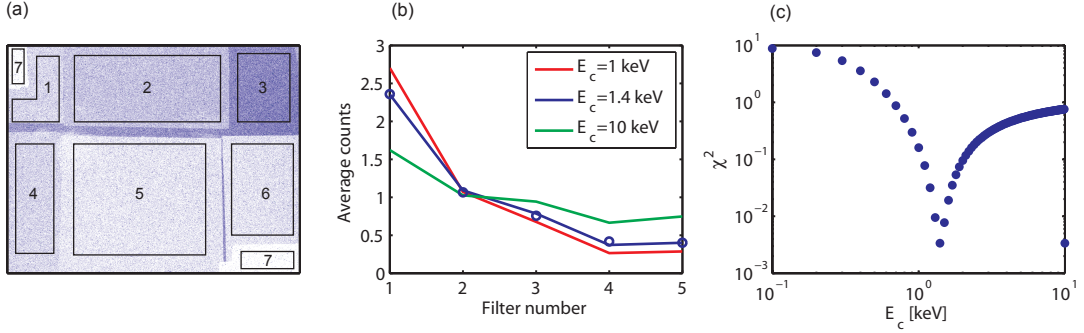


Figure 4.15. The x-ray CCD chip is covered with different metallic filters, labelled 1-6 in (a). The background is recorded behind a thick Cu filter (7). The signal behind each filter (open circles) is compared with synchrotron spectra of different critical energies, as shown in (b). For a given critical energy, a clear minimum is observed for χ^2 in (c). This is the best fit to the synchrotron spectrum.

The advantages of this method are that it allows single-shot measurements and also provides spatial information, as seen in Fig. 4.13. It is also quite insensitive to noise, as the background can be easily subtracted. The number of filters should be sufficient to avoid misinterpretation of the results, due to noise or other sources of radiation. However, the resolution of this method is limited as it relies on assuming the expected shape of the spectrum. If the x-ray beam had special spectral features, one would simply observe a poor fit of the filter transmission.

4.3.2 Single-hit counting

An x-ray CCD camera can also be used in direct detection mode. When a single x-ray photon hits a pixel of the x-ray CCD, a number of electrons is released, proportional to the energy of the photon. A CCD chip provides a large number of detectors, as each pixel acts as an independent detector, and a complete histogram of the spectrum can be obtained from a single x-ray pulse. This method offers better spectral resolution than the filter arrays, but provides no spatial information, and is quite sensitive to noise, e.g. Bremsstrahlung. The theoretical and experimental aspects of this method are described in detail in Ref. [102, 103]. It has been used previously to characterise repetitive x-ray sources [104, 105], where accumulation over many shots is possible. In this case, there is only one source of x-rays and the investigation is therefore much easier as there is no need to identify the origin of the x-rays. This method has recently also been applied to plasma wiggler x-rays, both by accumulating several shots [106] and in single-shot mode [80]. It was confirmed that the x-ray spectrum was indeed synchrotron-like opening the way for more detailed investigations of the x-ray spectral distribution in the

future. During my thesis work, a preliminary investigation of the method was carried out, and the results will be discussed below, together with an experimental example.

In order for this method to work, the beam intensity must be low enough to ensure that no more than one photon hits each pixel, to avoid pile-up. If the photon density is too high, it would be impossible to distinguish whether a single photon with high energy had hit the pixel or two photons with half the energy. A photon may also hit the boundary between several pixels, or a photon hitting a single pixel, might generate an electron cloud spreading over more than one pixel. These events are called multi-pixel events. To ensure that all the energy has been deposited in a single pixel, only single-pixel events are considered in the analysis. Only in the case of very low photon density can multi-pixel events be taken into account, as the probability of two photons or more hitting neighbouring pixels would be very low.

As no spatial information is available, it is difficult to determine whether the measured photons are x-rays originating from the plasma wiggler, or from another source, for example Bremsstrahlung. γ -rays and x-rays with a broad energy distribution are produced when energetic electrons hit a material, for example, the magnet. While any spectral structure in the beam varies from shot to shot, well-defined fluorescence lines of different materials observed at well defined energies, are an indication of the presence of a strong Bremsstrahlung background [106]. However, the main part of the Bremsstrahlung has a thermal distribution, with photons extending into the MeV range, which pass through the CCD chip without being stopped, but still giving rise to a signal in the pixel. It is then impossible to differentiate a low-energy photon that is completely stopped from a high-energy photon passing through the chip. This introduces an error in the measurement. It is, however, possible to estimate the amount of Bremsstrahlung by placing a thick sheet of metal in front of part of the chip, as this will block all the plasma wiggler x-rays but not the Bremsstrahlung. If the proportion of Bremsstrahlung is too high, the measurements will not be reliable. The amount of Bremsstrahlung reaching the camera can be reduced by using lead pinholes and shielding around the camera. Placing the camera far away from the source (a few metres) also helps. It is thus possible to obtain a sufficiently low density of photons impinging on the chip to achieve enough single-pixel events, and reduce the contribution from Bremsstrahlung due to their isotropic emission.

The method is illustrated in Fig. 4.16 by experimental data obtained in connection with the experiment presented in Paper VI. It was acquired with the camera described in Ref. [103]. The CCD chip consists of 512×512 pixels, each with a size of $24.8 \times 24.8 \mu\text{m}$. The gain setting used corresponded to 20.2 eV of x-ray energy per analogue-to-digital converter (ADC) unit, cali-

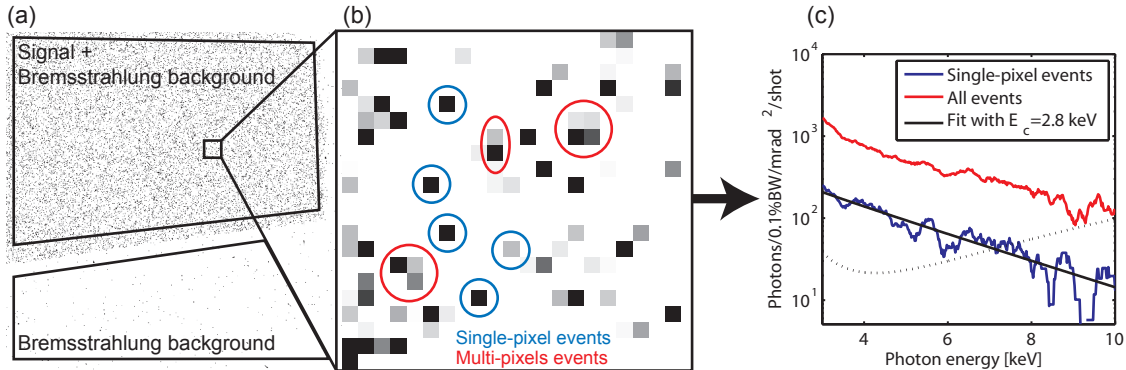


Figure 4.16. Illustration of the use of an x-ray CCD camera in direct detection mode together with an example of an experimental shot. By zooming in (b) on part of the raw image shown in (a), it is possible to discriminate between the different events. In (c), the blue curve shows the x-ray spectrum obtained from the raw image. It can be fitted with a synchrotron spectrum (solid black line). The dotted line shows the absorption correction ($\times 10$) applied to compensate for the filter absorption and the quantum efficiency of the camera.

brated using the emission lines from an ^{55}Fe source. Deconvolution from the calibration data gives a resolution of 210 ± 1 eV, which corresponds to about 10 ADC units. The resolution of the measurement is therefore not limited by the resolution of the analogue-to-digital converter, but by the statistical nature of the electron avalanche, which gives an uncertainty in the relation between the number of counts and the photon energy. The camera was placed behind a $300\text{ }\mu\text{m}$ thick Be window at a distance of 2.5 m from the laser focus. Taking the transmission curve of Be and the sensitivity of the chip into account, the statistics were sufficient above 3 keV. The camera was placed on-axis and the collection angle of the chip corresponded to $5 \times 5\text{ mrad}^2$.

In Fig. 4.16 (a), a raw experimental image, recorded with the camera, is shown. The different events are sorted during the analysis of the image, as can be seen in the enlargement in (b). Finally, a histogram is created, (c). The blue curve shows the result obtained when only the single-pixel events are considered. A moving average filter over 15 ADC units is applied to the data, without losing too much resolution (the resolution of the measurement corresponds to 10 ADC units). The corresponding histogram taking into account the multi-pixel events is shown in red. As discussed above, the single-pixel events give the most reliable information about the x-ray spectrum. In this case, a synchrotron spectrum with $E_c = 2.8$ keV gives the best fit to the data. It can be seen that single-pixel events above 8 keV are lacking, leading to a poor histogram for high-energy photons. In order to avoid pile-up, at most $\sim 10\%$ of the pixels should be irradiated. In this particular experimental shot, the x-ray flux was slightly too high, as 20% of

Table 4.4. Attenuation factors (minimal value) in [m^{-1}] of different materials of density ρ in [$g\text{ cm}^{-3}$] for Bremsstrahlung (B), low-energy neutrons (LEN), medium-energy neutrons (MEN) and high-energy neutrons (HEN).

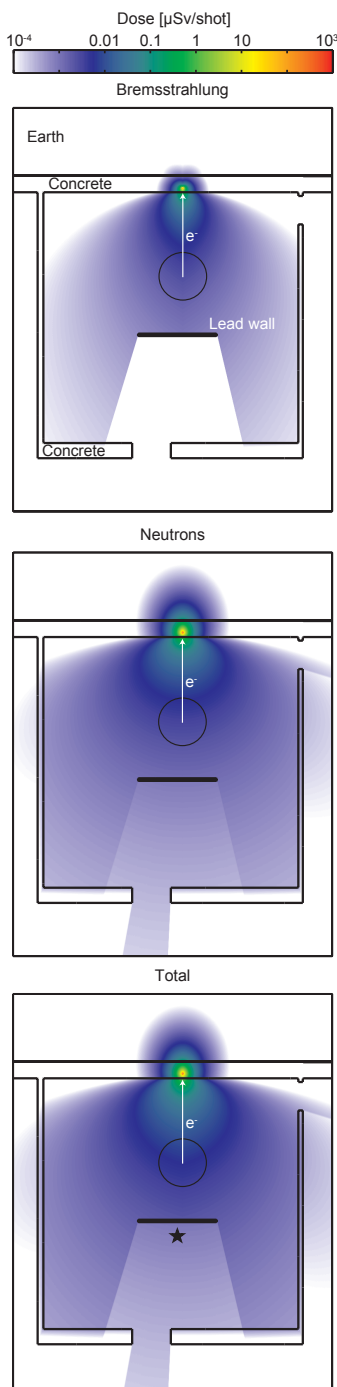
Material	ρ	B	LEN	MEN	HEN
Concrete	2.3	5.5	5.9	2.6	2.2
Lead	11.3	47	4	5.7	5.7
Steel	7.9	23	5.2	5.4	5.4
Plastic	1	2	9.6	—	—
Earth	1.6	2.3	4.9	3.1	1.8

the pixels were irradiated. This can also be seen from the ratio between multi- and single-pixel events, which is also rather high. The bottom part of the image in Fig. 4.16 (a) was blocked by a thick copper filter to estimate the amount of Bremsstrahlung. For this shot, the amount of Bremsstrahlung corresponded to 2% of the total amount of x-rays. The uncertainty in the measurement due to this source of noise is therefore low.

4.4 Radiation safety

As at any particle accelerator, radiation safety is an important issue for laser plasma accelerators. For the size and repetition rate of most of the high-power lasers (such as the multi-TW laser of the Lund Laser Centre), radiation protection is not a limiting factor yet. This is partly due to the limited repetition rate used in the experiments. It is important to estimate the amount of radiation produced in order to assess the risk associated with increasing particle energy or repetition rate. The discussion of radiation protection below is very brief, and is based on Ref. [107]. More detailed simulations can be done with Monte Carlo methods, using, for example, the code GEANT [108].

When a beam of high-energy electrons hits a material, it starts an electromagnetic shower. After travelling an average of one radiation length, an electron emits a photon due to Bremsstrahlung. The electron and the newly created photon share the energy approximately equally. The emitted photon also travels approximately one radiation length and produces an electron-positron pair. Meanwhile, the electron has emitted one more photon. For each radiation length, the number of particles doubles and the energy per particle is halved. At some point, the electrons have lost most of their energy, the shower decreases and eventually stops. Due to the presence of high-energy photons in the electromagnetic shower, neutrons are also produced by photonicuclear



reactions, with the giant photonuclear resonance being the dominant source.

In order to protect users from this radiation, radiation shielding is used. The attenuation coefficients for different materials depends on the energy of the radiation. The minimal values of the attenuation coefficients are used here and are given in Table 4.4. Shielding from Bremsstrahlung requires heavy elements such as lead or concrete. To shield against neutrons, hydrogen-rich materials, such as water or plastic, are more suitable, as neutrons can transfer a large amount of their energy through collisions, as the mass of the hydrogen nucleus is close to the neutron mass.

The so-called effective dose equivalent rate $H(r, \theta)$ gives the dose in mSv at a distance r from a point of loss S (a beam dump, for example) behind a shield of thickness t_k and is calculated using the expression [107]:

$$H(r, \theta) = \frac{S}{r^2} \sum P_j(\theta) \prod_k e^{-t_k \lambda_{k_j}}, \quad (4.7)$$

θ being the angle relative to the direction of the beam. The index j identifies the type of radiation (Bremsstrahlung, low-energy neutrons, medium-energy neutrons and high-energy neutrons), and the index k the different types of shielding materials. λ_{k_j} represents the different attenuation factors given in Table 4.4. $P_j(\theta)$ is the source production term. Its angular distribution and strength differ for each type of radiation. $S = E_e N_e$ gives the energy contained in the beam, where E_e is the electron energy and N_e the number of electrons (per shot, or per second, depending on whether we want to calculate the dose per shot or the average dose).

We will now study the particular case of our experimental lab, whose layout is shown in Fig. 4.17. The round experimental chamber, made of aluminium, is located in the centre of the room. The electrons are accelerated from the centre of the vacuum chamber towards one of the lab walls. Electrons with energies below about 25 MeV will be stopped in the chamber wall (after ~ 4.7 cm). As the lab is located underground, more energetic electrons will be stopped in the wall and the soil behind it, which act as a beam dump. The thick concrete walls and ceiling of the room protect the people working next to and above the lab from radiation. Finally, a 5 cm thick lead wall is located behind the vacuum chamber, behind which the experimentalists sit while running experiments. In the direction of the beam, the dose is massive, while in the backwards direction, it is much smaller. As a example, the radiation emitted from a beam of 200 MeV electrons and a charge of 100 pC was calculated using Eq. 4.7 and is shown in Fig. 4.17. The calculated dose is very small. Behind the lead wall (at the position indicated by the star), the dose per shot is 0.8 nSv. Note

Figure 4.17. Radiation emitted by a 200 MeV electron beam of 100 pC. The beam is hitting the wall in the direction indicated by the arrow.

that without the lead wall, the dose would be 1.7 nSv/shot. On a very good experimental day 300 shots are made (even though most of them have a charge below 100 pC). If we further estimate 200 days of operation per year, we obtain a dose of 0.048 mSv, which is not significant compared to the natural background radiation. The limit for workers at synchrotron facilities, for example, is typically about 5 mSv/year. It should be noted, however, that if the number of shots or the electron energy increases, the radiation levels will increase. Finally, it is most important to know where the beam goes, as the level of radiation is very high in the direction of the beam.

In the case of proton and ion acceleration, Bremsstrahlung is a negligible effect, and the emitted radiation is small. However, activation in the stopping material is possible. For this reason, the chamber is made of aluminium, where activation is not as important as in steel. In our experiments, the maximum proton energy is about 10 MeV and activation is not an issue.

EXPERIMENTAL RESULTS

This chapter presents a summary of the experimental results obtained during the work leading to this thesis. A brief description of each experiment is given together with the most important results. Links to the rest of the thesis are also provided. Most of these results are also presented in Papers II to VI.

5.1 Laser plasma interaction in dielectric capillary tubes

In many experiments in underdense plasmas a gas jet is used as a gas medium. In this work, however, dielectric capillary tubes (presented in Section 4.2.1) were investigated as a novel, long plasma target (Papers II to IV). In this section, two different uses of dielectric capillary tubes are presented: linear plasma wave generation in the monomode regime, and the production of electron and x-ray beams in such targets in the nonlinear regime.

5.1.1 Linear plasma waves in capillary tubes

In the experiments reported in Papers II and III, linear plasma waves were generated over long distances using dielectric capillary tubes. Guiding of high-power shots was achieved up to 8 cm, and characterised as a function of electron density, pulse energy and capillary length. Characterisation was performed by analysing the frequency changes experienced by the laser pulse while driving the wave, as described in Section 2.8.3. The longitudinal electric fields in the wave could then be inferred.

The laser pulse was focused by an f/30 spherical mirror inside glass capillary tubes of inner radius 50 μm and lengths varying from 12 to 81 mm. Gas flowed into the tube through two thin slits located close to each end. A filling pressure of 25 mbar corresponded to an electron density of $\sim 1.2 \times 10^{18} \text{ cm}^{-3}$. The peak

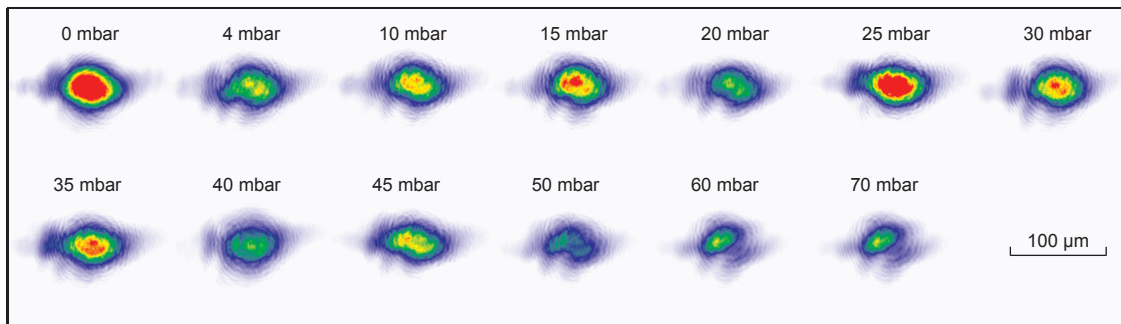


Figure 5.1. Energy spatial distribution at the exit of a 71 mm long capillary tube with a diameter of 100 μm as a function of the filling pressure of H_2 .

laser intensity was $3 \times 10^{17} \text{ W cm}^{-2}$ ($a_0 = 0.37$) and the pulse duration 45 fs. The light was collected after the interaction by two wedges and a collimating lens, and sent outside the chamber to reduce the laser intensity by several orders of magnitude. Nonlinear effects while passing through the chamber window were therefore avoided. The light was then sent to a spectrometer and a CCD camera equipped with an objective in order to record and analyse the spectral content of the laser pulse and its exit mode after interaction inside the capillary tube.

Guiding

As discussed in Section 4.2.1, monomode guiding allows the pulse to propagate in the capillary without too much loss over long distances. It is also important to operate in the monomode regime in order to ensure a homogeneous laser mode inside the capillary tube and to drive the plasma waves efficiently. To achieve monomode guiding the correct capillary diameter for the focal spot size must be chosen. In this case, $\alpha = R_{cap}/r_0 = 1.25$, which is between the optimum value for monomode coupling of an Airy pattern ($\alpha = 1$) and a gaussian beam ($\alpha = 1.55$). Figure 5.1 shows the laser mode at the exit of the tube for different electron densities. It was found that the laser pulse was guided well, even for high electron densities. The exit mode was homogeneous and close to the monomode guiding regime. At high density the transmission decreases as high-amplitude plasma waves are driven, and more energy is lost to the wave.

Characterisation of linear plasma waves

In order to characterise the plasma waves, the spectrum of the transmitted laser light was analysed. As shown in Section 2.8.3, the modulation of the electron density due to the plasma waves modifies the frequency of the driving laser pulse. As the frequency

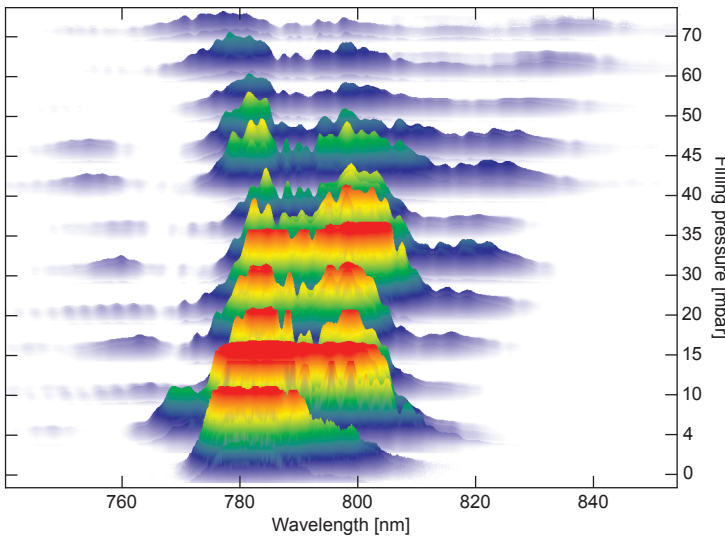


Figure 5.2. Montage of the transmitted spectra with increasing pressure. A blue shift is observed mainly due to ionisation, while the red shift becomes dominant at higher pressures due to the plasma wave.

shift depends on the length of the capillary and the amplitude of the plasma wave, it was used to determine the amplitude of the plasma wave. Figure 5.2 shows raw experimental spectra at different filling pressures. It can be seen that the spectrum is broadened by the interaction. At low pressures, there is mainly a shift towards shorter wavelengths due to ionisation. At higher pressures, a red shift is observed, which is a signature of high-amplitude plasma waves.

Paper III and Ref. [109] give detailed analytical and numerical solutions of the plasma wave generation in the case of capillary tubes. These were compared with the experimental results. For example, Fig. 5.3 (a) shows the experimental (black curve) and simulated (grey curve) wavelength shift as a function of pressure. The dashed curve corresponds to the analytical solution in the linear regime, and gives a resonance curve similar to Eq. 2.32. While at low electron densities all the curves agree well, a discrepancy can be seen at high pressure. At higher pressure the wave starts to become nonlinear, thus producing more frequency shift. The difference between the simulated and experimental data points at high pressure in Fig. 5.3 (a) is due to the fact that in the experiment, the focal spot was slightly asymmetric, while it was assumed to be symmetric in the simulations (therefore driving a higher-amplitude plasma wave). The simulations also provided an estimate of the electric fields inside the tubes by matching the wavelength shift with the maximum and average electric fields inside the tube, as shown in Fig. 5.3 (b).

When plotted as a function of length at a fixed pressure, the shift increases in longer capillaries. This does not mean that the

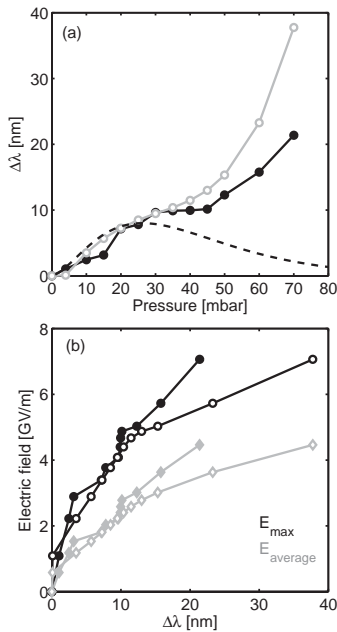


Figure 5.3. Wavelength shifts measured after a 71 mm long capillary tube. In (a), the experimental data (black solid curve) are compared with the numerical simulations (grey solid curve) and the analytical model in the linear regime (dashed curve). The correspondence between the wavelength shift and the maximum (in black) and average (in grey) longitudinal electric fields is shown in (b). The filled and open markers represent the experimental and simulated data, respectively.

amplitude of the plasma wave necessarily varies, but only that the wave is driven over a longer distance and the accumulated frequency shift therefore increases. More features of the spectrum, and its dependence on other parameters, such as energy, are discussed in detail in Paper III. The shape of the spectrum after the interaction was also simulated and agreed well with the experimental spectra. Good agreement between the simulation and the experiment shows that the process is well-understood. The longitudinal accelerating field was in the range of 1–10 GV/m and the average product of gradient and length achieved in this experiment was of the order of 0.4 GV at a filling pressure of 50 mbar for an 8 cm long capillary.

Outlook

The requirements of good pointing and symmetric focal spot make the use of dielectric capillary tubes very challenging. However, both are desirable for wakefield experiments. In particular, it has been observed that the focal spot quality is crucial for good acceleration in discharge capillaries [110] and Paper VI shows the importance of having a focal spot as close as possible to diffraction limit. The advantage of this method is being able to operate at an arbitrary low density, i.e. a long dephasing length, and therefore potentially being able to reach very high electron energies. The product of the electric field gradient and length could be increased by extending the length and diameter of the capillary tube with higher laser energy.

The next step is to inject electrons into this structure in order to accelerate them. Several schemes are possible, as mentioned in Section 2.7.2. A promising alternative would be to place a gas jet very close to the capillary tube. A first laser pulse would create low-energy electrons that could be directly injected into the long capillary tube, where a linear plasma wave is driven by a second laser pulse.

5.1.2 Electrons and x-rays from capillary tubes

As discussed above, capillary tubes can sustain linear plasma waves over long distances. They can also be used as long gas targets for the acceleration of self-injected electrons. In the experiment discussed in Paper IV, electrons were observed at relatively low laser intensities. Using large-diameter capillary tubes and multi-mode guiding, it was possible to trap and accelerate electrons at initial intensities as low as $5 \times 10^{17} \text{ W/cm}^2$ ($a_0 = 0.5$). The peak power in this experiment was 17.5 TW, which is above the theoretical critical power for self-focusing $P_c = 9.6 \text{ TW}$ (see Section 2.8.2), for the lowest density at which electrons were observed ($n_e = 3 \times 10^{18} \text{ cm}^{-3}$). Self-focusing could therefore play

a major role by increasing the intensity of the laser pulse as it propagates in the gas medium, making the trapping of electrons possible. The capillary tube helped to keep the beam self-focused over a long distance by also collecting and guiding energy outside the main peak in the focal plane.

Electrons have previously been accelerated in plasma discharge channels with external guiding to help maintain the laser pulse self-focus for a longer time, allowing the electrons to be accelerated to very high energies [12, 91, 92]. Dielectric capillaries are, however, different as the transverse density profile is homogeneous and a preformed plasma channel is not required.

Although the laser beam was focused by the same focusing optics as in the experiment presented in the previous section, different glass capillary tubes were used. They had diameters of 150 to 250 μm and lengths of 6 to 20 mm, compared to 100 μm diameter and 12 to 80 mm length, in Section 5.1.1. Hydrogen gas was pulsed inside the tube through two 300 μm slits. A Lanex screen and a CCD camera with an objective were used to detect the electrons, which could be deflected by a dipole magnet, similarly to the experimental set-up shown in Fig. 4.8. Electron beams were observed over a large range of plasma densities. However, there was a clear optimum for the total charge above 40 MeV as a function of electron density. The position of this optimum depended on the capillary diameter and the laser intensity. In this experiment, a region between the blow-out and the linear regime was investigated, and the threshold for electron self-injection in long plasmas was studied. Compared with the experiments using gas jets and the same laser system, e.g. those reported in Papers V and VI, a larger focal spot and a lower initial intensity were used. Trapping and acceleration of the electrons were still possible due to pulse evolution, while in a short gas medium this might not have been possible, as the pulse could not evolve sufficiently.

Simulations of the interaction using a 3D PIC code [111, 112] show that a_0 increases slowly as the pulse propagates inside the tube. Trapping occurs after several millimetres, and in some cases multiple injection points are observed in the simulation. As in the experiment, it was found that the electron beam properties depend strongly on both the electron density and the capillary parameters.

X-rays

X-rays were also detected, providing more insight into the interaction. An x-ray camera with an array of metallic filters was placed on the optical axis in order to obtain information about the spatial profile of the x-ray radiation and its spectral content, using the method described in Section 4.3.1. The critical energy of the x-rays was typically 1.3 keV and the number of x-ray photons

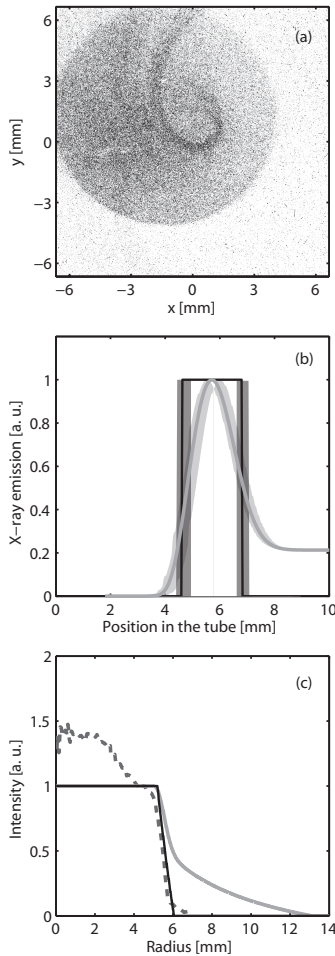


Figure 5.4. Experimental x-ray profile from a capillary tube (a). The edge is clearly visible and can be used to estimate the source position in the tube (b). The profile of the x-ray emission inside the tube, shown in (b), is used to simulate the radial profile shown in (c) for two cases: an off/on emission (black curves) and an emission corresponding to an electron following the orbit shown in Fig 2.9 (b) for $a_0 = 1$ (grey curves). This is compared with the experimental radial profile (dashed line in (c)). The shaded areas in (b) represent the error introduced by not taking into account a transverse source size, here estimated to be $3 \mu\text{m}$.

$\sim 5 \times 10^4$ photons/mrad²/shot. A typical x-ray far-field profile is shown in Fig. 5.4 (a), where the shadow of the edge of the capillary tube, which blocks part of the beam, can be seen. The shape of this edge was used to determine the position of the source inside the tube. Using ray tracing, the profile of the image could be traced back to different sources longitudinally in the tube, making it possible to estimate the beginning and the end of the x-ray emission, as illustrated in Fig. 5.4 (b) and (c). The x-ray emission in the tube was modelled with $z = 0$ corresponding to the beginning of the tube (b). The corresponding radial profile on the detector was simulated and is shown in (c). The black curve corresponds to off/on emission, while the grey curve corresponds to an electron following the orbit shown in Fig 2.9 (b) for $a_0 = 1$, which may be closer to reality. The dashed grey line in (c) shows the experimental radial profile of the image shown in (a). At some point, the signal falls below the noise level preventing the complete characterisation of the x-ray emission. This can be seen in (c), where the end of the simulated grey line would be in the noise.

In this calculation, the transverse source size was neglected. The shaded areas in Fig. 5.4 (b) correspond to the error introduced by this assumption for a transverse source size of $3 \mu\text{m}$, which is similar to the source size deduced in Paper V and Refs. [70, 75, 76]. If the images were of better quality it would have been possible to map the x-ray emission inside the tube, as has been done previously [113]. The slope of the profile recorded by the detector is related to the amount of radiation emitted in the tube through the relation: $dI(z)/dz = -(\partial S/\partial r) r^2/(R_{cap}L)$, where S is the signal recorded on the x-ray camera and L the distance between the capillary output and the camera.

Spatial features were also observed which may be due to x-ray emission corresponding to particular electron trajectories, as discussed in Section 3.3.1. The spiral-like feature in Fig. 5.4 (a) could correspond to a particle being accelerated, as mentioned in Ref. [79]. As discussed in Section 3.4, the oscillation amplitude then decreases due to the increase in relativistic mass, and this feature could correspond to electrons being rapidly accelerated or decelerated. However, the feature in Fig. 5.4 would correspond to a very small injection radius, corresponding to the undulator regime. The radiation profile would then consist of a coherent superposition of the emission from different parts of the trajectory. The shape and strength of the feature would depend on the photon energy, and the spatial feature might be washed out when integrating over all photon energies.

5.2 Influence of the quality of the focal spot

In many experiments, a flat laser wavefront, i.e. a diffraction-limited focal spot, is required. For example, for the experiments discussed in Papers **II** to **IV**, a symmetric focal spot was crucial to achieve good coupling into the capillary tubes. However, it is not always possible to obtain a perfect focal spot, and it is therefore interesting to investigate how the quality of the focal spot influences the acceleration process, as reported in Papers **V** and **VI**. It is also of interest to study how specially shaped focal spots can actually improve some parameters of the interaction, as described in Paper **V**. Note that, in contrast to the previous sections, gas jets were used and not dielectric capillary tubes.

The implementation of the deformable mirror in the laser system, described in Section 4.1.2, provided many possibilities for interesting experiments. Different amounts of aberration could be added to the wavefront in a controlled way in order to shape the focal spot.

5.2.1 Asymmetric focal spot

In the experiment presented in Paper **V**, an asymmetric focal spot was created by introducing different amounts of coma aberration in a controlled way. Figure 5.5 shows a horizontal profile of the focal spot (coma was introduced in the horizontal direction), and it can be seen that the waist for $x < 0$ remains the same as with the flat wavefront, while for $x > 0$ it has changed, thus an asymmetric focal spot has been produced.

After the deformable mirror, the laser beam was focused by an f/9 off-axis parabolic mirror onto a supersonic gas jet, as illustrated in Fig. 5.6. The x-rays were detected using the filter method described in Section 4.3.1. When detecting the x-rays, a dipole magnet was placed in the beam to deflect the electrons away from the detector. The Lanex screen was placed below the optical axis in order to allow the x-rays to reach the x-ray camera. Finally, the plasma channel was imaged from above and from the side through Thomson scattering, as discussed in Section 4.2.3.

As the amount of coma aberration was increased, the size of the electron beam profile observed on the Lanex screen increased. Oscillations in the electron spectra were also observed. Such oscillations have been first reported in Ref. [114], but in the present work they could be produced in a controlled way by adding coma aberration, which was not the case previously. Fig. 5.7 shows typical electron spectra for different amounts of coma aberration at an electron density $n_e = 1.5 \times 10^{19} \text{ cm}^{-3}$. In (a), the spectrum is straight, while in (b) some oscillations start to become visible. In (c) and (d), many different types and planes of oscillations of the electrons produce an electron spectrum with distinct spatial

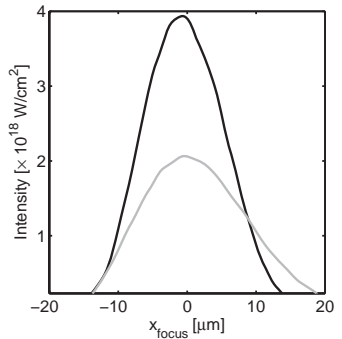


Figure 5.5. Profile of the focal spots used (Paper **V**). The black curve shows the profile corresponding to a flat wavefront. The grey curve shows the result of adding coma aberration.

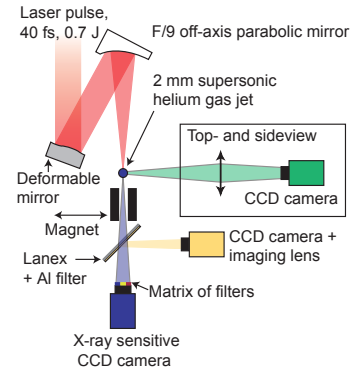


Figure 5.6. Schematic of the set-up used for the experiment reported in Paper **V**.

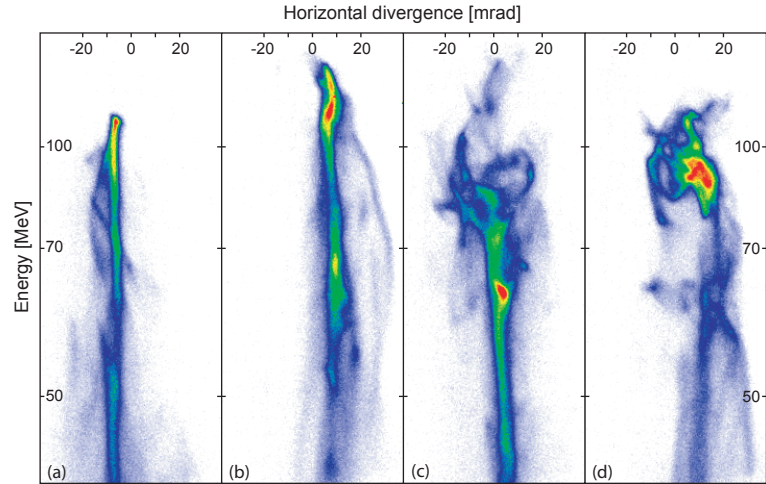


Figure 5.7. Raw data from the electron spectrometer for different amounts of rms amplitude of the coma aberration: 0 in (a), $0.06\text{ }\mu\text{m}$ in (b), $0.1\text{ }\mu\text{m}$ in (c) and $0.14\text{ }\mu\text{m}$ in (d). Energy dependant divergence is observed due the oscillation trajectories in the plasma.

features. The exit angle of the electrons from the plasma is energy dependent, due to the off-axis injection discussed in Section 3.2. In broad electron spectra, electrons with different energies have experienced different accelerating gradients (as they were injected at different phases of the plasma wave), and therefore exit the plasma at different phases of their transverse oscillation orbit, as the acceleration modifies the trajectory of the electrons (see Section 3.4). Although the shape of the electron spectrum varied considerably, the mean electron energy remained constant for different amounts of coma aberration. At high amounts of coma aberration, no beam was observed, as the peak intensity was too low for self-injection to occur.

From the electron data, it seems that asymmetric focal spots promote off-axis injection of electrons into the bubble structure. The quality of the electron beam therefore deteriorates as the size of the source and the transverse emittance increase. However, this is of interest for the production of x-rays, as will be discussed in the following section.

Using an asymmetric focal spot has other effects on the electron beam, such as inducing hosing of the plasma channel [98]. An example of such hosing obtained during this experiment can be seen in Fig. 4.11 (b). This effect is well-known theoretically [115–117]. As shown in Section 2.8, density perturbations and the ponderomotive potential of the laser can affect laser propagation in the plasma. Asymmetric pulses produce asymmetric plasma waves, steering the beam away from the optical axis, while the contribution from the ponderomotive potential tends to bring it back towards the centre. The wavelength of the hosing is of the order of $\sim 100\text{ }\mu\text{m}$ and depends on the electron density. It might be possible to control this hosing by carefully shaping the laser spot profile and possibly enhancing the x-ray emission. Unfortunately,

the magnification of the imaging system was not sufficiently high to study this effect quantitatively. Asymmetric laser focal spots could also affect the pointing of the electron beam. It was shown in Ref. [118], that the electron beam can be steered by introducing spatial chirp into the laser beam. One could expect that the same might happen for small amounts of coma aberration.

Increasing the critical energy of the x-ray spectrum.

In a plasma wiggler, the spectral distribution of the x-rays is described by the critical energy (Eq. 3.18). In order to obtain harder x-rays, either the electron energy must be increased and/or the oscillation amplitude, r_β . As it is not trivial to increase the electron energy without increasing the laser energy, Paper V presents a simple way of increasing r_β . As seen previously, when the focal spot was made asymmetric, the electron beam divergence increased, which indicates that off-axis injection was promoted and the oscillation amplitude of the electron in the plasma wiggler increased. The x-ray spectrum was analysed using filter arrays, as described in Section 4.3.1. It was found that the photon distribution was indeed shifted towards higher energies with increasing amount of coma aberration. Experimentally, the critical energy of the x-rays and the electron spectrum were measured simultaneously. It was then possible to calculate r_β , as $E_c = 3/4\hbar\gamma^2\omega_p^2r_\beta/c$. It was found that r_β increased from 1 to 3 μm , which should be compared with the radius of the wakefield, which at the electron density used ($n_e = 1.5 \times 10^{19} \text{ cm}^{-3}$) gives approximately $\lambda_p/2 = 4.5 \mu\text{m}$. Almost the entire bubble width is therefore utilised as a wiggler. By simply introducing asymmetry into the beam, it was thus possible to tune the wiggler parameter from $K = 5$ to $K = 17$, as shown in Fig. 5.8. In order to make this estimate, $\langle\gamma\rangle$ was used to characterise the electron energy. As shown in Section 3.5, the fact that a distribution of electrons was measured influences the analysis, but as the mean energy of the electrons remains roughly constant, it could be concluded that only r_β varies.

As the asymmetry was in one particular direction, one might also expect the electron trajectories to be promoted in a particular plane. This might in turn produce x-rays with some polarisation along the oscillation plane [119]. As it is easy to introduce asymmetry in any direction, it would be possible to produce an x-ray source with tunable polarisation. This would be of great interest as many applications require polarised x-rays. Further studies are clearly warranted.

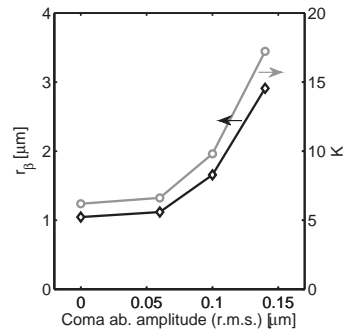


Figure 5.8. Effect of the coma aberration on the oscillation amplitude, r_β and the wiggler parameter, K .

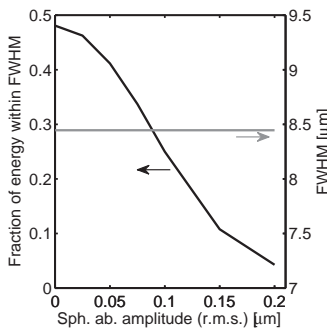


Figure 5.9. Influence of the amount of spherical aberration on the energy within FWHM and the FWHM.

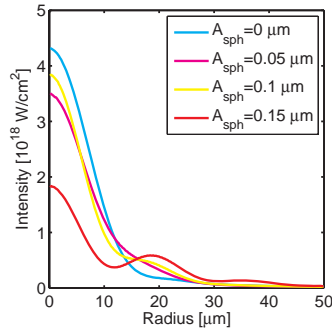


Figure 5.10. Radial profiles of focal spots with different amounts of spherical aberration.

5.2.2 Varying the fraction of energy inside the central part of the focal spot

By varying the quality of the focal spot in a controlled way, it was possible to study how the energy in the pulse is used in the interaction. It was found that only the energy within the FWHM drives the wakefield, and that a focal spot of poor quality is equivalent to a lower laser energy, which was also used to determine the threshold for self-injection (see Section 5.3 and Paper VI). By adding spherical aberration to the wavefront, the fraction of energy inside the FWHM, α , could be tuned without modifying the total laser energy or the size of the beam, as illustrated in Fig. 5.9. The radial profiles of the different focal spots used in this experiment are shown in Fig. 5.10.

The experimental set-up is shown schematically in Fig. 5.11. The beam was focused by an f/9 off-axis parabolic mirror onto a gas jet. The light after the interaction was collected by a wedge and sent through an imaging system outside the vacuum chamber, as described in Section 4.2.3. A spectrometer was used to analyse the transmitted spectrum, and the exit mode was imaged by a CCD camera. A Lanex screen was placed behind the wedge and imaged by a CCD camera equipped with an objective. Only the low-energy electrons were stopped by the wedge, and most of the electrons could be detected while simultaneously collecting the transmitted light.

Figure 5.12 shows the electron beam charge as a function of electron density for different values of α , while the total energy in the pulse is kept constant. It is clear that for decreasing α the self-injection threshold shifts to higher plasma densities. As will be discussed in Section 5.3, this is equivalent to decreasing the pulse energy, as αE defines the energy used to drive the plasma wave and self-inject electrons. When large amounts of spherical aberration were added to the wavefront, the electron beam charge did not reach the level corresponding to no aberration (for the density range investigated in this study).

Influence on the transmitted light

Optical diagnostics techniques have also been used to gain more insight into the interaction. These data were acquired simultaneously with the data presented in Paper VI, and the preliminary analysis is presented here. As for the electron beam data discussed above, the importance of the quality of the focal spot is clear. This confirms that the energy in the wings might not contribute to the production of the wakefield, and it is therefore crucial to have the maximum energy within the FWHM.

In the case of a gaussian beam, the whole beam experiences self-focusing. However, in the present experiments the beam was

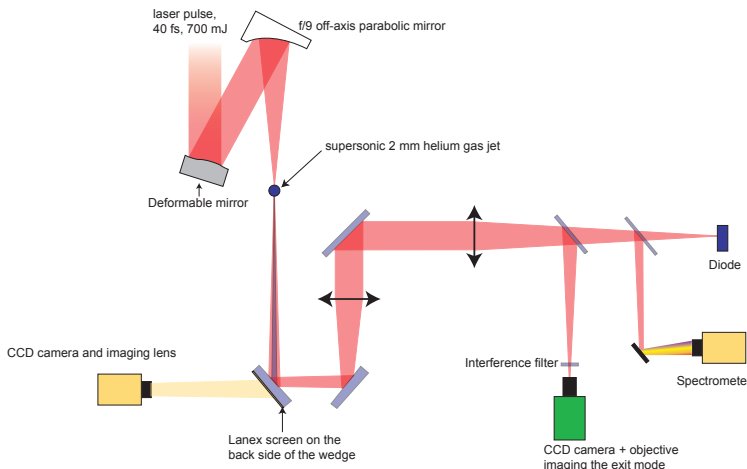


Figure 5.11. Experimental arrangement for the experiment discussed in Paper VI. The light after the interaction was collected by wedges and sent outside the vacuum chamber to different optical diagnostics.

rarely gaussian, and one might expect that only the central part of the beam, i.e. the most intense part, was self-focused, while the wings were not. When the amount of spherical aberration was increased, more energy was transferred to the wings of the beam, as can be seen in Fig. 5.10. By studying the beam as it exits the plasma, it was possible to see how the different parts of the beam were affected by the interaction. Figure 5.13 (a) shows the transmission of the energy within the FWHM. The data are normalized to the transmission in vacuum, and can be fitted using the etching model presented in Section 2.8.4. If we consider a gaussian laser pulse in which the front is being etched away in time at the etching speed, the energy transmission after a distance l is given by [120]:

$$T(l) = 1 - k \sqrt{\frac{2}{\pi}} \frac{v_{etch}}{\Delta\tau_0 c} \int_0^{l/c} \exp\left(-2 \frac{(\Delta\tau_0/2 - v_{etch}\tau/c)^2}{\Delta\tau_0^2}\right) d\tau, \quad (5.1)$$

where k is a free parameter that determines the point at which the pulse starts to be etched. For $k = 1$, the pulse starts to etch when the intensity reaches half the peak intensity in time. For this value of k , the energy remaining after depletion corresponds to the part of the pulse in front of the starting point, which is never depleted. The transmission of the energy within the FWHM after the gas medium ($l = 1.8$ mm) was calculated using Eq. 5.1. By using different values of k ($k = 1.2, 1.1, 1, 0.9$), good agreement was obtained between the experimental data and Eq. 5.1 (note that for clarity only 3 curves are shown in Fig. 5.13). This is an indication that only the central part of the beam is depleted, i.e. only this part drives the wave. As k describes the position where the front of the pulse starts to be etched away, the variation in k may therefore originate from the fact that the position at which the pulse starts to etch changes as the peak intensity decreases.

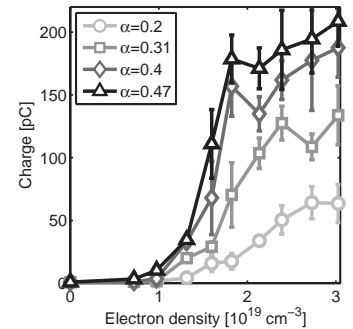


Figure 5.12. The total charge in the electron beam plotted as a function of electron density for different amounts of spherical aberration. The threshold shifts towards higher density as the energy within the FWHM decreases.

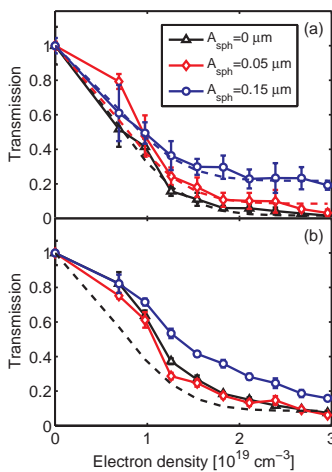


Figure 5.13. Transmission through the plasma for the energy inside the FWHM (a), and outside the FWHM (b). In (a), the depletion model for different values of k fits well (dashed curve). In (b) a different behaviour is observed at low densities, and the depletion model (black dashed line) does not fit as well as in (a).

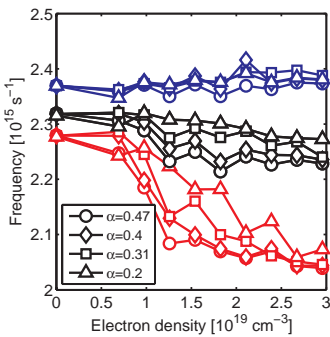


Figure 5.14. Frequency shifts as a function of electron density and α . The black curves show the evolution of the centroid of the spectrum, while the red and blue curves show the variation in the red and blue limits, respectively.

Figure 5.13 (b) shows the transmission of the energy outside the FWHM. At low densities, a different behaviour to that in (a) is seen. One explanation may be that while the central part of the beam self-focuses and drives the plasma wave, the wings of the beam experience ionisation defocusing. The intensity is low in the wings, and different ionisation states may produce a gradient in refractive index, as discussed in Sections 2.3 and 2.8.1. As the electron density increases, the beam becomes more defocused. As the beam becomes increasingly divergent, part of it will miss the collection lens, which may give the appearance of a decrease in transmission, as discussed in Refs. [121, 122].

The spectral content of the transmitted light also gives information on the interaction, similarly, to the case of the linear wave in capillaries in Papers II and III. In this case, however, the regime is nonlinear and the interpretation of the observed shift is more complex. The measured frequency shifts are shown as a function of electron density and α in Fig. 5.14. The black curves show how the centroid of the spectrum varies, while the red and blue curves show the variation in red and blue shifts. These shifts are defined as the points at which $1/e^2$ of the energy is at higher or lower frequency, respectively. The red curves show a different behaviour for the different amounts of aberration. For the best focal spot, the shift increases rapidly until $n_e = 1.25 \times 10^{19} \text{ cm}^{-3}$, after which it remains roughly constant. The same behaviour is seen for the other focal spots, but at higher densities. As discussed in Section 2.8.3, the red shift is mainly due to the density perturbation of the plasma wave. This depends on the length over which the wave is driven and the average density perturbation. A plasma wave will be driven even during pulse evolution, and the length can therefore be considered to be fixed. A greater shift therefore means on average higher amplitude waves, which agrees with Fig. 5.12. At a particular point, the shift no longer increases, perhaps when the wave amplitude no longer increases, i.e. when the wave breaks. With focal spots of poorer quality, wavebreaking therefore occurs at higher densities. Note that the blue shift does not vary as a function of α or n_e , which indicates that the ionisation is not significantly affected by the quality of the focal spot.

5.3 The self-injection threshold

In general, no electrons are observed at very low electron densities. When the density is increased, a beam suddenly appears: this is the threshold for self-injection. This threshold is a very important concept for laser plasma accelerators as it defines the minimum density at which trapping occurs and, ultimately, the final energy of the accelerated electrons. This is also an important concept for

other injection schemes, such as colliding pulses and ionisation injection, presented in Section 2.7.2, as they operate just below the self-injection threshold. A simple model predicting the point at which the plasma wave breaks and electrons are self-injected, was derived from experimental data in Paper VI and is presented here since it summarises the whole interaction rather well.

The threshold was investigated experimentally by varying different parameters and observing how the threshold was affected, using the set-up shown in Fig. 5.11 and the focal spots shown in Fig. 5.10. The energy in the laser pulse, E , the amount of energy within the FWHM, α and the pulse duration, τ , were varied. In the previous section it was already demonstrated that the electron beam charge depends strongly on the fraction of energy within the FWHM, αE . In fact, the influence of the total energy of the pulse, for a fixed value of α , was also studied in the experiment, and it was found that varying the total energy of the pulse and varying α were equivalent, i.e. αE is the important parameter. According to Ref. [123], a power threshold can be expected and the pulse duration should therefore be an important parameter. The effect of pulse duration and chirp on the charge is presented in the next section.

5.3.1 Influence of the pulse duration on self-injection

In order to discriminate between a power and an energy threshold, the effects of laser pulse duration on electron acceleration were investigated. At the threshold density, the pulse duration was increased by changing the separation between the gratings of the compressor. Electron beams were observed even when the pulse duration was increased to more than twice its initial value. In fact, for some settings of the grating separation, the charge was higher than at the optimum compression. This is shown in Fig. 5.15, where the charge is plotted as a function of pulse duration.

When elongating the pulse, by changing the grating separation, temporal chirp was also introduced, which obviously alters the interaction. The pulse shapes recorded using a frequency-resolved optical gating autocorrelator [124], corresponding to some of the grating settings, are shown in Fig. 5.16. The pulse clearly becomes asymmetric on either side of the optimum compression. This is a sign of remaining third-order phase in the spectrum of the laser pulse. It can also be seen that the asymmetry flips side when the sign of the chirp is changed.

This increase in charge for asymmetric pulses has been reported previously. In Ref. [125], it is stated that when the ponderomotive potential is larger on the leading side of the pulse, this creates a higher wave amplitude and therefore enhances self-injection. However, one would expect to see the highest pondero-

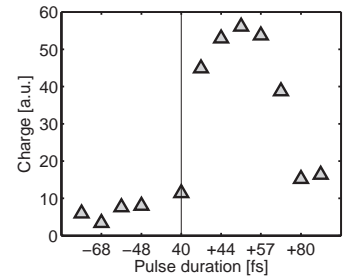


Figure 5.15. Electron beam charge as a function of pulse duration for $n_e = 1.6 \times 10^{19} \text{ cm}^{-3}$. The minus sign indicates that the pulse was made longer by adding a negative chirp, and the plus sign by adding a positive chirp.

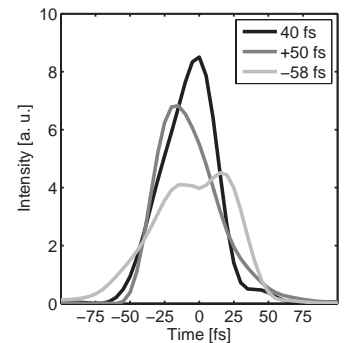


Figure 5.16. The different pulse shapes for three different settings of the grating compressor and different values of the temporal chirp.

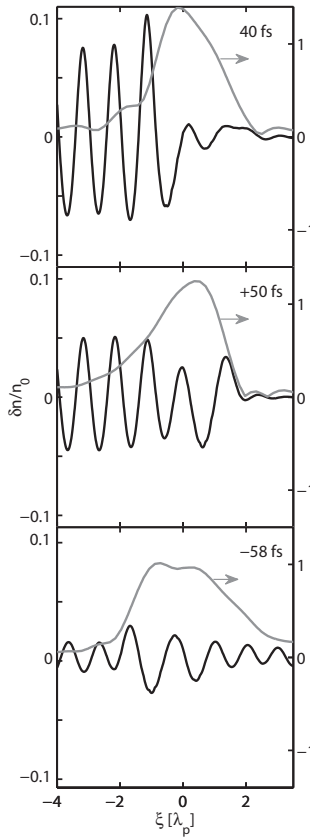


Figure 5.17. 1D simulations of plasma wave generation for the different pulse shapes shown in Fig. 5.16. The black lines represent the density perturbation and the grey lines the normalised potential of the pulse.

motive potential for perfectly compressed pulses where the peak intensity is highest. Figure 5.17 shows a 1D simulation of the plasma wave generated by the experimental pulses in Fig. 5.16. This was achieved by solving Eq. 2.37 numerically. The pulses corresponding to the duration +50 fs produce the greatest density perturbation within the pulse duration. After the laser pulse, the amplitude of the plasma wave is the highest for optimum compression. From this point of view, it is therefore not clear why a positive chirp is better. In Ref. [125], the pulses were longer and the laser plasma accelerator was operated in the self-modulated regime. The fast rise time resulted in a larger initial plasma wave, which acted as the seed for the self-modulation instability. However, under the present experimental conditions, i.e. shorter pulses, the influence of the pulse shape may be different.

An alternative explanation may be pulse compression in the plasma, as discussed in Section 2.8.3. When compressing the pulse, higher-order phase terms are introduced by the plasma. If the pulse is chirped before entering the plasma, the higher-order compression terms are precompensated and shorter pulse duration, i.e. higher intensity, is achieved through pulse compression. It is actually mentioned in Ref. [63] that asymmetric pulses were observed after the plasma. This shows that by starting with the opposite asymmetric pulse, one could come closer to transform-limited pulses inside the plasma.

5.3.2 A self-injection threshold model

The main conclusions drawn from the experimental data presented in the previous sections is that the threshold depends strongly on αE , and that the pulse duration does not affect self-injection significantly. As will be shown below, the threshold density does not vary linearly with αE , but is a more complicated expression.

Most experiments start with a laser pulse, which is not optimal for laser wakefield acceleration. As discussed in Sections 2.4.2 and 2.5, this pulse should have the appropriate dimensions in both space and time in order to efficiently drive a wake, reach wavebreaking, inject electrons and accelerate them. The point at which the wake will break and electrons be self-injected therefore depends on the pulse evolution (spatial self-focusing and temporal pulse compression). The model presented in Paper VI predicts the threshold position from the initial pulse parameters, taking pulse evolution into account.

The model is based on the 3D scaling laws for the bubble regime [39] presented in Table 2.3. Different criteria can be found in the literature to determine whether an electron will be trapped or not. These criteria are obtained by examining the trajectories of electrons around the bubble. In this work, the criterion given

in Ref. [83] was used, where it was found that by reproducing the behaviour observed in PIC simulations, electrons travelled around the bubble in an approximately elliptical orbit. When following such an orbit in the bubble fields, an electron is trapped if it reaches a velocity greater than the bubble phase velocity by the time it reaches the back of the bubble. In this case, trapping occurs when the bubble radius, r_b , is larger than a certain value, given by:

$$k_p r_b > 2\sqrt{\ln(2\gamma_p^2) - 1}, \quad (5.2)$$

where $\gamma_p = \sqrt{n_c/(3n_e)} = \omega_0/(\omega_p \sqrt{3})$ is the 3D relativistic factor associated with the plasma wave. The bubble radius was assumed to be the matched spot size, w_0 , discussed in Section 2.5, and a_0 is related to the peak intensity I_0 through Eq. 2.7. In the case of a gaussian beam, the whole beam experiences self-focusing and the energy of the full beam should be considered. In reality, the beam is rarely purely gaussian and, as shown in Section 5.2.2, only the most intense part of the beam is self-focusing, i.e. only αE . Using Eq. 2.4, I_0 can be replaced by $2\alpha E/(\tau\pi w_0^2)$ and a condition for wavebreaking is obtained. Finally, as discussed in Section 2.8.3, the pulse is also compressed in time by the plasma. A simple model for pulse compression has recently been presented [63] and is used here. The pulse duration varies according to $\tau(l) \approx \tau_0 - n_e l / (2cn_c)$. In the nonlinear regime, pulse compression may be more complicated than this simple linear compression model, as discussed in Section 5.3.1. However, it is the author's belief that it is a good first approximation of the pulse compression process. An equation relating the initial pulse energy, E , and the interaction length, l , is finally obtained:

$$\alpha E > \frac{\pi\epsilon_0 m_e^2 c^5}{e^2} \left[\ln \left(\frac{2n_c}{3n_e} \right) - 1 \right]^3 \frac{n_c}{n_e} \left(\tau_0 - \frac{n_e l}{2cn_c} \right). \quad (5.3)$$

The interaction length is limited by either the length of the gas medium, l_g , or the depletion length, $l_{pd} = c\tau_0\omega_0^2/\omega_p^2$, given by Eq. 2.56. When the pulse is depleted, self-focusing cannot be sustained, the pulse diffracts, and the plasma wave disappears. The condition for trapping then becomes $l(\alpha E) < \min(l_g, l_{pd})$.

When limited by depletion, the wavebreaking threshold becomes a power threshold, while in other cases there is a more complex relationship between energy and pulse duration. From Eq. 5.3, we can determine the electron density at which the wave will break, n_t . For $n_e > n_t$, the wave breaks before the end of the interaction, and electrons are trapped and accelerated over a certain distance. At a given density, the acceleration length is given by $\min(l_g, l_{pd}) - l_t$. If the electron density is too close to n_t , electrons are trapped but not actually accelerated.

To develop the threshold model, the bubble regime was assumed. However, this assumption is not valid for long pulses, i.e. many times the plasma wavelength, and the self-modulated wake-field regime might be more suitable to describe the interaction. This, and the previously discussed issues concerning asymmetric pulses, might explain why electron beams are seen below the threshold given in Eq. 5.3 in the case of long pulse durations.

The predictions of the model were compared with the experimental data given in Section 5.2.2, and show very good agreement. To further strengthen the validity of the model, it has also been compared with previously published data obtained using other experimental parameters [10, 123, 126, 127]. The agreement between the predicted and observed thresholds validates the model for a large range of laser parameters (pulse duration $\tau = 8 - 60$ fs and pulse energy $\alpha E = 0.5 - 6$ J).

PROTON ACCELERATION

This chapter gives an introduction to laser-driven acceleration of protons, which relies on a mechanism other than electron acceleration. The theoretical background and experimental methods are presented, and highlights of two experiments performed are given.

6.1 Introduction

Ultra-intense lasers are able to accelerate protons and heavy ions. As protons are much heavier than electrons, it would be necessary to accelerate them to relativistic energies in order to inject them into a wakefield structure, as discussed for electrons in the previous chapters. Therefore, other mechanisms, relying on quasi-static electric fields from solid targets are used. In particular, for the laser intensities achievable with the Lund multi-TW laser, target normal sheath acceleration (TNSA) efficiently accelerates protons and heavy ions to several MeV laminar beams.

In the year 2000, proton beams were observed for the first time from the interaction of short-pulse lasers with thin metallic foils at intensities above 10^{19} W/cm² [128–131]. These beams were highly charged and exhibited a thermal spectral distribution with proton energies up to a few tens of MeV. At that time, the interaction was not well-understood, but since then many experimental and theoretical investigations have led to a clearer picture of the interaction. Many applications were directly foreseen, such as proton therapy [132, 133], which would require proton beams with higher energies, ~ 100 MeV. Therefore, in recent years, much work has been devoted to increasing the maximum proton energy by using, for example, ultra-thin foils (< 100 nm) [134–136]. Beams with protons of higher energies and with a better spectral distribution are expected in the future as several new acceleration schemes, using more powerful lasers ($I > 10^{23}$ W/cm²), have been proposed.

In particular, protons could be directly accelerated by the light pressure [137–141].

However, other solutions must be investigated in order for this technology to work with reasonably sized lasers. Papers **VII** and **VIII** report on two experiments in which ways of increasing the maximum proton energy, without increasing the laser energy, or of changing their spectral distribution, have been explored. In the first experiment another laser beam was used to enhance the interaction, and in the second a target geometry that recycles some of the energy was employed.

6.2 Intense laser–matter interactions with solids

6.2.1 Electron heating

When the laser hits the target, the medium is ionised by the leading edge of the pulse. A plasma is formed and starts to expand, establishing a density gradient, which increases in length at the ion sound velocity, which in turn depends on the electron temperature. The main part of the laser pulse thus interacts with this expanding plasma, transferring part of its energy to the plasma electrons. At relativistic laser intensities, the laser energy is converted into electrons with temperatures of the order of MeV.

The laser propagates into the plasma gradient in front of the target. When it reaches the critical density, n_c , given by Eq. 2.16, the laser can not propagate any further and is reflected. At high laser intensities, the ponderomotive force of the laser (Section 2.4.1) pushes the electrons forwards and sideways. It also decreases the density around the critical surface and deforms the target surface in a process called hole boring [142]. The direction of acceleration of the electrons in the solid is along the direction of $\mathbf{v} \times \mathbf{B}$, i.e. along the propagation direction of the laser. In this case, the mean energy of the electrons (or the temperature) is given by the ponderomotive energy, which can be inferred from the calculation presented in Section 2.4.1. In the relativistic case, it is given by [143] :

$$T_e = m_e c^2 \left(\sqrt{1 + \frac{e^2 I_0 \lambda_0^2}{4\pi^2 \epsilon_0 m_e^2 c^5}} - 1 \right). \quad (6.1)$$

Note that the electron energy increases with the laser intensity. This process converts the laser energy into electron kinetic energy with an efficiency that can be higher than 30%. At high laser intensities, this is the main heating effect.

When the laser is focused at an angle different from target normal, resonance absorption is also an important process. The laser pulse is refracted in the underdense plasma present in front of

the target. When approaching the critical surface (where the laser frequency is resonant with the plasma frequency), it is reflected. As illustrated in Fig. 6.1, at this point, for p-polarised light, the electric field is normal to the target surface and is able to drive the electron resonantly into a plasma wave. The wave energy is then thermalised by collision or wavebreaking. Hot electrons propagate along the target normal with a cone angle of about 30° [144] and the electron temperature scales as $(I_0\lambda^2)^{1/3}$ [145]. In the case of a steep gradient, the amplitude of the electron oscillation in the laser field can be greater than this gradient. This means that electrons are driven out into vacuum and then back into the target when the laser field is reversed. As the electrons are driven into the target, beyond the critical density, the laser field can no longer reach them. This effect is known as Brunel heating [146]. Note that if the laser impinges normally on the target, these effects do not occur.

6.2.2 Target normal sheath acceleration

For the experiments discussed in this chapter, the main mechanism of ion acceleration is TNSA, which is illustrated schematically in Fig. 6.2. As discussed in the previous section, the leading edge of the laser creates a plasma on the front of the foil (a). Electrons are heated and pushed through the target by the laser pulse, as shown in (b). When the electrons reach the back of the foil and expand into vacuum, a large electrostatic field is created, of the order of TV/m , at the sharp solid-vacuum interface (c). Contaminants (water vapour, oil residues) on the back of the foil are ionised by this field. The plasma rapidly expands, pulling the protons, while an electron sheath is formed at the ion front (d). The protons are accelerated into a laminar beam. Most of the electrons turn around and go back into the target and, if the laser pulse is still present, can participate in the interaction again in a process called recirculation [147]. An electron sheath, however, remains in front of the protons as the fields are shielded over the Debye length, $\lambda_D = \sqrt{\epsilon_0 T / (n_e e^2)}$, which is typically the thickness of the sheath, i.e. of the order of 0.1 to 1 μm .

The electrons do not transfer their energy directly to the protons, which therefore remain cold and exhibit a low transverse emittance. Because the field is perpendicular to the target, the protons are accelerated in the direction of the target normal. The local shape of the back of the foil can therefore influence the direction and divergence of the beam [148–151]. If the back of the target is concave the proton beam will be focused, as discussed in Paper VIII. Because of their charge-to-mass ratio, protons are accelerated faster than other ions, and thus shield the other ions from the fields. In order to efficiently accelerate heavy ions, the proton layer must be removed. Note that the resulting beam is

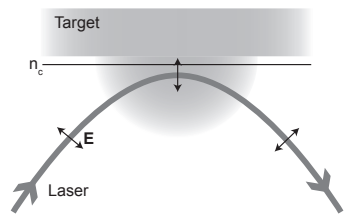


Figure 6.1. Schematic illustration of the resonance absorption heating process. For a p-polarised laser beam striking the target at a glancing angle, resonance absorption occurs when the electric field is normal to the target.

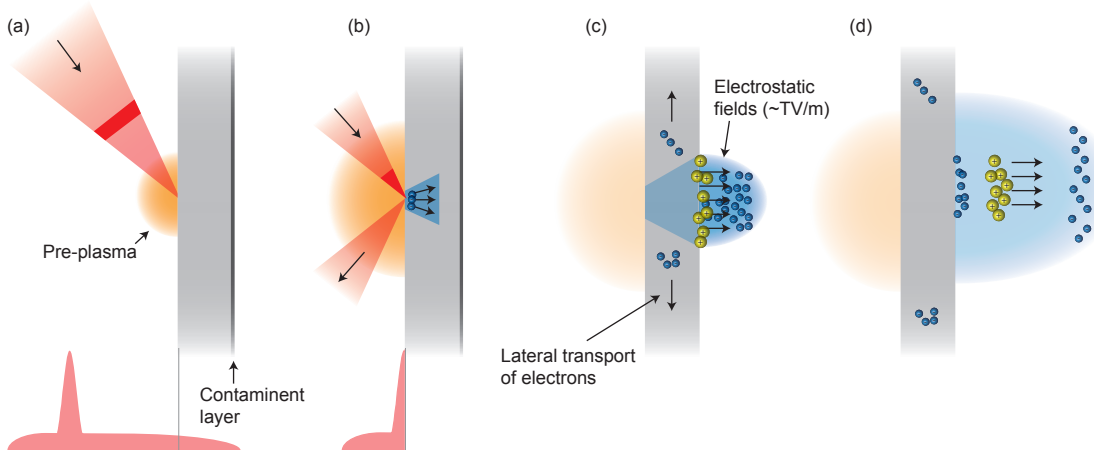


Figure 6.2. Schematic explanation of the TNSA process. In (a), the leading edge of the laser pulse ionises the medium, creating an expanding plasma. Electrons are then pushed through the target, by the ponderomotive force of the laser and the thermal expansion of the plasma (b). They establish a strong electrostatic field on the back of the foil (c), which field-ionises and accelerates protons (d).

quasi-neutral, as protons and electrons are accelerated together. This prevents the non-relativistic proton beam from blowing up because of space charge.

6.2.3 Electron transport

As mentioned above, the ponderomotive force of the laser and the thermal expansion of the plasma “push” the electrons through the target. At the same time, some electrons are also pushed sideways. They will then travel through the target until they reach the end, at a speed corresponding to their mean energy, given by Eq. 6.1. For example, an electron with an energy of 1 MeV has a velocity of $0.9c$. At the edge of the target they also establish an electrostatic field that can accelerate particles. However, the accelerating fields are weaker than directly on the back of the foil, as the sheath is thinner. This edge emission can occur at considerable distances from the interaction point [152]. The electrons can even return to the interaction point, in a fashion similar to the recirculation effect. This effect can be utilised with a mass-limited target to enhance the acceleration process [153, 154].

6.3 Experimental methods

The experiments reported in Papers VII and VIII were performed using the multi-TW laser at the Lund Laser Centre, presented in Section 4.1. A main concern was the temporal pulse contrast, which will be discussed in the next section. Compared

to the underdense plasma experiments, discussed in the previous chapters, a tighter focus was used for proton acceleration in order to achieve higher intensities. An f/3 off-axis parabola was used to focus the laser pulses onto a thin foil of thickness up to a few μm , and a peak intensity of the order of $\sim 10^{19} \text{ W/cm}^2$ was achieved. Protons are emitted normal to the back of the foil, and can be directly detected to give a beam profile. In this case, metallic foils must be placed in front of the detector to protect it from laser damage. Foils of different thicknesses can be combined to give information about the energy distribution of the protons. To obtain a more precise energy measurement, a pinhole and a magnet can be inserted between the target and the proton detector to record proton energy spectra.

Generally, the laser fired onto the target at an angle for two reasons. First, the reflected laser will not be reflected back into the laser system, which could potentially damage elements such as amplifier crystals. Secondly, as discussed in Section 6.2.1, resonant absorption does not occur if the laser impinges on the target normally. The efficiency of the coupling between the laser and the target is optimum at an angle of $\sim 30^\circ$. The lack of return current in targets of dielectric materials leads to filamentation in the electron flow through the target, affecting the quality of the ion beam. Therefore, metallic foils are usually preferred as target.

6.3.1 Contrast

Unlike electron acceleration, the pulse contrast is a major problem in experiments with solid targets. Usually, the high-power pulse is superimposed on top of a low-power nanosecond pedestal, due to the very large gain (mainly in the regenerative amplifier), which creates amplified spontaneous emission (ASE). An additional picosecond pedestal is also present, due the fact that part of the stretched pulse cannot be properly compressed. Any energy prior to the main laser pulse may pre-ionise the target. For the thin foils used in these experiments, shock waves quickly reaches the rear surface and expands in vacuum. The solid-vacuum interface is no longer sharp, which reduces the accelerating electric field and the maximum proton energy. In our laser system, the contrast is improved by pre-amplifying the laser pulse in a multi-pass amplifier. This allowed the gain in the regenerative amplifier to be reduced and therefore also the amount of ASE, as shown in Fig. 6.3. A contrast of $\sim 10^9$ was achieved and was used for the experiment reported in Paper VII. Even with this very good contrast, the intensity before the main pulse is too high for the very thin foils, as illustrated by the experimental data in Fig. 6.4. By moving the target along the optical axis z , it was found that for thick targets the highest proton energies are achieved close to the laser focus, i.e. the most intense point. For thinner foils, the

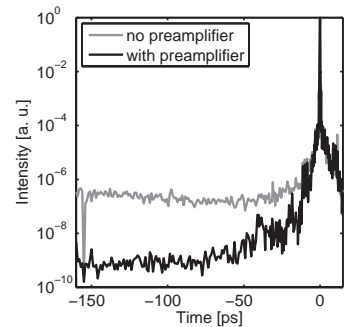


Figure 6.3. Contrast measured with a third-order autocorrelator. The effect of the use of the preamplifier on the contrast is clear, as it decreases from 2×10^7 to 10^9 .

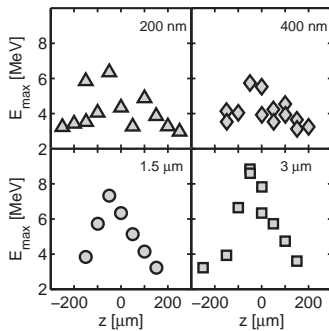


Figure 6.4. Maximum proton energy as a function of the target distance from the laser focus z for different target thicknesses. For the thinnest foils, the intensity before the main pulse deteriorates the acceleration process because the pre-plasma has time to expand on the rear side of the foil.

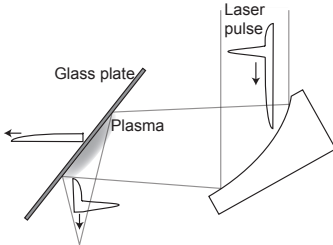


Figure 6.5. Schematic view of the principle of the plasma mirror. Any energy before the main laser pulse is transmitted through the glass. The mirror starts to reflect light only when the density of the plasma formed on the glass plate reaches n_c .

acceleration process is reduced at the most intense point because the energy before the main pulse affects the target. The ASE can also launch shock waves into the foil that deform the back of it [148, 149].

For the ultra-thin foils in Fig. 6.4, the contrast achieved with only the pre-amplifier is not sufficient. One way to achieve better contrast is to use a plasma mirror [155]. A flat piece of glass is placed in the focusing beam at an angle close to the Brewster angle in the case of p-polarised light. Any energy before the main pulse is then simply transmitted through the piece of glass. When the leading edge of the main laser pulse arrives on the glass, the medium starts to become ionised at around 10^{14} W/cm^2 forming a plasma [156]. When the density of this plasma reaches the critical density, the laser pulse is reflected, as illustrated in Fig. 6.5. Thus, the energy prior to the main part of the pulse does not reach the target. As this process takes place on a short time scale, instabilities do not have time to develop, and the surface quality of the mirror remains good [157]. By moving the piece of glass relative to the focus of the laser, the timing of the switch can be tuned and the contrast optimised, which is usually done by finding the best conditions for proton acceleration. This leads to a gain of approximately two orders of magnitude in contrast. Note that the better the contrast before the glass plate, the better the final contrast. Improving the intrinsic contrast of the laser should therefore not be neglected. The main drawbacks of this method are that the reflectivity of the plasma mirror is low ($\sim 50\%$) and that the piece of glass has to be moved after each shot to always expose a flat surface, adding complexity to the experiment. This method was used for the experiment discussed in Paper VIII, as the microspheres used as targets had a wall thickness of less than $1 \mu\text{m}$.

6.3.2 Detection

The protons accelerated by TNSA in the experiments described in this thesis were in the range 1–10 MeV, and are not easy to detect. Due to their high sensitivity, CR-39 plastic nuclear track detectors are commonly used in laser-driven ion acceleration experiments. When a proton or a heavy ion travels through this kind of detector, it breaks bonds along its path. When the material is submerged in a warm aqueous solution of NaOH for about 30 min, the broken bonds are etched away and a visible track appears for each proton or ion. This method is very sensitive to protons and ions and has the advantage of being completely insensitive to electrons and x-rays. However, each CR-39 detector can only be used once, and the delay between conducting the experiment and obtaining the results makes their use less attractive. The analysis of the data is also tedious because the pits have to be digitalised first. Other

detectors, such as radiochromic films or microchannel plates, are also available, but were not used in the experiments described in this thesis.

As part of this thesis, a new detection scheme was developed using a scintillator and an electron-multiplying CCD camera (EM-CCD). When a particle hits the scintillator, some of its energy is converted into photons that are detected by the camera. Compared to the CR-39 detector, a scintillator has the advantage of giving immediate results. Its efficiency is, however, rather low and an EMCCD is used to amplify the signal. The main challenge in using this detector is discriminating between different types of particles. In contrast to CR-39 detectors, electrons and x-rays are detected, as they also induce scintillation. In order to reduce the contribution from electrons, small permanent magnets were placed before the scintillator to deflect low-energy electrons, while the proton beam remained essentially unaffected by this weak magnetic field. The scintillator was also wrapped in metallic foil to protect it from the laser light, to block part of the x-rays and to stop heavy ions.

Paper [VII](#) describes how a BC-400 scintillating screen from Saint-Gobain was successfully used. The wavelength of its maximal emission is 423 nm and it has a decay time of 2.4 ns. Figure [6.6](#) shows a proton profile recorded with this scintillator. Subtraction of the background, consisting of the x-rays produced in the interaction, was necessary to obtain a useful image. The lower part of the image shows the proton beam recorded by a CR-39 detector. It can be seen that the overlap is good. However, because the yield of x-rays varies, it is difficult to perform background subtraction accurately, and the CR-39 remains a more reliable detector for recording proton beam profiles. On the other hand, the scintillating screen is the perfect tool to record spectra using a magnetic spectrometer, as only positively charged particles are deflected towards the detector. Examples of spectra recorded using this instrument are given in Paper [VII](#). The use of the scintillator allowed for more systematic studies such as the one presented in Paper [VII](#), as the number of shots was not limited by the detection system.

6.4 Use of a prepulse

As discussed previously, if energy is present before the main pulse (for example in the case of poor contrast), the expansion of the plasma starts before the arrival of the most intense part of the laser pulse and the acceleration is reduced. In most cases, the best possible contrast is desirable in order to obtain the most efficient acceleration. The energy present before the main pulse increases the length of the gradient in the pre-plasma, thus decreasing the

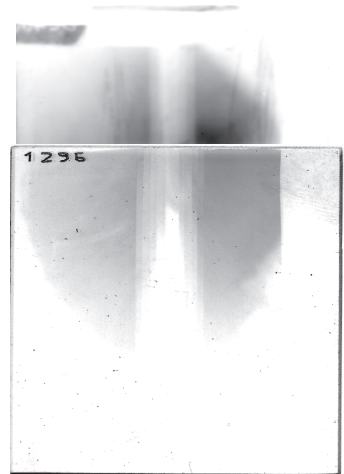


Figure 6.6. Comparaison between a profile acquired with the scintillator and a CR-39 detector. The shadow of metallic filters with different thicknesses are visible, providing a rough energy measurement.

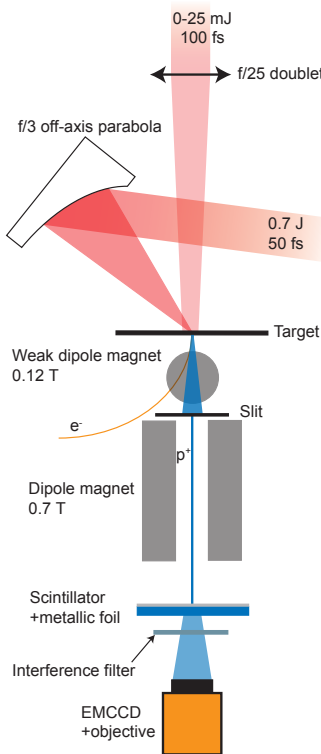


Figure 6.7. Experimental set-up used for the experiment reported in Paper VII. One particular feature is that protons were detected by a plastic scintillator and an EMCCD.

maximum proton energy. However, in some cases, a prepulse may be beneficial for the acceleration process. It has been found that a soft prepulse could enhance the heating of the plasma and thus improve the acceleration [131, 158–162].

In the experiment discussed in Paper VII, the use of a prepulse was explored for a set of parameters (delay and intensity) that had not been investigated previously. A femtosecond prepulse was used, while longer pulses or a limited number of parameters have been used in other similar studies.

The experimental set-up is illustrated in Fig. 6.7. The main feature of this set-up is the scintillator described in Section 6.3.2 to detect the protons, instead of the CR-39 detectors used in earlier experiments. The laser pulse was focused onto a $3\ \mu\text{m}$ thick aluminium foil. Another pulse, in a separate beam, focused by an f/25 doublet lens, was used as a prepulse. As the prepulse focal spot ($28\ \mu\text{m}$ FWHM) was much larger than the main beam focal spot ($5\ \mu\text{m}$), pointing fluctuations were not a problem. The delay between the two pulses could be adjusted by a translation stage, between 0 and 1.5 ns, and the intensity of the prepulse could be varied in the range $0\text{--}2.5 \times 10^{16}\ \text{W}/\text{cm}^2$. Finally, a magnetic spectrometer was placed along the target normal and the protons detected by the scintillator and the EMCCD camera.

6.4.1 Results and discussion

While for most prepulse settings, the acceleration efficiency was reduced, it was found that for a particular set of parameters the acceleration process was enhanced. An increase of $\sim 10\%$ in maximum proton energy was attributed to the enhanced electron heating due to the prepulse, as shown in Fig. 6.8, where spectra with and without the prepulse are shown. When the prepulse was too intense, the preplasma was too large and the acceleration was less efficient. The proton energy was only increased with a prepulse intensity below $5 \times 10^{14}\ \text{W}/\text{cm}^2$. If the delay between the two pulses was short, it had little effect on the proton energy, and the proton energy was increased only with delays longer than 50 ps.

In addition to the increase in maximum proton energy, the shape of the proton spectrum was altered by the presence of a prepulse. This is also shown in Fig. 6.8, where a clear redistribution of some of the low-energy protons towards higher energies can be seen. This effect was always present when the proton energy was enhanced, but was more or less prominent depending on the prepulse parameters.

The fact that an effect is observed only for long delays suggests that effects on both the front and back of the target are responsible for the increase in proton energy. The shock induced by the prepulse breaks out through the foil after a few hundreds of ps. On the front, the prepulse initiates expansion of the plasma

which, under the right conditions, increases the efficiency for resonant absorption, described in Section 6.2.1[160]. The prepulse also triggers an expansion of the plasma on the back. The target thickness therefore effectively increases and competes with the positive effects due to enhanced absorption. The interplay between the expanding plasma and the main laser pulse is complex, and many other effects may play a role, such as self-focusing, refraction, or instabilities in the underdense plasma, relativistic transparency or hole boring [131]. The effects on the front of the target are not likely to produce the spectral redistribution, i.e. a reduction of the population of the low-energy protons, observed in Fig. 6.8. This may arise from the breaking of the ion wave on the back of the target, which can temporarily increase the ion population at high energies and affect the interaction [158, 161].

Finally, the effect on the electron spectrum could be due to a spatial redistribution of the protons [148]. As the spectrometer axis is along the target normal, any energy-dependent variation of the divergence of the proton beam will modify the shape of the spectrum along the line of view of the spectrometer.

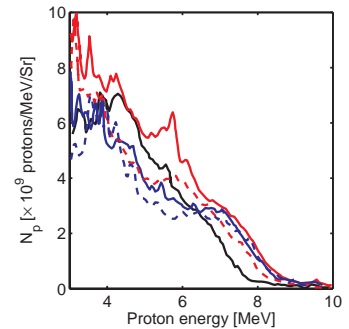


Figure 6.8. Typical proton spectra for different prepulse parameters: without prepulse (black solid line), with a prepulse with intensities $I = 1 \times 10^{14} \text{ Wcm}^{-2}$ (blue lines) and $I = 5 \times 10^{14} \text{ Wcm}^{-2}$ (red lines). The solid lines represent a delay of 300 ps between the two pulses and the dashed lines a delay of 700 ps.

6.5 Hollow microspheres

Paper **VIII** describes the demonstration of the feasibility of using hollow microspheres for proton acceleration. The idea is illustrated in Fig. 6.9. The laser beam hits the target at the bottom, producing a plasma and pushing electrons through the wall of the sphere (a). The ponderomotive force not only pushes electrons through the sphere wall, but also laterally along the surface of the sphere, as discussed in Section 6.2.3. Protons are accelerated inside the sphere by TNSA, while some electrons travel along the surface of the sphere (b). They will then exit at the top of the sphere, establishing an electric field, which can accelerate the protons further (c). The electrons travel back to the other side of the sphere and oscillate back and forth between the two sides of the sphere several times (d). As the protons are not relativistic, the electrons travel much faster than the protons, and will therefore experience the field established by the electrons several times. The effect will be greatest when the protons are close to the opening. As the spectral distribution of the protons is broad, protons of different energies will travel at different speeds and will experience the field established by the electrons differently.

The laser pulse was focused onto the microsphere at normal incidence. Although the inherent contrast of the Lund multi-TW laser is good ($\sim 10^9$), an even better contrast was necessary for this experiment as the thickness of the sphere is less than $1 \mu\text{m}$. A plasma mirror, described in Section 6.3.1, was therefore included in the set-up allowing a contrast of $\sim 10^{11}$ to be achieved.

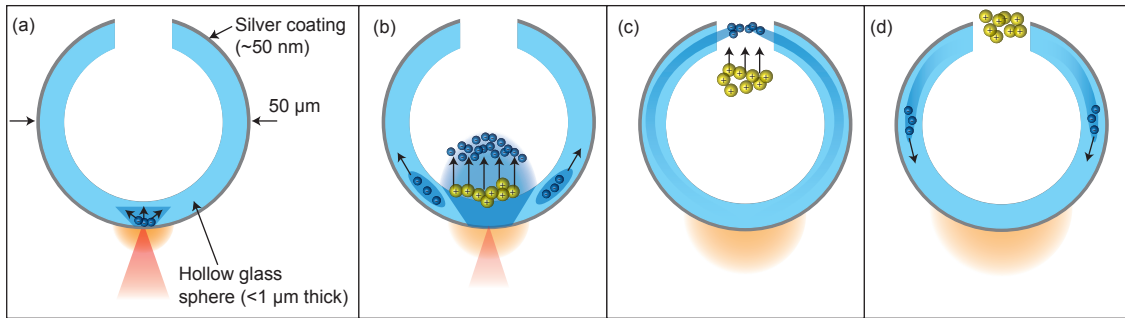


Figure 6.9. Principle of the hollow microsphere targets. In (a), electrons are pushed through the sphere and around its surface by the ponderomotive force of the laser and the thermal expansion of the plasma. TNSA occurs inside the sphere and protons are accelerated (b). The electrons spreading laterally meet again at the opening of the sphere, where they establish a new field that can accelerate the protons again (c). The electrons oscillate back and forth between the top and the bottom of the sphere (d).

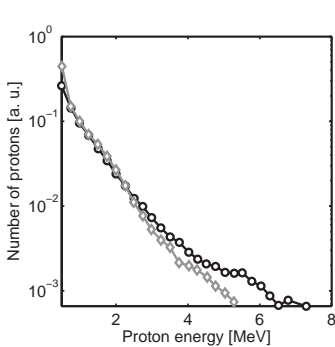


Figure 6.10. Normalised proton spectra from a microsphere target (black) and a Mylar foil (grey).

Protons were detected using CR-39 plates. A CR-39 detector was placed before a magnetic spectrometer, and a small hole in the plate allowed the centre part of the beam to reach the spectrometer and be detected by another CR-39 detector. This set-up allowed spatial and spectral information to be obtained at the same time. The more sensitive CR-39 detectors were used instead of the scintillator described in Paper **VII** because of the low number of protons and the fact that it was a completely new kind of target.

6.5.1 Results and discussion

In order to compare the effects of the electrons establishing a new field at the top of the sphere, the acceleration process was compared with that from a flat Mylar foil with a thickness of $0.9 \mu\text{m}$. Figure 6.10 shows typical experimental spectra from a microsphere and a Mylar foil. Redistribution of the protons to higher energies was observed, which can be attributed to a second stage of acceleration. The particle yield is different for the two targets (~ 30 times more particles with the foil), but the shapes of the spectra could still be compared.

Further development is necessary to fully utilise the potential of this new acceleration scheme. Among the ideas to explore, one of the most promising is to adjust the timing between the protons and the electrons reaching the top of the sphere, such that the protons arrive close to the opening at the same time as one of the passages of the electrons (ideally the first one, because the strength of the field decreases with time). In the experiment reported in Paper **VIII**, the timing was not optimised, and only a small effect on the proton spectra was observed. One way to adjust the timing, is to accelerate the protons to higher ener-

gies. Being non-relativistic, this will modify their speed. Oblate spheroidal targets would lengthen the travelling time of the electrons, but are not easily available. Finally, the electrons could possibly be slowed down by surrounding the sphere with a dielectric material.

SUMMARY AND OUTLOOK

This thesis introduces the concepts of laser-plasma acceleration of electrons and protons, as well as experimental investigations. The papers included in this thesis originate from experiments performed with the multi-TW laser at the Lund Laser Centre. Efforts were concentrated on ways of improving some characteristics of the accelerator without increasing the laser energy. In Papers **II** and **III**, linear plasma waves in dielectric capillary tubes are discussed. The principle demonstrated in these experiments may allow plasma waves to be driven over very long distances at a low electron density in the future. Injected electrons could then be accelerated to GeV energies. For these experiments to be successful, the pointing of the laser system was actively controlled, as reported in Paper **I**. Although the motivation for improving the pointing stability was the feasibility of experiments with dielectric capillary tubes, it will also benefit other experiments, as they proceed towards greater stability and control over the parameters of the laser, as well as of the interaction. Paper **IV** presents a study of electron and x-ray beams at a relatively low laser intensity. This study highlights the fact that even with a relatively low initial intensity, self-injection of electrons is possible due to non-linear pulse evolution in the plasma. The influence of the quality of the focal spot is discussed in Papers **V** and **VI**. The photon energy of the radiation produced in a plasma wiggler could be increased by using asymmetric focal spots, without increasing the laser energy, as reported in Paper **V**. At constant laser energy, it was shown in Paper **VI** that it is crucial not only to have a symmetric focal spot, but also to have as much energy as possible in the central part of the focal spot, since only this part will be used to drive the plasma wave. Finally, in two proton acceleration experiments, means of increasing the maximum energy of the proton and their spectral distribution were explored. For this purpose, a prepulse was used (Paper **VII**) and novel targets, namely hollow

microspheres (Paper [VIII](#)).

At the moment, laser-driven accelerators cannot compete with conventional accelerators in terms of repetition rate, stability and reliability of the beams. In the short term, one focus should, therefore, be to improve the stability and reliability of plasma accelerators. New injection schemes, such as colliding pulses or gradient injection, have been shown to produce more stable electron beams and should be studied further. Control over the laser parameters is also very important, as they are the main components of the experiment. In Lund, the experiments and the laser are mainly operated by the same people, allowing experimentalists (including PhD students and post-docs) to have full control over the laser parameters, favouring synergies between experimental investigations and laser development. A good example of this is Paper [I](#), where the requirement of the experiment using dielectric capillaries led to a major improvement in the pointing of the laser system. In the same spirit, the experiments reported in Papers [V](#) and [VI](#) were also performed in connection with the laser operation as the wavefront was shaped in a controlled way allowing parameters of the experiment to be improved. Work has also been done to achieve a laser contrast sufficient for proton acceleration experiments (Papers [VII](#) and [VIII](#)).

At the same time, the potential of these accelerators can already be demonstrated by performing proof-of-principle applications. So far, electron beams have been used in other laboratories, for example, for high-resolution gamma-ray radiography [[163](#), [164](#)] and radiobiological research [[165](#)]. Compared to other electron accelerators, the main features of laser-driven accelerators are, beside their small size, their short bunch duration and low emittance. In addition, the perfect synchronisation between laser pulses and particles or x-ray pulses, could greatly simplify experiments, in which different beams are used together. The source can be used for time-resolved experiments, taking advantage of its short pulse duration. Similarly, the high peak brightness and short pulse duration of the plasma wiggler source could be used to perform experiments that can only be carried out in a few places in the world at present. Their low emittance also makes them good candidates as injectors for large conventional accelerators. For the same reason, laser-driven electron beams are good candidates to be sent into undulators and may even allow compact x-ray free-electron lasers to be constructed [[166](#)]. Radiation from undulators has already been produced as a proof of principle [[167](#), [168](#)]. Concerning laser-driven proton acceleration, proton therapy is at the top of the list of foreseen applications [[132](#), [133](#)]. In the long term, future generations of high-energy accelerators might include laser wakefield acceleration.

ROLE OF THE AUTHOR

All experiments described in the papers were performed using the Lund multi-TW laser. In particular, I was responsible for its operation and the operation of the experimental area in the experiments described in Papers **I** to **VI**.

I Active control of the pointing of a multi-terawatt laser

An active pointing stabilisation system was developed and implemented on the multi-TW laser. I was responsible for the design and implementation of the system, including writing the code used for the feedback control. I recorded the experimental data, analysed them and wrote the manuscript.

II Laser-driven plasma waves in capillary tubes

This paper reports on the generation and characterisation of linear plasma waves in dielectric capillary tubes. I made a major contribution to the experimental work. In the preparation phase, I improved the pointing of the laser in order to make the experiment successful. I contributed to the data analysis and gave feedback on the manuscript.

III Analysis of laser wakefield dynamics in capillary tubes

This paper gives the theoretical background behind the characterisation of linear plasma waves in dielectric capillary tubes. Agreement with the experimental data reported in Paper **II** and additional data is discussed. I contributed primarily to the experimental part of the work.

IV Laser-plasma electron acceleration in dielectric capillary tubes

Electrons and x-ray beams produced in dielectric capillary tubes were studied. This particular target extended the length of the gas medium compared with gas jets. Multi-mode propagation in the tube was possible due to large tube diameters, producing interesting relations between the electron acceleration and x-ray production and the capillary parameters and electron density. I played a major part in the experimental work, did most of the analysis and wrote the manuscript.

V Controlling the spectrum of x-rays generated in a laser-plasma accelerator by tailoring the laser wavefront

Asymmetric focal spots were produced by introducing coma aberration into the wavefront, and it was found that off-axis injection of electrons was promoted. This led to harder x-rays because of the greater transverse amplitude of the electron motion. I was involved in all parts of the experiment. I participated in the analysis and contributed to the manuscript by giving feedback.

VI Experimental study of the wavebreaking threshold in a laser wakefield accelerator

The wavebreaking threshold was studied by varying the quality of the focal spot, the energy in the pulse and the pulse duration. A simple model predicting if, and when, the wave would break was developed, showing good agreement with the experimental data. I played a major role in the experimental work, I participated in the analysis and gave feedback on the manuscript.

VII Evolution of energy spectrum from laser-accelerated protons with a 100 fs intense prepulse

A prepulse was used to enhance the laser absorption on the front of the target foil used for proton acceleration in order to enhance the TNSA process. An increase in proton energy was obtained for a particular set of parameters. I played a major role in the experimental work and wrote part of the manuscript.

VIII Hollow microspheres as targets for staged laser-driven proton acceleration

This paper reports on the use of hollow microspheres as targets for laser-driven proton acceleration. It uses the particular geometry of the target to enhance the acceleration process. I participated in the experimental work and contributed to the manuscript by giving feedback.

ACKNOWLEDGMENTS

People from outside the academic world often asked me: “When are you going to finish studying?” I would answer that I am not really studying, being a PhD student is more like being a researcher. I realise now that I have never been more of a student than during my PhD studies, because I have learned so much every day; not only from the courses I took or the books I read, but from other people, like my supervisor, my fellow PhD students and collaborators. I would like therefore to thank all of them as they have taught me so much during these past four and a half years.

Although being very busy as Head of Division, my supervisor Claes-Göran Wahlström has always had time to discuss and share his knowledge with me. If something did not work as expected in the lab, we would often find a solution by discussing it together. And, if we realised we had made a mistake, and I became discouraged, he would always see the positive side of it by saying: “at least we learned something”. I would also like to thank my co-supervisor Mikael Eriksson for his insight into accelerator physics.

I am grateful to the whole ultra-high-intensity laser physics group, present and past members: Yannick Glinec, with whom I did my first experiment, and who gave me the best start I could imagine for my PhD; Frank Wojda, for sharing his passion for capillaries; Kristoffer Svensson and Christos Kamperidis, for sharing an office with me; Olle Lundh, for always being so enthusiastic about working in the lab, and for correcting my thesis; Anders Persson, who always managed to fix the laser even in the most desperate situations, and who taught me many tricks in optics; as well as Matthias Burza, Filip Lindau, Colin Wood, Lovisa Senje and Martin Hansson.

I would also like to thank Anne L’Huillier, who invited me to Lund in the first place for my Masters dissertation. This has influenced my life in many ways. I would also like to thank her for giving me the opportunity to teach on her courses, which was a very rewarding experience. I am also grateful to the people who made everything run smoothly at the Division: Sune Svanberg, former head; Minna Ramkull, Camilla Nilsson, Henrik Steen, Har-

riett Lindahl and Bertil Hermansson, for all their administrative and technical help.

I had the opportunity to work with many international collaborators. I would like to thank the team from LPGP in France, in particular Brigitte Cros and Kevin Cassou, for all the fun we had with the capillaries. Thanks to their visit in Lund, I could also keep my French alive, which I had a tendency to forget while living abroad and not speaking it every day. I would also like to thank the British team from Imperial College: Stuart Mangles, Michael Bloom, Nick Dover and Stefan Kneip. Not did only our long nights in the lab not seem so long, I also learned many things as diverse as the rules of cricket and how to make a proper cup of tea.

Thanks to the MAXLAS project, I had the chance to get to know other PhD students from different backgrounds and from different fields of physics. I would like to thank Marko Swoboda, Jörg Schwenke, Nino Čutić , Ralf Nüske and Jens Uhlig for the many good times we had talking about physics and many other topics. As I spent many hours every day at work, I appreciated meeting people outside of the group who made me look forward to coming to work. I would therefore like to thank Kathrin Klünder, Miguel Miranda, Marcus Dahlström, Thomas Fordell, Thomas Remetter and Thierry Ruchon for sharing coffee and lunch breaks and many other things, and most of all for being great friends.

Enfin, je tiens à remercier mes amis et ma famille pour leur soutien, bien que j'ai vécu depuis plusieurs années de l'autre côté de l'Europe. Je suis très reconnaissant envers mes parents qui m'ont donné tout ce dont j'avais besoin pour poursuivre mes (longues) études. Je remercie aussi Noa et Satu pour leurs encouragements durant la rédaction de ma thèse: merci Noa pour m'avoir remonté le moral à ta façon après mes longues journées de travail. Merci Satu pour m'avoir motivé durant ces derniers mois et pour toujours s'être intéressée à ce que je fais.

REFERENCES

1. D. Strickland and G. Mourou. *Compression of amplified chirped optical pulses.* Opt. Commun. **56**, 219 (1985).
2. Robert F. Service. *Battle to Become the Next-Generation X-ray Source.* Science **298**, 1356 (2002).
3. H. N. Chapman *et al.* *Femtosecond X-ray protein nanocrystallography.* Nature **470**, 73 (2011).
4. M. M. Seibert *et al.* *Single mimivirus particles intercepted and imaged with an X-ray laser.* Nature **470**, 78 (2011).
5. A. I. Akhiezer and R. V. Polovin. *Theory of Wave Motion of An Electron Plasma.* J. Exp. Theor. Phys. **3**, 696 (1956).
6. T. Tajima and J. M. Dawson. *Laser Electron Accelerator.* Phys. Rev. Lett. **43**, 267 (1979).
7. A. Modena *et al.* *Electron acceleration from the breaking of relativistic plasma waves.* Nature **377**, 606 (1995).
8. V. Malka *et al.* *Electron Acceleration by a Wake Field Forced by an Intense Ultrashort Laser Pulse.* Science **298**, 1596 (2002).
9. C. G. R. Geddes *et al.* *High-quality electron beams from a laser wakefield accelerator using plasma-channel guiding.* Nature **431**, 538 (2004).
10. J. Faure *et al.* *A laser-plasma accelerator producing monoenergetic electron beams.* Nature **431**, 541 (2004).
11. S. P. D. Mangles *et al.* *Monoenergetic beams of relativistic electrons from intense laser-plasma interactions.* Nature **431**, 535 (2004).
12. W. P. Leemans *et al.* *GeV electron beams from a centimetre-scale accelerator.* Nature Phys. **2**, 696 (2006).

13. J. Faure *et al.* *Controlled injection and acceleration of electrons in plasma wakefields by colliding laser pulses*. Nature **444**, 737 (2006).
14. O. Lundh *et al.* *Few femtosecond, few kiloampere electron bunch produced by a laser-plasma accelerator*. Nature Phys. **7**, 219 (2011).
15. A. Buck *et al.* *Real-time observation of laser-driven electron acceleration*. Nature Phys. **7**, 543 (2011).
16. C. M. S. Sears *et al.* *Emittance and divergence of laser wake-field accelerated electrons*. Phys. Rev. ST Accel. Beams **13**, 092803 (2010).
17. E. Brunetti *et al.* *Low Emittance, High Brilliance Relativistic Electron Beams from a Laser-Plasma Accelerator*. Phys. Rev. Lett. **105**, 215007 (2010).
18. I. Blumenfeld *et al.* *Energy doubling of 42 GeV electrons in a metre-scale plasma wakefield accelerator*. Nature **445**, 741 (2007).
19. A. Caldwell *et al.* *Proton-driven plasma-wakefield acceleration*. Nature Phys. **5**, 363 (2009).
20. E. Esarey, C. B. Schroeder, and W. P. Leemans. *Physics of laser-driven plasma-based electron accelerators*. Rev. Mod. Phys. **81**, 1229 (2009).
21. P. Gibbon. *Short Pulse Laser Interactions with Matter*. Imperial College Press (2005).
22. W. L. Kruer. *The physics of laser plasma interactions*. Addison-Wesley, New-York (1988).
23. E. A. Startsev and C. J. McKinstry. *Multiple scale derivation of the relativistic ponderomotive force*. Phys. Rev. E **55**, 7527 (1997).
24. B. Quesnel and P. Mora. *Theory and simulation of the interaction of ultraintense laser pulses with electrons in vacuum*. Phys. Rev. E **58**, 3719 (1998).
25. L. M. Gorbunov and V. I. Kirsanov. *Excitation of Plasma-waves By Short Electromagnetic-wave Packets*. J. Exp. Theor. Phys. **93**, 509 (1987).
26. C. E. Clayton *et al.* *Ultrahigh-gradient acceleration of injected electrons by laser-excited relativistic electron plasma waves*. Phys. Rev. Lett. **70**, 37 (1993).

27. F. Amiranoff *et al.* *Electron Acceleration in Nd-Laser Plasma Beat-Wave Experiments*. Phys. Rev. Lett. **74**, 5220 (1995).
28. K. Nakajima *et al.* *Observation of Ultrahigh Gradient Electron Acceleration by a Self-Modulated Intense Short Laser Pulse*. Phys. Rev. Lett. **74**, 4428 (1995).
29. F. Amiranoff *et al.* *Observation of Laser Wakefield Acceleration of Electrons*. Phys. Rev. Lett. **81**, 995 (1998).
30. P. Sprangle, E. Esarey, and A. Ting. *Nonlinear theory of intense laser-plasma interactions*. Phys. Rev. Lett. **64**, 2011 (1990).
31. E. Esarey and M. Pilhoff. *Trapping and acceleration in nonlinear plasma waves*. Phys. Plasmas **2**, 1432 (1995).
32. C. B. Schroeder *et al.* *Trapping, dark current, and wave breaking in nonlinear plasma waves*. Phys. Plasmas **13**, 033103 (2006).
33. T. Katsouleas and W. B. Mori. *Wave-Breaking Amplitude of Relativistic Oscillations in a Thermal Plasma*. Phys. Rev. Lett. **61**, 90 (1988).
34. J. B. Rosenzweig. *Trapping, thermal effects, and wave breaking in the nonlinear plasma wake-field accelerator*. Phys. Rev. A **38**, 3634 (1988).
35. A. Pukhov and J. Meyer-ter Vehn. *Laser wake field acceleration: the highly non-linear broken-wave regime*. Appl. Phys. B **74**, 355 (2002).
36. W. Lu *et al.* *Nonlinear Theory for Relativistic Plasma Wakefields in the Blowout Regime*. Phys. Rev. Lett. **96**, 165002 (2006).
37. W. Lu *et al.* *A nonlinear theory for multidimensional relativistic plasma wave wakefields*. Phys. Plasmas **13**, 056709 (2006).
38. S. P. D. Mangles *et al.* *Laser-wakefield acceleration of monoenergetic electron beams in the first plasma-wave period*. Phys. Rev. Lett. **96**, 215001 (2006).
39. W. Lu *et al.* *Generating multi-GeV electron bunches using single stage laser wakefield acceleration in a 3D nonlinear regime*. Phys. Rev. ST Accel. Beams **10**, 061301 (2007).
40. C. Rechatin *et al.* *Observation of Beam Loading in a Laser-Plasma Accelerator*. Phys. Rev. Lett. **103**, 194804 (2009).

41. T. Katsouleas *et al.* *Beam loading in plasma accelerators*. Part. Accel. **22**, 81 (1987).
42. M. Tzoufras *et al.* *Beam Loading in the Nonlinear Regime of Plasma-Based Acceleration*. Phys. Rev. Lett. **101**, 145002 (2008).
43. C. Rechatin *et al.* *Controlling the Phase-Space Volume of Injected Electrons in a Laser-Plasma Accelerator*. Phys. Rev. Lett. **102**, 164801 (2009).
44. X. Davoine *et al.* *Cold Optical Injection Producing Monoenergetic, Multi-GeV Electron Bunches*. Phys. Rev. Lett. **102**, 065001 (2009).
45. K. Schmid *et al.* *Density-transition based electron injector for laser driven wakefield accelerators*. Phys. Rev. ST Accel. Beams **13**, 091301 (2010).
46. J. Faure *et al.* *Injection and acceleration of quasimonoenergetic relativistic electron beams using density gradients at the edges of a plasma channel*. Phys. Plasmas **17**, 083107 (2010).
47. C. G. R. Geddes *et al.* *Plasma-Density-Gradient Injection of Low Absolute-Momentum-Spread Electron Bunches*. Phys. Rev. Lett. **100**, 215004 (2008).
48. A. Pak *et al.* *Injection and Trapping of Tunnel-Ionized Electrons into Laser-Produced Wakes*. Phys. Rev. Lett. **104**, 025003 (2010).
49. C. McGuffey *et al.* *Ionization Induced Trapping in a Laser Wakefield Accelerator*. Phys. Rev. Lett. **104**, 025004 (2010).
50. C. E. Clayton *et al.* *Self-Guided Laser Wakefield Acceleration beyond 1 GeV Using Ionization-Induced Injection*. Phys. Rev. Lett. **105**, 105003 (2010).
51. A. G. Khachatrian *et al.* *Conceptual design of a laser wakefield acceleration experiment with external bunch injection*. Nucl. Instr. Meth. Phys. Res. **566**, 244 (2006).
52. J. S. Liu *et al.* *All-Optical Cascaded Laser Wakefield Accelerator Using Ionization-Induced Injection*. Phys. Rev. Lett. **107**, 035001 (2011).
53. B. B. Pollock *et al.* *Demonstration of a Narrow Energy Spread, ~ 0.5 GeV Electron Beam from a Two-Stage Laser Wakefield Accelerator*. Phys. Rev. Lett. **107**, 045001 (2011).

54. W. B. Mori. *The physics of the nonlinear optics of plasmas at relativistic intensities for short-pulse lasers.* IEEE J. Quant. Elec. **33**, 1942 (1997).
55. R. Fonseca *et al.* *OSIRIS: A Three-Dimensional, Fully Relativistic Particle in Cell Code for Modeling Plasma Based Accelerators.* Lect. Notes Comput. Sci. **2331**, 342 (2002).
56. P. Sprangle, C.-M. Tang, and E. Esarey. *Relativistic Self-Focusing of Short-Pulse Radiation Beams in Plasmas.* IEEE Trans. Plasma Sci. **15**, 145 (1987).
57. G. Z. Sun *et al.* *Self-focusing of short intense pulses in plasmas.* Phys. Fluids **30**, 526 (1987).
58. E. Esarey *et al.* *Self-focusing and guiding of short laser pulses in ionizing gases and plasmas.* IEEE J. Quant. Elec. **33**, 1879 (1997).
59. J. E. Ralph *et al.* *Self-Guiding of Ultrashort, Relativistically Intense Laser Pulses through Underdense Plasmas in the Blowout Regime.* Phys. Rev. Lett. **102**, 175003 (2009).
60. J. Faure *et al.* *Effects of pulse duration on self-focusing of ultra-short lasers in underdense plasmas.* Phys. Plasmas **9**, 756 (2002).
61. C. Delfin *et al.* *Influence of laser pulse duration on relativistic channels.* Phys. Plasmas **9**, 937 (2002).
62. J. Faure *et al.* *Observation of Laser-Pulse Shortening in Nonlinear Plasma Waves.* Phys. Rev. Lett. **95**, 205003 (2005).
63. J. Schreiber *et al.* *Complete Temporal Characterization of Asymmetric Pulse Compression in a Laser Wakefield.* Phys. Rev. Lett. **105**, 235003 (2010).
64. C. D. Decker *et al.* *The evolution of ultra-intense, short-pulse lasers in underdense plasmas.* Phys. Plasmas **3**, 2047 (1996).
65. A. Butler, D. J. Spence, and S. M. Hooker. *Guiding of High-Intensity Laser Pulses with a Hydrogen-Filled Capillary Discharge Waveguide.* Phys. Rev. Lett. **89**, 185003 (2002).
66. E. Esarey *et al.* *Synchrotron radiation from electron beams in plasma-focusing channels.* Phys. Rev. E **65**, 056505 (2002).
67. S. Wang *et al.* *X-Ray Emission from Betatron Motion in a Plasma Wiggler.* Phys. Rev. Lett. **88**, 135004 (2002).

68. S. Kiselev, A. Pukhov, and I. Kostyukov. *X-ray Generation in Strongly Nonlinear Plasma Waves*. Phys. Rev. Lett. **93**, 135004 (2004).
69. A. Rousse *et al.* *Production of a keV X-Ray Beam from Synchrotron Radiation in Relativistic Laser-Plasma Interaction*. Phys. Rev. Lett. **93**, 135005 (2004).
70. R. C. Shah *et al.* *Coherence-based transverse measurement of synchrotron x-ray radiation from relativistic laser-plasma interaction and laser-accelerated electrons*. Phys. Rev. E **74**, 045401 (2006).
71. K. Ta Phuoc *et al.* *Demonstration of the ultrafast nature of laser produced betatron radiation*. Phys. Plasmas **14**, 080701 (2007).
72. F. Albert *et al.* *Full characterization of a laser-produced keV x-ray betatron source*. Plasma Phys. Control. Fusion **50**, 124008 (2008).
73. F. Albert *et al.* *Betatron oscillations of electrons accelerated in laser wakefields characterized by spectral x-ray analysis*. Phys. Rev. E **77**, 056402 (2008).
74. S. Kneip *et al.* *Observation of Synchrotron Radiation from Electrons Accelerated in a Petawatt-Laser-Generated Plasma Cavity*. Phys. Rev. Lett. **100**, 105006 (2008).
75. S. Kneip *et al.* *Bright spatially coherent synchrotron X-rays from a table-top source*. Nature Phys. **6**, 980 (2010).
76. K. Ta Phuoc *et al.* *Imaging Electron Trajectories in a Laser-Wakefield Cavity Using Betatron X-Ray Radiation*. Phys. Rev. Lett. **97**, 225002 (2006).
77. J. Larmor. *A Dynamical Theory of the Electric and Luminiferous Medium. Part III. Relations with Material Media*. Phil. Trans. R. Soc. Lond. A **190**, 205 (1897).
78. J. D. Jackson. *Classical Electrodynamics* chapter 14. John Wiley & sons, New York third edition (1975).
79. K. Ta Phuoc *et al.* *Analysis of wakefield electron orbits in plasma wiggler*. Phys. Plasmas **15**, 073106 (2008).
80. S. Fourmaux *et al.* *Demonstration of the synchrotron-type spectrum of laser-produced Betatron radiation*. New J. Phys. **13**, 033017 (2011).
81. D. H. Whittum, A. M. Sessler, and J. M. Dawson. *Ion-channel laser*. Phys. Rev. Lett. **64**, 2511 (1990).

82. A. G. Khachatryan, F. A. van Goor, and K.-J. Boller. *Coherent and incoherent radiation from a channel-guided laser wakefield accelerator.* New J. Phys. **10**, 083043 (2008).
83. A. G. R. Thomas. *Scalings for radiation from plasma bubbles.* Phys. Plasmas **17**, 056708 (2010).
84. S. Backus *et al.* *High power ultrafast lasers.* Rev. Sci. Instrum. **69**, 1207 (1998).
85. D. E. Spence *et al.* *Regeneratively initiated self-mode-locked Ti:sapphire laser.* Opt. Lett. **16**, 1762 (1991).
86. E. Gerstner. *Laser physics: Extreme light.* Nature **446**, 16 (2007).
87. K. J. Åström and R. M. Murray. *Feedback Systems: An Introduction for Scientists and Engineers.* Princeton University Press (2008).
88. K. J. Åström and T. Hägglund. *PID Controllers: Theory, Design, and Tuning.* International Society for Measurement and Control second edition (1995).
89. S.K. Mitra and J. Kaiser. *Handbook for Digital Signal Processing.* John Wiley and Sons, Inc (1993).
90. J. Primot and L. Sogno. *Achromatic three-wave (or more) lateral shearing interferometer.* J. Opt. Soc. Am. A **12**, 2679 (1995).
91. S. Karsch *et al.* *GeV-scale electron acceleration in a gas-filled capillary discharge waveguide.* New J. Phys. **9**, 415 (2007).
92. T. P. Rowlands-Rees *et al.* *Laser-Driven Acceleration of Electrons in a Partially Ionized Plasma Channel.* Phys. Rev. Lett. **100**, 105005 (2008).
93. B. Cros *et al.* *Eigenmodes for capillary tubes with dielectric walls and ultraintense laser pulse guiding.* Phys. Rev. E **65**, 026405 (2002).
94. M. Veysman *et al.* *Theoretical and experimental study of laser beam propagation in capillary tubes for non-symmetrical coupling conditions.* J. Opt. Soc. Am. B **27**, 1400 (2010).
95. Y. Glinec *et al.* *Absolute calibration for a broad range single shot electron spectrometer.* Rev. Sci. Instrum. **77**, 103301 (2006).

96. R. Nowotny and A. Taubeck. *A method for the production of composite scintillators for dosimetry in diagnostic radiology*. Phys. Med. Biol. **54**, 1457 (2009).
97. A. Chiron *et al.* *Experimental observations and simulations on relativistic self-guiding of an ultra-intense laser pulse in underdense plasmas*. Phys. Plasmas **3**, 1373 (1996).
98. M. C. Kaluza *et al.* *Observation of a Long-Wavelength Hosing Modulation of a High-Intensity Laser Pulse in Underdense Plasma*. Phys. Rev. Lett. **105**, 095003 (2010).
99. P. Ross. *Minutes of the Oakland Meeting, June 17, 1926*. Phys. Rev. **28**, 425 (1926).
100. P. Kirkpatrick. *On the Theory and Use of Ross Filters*. Rev. Sci. Instrum. **10**, 186–191 (1939).
101. P. Kirkpatrick. *Theory and Use of Ross Filters. II*. Rev. Sci. Instrum. **15**, 223 (1944).
102. B. R. Maddox *et al.* *Calibration and characterization of single photon counting cameras for short-pulse laser experiments*. Rev. Sci. Instrum. **79**, 10E924 (2008).
103. W. Fullagar *et al.* *The use and characterization of a backilluminated charge-coupled device in investigations of pulsed x-ray and radiation sources*. Rev. Sci. Instrum. **79**, 103302 (2008).
104. W. Fullagar *et al.* *A broadband laser plasma x-ray source for application in ultrafast chemical structure dynamics*. Rev. Sci. Instrum. **78**, 115105 (2007).
105. C. Fourment *et al.* *Broadband, high dynamics and high resolution charge coupled device-based spectrometer in dynamic mode for multi-keV repetitive x-ray sources*. Rev. Sci. Instrum. **80**, 083505 (2009).
106. D. B. Thorn *et al.* *Spectroscopy of betatron radiation emitted from laser-produced wakefield accelerated electrons*. Rev. Sci. Instrum. **81**, 10E325 (2010).
107. National Council on Radiation Protection and Measurements. *Radiation protection for particle accelerator facilities* (2003). NCRP Report No. 144.
108. S. Agostinelli *et al.* *G4—a simulation toolkit*. Nucl. Instr. Meth. Phys. Res. **506**, 250 (2003).
109. N. Andreev and M. Chegotov. *Wakefield generation as the mechanism behind spectral shift of a short laser pulse*. J. Exp. Theor. Phys. **101**, 56 (2005).

110. T. P. A. Ibbotson *et al.* *Laser-wakefield acceleration of electron beams in a low density plasma channel.* Phys. Rev. ST Accel. Beams **13**, 031301 (2010).
111. H. E. Ferrari, A. F. Lifschitz, and B. Cros. *Modelling of laser-plasma electron acceleration in capillary tubes.* Plasma Phys. Control. Fusion **53**, 014005 (2010).
112. H. E. Ferrari *et al.* *Electron acceleration by laser wakefield and X-ray emission at moderate intensity and density in long plasmas.* Phys. Plasmas (2011). In Press.
113. S. Corde *et al.* *Mapping X-ray emission in a laser-plasma accelerator.* arXiv:1104.2451v1 (2011).
114. Y. Glinec *et al.* *Direct observation of betatron oscillations in a laser-plasma electron accelerator.* Europhys. Lett. **81**, 64001 (2008).
115. P. Sprangle, J. Krall, and E. Esarey. *Hose-Modulation Instability of Laser Pulses in Plasmas.* Phys. Rev. Lett. **73**, 3544 (1994).
116. B. J. Duda *et al.* *A Long-Wavelength Hosing Instability in Laser-Plasma Interactions.* Phys. Rev. Lett. **83**, 1978 (1999).
117. C. Ren and W. B. Mori. *Physical picture for the laser hosing instability in a plasma.* Phys. Plasmas **8**, 3118 (2001).
118. A. Popp *et al.* *All-Optical Steering of Laser-Wakefield-Accelerated Electron Beams.* Phys. Rev. Lett. **105**, 215001 (2010).
119. P. Cummings and A. G. R. Thomas. *A computational investigation of the impact of aberrated Gaussian laser pulses on electron beam properties in laser-wakefield acceleration experiments.* Phys. Plasmas **18**, 053110 (2011).
120. C. Bellei. *Measurements of Optical Radiation from High-Intensity Laser-Plasma Interactions.* PhD thesis Imperial College, London (2009).
121. T. Auguste *et al.* *Defocusing effects of a picosecond terawatt laser pulse in an underdense plasma.* Opt. Commun. **89**, 145 (1992).
122. P. Monot *et al.* *Focusing limits of a terawatt laser in an underdense plasma.* J. Opt. Soc. Am. B **9**, 1579 (1992).
123. D. H. Froula *et al.* *Measurements of the Critical Power for Self-Injection of Electrons in a Laser Wakefield Accelerator.* Phys. Rev. Lett. **103**, 215006 (2009).

124. P. O'Shea *et al.* *Highly simplified device for ultrashort-pulse measurement.* Opt. Lett. **26**, 932 (2001).
125. W. P. Leemans *et al.* *Electron-Yield Enhancement in a Laser-Wakefield Accelerator Driven by Asymmetric Laser Pulses.* Phys. Rev. Lett. **89**, 174802 (2002).
126. S. Kneip *et al.* *Near-GeV Acceleration of Electrons by a Non-linear Plasma Wave Driven by a Self-Guided Laser Pulse.* Phys. Rev. Lett. **103**, 035002 (2009).
127. K. Schmid *et al.* *Few-Cycle Laser-Driven Electron Acceleration.* Phys. Rev. Lett. **102**, 124801 (2009).
128. R. A. Snavely *et al.* *Intense High-Energy Proton Beams from Petawatt-Laser Irradiation of Solids.* Phys. Rev. Lett. **85**, 2945 (2000).
129. E. L. Clark *et al.* *Measurements of Energetic Proton Transport through Magnetized Plasma from Intense Laser Interactions with Solids.* Phys. Rev. Lett. **84**, 670 (2000).
130. E. L. Clark *et al.* *Energetic Heavy-Ion and Proton Generation from Ultraintense Laser-Plasma Interactions with Solids.* Phys. Rev. Lett. **85**, 1654 (2000).
131. A. Maksimchuk *et al.* *Forward Ion Acceleration in Thin Films Driven by a High-Intensity Laser.* Phys. Rev. Lett. **84**, 4108 (2000).
132. V. Malka *et al.* *Practicability of protontherapy using compact laser systems.* Med. Phys. **31**, 1587 (2004).
133. U. Linz and J. Alonso. *What will it take for laser driven proton accelerators to be applied to tumor therapy?* Phys. Rev. ST Accel. Beams **10**, 094801 (2007).
134. D. Neely *et al.* *Enhanced proton beams from ultrathin targets driven by high contrast laser pulses.* Appl. Phys. Lett. **89**, 021502 (2006).
135. P. Antici *et al.* *Energetic protons generated by ultrahigh contrast laser pulses interacting with ultrathin targets.* Phys. Plasmas **14**, 030701 (2007).
136. T. Ceccotti *et al.* *Proton Acceleration with High-Intensity Ultrahigh-Contrast Laser Pulses.* Phys. Rev. Lett. **99**, 185002 (2007).
137. T. Esirkepov *et al.* *Highly Efficient Relativistic-Ion Generation in the Laser-Piston Regime.* Phys. Rev. Lett. **92**, 175003 (2004).

138. W. Yu *et al.* *Direct acceleration of solid-density plasma bunch by ultraintense laser.* Phys. Rev. E **72**, 046401 (2005).
139. F. Pegoraro and S. V. Bulanov. *Photon Bubbles and Ion Acceleration in a Plasma Dominated by the Radiation Pressure of an Electromagnetic Pulse.* Phys. Rev. Lett. **99**, 065002 (2007).
140. A. P. L. Robinson *et al.* *Radiation pressure acceleration of thin foils with circularly polarized laser pulses.* New J. Phys. **10**, 013021 (2008).
141. O. Klimo *et al.* *Monoenergetic ion beams from ultrathin foils irradiated by ultrahigh-contrast circularly polarized laser pulses.* Phys. Rev. ST Accel. Beams **11**, 031301 (2008).
142. S. C. Wilks *et al.* *Absorption of ultra-intense laser pulses.* Phys. Rev. Lett. **69**, 1383 (1992).
143. S.C. Wilks and W.L. Kruer. *Absorption of ultrashort, ultra-intense laser light by solids and overdense plasmas.* IEEE J. Quant. Elec. **33**, 1954 (1997).
144. M. I. K. Santala *et al.* *Effect of the Plasma Density Scale Length on the Direction of Fast Electrons in Relativistic Laser-Solid Interactions.* Phys. Rev. Lett. **84**, 1459 (2000).
145. F. N. Beg *et al.* *A study of picosecond laser-solid interactions up to $10^{19} \text{ W cm}^{-2}$.* Phys. Plasmas **4**, 447 (1997).
146. F. Brunel. *Not-so-resonant, resonant absorption.* Phys. Rev. Lett. **59**, 52 (1987).
147. A. J. Mackinnon *et al.* *Enhancement of Proton Acceleration by Hot-Electron Recirculation in Thin Foils Irradiated by Ultraintense Laser Pulses.* Phys. Rev. Lett. **88**, 215006 (2002).
148. F. Lindau *et al.* *Laser-Accelerated Protons with Energy-Dependent Beam Direction.* Phys. Rev. Lett. **95**, 175002 (2005).
149. O. Lundh *et al.* *Influence of shock waves on laser-driven proton acceleration.* Phys. Rev. E **76**, 026404 (2007).
150. O. Lundh *et al.* *Active steering of laser-accelerated ion beams.* Appl. Phys. Lett. **92**, 011504 (2008).
151. M. Roth *et al.* *Energetic ions generated by laser pulses: A detailed study on target properties.* Phys. Rev. ST Accel. Beams **5**, 061301 (2002).

152. P. McKenna *et al.* *Lateral Electron Transport in High-Intensity Laser-Irradiated Foils Diagnosed by Ion Emission*. Phys. Rev. Lett. **98**, 145001 (2007).
153. S. Ter-Avetisyan *et al.* *Quasimonoenergetic Deuteron Bursts Produced by Ultraintense Laser Pulses*. Phys. Rev. Lett. **96**, 145006 (2006).
154. S. Buffeouchou *et al.* *Hot Electrons Transverse Refluxing in Ultraintense Laser-Solid Interactions*. Phys. Rev. Lett. **105**, 015005 (2010).
155. B. Dromey *et al.* *The plasma mirror-A subpicosecond optical switch for ultrahigh power lasers*. Rev. Sci. Instrum. **75**, 645 (2004).
156. Ch. Ziener *et al.* *Specular reflectivity of plasma mirrors as a function of intensity, pulse duration, and angle of incidence*. J. Appl. Phys. **93**, 768 (2003).
157. G. Doumy *et al.* *Complete characterization of a plasma mirror for the production of high-contrast ultraintense laser pulses*. Phys. Rev. E **69**, 026402 (2004).
158. J. Fuchs *et al.* *Laser-Foil Acceleration of High-Energy Protons in Small-Scale Plasma Gradients*. Phys. Rev. Lett. **99**, 015002 (2007).
159. A. Yogo *et al.* *Laser prepulse dependency of proton-energy distributions in ultraintense laser-foil interactions with an online time-of-flight technique*. Phys. Plasmas **14**, 043104 (2007).
160. Y. Sentoku *et al.* *High-energy ion generation in interaction of short laser pulse with high-density plasma*. Appl. Phys. B **74**, 207 (2002).
161. T. Grismayer and P. Mora. *Influence of a finite initial ion density gradient on plasma expansion into a vacuum*. Phys. Plasmas **13**, 032103 (2006).
162. F. Dollar *et al.* *Control of Energy Spread and Dark Current in Proton and Ion Beams Generated in High-Contrast Laser Solid Interactions*. Phys. Rev. Lett. **107**, 065003 (2011).
163. Y. Glinec *et al.* *High-Resolution γ -Ray Radiography Produced by a Laser-Plasma Driven Electron Source*. Phys. Rev. Lett. **94**, 025003 (2005).
164. A. Ben-Ismaïl *et al.* *Compact and high-quality gamma-ray source applied to 10 μ m-range resolution radiography*. Appl. Phys. Lett. **98**, 264101 (2011).

-
165. O. Rigaud *et al.* *Exploring ultrashort high-energy electron-induced damage in human carcinoma cells.* Cell Death and Dis. **1**, e73 (2010).
 166. K. Nakajima. *Compact X-ray sources: Towards a table-top free-electron laser.* Nature Phys. **4**, 92 (2008).
 167. H.-P. Schlenvoigt *et al.* *A compact synchrotron radiation source driven by a laser-plasma wakefield accelerator.* Nature Phys. **4**, 130 (2008).
 168. M. Fuchs *et al.* *Laser-driven soft-X-ray undulator source.* Nature Phys. **5**, 826 (2009).



PAPERS

PAPER I

Active control of the pointing of a multi-terawatt laser

G. Genoud, F. Wojda, M. Burza, A. Persson, and C.-G. Wahlström.
Rev. Sci. Instrum. **82**, 033102 (2011).

Active control of the pointing of a multi-terawatt laser

G. Genoud,¹ F. Wojda,^{1,2} M. Burza,¹ A. Persson,¹ and C.-G. Wahlström^{1,a)}

¹Department of Physics, Lund University, P.O. Box 118, S-22100 Lund, Sweden

²Laboratoire Physique Gaz et Plasmas (UMR 8578) – Université Paris-Sud 11, F-91405 Orsay Cedex, France

(Received 30 July 2010; accepted 28 January 2011; published online 7 March 2011;
publisher error corrected 3 August 2011)

The beam pointing of a multi-terawatt laser is stabilized on a millisecond time scale using an active control system. Two piezo mirrors, two position sensing detectors, and a computer based optimization program ensure that both near- and far-field are stable, even during single shot operation. A standard deviation for the distribution of laser shots of $2.6 \mu\text{rad}$ is achieved. © 2011 American Institute of Physics. [doi:[10.1063/1.3556438](https://doi.org/10.1063/1.3556438)]

I. INTRODUCTION

In recent years, high power lasers have made tremendous progress and allowed scientists to access new and exciting fields of research. The advent of the chirped pulse amplification technique¹ allowed relativistic intensities to be reached even with compact laser systems. However, in order to fully utilize the potential of available high-power lasers, some quality issues still need to be addressed. In particular, the stability of laser parameters such as beam pointing, wavefront, and pulse energy are crucial in order for these lasers and their applications to benefit a broader community of scientific users. This paper addresses one of these issues, as the beam pointing of a multi-terawatt (TW) laser is actively stabilized.

The production of laser pulses of multi-TW peak power frequently causes the environment to become very noisy (electronically and mechanically). This makes the project particularly challenging in comparison with similar projects on more conventional lasers. In addition, experiments using multi-TW lasers usually require single-shot operation. Active beam pointing stabilization has been previously addressed for less powerful lasers, with high repetition rate, e.g., a 1 kHz Ti:sapphire femtosecond laser.² The principle used then is similar to ours, but it cannot operate in single-shot and only one piezo mirror was used, whereas in the work presented here single-shot operation is possible and two mirrors are used. More advanced schemes have also been demonstrated,^{3,4} but are not suitable to the present situation. In Ref. 3, the pointing stability is controlled using neural networks and a feedforward algorithm. However, this cannot be used in single-shot operation. On the other hand, the method described in Ref. 4 can be used in a single-shot mode, but since it is based on image rotation and sum-frequency generation it is not suitable for high power lasers.

The driving force for the present work was to improve the feasibility of electron acceleration experiments, with laser driven plasma waves in dielectric capillary tubes.^{5,6} Laser plasma wake fields can accelerate electrons to relativistic energies over a very short distance.⁷ However, in order to increase the energy of the electrons to the GeV range and above, the interaction length must be increased. With the help of

guiding structures, such as dielectric capillaries or plasma discharge channels, diffraction effects can be circumvented and plasma waves can be excited over several centimeters.^{5,8} The requirement of good laser beam pointing is crucial to achieve good guiding in this kind of structure.⁹ Good pointing stability is particularly important when using dielectric capillary tubes with inner diameter similar to the laser spot size to prevent damaging the capillary opening. In addition, the stability of the resulting electron beam depends on the pointing stability of the driving laser, among other parameters. Thus, in order to reach a good electron beam stability, the pointing of the driving laser beam must be controlled.

At the Lund Laser Centre, extensive work has been devoted to improve the pointing of its multi-TW laser. The first step was to improve it passively. The laser beam path was covered as much as possible to avoid air turbulences. Mechanical vibrations were also reduced. However, to further reduce remaining pointing instabilities, active control was necessary. This paper presents the active stabilization system developed at the Lund Laser Centre. The stabilization system was designed for single shot operation. Thus, corrections need to be made for both slow and fast effects that may have happened since the previous shot, which may be seconds, minutes, or even hours ago. The sources of pointing instabilities can be divided into three different types: (1) thermal drifts (on the time scale of minutes, hours), (2) air turbulence and slow mechanical vibrations (on the time scale of seconds, $>10\text{ ms}$), and (3) mechanical vibrations ($>10\text{ Hz}$). According to the Nyquist sampling theorem, in order to detect (and then correct) fluctuations with a given frequency, sampling has to be made at at least twice the frequency. The first type is, thus, very easily taken care of. Slow mirrors can be used to compensate for such drifts. The active stabilization system needs to be fast in order to correct for the two other types of fluctuations. The goal of our beam stabilization system is to take care of all of the first and the second type of instabilities and part of the third.

II. SETUP

The basic setup for the active stabilization system consists of two piezo mirrors and two position sensing detectors (PSDs). Each PSD records the offset of the laser beam from

a)Electronic mail: claes-goran.wahlstrom@fysik.lth.se.

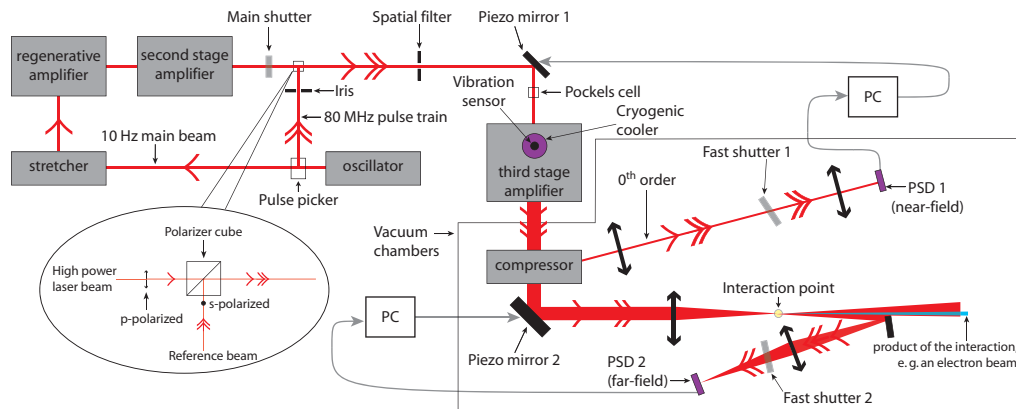


FIG. 1. (Color online) Schematic view of the beam pointing stabilization system of the Lund Laser Centre multi-TW laser (details in the text). The inset shows a side view of the injection point of the reference beam. The system works in the following way: two piezo mirrors are compensating for fluctuations in the beam pointing, one controls the near-field and other the far-field. Right before a main laser pulse arrives, the mirrors are fixed while fast shutters close to protect the detectors from the high power laser pulse. Once the laser pulse has passed the shutters open and the system starts regulating again.

the desired position and provides a voltage proportional to this offset. A fast computer and a custom made program is used to read the signals from the detector and to send appropriate voltages to the piezo mirror. For each mirror two signals are sent: one for corrections in the horizontal direction and one for the vertical direction. In order to get the beam axis right and not only the far-field position, one piezo mirror regulates the near-field while the other one takes care of the far-field.

A schematic view of the active control setup is given in Fig. 1. The high-intensity Ti:sapphire based chirped pulse amplification laser system at the Lund Laser Centre delivers up to 40 TW onto the target, with a FWHM pulse duration down to 35 fs and a beam diameter before focusing of 50 mm. The laser repetition rate is 10 Hz. Therefore, it is not possible to use the laser beam itself as a reference, if we want to correct for fluctuations faster than 5 Hz. Another reference beam is necessary that follows the same path as the TW beam. For this purpose we use part of the oscillator beam. This beam is at 80 MHz, which on the time scale we want to correct for, can be considered as continuous. A pulse picker takes ten pulses per second from this oscillator beam to be amplified, but all the remaining pulses can be used. This beam is injected into the laser system, after the second amplification stage, and follows the same path as the main laser beam. Both beams are going through a spatial filter, placed right after the injection point, and the reference beam is aligned on an iris used for the alignment of the main beam. This ensures that from this point both beams are colinear.

The reference beam is apertured by an iris before entering into the spatial filter, and the diameter of the focused beam is significantly larger than the hole of the spatial filter. Fluctuations in the pointing of the reference beam prior to the filter are, therefore, not transmitted. As the spatial filter is not diffraction limited for the main beam, fluctuations of the main beam occurring before the spatial filter are transmitted.

The system compensates only for fluctuations experienced by the main beam after the spatial filter. Before the spatial filter, two slow piezo mirror systems using the 10 Hz beam itself as a reference are used to compensate for slow drifts and to keep the laser well aligned up to the spatial filter. The reference beam has a polarization perpendicular to the main beam polarization and the two beams can, therefore, be combined using a polarizing cube, where the main laser beam is transmitted and the reference beam is reflected (see inset in Fig. 1). Later in the laser chain, before the third and final amplification stage, a Pockels cell rotates the plane of polarization of the amplified pulse, while most of the time, between the laser shots, the reference beam is not affected. Thus, both beams have the same polarization further on.

The two-dimensional PSDs used in this setup are duo-lateral PSDs (from SiTek Electro Optics), which have four terminals, two on the back side and two on the front side, where the terminals on the back side are placed perpendicular to the terminals on the front side. The photoelectric current, generated by the incident light, flows through the device and the relationship between the currents on the four terminals gives the light spot position. Unlike quadrant sensors, which require overlap in all quadrants, this kind of PSD provides the position of any spot within the detector region, independent of beam shape, size, and power distribution. They have very good resolution and linearity. Their fast response (400 kHz bandwidth) gives them an advantage over CCD cameras.

Two different types of piezo mirrors are used in the setup, as the beam has different size at the position of the mirrors. The first mirror (a 1 inch optic) sits in a piezoelectric mount (KC1-PZ from Thorlabs). The second mirror is a 4 inches optic and is mounted into a Piezo Tip/Tilt-Platform (S-340 from Physik Instrumente). Each mirror mount must be firmly mounted, or the movements of the piezo may drive the mirror mount itself into resonance. This is especially

important for the second mirror due to its large size and weight. The limiting factor of the hardware is the resonance frequency of the large piezo mirror, which is about 500 Hz.

The detectors need to record both the near- and far-field positions of the reference beam without blocking the path for the main pulse as it arrives. The first detector, for the near-field, monitors the zeroth order reflection from the first grating of the laser pulse compressor, placed under vacuum. The second detector monitors an image of the laser focal spot at the final interaction point. The first PSD controls a piezo mirror placed before the final stage of amplification. As this PSD monitors the near-field, a two lens system is used to project the transverse position of the full beam onto the PSD. The first lens (2 m focal length) focuses the beam in order to make the full beam small enough to fit on the PSD. The second lens (5 cm focal length) is used to image the position of the beam on the first lens onto the PSD. The second detector controls the large piezo mirror placed after the pulse compressor. PSD 2 is placed in the image plane of a lens collecting the light after the interaction point and, therefore, monitors the far-field. The lens is imaging the focal point onto the PSD with a magnification of two in order to increase the sensitivity. In many experiments using this kind of laser, the laser beam is focused into a gas jet. Part of the reference beam can then be collected after the focus point by a mirror and sent to the lens and the PSD. As the center part of the laser beam is not collected, the product of the interaction, e.g., an electron beam, can still pass through. For other types of experiments, other arrangement to image the focal spot of the reference beam might be needed. For the results presented below, the focusing optics had a focal length of 47.5 cm and the imaging lens a focal length of 20 cm. One should notice that the two piezo-controlled mirrors are far apart from each other in order to uncouple their actions.

In order for the active stabilization system to work efficiently, it must be optimized for speed. A properly adapted software must be used. We chose LABVIEW field-programmable gate array (FPGA) for its reliability, determinism, and parallelism. In addition, proportional-integral-derivative (PID) controllers were implemented in the code, which allows for faster corrections than simple proportional controllers.¹⁰ The PID loop runs at a fast rate and corrections were sent to the mirrors at 4 and 2 kHz for the small and large piezo mirrors, respectively. These rates are higher than the resonance frequencies of the mirrors and, thus, the output signal is smoothed. In addition, in order to reduce the step-like behavior of the output signal, the program interpolates between the consecutive points of the output signal.

Filtering of the detector signal is also necessary to eliminate high frequency components above the resonance frequencies of the piezo mirrors. If fed to the piezo mirrors, these high frequency components drive the mirrors unstable, disturbing the stabilization. However, filter always introduces a time delay between the observed error and the correction. In order to operate the stabilization system at a fast rate, this delay must be minimized. This is done using low-pass finite impulse response digital filters. Such filters produce much shorter delays than conventional ones and have the advantage of producing the same delay for all frequencies.¹¹

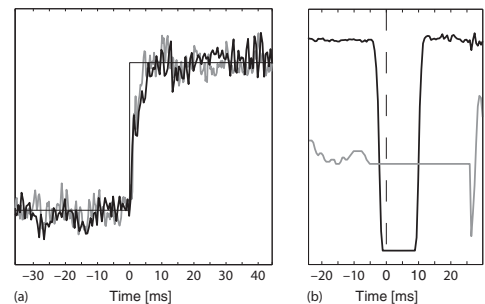


FIG. 2. (a) Typical step responses of the system. The gray and black curves are the signals recorded by the horizontal axis of the PSDs monitoring the far-field and near-field, respectively. In (b) the timing of the fast shutter used to protect the detectors is described. The black line shows the intensity recorded by the PSD and the gray line is the voltage sent to the piezo mirror. The dashed line corresponds to the time when the TW laser pulse arrives.

The time response of the system has been investigated by recording the error signal from the PSDs inside the loop. By frequency analysis of the open- and close-loop signals, it is found that frequency components up to 150 Hz for the near-field mirror and up to 100 Hz for the far-field mirror are successfully attenuated by the feedback loop. The response to set point changes was also investigated. A step of the order of the pointing fluctuations (corresponding to $6.8 \mu\text{rad}$ for the far-field and $900 \mu\text{m}$ for the near-field) was introduced in the set point value as shown in Fig. 2(a). We observe that it takes about 5 ms for the system to settle to the new set point values in both the far-field and the near-field. These are evidences that the system is able to act on a millisecond time scale.

In order to avoid the PSD to be destroyed by the high power laser shots, fast mechanical shutters (approximately millisecond response time, VS14 from Uniblitz) are protecting the PSDs when the main laser shots arrive. Each piezo mirror is regulating until just before the shutter closes and then holds the voltage, as described in Fig. 2(b). The delay between the laser shot and the end of regulation is very short, typically only a few ms, and the introduced error is, therefore, negligible. The timing between the shutter and the laser is shown in Fig. 2(b), where it is seen that the piezo mirrors are held at a fixed voltage 5 ms before the laser shot and the shutter starts closing 4 ms before the shot.

Some fluctuations are too dominant to be efficiently compensated for by the active control system. For example, the cryogenic cooler produces short but intense burst of high frequency vibrations that are difficult to handle because of their high frequency. We instead circumvent these vibration bursts. The cryogenic cooler is used to cool the crystal of the final stage of amplification. A pump circulates helium to the crystal at a rate of 1 Hz. During its operating cycle, when the piston reaches its stop, it makes the optical table vibrate. Given that the cycle consists of the piston going back and forth, there are two stops, giving a repetition frequency of 2 Hz for these bursts. After each shock, the optical table reacts and vibrates for some hundred milliseconds while damping the waves, as

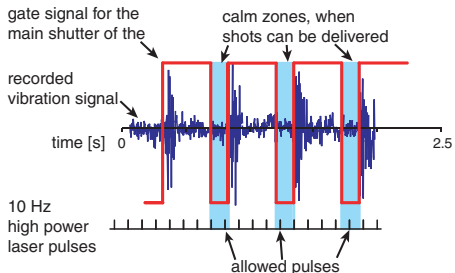


FIG. 3. (Color online) Filtering of the laser shots is necessary to avoid the short but intense burst of high frequency vibrations produced by the cryogenic cooler. The main shutter of the laser delivers shots only when the vibrations are minimal.

illustrated in Fig. 3. The vibrations are recorded and a gate signal is produced which allows the main shutter of the laser to deliver shots only when the vibrations are minimal. The calm period starts about 400 ms after the beginning of the shock and lasts 100 ms. This allows a laser shot to be delivered during this calm period. The dominant fluctuations are thus simply avoided. The control loop runs all the time but it is not able to regulate well during the shocks. However when the calm period starts, it has enough time to settle before the laser shot arrives. This mode of operation works well for single shot operation or repetition rate below 2 Hz. This is indeed the case for most types of ultrahigh intensity experiments. Modifications will be necessary if 10 Hz operation is required.

To summarize, the system works in the following way: two piezo mirrors are regulating and compensating for fluctuations in the beam pointing, one controls the near-field and one the far-field. When a high power laser shot is requested, the main shutter delivers a pulse during the calm time window of the cryogenic cooler. Right before the pulse comes, the voltages to the mirrors are fixed while fast shutters close to protect the detectors from the high power laser shot. Once the laser pulse has passed, the shutters open and the mirrors start regulating again.

III. EXPERIMENTAL RESULTS AND DISCUSSION

In order to assess the quality of the beam stabilization, signals recorded with the reference beam on the PSDs are not enough, actual laser shots must be recorded. To do so, a beam splitter was placed in the beam and the focal spot imaged by a 40 times microscope objective and recorded with a CCD camera. Two hundred consecutive laser shots in the high power configuration (the laser was attenuated, but everything else was running in the full power experimental conditions) were recorded with 3 s between each shot. The results are presented in Fig. 4. In the panels on the left, each point represents one laser shot. The origin (0,0) corresponds to the mean position of all the points. The positions recorded by the CCD camera are divided by the focal length of the laser focusing optics used and the scales are, therefore, shown in μrad , which is

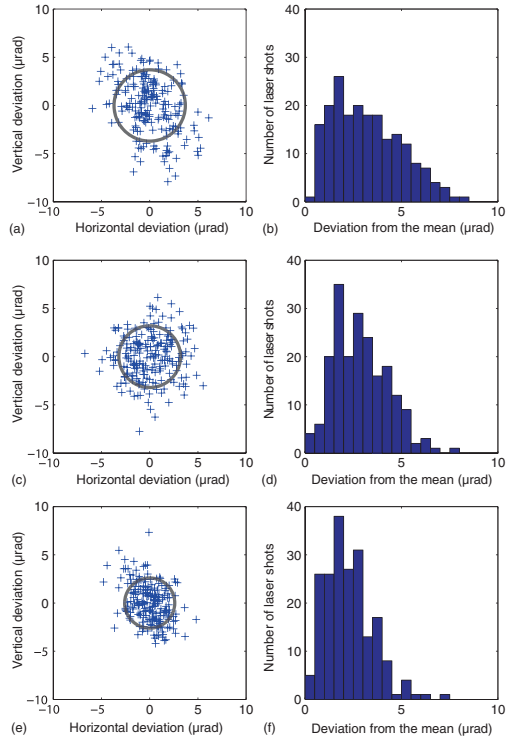


FIG. 4. (Color online) Pointing of 200 consecutive laser shots recorded by a microscope objective and a CCD camera. On the right side corresponding distributions of deviations from the mean. In (a) and (b) no active stabilization is used. In (c) and (d) the laser shots are gated in time in order to avoid firing when intense vibrations are produced by the cryogenic cooler in the laser amplifier. Finally, in (e) and (f), active stabilization is added with the help of two piezo mirrors. The circle represents the deviation corresponding to one standard deviation and its radius decreases for each step of the stabilization.

independent of the focusing optic used. In (a) no active stabilization is used. The beam pointing is, however, already fairly good thanks to all the work done on passive stabilization of the laser system. (c) Shows laser shots recorded with the gating system, delivering shots only in the calm section of the vibration cycle of the cryogenic cooler. (e) Presents shots with both gating and piezo mirror stabilization active. Each step of the stabilization shows an improvement in both the extremes and the mean of the distances between the laser shots.

On the right-hand side in Fig. 4, the distribution of the laser shots as function of their distance from the mean position is presented. This gives a better understanding of the effect of each step of the stabilization. We see that the gating of the shots already reduce the extreme points. The active stabilization further reduces it and no laser shots are more than $7.3 \mu\text{rad}$ away from the center. If we calculate the standard deviation of the distribution, we also observe a clear improvement: $3.7 \mu\text{rad}$ for (a), $3.2 \mu\text{rad}$ in (c), and $2.6 \mu\text{rad}$ in (e), which corresponds to an overall improvement of 30%. At the beginning of this project, i.e., before passive stabilization, the

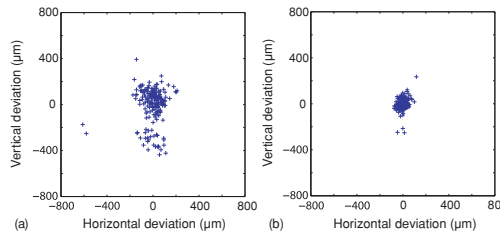


FIG. 5. (Color online) Near-field position of the reference beam for 200 consecutive shots recorded by a CCD camera imaging the position of the beam on the focusing optics. In (a) no active stabilization is used and in (b) the active stabilization is added.

mean was $6.7 \mu\text{rad}$. It shows the importance of doing passively what can be done first. It is interesting to compare the obtained pointing fluctuations with the focal spot size. In the experiments reported in Refs. 5 and 6, using a $f = 1.5 \text{ m}$ focusing mirror, the focal spot size was $40 \mu\text{m}$ (radius of the first minimum of an Airy-like pattern). The mean of the resulting pointing fluctuations with this focusing optics would be $3.9 \mu\text{m}$. The resulting pointing fluctuations, thus, correspond to only 10% of the focal spot size.

When only the second piezo mirror is regulating, the standard deviation is $2.8 \mu\text{rad}$, which is similar to the value obtained with two piezo mirrors. This is expected as the CCD is monitoring the position of the beam in the focal plane, i.e., the far-field, and the second piezo mirror regulates only the far-field. In this case, the laser beam is hitting the right point in the focal plane but not necessarily along the correct axis. The use of two mirrors improves the overall pointing stability. This further shows that the use of two piezo mirrors in this configuration does not produce any interference effect.

The stability of the near-field was also investigated. To do so, a lens was placed after the focal spot to image the position of the beam on the parabolic mirror onto the CCD camera. To avoid problems with varying intensity profile, we assess the near-field stability of the reference beam instead of the main beam. Figure 5 shows the effect of the active stabilization on the position of the reference beam on the focusing optics, i.e., the near-field. In (a) there is no stabilization active, whereas in (b) the system is regulating. It is clearly observed that the near-field position of the beam is well stabilized and that the reference beam can be used to keep the main beam axis stable, as its intensity profile is very stable.

Depending on the requirements of the experiment, one might not need any active stabilization or one might want to use only one mirror. When only far-field stability is needed. For guiding experiments in capillaries, one mirror is enough in order not to damage the entrance of the capillary and it was used in this configuration in Refs. 5 and 6 with PSD 1 acting as a far-field detector. With two mirrors it should be possible to achieve even better guiding.⁹ In gas jet experiments for electron acceleration, pointing stabilization is not crucial for the generation of the electron beams. However, in order to obtain an electron beam with good pointing stability, the laser pointing stability of both the near- and far-field is important. Experiments on solid target (for example, target normal

sheath acceleration on flat foils) might not require very high pointing stability, however, for mass-limited targets one may need fast active stabilization with at least one mirror.

IV. CONCLUSION AND OUTLOOK

A system that actively stabilizes both the near-field and the far-field beams pointing of a multi-TW laser on the few millisecond time scale is introduced. The work presented above shows that a beam stabilization system can be implemented on an existing TW laser system without modifying its layout despite the high power laser pulses delivered and the resulting noisy environment due to the production of such pulses. Laser shots can be contained within a circle of $7.3 \mu\text{rad}$ radius with a standard deviation of $2.6 \mu\text{rad}$. In addition, both the near- and far-field are stabilized. The results on monomode guiding in dielectric capillaries presented in Refs. 5 and 6 were possible thanks to this work. This opens prospects for further experiments, where the beam pointing is an important parameter.

Of course, this stabilization system can further be improved. Sources of high frequency vibrations should be isolated better from the laser system. The implementation of a feed-forward loop could predict the position of the beam in the gap between the shutter closing and the laser shot. When designing a new laser system, issues related to beam pointing can be taken into account from the start, making the implementation of such stabilization system much easier.

ACKNOWLEDGMENTS

The authors would like to acknowledge the fruitful discussions and collaboration within Lund University with L. Österman, B. Lundberg, B. Wittenmark, K. J. Åström, A. Cervin, and L. Sörnmo. The authors acknowledge the financial support from the Swedish Research Council and the Knut and Alice Wallenberg Foundation. This research was supported by the Marie Curie Early Stage Training Site MAXLAS (Contract No. MEST-CT-2005-020356) within the 6th European Community Framework Programme and the NEST Activity under the FP6 Structuring the European Research Area programme (project EuroLEAP, Contract No. 028514).

- ¹D. Strickland and G. Mourou, *Opt. Commun.* **56**, 219 (1985).
- ²T. Kanai, A. Suda, S. Bohman, M. Kaku, S. Yamaguchi, and K. Midorikawa, *Appl. Phys. Lett.* **92**, 061106 (2008).
- ³F. Breitling, R. S. Weigel, M. C. Downer, and T. Tajima, *Rev. Sci. Instrum.* **172**, 1339 (2001).
- ⁴Y. Wu, D. French, and I. Jovanovic, *Opt. Lett.* **35**, 250 (2010).
- ⁵F. Wojda, K. Cassou, G. Genoud, M. Burza, Y. Glinec, O. Lundh, A. Persson, G. Vieux, E. Brunetti, R. Shanks, D. Jaroszynski, N. E. Andreev, C.-G. Wahlström, and B. Cros, *Phys. Rev. E* **80**, 066403 (2009).
- ⁶N. E. Andreev, K. Cassou, F. Wojda, G. Genoud, M. Burza, O. Lundh, A. Persson, B. Cros, V. E. Fortov, and C.-G. Wahlström, *New J. Phys.* **12**, 045024 (2010).
- ⁷S. P. D. Mangles, C. D. Murphy, Z. Najmudin, A. G. R. Thomas, J. L. Collier, A. E. Dangor, E. J. Divall, P. S. Foster, J. G. Gallacher, C. J. Hooker, D. A. Jaroszynski, A. J. Langley, W. B. Mori, P. A. Norreys, F. S. Tsung, R. Viskup, B. R. Walton, and K. Krushelnick, *Nature (London)* **431**, 535 (2004); C. G. R. Geddes, C. Toth, J. van Tilborg, E. Esarey, C. B. Schroeder, D. Bruhwiler, C. Nieter, J. Cary, and

⁷W. P. Leemans, *Nature (London)* **431**, 538 (2004); J. Faure, Y. Glinec, A. Pukhov, S. Kiselev, S. Gordienko, E. Lefebvre, J.-P. Rousseau, F. Burgy, and V. Malka, *Nature (London)* **431**, 541 (2004).
⁸W. P. Leemans, B. Nagler, A. J. Gonsalves, C. Tóth, K. Nakamura, C. G. R. Geddes, E. Esarey, C. B. Schroeder, and S. M. Hooker, *Nat. Phys.* **2**, 696 (2006).

⁹M. Veysman, N. E. Andreev, K. Cassou, Y. Ayoul, G. Maynard, and B. Cros, *J. Opt. Soc. Am. B* **27**, 1400 (2010).

¹⁰K. J. Åström and R. M. Murray, *Feedback Systems: An Introduction for Scientists and Engineers* (Princeton University Press, Princeton, NJ, 2008).

¹¹S. K. Mitra and J. Kaiser, *Handbook for Digital Signal Processing* (Wiley, New York, 1993).

PAPER II

Laser-driven plasma waves in capillary tubes

F. Wojda, K. Cassou, G. Genoud, M. Burza, Y. Glinec, O. Lundh, A. Persson, G. Vieux, E. Brunetti, R.P. Shanks, D. Jaroszynski, N. E. Andreev, C.-G. Wahlström and B. Cros.

Phys. Rev. E **80**, 066403 (2009).

Laser-driven plasma waves in capillary tubes

F. Wojda,¹ K. Cassou,¹ G. Genoud,² M. Burza,² Y. Glinec,² O. Lundh,² A. Persson,² G. Vieux,³ E. Brunetti,³ R. P. Shanks,³ D. Jaroszynski,³ N. E. Andreev,⁴ C.-G. Wahlström,² and B. Cros^{1,*}

¹Laboratoire Physique Gaz et Plasmas, CNRS–Université Paris-Sud 11, F-91405 Orsay Cedex, France

²Department of Physics, Lund University, P.O. Box 118, S-22100 Lund, Sweden

³Department of Physics, University of Strathclyde, Glasgow G4 0NG, United Kingdom

⁴Joint Institute for High Temperatures, Russian Academy of Sciences, Moscow 125412, Russia

(Received 8 July 2009; revised manuscript received 3 November 2009; published 4 December 2009)

The excitation of plasma waves over a length of up to 8 cm is demonstrated using laser guiding of intense laser pulses through hydrogen-filled glass capillary tubes. The plasma waves are diagnosed by spectral analysis of the transmitted laser radiation. The dependence of the spectral redshift—measured as a function of filling pressure, capillary tube length, and incident laser energy—is in excellent agreement with simulation results. The longitudinal accelerating field inferred from the simulations is in the range of 1–10 GV/m.

DOI: 10.1103/PhysRevE.80.066403

PACS number(s): 52.38.Kd, 41.75.Jv, 52.35.Mw, 52.38.Hb

Electrons accelerated in laser wakefield accelerators (LWFAs) [1–3] acquire momentum from the electrostatic fields of a plasma density wave or wake, excited by an intense laser pulse passing through plasma. As they can achieve ultrarelativistic energies over very short distances, they have attracted great interest as novel routes to a new generation of ultra-compact accelerators, which could be relevant to a wide range of applications, including high-energy physics and compact free-electron lasers. At high laser intensities large amplitude plasma waves with longitudinal electric fields, up to hundreds of GV/m, are excited, which are several orders of magnitude higher than those possible in conventional accelerators. When electrons are injected into the accelerating regions of such plasma waves, either from an external source [4] or by self-trapping of plasma electrons by nonlinear effects, they have been observed to reach energies up to hundreds of MeV over acceleration distances of only a few mm [5–8]. However, even with fields as high as 100 GV/m, the acceleration distance must be extended to tens of cm in order to reach electron energies of, say, tens of GeV. This is a range not yet realized experimentally.

There are two main requirements that must be fulfilled before a viable multi-GeV LWFA can be realized. First, the intense laser pulse driving the plasma wave must be guided over the full length of the accelerator. Second, the dephasing length, which is the distance over which the accelerating electrons outrun the accelerating region of the plasma wave, must be at least as long as the accelerating medium. To date, most experiments have been performed with a few mm long gas jets, where self-guiding due to relativistic self-focusing provides a simple guiding solution. However, the threshold power for self-focusing is, for a given laser wavelength, inversely proportional to the plasma density, thus requiring a minimum density for a given laser. As an example, for a laser with 10 TW peak power and 800 nm wavelength, this density is $n_e \approx 3 \times 10^{18} \text{ cm}^{-3}$. An alternative approach is to guide the laser in a preformed plasma channel produced by an electric discharge in a gas-filled capillary tube. In this way guiding

up to several centimeter long plasma waveguide has been demonstrated [9]. However, this approach is limited to plasma densities in excess of $n_e \sim 10^{18} \text{ cm}^{-3}$. Long dephasing lengths require very low plasma densities [3], which is clearly in conflict with the density requirements for relativistic self-guiding and guiding by discharge-formed plasma channels.

A method of guiding the intense laser pulse over long distance, while allowing very low plasma density, is thus required. This can be realized using capillary tubes as waveguides [10] where guiding is achieved by reflection from the walls. Laser guiding through gas-filled capillary tubes allows for a smooth transverse profile in monomode propagation [11] and a minimum attenuation of the laser pulse through refraction losses. As a first step in developing the waveguide as a medium for a wakefield accelerator, we have characterized the properties of the plasma wave in the moderately nonlinear regime over several centimeters. Working in the linear or moderately nonlinear regime allows control of the amplitude of the plasma waves while providing a focal spot of sufficient dimensions to effectively create quasi-one-dimensional longitudinal oscillations as shown by theoretical studies [12,13]. This regime enables a controlled and reproducible injection of an external electron bunch into the accelerating field, which provides a means of attaining high stability and reproducibility for future staging of several LWFA stages.

In this paper, we report on an observation of plasma waves excited by a guided high-intensity laser pulse inside hydrogen-filled capillary tubes with lengths up to 8 cm. The plasma wave excitation is diagnosed using a method based on spectral modifications of the laser pulse, due to local spatiotemporal variations of the density of the plasma [14].

An experiment was performed using the high-intensity Ti:sapphire laser system at the Lund Laser Centre which delivers up to 40 TW onto the target, with a full width at half maximum (FWHM) pulse duration down to $\tau_L = 35 \text{ fs}$. The setup is shown schematically in Fig. 1. The 30-mm-diameter beam was focused with an $f=1.5 \text{ m}$ spherical mirror at the entrance of a capillary tube. A deformable mirror was placed after the compressor (not shown) to correct the main aberrations of the phase front in the focal plane.

*brigitte.cros@u-psud.fr

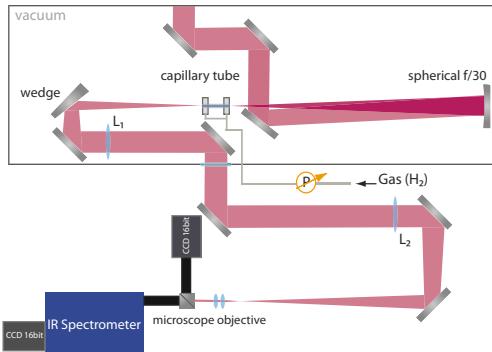


FIG. 1. (Color online) Schematic view of the experiment setup. Elements within the gray line box are under vacuum.

The laser beam transmitted through the capillary tube was attenuated by reflecting it on an optically flat glass wedge and then collimated by an achromatic lens (L_1), which could be translated in vacuum along the beam axis to collect light either from the focal plane (i.e., with the capillary tube removed) or from the exit plane of the tube. The beam was then focused by a $f_2=1$ m achromatic lens (L_2) and magnified 10× by a microscope objective. The beam was split in two parts. Focal spot or capillary tube output images were recorded by a 16-bit charge-coupled device (CCD). The transmitted part was sent to a visible to near-infrared imaging spectrometer equipped with a 16-bit CCD camera. The spectral resolution was 0.1 nm.

Glass capillary tubes with inner radius $r_c=50\ \mu\text{m}$ and length varying between 1.2 and 8.1 cm were used. Hydrogen gas flowed into the tubes through two thin ($\sim 100\ \mu\text{m}$) slits located between 2.5 and 5 mm from each end of the tube. The filling pressure was varied between 0 and 70 mbar. Each capillary tube could be used for at least 100 laser shots, when the laser beam remained well centered at the capillary entrance. Pointing variations due to thermal drifts and mechanical vibrations were therefore minimized or compensated for. Laser guiding at input intensities up to $10^{18}\ \text{W/cm}^2$ was achieved with more than 90% energy transmission in evacuated or hydrogen-filled gas tubes up to 8 cm long.

For the data presented here, in order to investigate the moderately nonlinear regime, the input intensity was kept lower than $3 \times 10^{17}\ \text{W/cm}^2$. The laser pulse duration was $\tau_L=45\pm 5$ fs and the associated bandwidth was approximately 25 nm (FWHM); each pulse had a small negative linear chirp ($-550\ \text{fs}^2$), i.e., short wavelengths preceded longer wavelengths, and the center wavelength was 786 nm. The energy distribution in the focal plane exhibited an Airy-like pattern with a radius at first minimum of $r_0=40\pm 5\ \mu\text{m}$.

Spectra of the laser light transmitted through gas-filled capillary tubes exhibit blue and red broadening. In the range of parameters relevant to this experiment, spectral modifications of the wake-driving laser pulse—after propagating in the plasma over a large distance—are mainly related to changes in the index of refraction of the plasma during the

creation of the plasma wave. The front of the laser pulse creates an increase in electron density, leading to a blueshift at the front of the pulse, while the rear of the pulse creates a decrease in electron density with larger amplitude, and thus a redshift of the spectrum. This effect has been proposed [14] to determine the amplitude of the electron plasma density perturbation in the linear or moderately nonlinear regime.

An averaged wavelength shift $\Delta\lambda(l)$ is calculated from the experimentally measured spectra $S(\lambda, l)$ at the exit of a capillary of length l and is defined as

$$\Delta\lambda(l) = \frac{\int_0^\infty \lambda S(\lambda, l) d\lambda}{\int_0^\infty S(\lambda, l) d\lambda} - \lambda_L, \quad (1)$$

where $\lambda_L=[\int_0^\infty S(\lambda, l=0) d\lambda]^{-1} \int_0^\infty \lambda S(\lambda, l=0) d\lambda = 2\pi c/\omega_L$ is the center wavelength of the incident laser pulse in vacuum and ω_L is the laser frequency. For an underdense plasma and laser intensity well above the ionization threshold, when the blueshift due to gas ionization inside the interaction volume V can be neglected and the wavelength shift given by Eq. (1) remains small compared to λ_L , this shift is directly related to the energy of the plasma wave electric field E_p excited in the plasma [14],

$$\frac{\Delta\lambda(l)}{\lambda_L} \approx \frac{1}{16\pi\mathcal{E}_{out}} \int_V E_p^2 dV, \quad (2)$$

where \mathcal{E}_{out} is the total energy of the transmitted pulse. For monomode propagation of a laser pulse with Gaussian time envelope, generating a wakefield in the weakly nonlinear regime, the wavelength shift can be expressed analytically. For small energy losses, it is proportional to the peak laser intensity on the capillary axis and to the length of the capillary and exhibits a resonantlike dependence on gas pressure described by the function $D(\Omega)$ as

$$\Delta\lambda(l) \approx \left[0.178 + 1.378 \frac{c^2}{(\omega_p r_c)^2} \right] \left(\frac{\omega_p}{\omega_L} \right)^3 a_L^2 D(\Omega) l, \quad (3)$$

where $a_L=eE_L/m_e\omega_L c$ is the normalized amplitude of laser electric field E_L , $D(\Omega)=\Omega \exp(-\Omega^2/4)$ with $\Omega=\omega_p\tau_L/\sqrt{2\ln 2}$, and $\omega_p=\sqrt{n_e e^2/\epsilon_0 m_e}$ is the electron plasma frequency.

The value of the wavelength shift $\Delta\lambda$ obtained from measured spectra is plotted as a series of black squares in Fig. 2 for a tube of length 7.1 cm as a function of filling pressure. Nonlinear laser pulse propagation in the gas-filled capillary tube including optical field ionization of gas, wakefield generation, and the self-consistent laser pulse spectrum modification was simulated numerically using the code described in [12]. The parameters used at the capillary entrance are $\tau_L=51$ fs, with a negative chirp, and an incident laser energy $\mathcal{E}_L=0.12$ J, with a radial profile corresponding to the one measured in the focal plane in vacuum, averaged over the angle. Simulation results are plotted as a red triangle curve in Fig. 2. For comparison, the analytical behavior given by Eq. (3) is plotted as a blue dashed curve, for the same (τ_L, \mathcal{E}_L) . The simulated wavelength shifts fit closely the experimen-

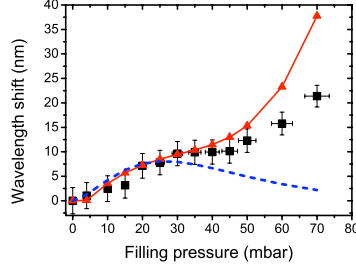


FIG. 2. (Color online) Wavelength shift as a function of hydrogen H₂ filling pressure at the exit of a 7.1-cm-long capillary tube obtained from experimental data (black squares); simulation results (red triangle curve) with $(\tau_L, \mathcal{E}_L) = (51 \text{ fs}, 0.12 \text{ J})$ and a negative chirp; analytical result from Eq. (3) for the same parameters (dashed blue line).

tally measured ones up to a filling pressure of 50 mbar. Analytical curve and measured and modeled wavelength shifts have the same behavior up to the linear resonant pressure of 25 mbar ($n_e \approx 1.2 \times 10^{18} \text{ cm}^{-3}$). For pressures higher than 25 mbar, the experimental data and simulation exhibit a larger redshift than the analytical prediction. The analysis of the pulse evolution in the simulation shows that a steepening of the laser pulse front edge, due to propagation in the ionizing gas [15], occurs followed in time by pulse self-modulation [12]. A steepened pulse front is more efficient than a Gaussian time envelope to generate the wakefield at pressures larger than the resonant one. The values of the wavelength shift in the simulation are larger than the measured ones for pressures above 50 mbar. This behavior is related to the assumption of cylindrical symmetry used in the simulation, which leads to more pronounced nonlinear effects including laser pulse shortening [12,16].

Figure 3 shows examples of the spectra of the laser pulse measured (black lines) in the focal plane in vacuum [Fig. 3(a)] and at the output of the 7.1 cm capillary tube and the corresponding simulated spectra (dashed red lines) for filling pressures of 30 mbar [Fig. 3(b)] and 40 mbar [Fig. 3(c)]; two different shots are shown for each pressure.

All spectra are normalized to their maximum amplitude and integrated over the radial coordinate. The spectral modifications in the experiment and the simulations are in excellent agreement over a large range of amplitude. This agreement on the detailed structure of the spectra confirms the one, shown in Fig. 2, achieved on the wavelength shift, which is an integrated and averaged quantity.

The wavelength shift measured at the output of the capillary tubes as a function of the tube length is plotted in Fig. 4 for different filling pressures as well as the corresponding simulated results. A linear behavior of the wavelength shift as a function of length is observed at 20 mbar. The fit of experimental data by simulation results demonstrates that the plasma wave is excited over a length as long as 8 cm. As the pressure is increased, the nonlinear laser pulse evolution is amplified with the propagation length leading to a larger plasma wave amplitude.

The wavelength shift as a function of input laser energy is

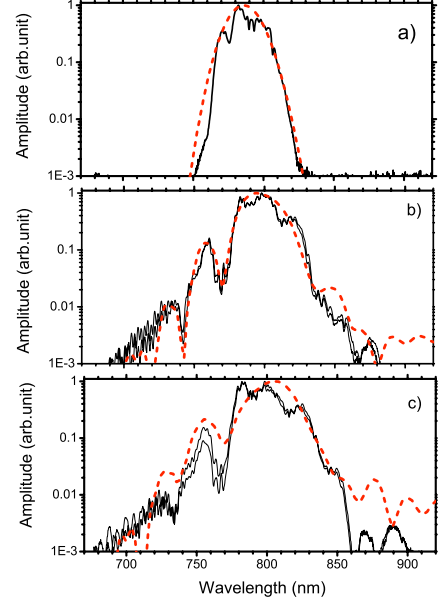


FIG. 3. (Color online) Spectra measured (black lines) (a) in the focal plane in vacuum and at the output of the 7.1 cm capillary tube for filling pressures of (b) 30 and (c) 40 mbar; two shots are shown for each pressure; corresponding simulated spectra (red dashed line).

shown in Fig. 5 at the exit of a 7.1-cm-long capillary tube for a filling pressure of 40 mbar, obtained from experimental data, simulation results, and analytical prediction. For $\mathcal{E}_L > 0.1 \text{ J}$, the growth of the wavelength shift is faster than the linear one predicted analytically and the experimental and numerical results are in excellent agreement. For lower energy ($\approx 0.05 \text{ J}$), gas ionization occurs closer to the maximum of the pulse and, combined with radial structure, leads to a more pronounced steepening of the front edge of the pulse and increased wakefield amplitude and wavelength

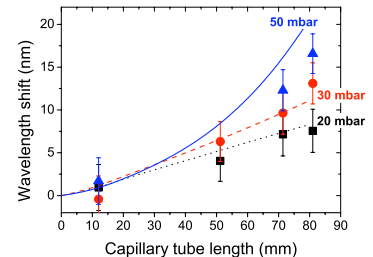


FIG. 4. (Color online) Wavelength shift measured at the output of the capillary tubes as a function of the tube length for filling pressures of 20 mbar (black square), 30 mbar (red dots), and 50 mbar (blue triangles) and the corresponding simulated shifts (dotted, dashed, and solid lines).

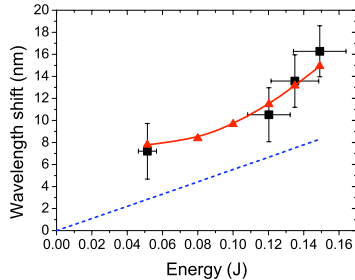


FIG. 5. (Color online) Wavelength shift as a function of input energy, at the exit of a 7.1-cm-long capillary tube for a filling pressure of 40 mbar obtained from experimental data (black squares), simulation results (red triangle curve), and analytical prediction (blue dashed curve).

shift compared to the analytical prediction [Eq. (3)].

In conclusion, we have generated and characterized a laser-driven plasma wave in the moderately nonlinear regime over a distance as long as 8 cm inside dielectric capillary tubes. An excellent agreement is found between the mea-

sured wavelength shift and the results from simulations as concerns pressure, length, and energy dependences. In the linear and weakly nonlinear regimes, this diagnostic provides a robust and reproducible measurement of the plasma wave amplitude over a long distance. The value of the longitudinal accelerating field in the plasma obtained from the simulation is in the range of 1–10 GV/m. The average product of gradient and length achieved in this experiment is on the order of 0.4 GV at a pressure of 50 mbar; it could be increased to several GV by extending the length and diameter of the capillary tube with higher laser energy.

We acknowledge the support of the European Community-New and Emerging Science and Technology Activity under the FP6 “Structuring the European Research Area” program (project EuroLEAP, Contract No. 028514) and Marie Curie Early Stage Training Site MAXLAS (Contract No. MEST-CT-2005-020356). This work was also supported by the Swedish Research Council, the Knut and Alice Wallenberg Foundation, the EU Access to Research Infrastructures activity (Contract No. RII3-CT-2003-506350, Laserlab Europe), the Russian Foundation for Basic Research (Project No. 07-02-92160), and the EPSRC U.K.

- [1] T. Tajima and J. M. Dawson, Phys. Rev. Lett. **43**, 267 (1979).
- [2] P. Sprangle *et al.*, Appl. Phys. Lett. **53**, 2146 (1988).
- [3] E. Esarey *et al.*, IEEE Trans. Plasma Sci. **24**, 252 (1996).
- [4] F. Amiranoff *et al.*, Phys. Rev. Lett. **81**, 995 (1998).
- [5] S. Mangles *et al.*, Nature (London) **431**, 535 (2004).
- [6] C. Geddes *et al.*, Nature (London) **431**, 538 (2004).
- [7] J. Faure *et al.*, Nature (London) **431**, 541 (2004).
- [8] W. Leemans *et al.*, Nat. Phys. **2**, 696 (2006).
- [9] D. J. Spence and S. M. Hooker, Phys. Rev. E **63**, 015401(R) (2000).
- [10] F. Dorchies *et al.*, Phys. Rev. Lett. **82**, 4655 (1999).
- [11] B. Cros, C. Courtois, G. Matthieu, A. Di Bernardo, D. Batani, N. Andreev, and S. Kuznetsov, Phys. Rev. E **65**, 026405 (2002).
- [12] N. E. Andreev, Y. Nishida, and N. Yugami, Phys. Rev. E **65**, 056407 (2002).
- [13] N. E. Andreev *et al.*, Phys. Plasmas **9**, 3999 (2002).
- [14] N. E. Andreev and M. Chegotov, JETP **101**, 56 (2005).
- [15] N. E. Andreev *et al.*, JETP **96**, 885 (2003).
- [16] S. A. Skobelev *et al.*, JETP Lett. **89**, 540 (2009).

PAPER III

Analysis of laser wakefield dynamics in capillary tubes

N. E. Andreev, K. Cassou, F. Wojda, G. Genoud, M. Burza, O. Lundh, A. Persson, B. Cros, V. E. Fortov and C-G Wahlström.
New J. Phys. **12**, 045024 (2010).

New Journal of Physics

The open-access journal for physics

Analysis of laser wakefield dynamics in capillary tubes

N E Andreev^{1,2,5}, K Cassou³, F Wojda³, G Genoud⁴, M Burza⁴, O Lundh⁴, A Persson⁴, B Cros³, V E Fortov^{1,2} and C-G Wahlstrom⁴

¹ Joint Institute for High Temperatures of RAS, Russian Academy of Sciences, Moscow 125412, Russia

² Moscow Institute of Physics and Technology (State University), Moscow 113303, Russia

³ Laboratoire de Physique des Gaz et des Plasmas, CNRS – Université Paris-Sud 11, F-91405 Orsay Cedex, France

⁴ Department of Physics, Lund University, PO Box 118, S-22100 Lund, Sweden

E-mail: andreev@ras.ru

New Journal of Physics **12** (2010) 045024 (17pp)

Received 28 November 2009

Published 30 April 2010

Online at <http://www.njp.org/>

doi:10.1088/1367-2630/12/4/045024

Abstract. A general approach to the modifications of the spectrum of a laser pulse interacting with matter is elaborated and used for spectral diagnostics of laser wakefield generation in guiding structures. Analytical predictions of the laser frequency red shift due to the wakefield excited in a capillary waveguide are confirmed by self-consistent modeling results. The role of ionization blue shift, and nonlinear laser pulse and wakefield dynamics on the spectrum modification, is analyzed for recent experiments on plasma wave excitation by an intense laser pulse guided in hydrogen-filled glass capillary tubes up to 8 cm long. The dependence of the spectral frequency shift, measured as a function of filling pressure, capillary tube length and incident laser energy, is in excellent agreement with the simulation results, and the associated longitudinal accelerating field is in the range 1–10 GV m⁻¹.

⁵ Author to whom any correspondence should be addressed.

Contents

1. Introduction	2
2. Analytical theory (general approach)	3
3. Modeling results and comparison with analytical predictions	5
4. Experimental arrangement	9
5. Comparison between modeling results and experimental data	11
6. Conclusion	15
Acknowledgments	16
References	16

1. Introduction

The interaction of short, intense laser pulses with plasmas produces large amplitude wakes. The high-field amplitude associated with these wake waves can be used to accelerate particles to high energies over very short lengths compared with the conventional accelerator technology [1]–[3]. In linear or moderately nonlinear regimes, these fields are of the order of $1\text{--}10 \text{ GV m}^{-1}$, and relativistic electrons injected into the wave can acquire an energy of the order of 1 GeV over a length of the order of a few centimeters. The control of the characteristics of the electron beam as it is accelerated is crucial for achieving a usable laser–plasma accelerator unit. It is linked to the control of the accelerating electric field structure over several centimeters in a plasma. Diagnostics providing a detailed knowledge of the field structure and time evolution are therefore important for the progress of accelerator development.

Several diagnostics methods have been used to measure plasma waves created by the laser wakefield, in particular multi-shot or single-shot frequency domain interferometry [4, 5]. They rely on the interference in the frequency domain of two separate probe pulses and have been used to measure density perturbations over lengths of the order of a few millimeters. The dispersion effects on the probe pulse and the variations of the phase velocity of the excited plasma wave make these diagnostic techniques difficult to use over longer propagation distances [6]. Modifications of the spectrum of a single probe pulse propagating in a time- and space-varying plasma density [7] can be used to diagnose the laser wakefields [6, 8] without restrictions to the wake wave amplitude and dispersion effects.

The amplitude of the plasma wave excited by the laser pulse over a large length can be obtained in a single shot by the analysis of the modifications of the spectrum of the driving pulse. This method, proposed in [9, 10] and compared with the experimental measurements for a supersonic helium gas jet target of sub-millimeter length in [11], relies on the modifications of the spectrum induced by the time-varying plasma density within the pulse duration. Recently, it has been used successfully to measure the plasma wave excited in the wake of an intense laser guided in a gas-filled capillary tube over 8 cm [12].

In this paper, analytical expressions for the frequency shift due to the laser wakefield excited in a capillary tube are derived and compared with self-consistent modeling including gas ionization, nonlinear laser pulse and wakefield dynamics. A detailed comparison with experimental data shows that excellent agreement is obtained in a broad range of plasma densities, which allows us to determine the value of the accelerating field amplitude.

2. Analytical theory (general approach)

The general frequency momentum theory [13] describes the relation between the frequencies, ω , averaged over the spectrum of incident and output radiation of intensity $I_\alpha(\omega, R)$ from the interaction volume V :

$$\langle \omega^2 \rangle_\alpha = \oint_S \int_0^{+\infty} \omega^2 I_\alpha(\omega, \mathbf{R}) d\omega \mathbf{n} ds \left[\oint_S \int_0^{+\infty} I_\alpha(\omega, \mathbf{R}) d\omega \mathbf{n} ds \right]^{-1}, \quad \alpha = \text{in, out}, \quad (1)$$

where ds is the vector element normal to the surface S and \mathbf{n} is the unit Poynting vector at a given point on the surface S . It can be shown without any restrictions on the radiation intensity and geometry that the frequency shift of the output radiation $\langle \omega^2 \rangle_{\text{out}}$ relative to the incident one, $\langle \omega^2 \rangle_{\text{in}} = \omega_0^2$, has the form [9, 13]

$$\begin{aligned} \langle \omega^2 \rangle_{\text{out}} - \omega_0^2 = & \frac{1}{\varepsilon_{\text{out}}} \left\{ \int_V d^3 \mathbf{r} \int_{-\infty}^{+\infty} dt \left[\omega_0^2 \mathbf{E} \cdot \mathbf{j} - \frac{\partial \mathbf{E}}{\partial t} \cdot \frac{\partial \mathbf{j}}{\partial t} \right] + \frac{1}{8\pi} \int_V d^3 \mathbf{r} \right. \\ & \times \left. \left[\omega_0^2 (\mathbf{E}^2 + \mathbf{B}^2) - \left(\left(\frac{\partial \mathbf{E}}{\partial t} \right)^2 + \left(\frac{\partial \mathbf{B}}{\partial t} \right)^2 \right) \right] \Big|_{t=-\infty}^{t=+\infty} \right\}, \end{aligned} \quad (2)$$

where $f|_{t=-\infty}^{t=+\infty} \equiv f(t = +\infty) - f(t = -\infty)$, \mathbf{E} (\mathbf{B}) and \mathbf{j} are the electric (magnetic) field and the current in the medium of volume V , respectively, ε_{in} is the energy of incident radiation and ε_{out} is the energy of radiation coming out of the volume V . The zero-frequency moment of Maxwell equations gives the energy conservation law for ε_{in} and ε_{out} :

$$\varepsilon_{\text{out}} = \varepsilon_{\text{in}} - \int_V d^3 \mathbf{r} \int_{-\infty}^{+\infty} dt \mathbf{E} \cdot \mathbf{j} - \frac{1}{8\pi} \int_V d^3 \mathbf{r} (\mathbf{E}^2 + \mathbf{B}^2) \Big|_{t=-\infty}^{t=+\infty}. \quad (3)$$

The first integral term in (2) describes in particular a blue frequency shift due to optical field ionization (OFI), while the last summands in (2) and (3) account for the plasma wave existing after the laser pulse. When the peak pulse intensity is much higher than the one corresponding to the optical ionization threshold, ionization and wakefield generation are separated in space and time. In this case, it can be shown that the total frequency shift due to both processes is the sum of the shift $\delta\omega_{\text{ion}}$ due to ionization and the shift $\delta\omega_{\text{wf}}$ associated with wakefield generation:

$$\frac{\delta\omega}{\omega_0} = \frac{\langle \omega^2 \rangle_{\text{out}} - \omega_0^2}{2\omega_0^2} \cong \frac{\delta\omega_{\text{ion}}}{\omega_0} + \frac{\delta\omega_{\text{wf}}}{\omega_0}, \quad (4)$$

where, in accordance with (2), the shift due to plasma wake generation is determined from the energy of the wake electric field, E_p , excited in the plasma [10]:

$$\frac{\delta\omega_{\text{wf}}}{\omega_0} \cong -\frac{1}{\varepsilon_{\text{out}}} \frac{1}{16\pi} \int_V \mathbf{E}_p^2 dV. \quad (5)$$

Assuming that the pulse intensity distribution is cylindrically symmetric with a characteristic radius larger than the plasma skin depth $k_p^{-1} = c/\omega_p$ (where c is the speed of light and $\omega_p = \sqrt{4\pi e^2 n_0/m}$ is the electron plasma frequency, where e , m and n_0 are the electron charge,

mass and background plasma density), the plasma wakefields can be found with the help of the equation for the wakefield potential, Φ , [14]

$$\left\{ \left(\Delta_{\perp} - k_p^2 \right) \frac{\partial^2}{\partial \xi^2} - \frac{\partial \ln n_0}{\partial r} \frac{\partial^3}{\partial r \partial \xi^2} + k_p^2 \Delta_{\perp} \right\} \Phi - \frac{k_p^4}{2} \left[1 - \frac{1 + |\mathbf{a}|^2 / 2}{(\Phi + \delta \Phi_S)^2} \right] = \frac{k_p^2}{4} \Delta_{\perp} |\mathbf{a}|^2, \quad (6)$$

where $\Delta_{\perp} = (1/r) \partial/\partial r (r \partial/\partial r)$ is the transverse part of the Laplace operator, $\xi = z - ct$, $\mathbf{a}(\xi, z, r) = e \mathbf{E}_L / (mc\omega_0)$ is the normalized complex envelope of the laser field, related to the high-frequency laser field by

$$\tilde{\mathbf{E}}_L(\mathbf{r}, t) = \text{Re} \{ \mathbf{E}_L(\xi, z, r) \exp(i k_0 \xi) \}, \quad (7)$$

where $k_0 = \omega_0/c = 2\pi/\lambda_0$ is the vacuum laser wave vector and $\delta \Phi_S$ describes the effect of OFI on wakefield generation [14]. In the weakly relativistic approximation ($|\mathbf{a}| \ll 1$, $|\delta \Phi| \equiv |\Phi - 1| \ll 1$), assuming that the contribution due to ionization is negligible, and for the background plasma density n_0 uniform in space (or weakly inhomogeneous over lengths of the order of k_p^{-1}), the equation for the potential derived from (6) is

$$\left(\frac{\partial^2}{\partial \xi^2} + k_p^2 \right) \delta \Phi = \frac{1}{4} |\mathbf{a}|^2. \quad (8)$$

With the help of $\partial \Phi / \partial \xi = e E_{p,z} / m_e c^2$ and $\partial \Phi / \partial r \cong e E_{p,r} / m_e c^2$, equation (8) yields the wakefield amplitude \mathbf{E}_p [10]:

$$\mathbf{E}_{p,\max}^2 = \frac{m^2 c^2 \omega_p^2}{e^2} \frac{1}{16} \left\{ k_p^2 \left| \int_{-\infty}^{\infty} d\xi e^{-ik_p \xi} |\mathbf{a}|^2 \right|^2 + \left| \frac{\partial}{\partial r} \int_{-\infty}^{\infty} d\xi e^{-ik_p \xi} |\mathbf{a}|^2 \right|^2 \right\}. \quad (9)$$

An expression similar to (9) was obtained for the electron density perturbations in [15] (see also [2]).

In order to obtain an analytical expression for the frequency shift of (5), a simplified expression for the laser pulse envelope is used in (9), where the reciprocal effect of the wakefield plasma wave on pulse propagation is neglected. Let us consider a Gaussian laser pulse focused at the capillary entrance, $z = 0$, as

$$\mathbf{a}(\xi, r, z = 0) = a_0 \exp \left[-\frac{r^2}{r_0^2} - \frac{(\xi - \xi_0)^2}{c^2 \tau^2} \right], \quad (10)$$

where $a_0 \cong 0.86 \times 10^{-9} (I_0 [\text{W cm}^{-2}])^{1/2} \lambda_0 [\mu\text{m}]$ is the normalized laser pulse amplitude (I_0 is the laser peak intensity). When the focal spot size of the laser pulse r_0 is matched to the inner radius of the capillary tube, R_{cap} , i.e. when $r_0 \cong 0.65 R_{\text{cap}}$, about 98% of the incident energy is transferred to the fundamental capillary mode, which can be described as [8, 14, 16,]

$$|\mathbf{a}(\xi, z, r)|^2 = |a_0|^2 \exp \left(-2\delta k''_{z1} z - 2 \frac{(\xi - \xi_0)^2}{c^2 \tau^2} \right) J_0^2 \left(b_1 \frac{r}{R_{\text{cap}}} \right), \quad (11)$$

where $b_1 \cong 2.405$ is the first root of $J_0(x) = 0$, J_0 is the Bessel function of integer order 0 and $\delta k''_{z1}$ is the damping coefficient associated to the loss of energy by refraction through the capillary wall with dielectric constant ε_w :

$$\delta k''_{z1} = \frac{b_1^2}{2k_0^2 R_{\text{cap}}^3} \frac{1 + \varepsilon_w}{\sqrt{\varepsilon_w - 1}}.$$

Using (11) and (9) in (5), the frequency shift as a function of the laser pulse propagation distance z can be written as

$$\frac{\delta\omega_{wf}(z)}{\omega_0} = -\frac{1}{64}\sqrt{\frac{\pi}{2}} \left(C_1 + \frac{C_2}{k_p^2 R_{cap}^2} \right) \left(\frac{\omega_p}{\omega_0} \right)^2 |a_0|^2 D(\Omega) \frac{k_p}{\delta k_{z1}''} [1 - \exp(-4\delta k_{z1}'' z)], \quad (12)$$

where the constants C_1 and C_2 are determined by the radial laser intensity distribution for the fundamental mode

$$C_1 \equiv \int_0^{b_1} x J_0^4(x) dx \left(\int_0^{b_1} x J_0^2(x) dx \right)^{-1} \cong 0.5655,$$

$$C_2 \equiv 4b_1^2 \int_0^{b_1} x J_0^2(x) J_1^2(x) dx \left(\int_0^{b_1} x J_0^2(x) dx \right)^{-1} \cong 4.361,$$

and the function $D(\Omega) = \Omega \exp(-\Omega^2/4)$, with $\Omega = \omega_p \tau$, reflects the resonant behavior of wakefield generation, depending on the laser pulse duration with Gaussian time envelope in (11). Note that for a small energy loss by refraction through the capillary wall, when $\delta k_{z1}'' z \ll 1$, the frequency shift (12) grows linearly with the capillary length z .

In the following sections, the analytical prediction for the frequency shift due to wakefield generation of (12) will be compared with the results of fully self-consistent modeling, including gas ionization and nonlinear multi-mode laser pulse propagation in a capillary tube.

3. Modeling results and comparison with analytical predictions

To describe nonlinear laser pulse propagation in a gas-filled capillary, the following wave equation for the pulse envelope was used [14]

$$\left\{ 2ik_0 \frac{\partial}{\partial z} + 2 \frac{\partial^2}{\partial z \partial \xi} + \Delta_\perp \right\} a = k_0^2 \left(\frac{n}{n_c \gamma} a - iG^{(ion)} \right), \quad (13)$$

where n is the slowly varying electron density, $n_c = m\omega_0^2/(4\pi e^2)$ is the critical density for the laser frequency ω_0 , $\gamma = [1 + (\mathbf{p}/mc^2 + |\mathbf{a}|^2/2)]^{1/2}$ is the relativistic factor of plasma electrons with momentum \mathbf{p} slowly varying in time and the last term on the right-hand side of (13) is the normalized ionization current, which represents the laser energy losses in the process of OFI [17]. In the quasi-static approximation [18], the relativistic plasma response n/γ can be expressed through a single scalar function, the potential Φ determined by (6) [14]:

$$\frac{n}{\gamma} = n_0 \frac{1 + k_p^{-2} \Delta_\perp \Phi}{\Phi + \delta \Phi_S}. \quad (14)$$

When the laser pulse propagates in ionizing gas, equations (13), (14) and (6) should be supplemented with the equations for ionization kinetics, which determine the electron density $n_0(\mathbf{r}, \xi)$ produced by OFI [14, 17, 19]

$$\frac{\partial n_0}{\partial \xi} = -\frac{1}{c} \sum_{k=0}^{Z_n-1} \bar{W}_k N_k, \quad (15)$$

where N_k and \bar{W}_k are the averages over the laser period of the ion densities and probabilities of tunneling ionization of ions [20] with charge state k , $k = 0, 1, \dots, Z_n$ and Z_n is the atomic charge number.

For the numerical modeling of laser pulse propagation and wakefield generation inside a gas-filled capillary tube by (6) and (13), boundary conditions have to be supplied. For linearly polarized laser pulses, the following boundary condition at the capillary tube wall, $r = R_{\text{cap}}$, is used:

$$\frac{\partial a}{\partial r} = 2ik_0 \frac{(\varepsilon_w - 1)^{1/2}}{\varepsilon_w + 1} \left(1 - \frac{i}{k_0} \frac{\partial}{\partial \xi} \right) a, \quad (16)$$

which describes correctly the structure of eigenmodes and their damping due to the energy loss through the capillary walls (see [14, 16]). The boundary conditions for the wakefield potential are $\Phi = 1$ in the unperturbed gas in front of the laser pulse, $\xi \rightarrow +\infty$, and at the capillary wall $r = R_{\text{cap}}$.

Taking into account (7), the mean-square frequency, defined by (1), at a distance z in the capillary is expressed using the laser envelope as follows:

$$\langle \omega^2 \rangle(z) \equiv \left(\int_{-\infty}^{\infty} \int_0^{R_{\text{cap}}} |a(\omega, r, z)|^2 r dr d\omega \right)^{-1} \int_{-\infty}^{\infty} (\omega + \omega_0)^2 \int_0^{R_{\text{cap}}} |a(\omega, r, z)|^2 r dr d\omega, \quad (17)$$

where $a(\omega, r, z)$ is the dimensionless laser pulse envelope in Fourier space. The corresponding frequency shift is defined as

$$\delta\omega(z) = \frac{\langle \omega^2 \rangle(z) - \omega_0^2}{2\omega_0}. \quad (18)$$

The solution to the system of equations (13)–(16) and (6) permits us to also obtain the normalized spectrum of the propagating laser field, centered at the carrier frequency ω_0 , integrated over the transverse cross section:

$$I(\omega + \omega_0, z) \equiv \left(\max_{\omega} \int_0^{R_{\text{cap}}} |a(\omega, r, z)|^2 r dr \right)^{-1} \int_0^{R_{\text{cap}}} |a(\omega, r, z)|^2 r dr. \quad (19)$$

This solution and spectrum (19) will be analyzed below and the resulting frequency shift given by (18) will be compared with the analytical expression (12), and to the experimental results in section 5. In order to compare with the experimental results, it is useful to define the relative wavelength shift. For a mean-square frequency shift $\delta\omega$ small compared with ω_0 , determined by (1), (4) and (17), (18), the relative wavelength shift and the relative frequency shift are of opposite signs:

$$\frac{\Delta\lambda z}{\lambda_0} \equiv \left[\frac{1}{\Delta\omega(z)/\omega_0 + 1} - 1 \right] \cong -\frac{\Delta\omega(z)}{\omega_0} \cong -\frac{\delta\omega(z)}{\omega_0}, \quad (20)$$

where

$$\Delta\lambda(z) \equiv \left(\int_0^{\infty} I(\lambda, z) d\lambda \right)^{-1} \int_0^{\infty} \lambda I(\lambda, z) d\lambda - \lambda_0 \quad (21)$$

and $\Delta\omega(z) \equiv (\int_0^{\infty} I(\omega, z) d\omega)^{-1} \int_0^{\infty} \omega I(\omega, z) d\omega - \omega_0$ are the averaged wavelength and frequency shifts and $I(\lambda, z)$ and $I(\omega, z)$ are the spectral intensity, averaged over the radius, as functions of wavelength and frequency, respectively.

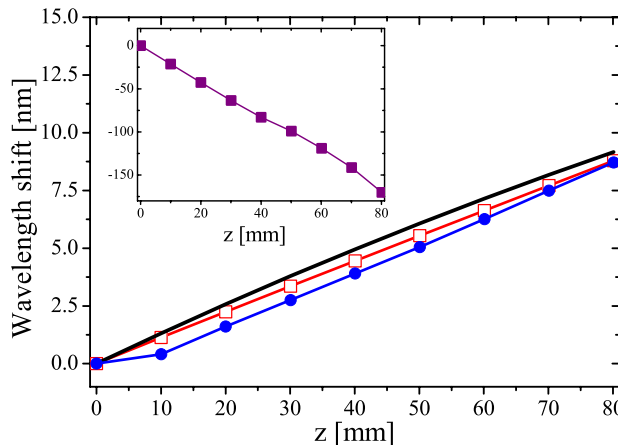


Figure 1. Wavelength shift calculated with (12), the solid line (not marked), and obtained in simulations as functions of the laser propagation distance in a capillary filled with 20 mbar of hydrogen; lines with markers: OFI included (dots) and pre-ionized plasma (open squares). The inset shows the wavelength shift for the same parameters but in a capillary filled with helium. Parameters are indicated in the text.

The results of self-consistent modeling by (13)–(16) and (6) are illustrated in figures 1–4 for quasi-monomode laser pulse propagation, when the Gaussian laser pulse of (10) is focused at the entrance of a capillary of radius $R_{\text{cap}} = 50 \mu\text{m}$, with the matched spot size $r_0 = 0.67R_{\text{cap}} = 33.5 \mu\text{m}$ and $a_0 = 0.24$; for a full-width at half-maximum (FWHM) pulse duration $\tau_{\text{FWHM}} = \sqrt{2 \ln 2} \tau = 51 \text{ fs}$ and $\lambda_0 = 0.8 \mu\text{m}$, it corresponds to a laser pulse energy of 0.12 J and an intensity $I_0 = 1.3 \times 10^{17} \text{ W cm}^{-2}$.

The red wavelength shift (20) due to wakefield generation in a capillary filled with hydrogen at a pressure of 20 mbar is shown in figure 1 by lines with markers for OFI included (marked by dots) and for a pre-ionized plasma (marked by open squares). The corresponding spectra are shown in figure 2. They are in good agreement with the analytical prediction from (12) shown in figure 1 by a solid line (not marked). At this laser pulse intensity, well above the threshold value for the OFI of hydrogen gas, the laser pulse propagates in the capillary in the quasi-monomode regime over a few centimeters without substantial distortions and visible influence of ionization to the laser spectrum.

For the same parameters, when the capillary is filled with helium (with an atomic density half that of hydrogen in order to get the same free electron density at full ionization), the wavelength shift is determined completely by OFI: it is blue (negative) and of much larger amplitude than the red shift in hydrogen, as seen in the inset of figure 1 and in figure 2 for the lines marked by solid squares. Note that the integral wavelength shift (see (17), (18) and (20)) is determined not only by the shift of the maximum of the spectrum, but also by the ‘blue tail’ of the spectrum, not seen completely in figure 2 and extending in this case up to 400 nm. The laser pulse and the wakefield generated in the capillary filled with helium reveal in this case

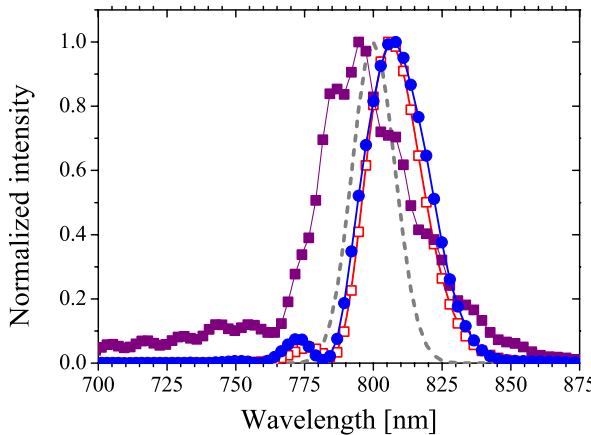


Figure 2. Spectra of transmitted laser pulses integrated over the radius obtained in simulations after propagation over a length of 70 mm in a capillary filled with 20 mbar of hydrogen: OFI included (marked by dots) and pre-ionized plasma (open squares); the same for capillary filled with helium, the line is marked by solid squares. The dashed line shows the spectrum at the capillary entrance. Parameters are the same as in figure 1.

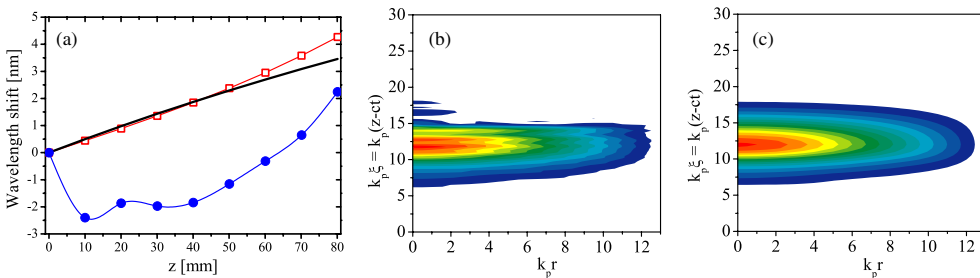


Figure 3. (a) Wavelength shift calculated with (12), unmarked solid line, and obtained in simulations as functions of the laser propagation distance in a capillary filled with 40 mbar of hydrogen, for $\varepsilon_L = 50 \text{ mJ}$: OFI included (marked by dots) and pre-ionized plasma (open squares). (b) Normalized laser pulse envelope $|a(r, \xi)|$ after propagating in a capillary of 50 mm long filled with 40 mbar of hydrogen (OFI included). All parameters are the same as in (a). (c) The same as in (b), but in pre-ionized plasma.

a pronounced longitudinal and radial modulation caused by the variation of electron density produced self-consistently by the OFI of helium [14, 21].

For higher gas pressure and lower laser pulse intensities, gas ionization starts to play a substantial role in the laser pulse spectrum modification even for capillaries filled with hydrogen. As an example, figure 3(a) shows the wavelength shifts for a capillary filled with

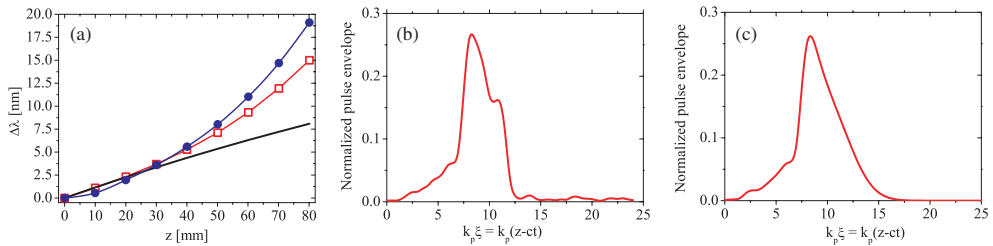


Figure 4. (a) The same as in figure 3(a) for a capillary filled with 40 mbar of hydrogen and laser pulse intensity $I_0 = 1.3 \times 10^{17} \text{ W cm}^{-2}$ and an energy of 0.12 J. (b) Normalized laser pulse envelope $a(r = 0, \xi)$ on the axis at a distance of 70 mm with OFI included. All parameters are the same as in (a). (c) The same as in (b), but in pre-ionized plasma.

40 mbar of hydrogen, a laser pulse energy of 50 mJ, and intensity $I_0 = 0.54 \times 10^{17} \text{ W cm}^{-2}$. All other parameters are the same as for figure 1. Ionization dominates the spectrum modification and leads to a net blue shift for capillary lengths smaller than 70 mm. The shift due to ionization is partly compensated by the shift due to wakefield, whose amplitude increases with pressure and capillary length as nonlinear effects modify the pulse shape. Note that the laser pulse intensity in this case is still well above the threshold value for the OFI of hydrogen (of the order of $10^{14} \text{ W cm}^{-2}$), but the OFI contributes substantially to the laser pulse dynamic and spectrum modification. Figures 3(b) and (c) exhibit the amplitude of the normalized laser pulse envelope $|a(r, \xi)|$ at a distance $z = 50$ mm for the same parameters as figure 3(a). In figure 3(b), where ionization is included, the front of the pulse at $k_p\xi \simeq 17$ is eroded due to refraction-induced ionization [21]. At the same time, there is no significant influence of the nonlinearity of pre-ionized plasma on the pulse propagation, as seen in figures 3(a) and (c).

For the same pressure of hydrogen (40 mbar), but higher laser intensity, $I_0 = 1.3 \times 10^{17} \text{ W cm}^{-2}$, the plasma nonlinearity starts to play a substantial role in the pulse dynamics and transmitted laser spectrum, as illustrated in figure 4.

Comparison of figures 4(b) and (c) shows that the OFI of gas leads to the shortening and sharpening of the front of the pulse [21]; in addition, the self-phase modulation and nonlinear group velocity dispersion in the plasma causes a sharpening of the pulse tail just after the intensity maximum [22] (see figure 4(b)). Both these effects lead to pulse shortening that increases the wakefield generation [14, 23] and the subsequent red wavelength shift, as seen in figure 4(a), as the initial pulse length for this pressure was about twice as long as the linear resonant one.

4. Experimental arrangement

An experiment was performed using the multi-TW Ti:sapphire laser system at the Lund Laser Centre, which provided up to 0.5 J energy pulses onto the target, with an FWHM pulse duration of 40 ± 5 fs at a central wavelength of $\lambda_0 = 786$ nm. The experimental setup scheme is presented in figure 5. The 30 mm-diameter laser beam was focused with an $f = 1.5$ m spherical mirror

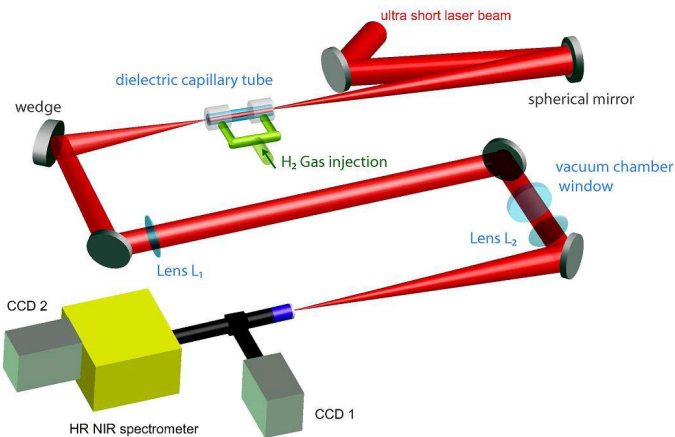


Figure 5. Schematic view of the experimental setup. All the elements up to the vacuum chamber window were under vacuum.

at the entrance of a capillary tube. In order to correct the aberrations of the phase front, a deformable mirror was used after the compressor. The laser beam transmitted through the capillary tube was attenuated by reflecting it from a glass wedge and then collimated by an achromatic $f_1 = 1$ m lens (L_1), which could be translated in vacuum along the beam axis to collect light either from the focal plane (i.e. with the capillary tube removed) or from the exit plane of the tube. The beam was then focused by an $f_2 = 1$ m achromatic lens (L_2) and magnified 10 \times by a microscope objective. The beam was split into two parts. Focal spot or capillary tube output images were recorded by a 16-bit charged-couple device (CCD 1 in figure 5). The transmitted part was sent to a visible-to-near-infrared imaging spectrometer equipped with a 16-bit CCD camera (CCD 2 in figure 5). The spectral resolution was 0.1 nm. The laser beam path up to the vacuum chamber window was under vacuum. Glass capillary tubes with inner radius $R_{\text{cap}} = 50 \pm 1 \mu\text{m}$ and length varying between 1.2 and 8.1 cm were used. Hydrogen gas (H_2) was injected into the tubes through two thin ($\cong 100 \mu\text{m}$) slits located between 2.5 and 5 mm from each end of the tube. The filling pressure was varied between 0 and 80 mbar. Each capillary tube could be used for at least a hundred laser shots, when the laser beam remained well centered at the capillary entrance. Pointing variations due to thermal drifts and mechanical vibrations were therefore minimized or compensated for. Laser guiding at input intensities up to $10^{18} \text{ W cm}^{-2}$ was achieved with more than 90% energy transmission in evacuated or hydrogen-filled gas tubes up to 8 cm long.

For the data presented here, in order to investigate the moderately nonlinear regime, the input intensity was kept lower than $3 \times 10^{17} \text{ W cm}^{-2}$. The laser pulse duration was $\tau_0 = 45 \pm 5 \text{ fs}$ and the associated bandwidth was approximately 25 nm (FWHM); each pulse had a small negative linear chirp, i.e. short wavelengths preceded longer wavelengths. The energy distribution in the focal plane exhibited an Airy-like pattern with a radius at first minimum of $r_0 = 40 \pm 5 \mu\text{m}$.

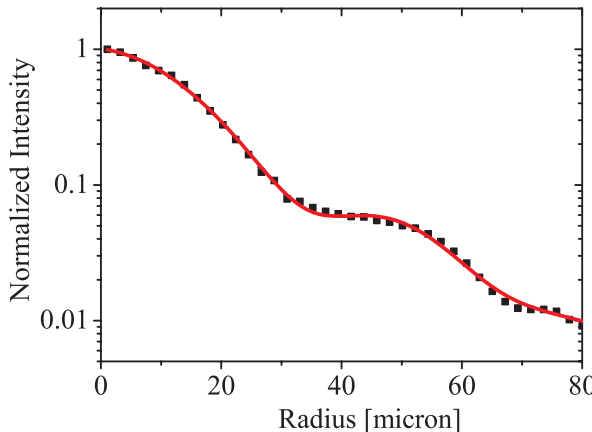


Figure 6. Normalized laser intensity distribution averaged over the azimuthal angle measured in the experiment (squares) and its multi-picks approximation used in simulations (the solid line).

5. Comparison between modeling results and experimental data

To model wakefield generation and laser pulse spectrum modifications with initial conditions as close as possible to the experimental ones, the measured radial laser intensity distribution was approximated by a radial profile averaged over the azimuthal angle as shown in figure 6. This approximation was used for all the modeling results shown below. In the simulations, the FWHM laser pulse duration was 51 fs with a linear negative chirp of -550 fs^2 , which corresponds to the experimentally measured laser spectrum width at the focal plane in vacuum.

Figure 7 shows the wavelength shift (21) measured in the experiment (squares with error bars) and obtained in the modeling (line with circles) for the experimentally measured radial distribution of laser intensity at the capillary entrance as a function of the laser pulse energy for a 7 cm-long capillary filled with hydrogen molecular gas at a pressure of 40 mbar. The dashed line is the analytical prediction (12) with the on-axis laser pulse amplitude adjusted so that the laser pulse energy in the main mode (11) equals the experimental measurement. The measured and modeled red wavelength shifts are in a good agreement in all the energy range shown in figure 7 and they are larger than the linear analytical prediction (12). At this gas pressure, above the linear resonant one equal to 25 mbar, and for laser pulse energies higher than 100 mJ, both ionization and nonlinear group velocity dispersion are responsible for the laser pulse shortening and consequently are more effective for wakefield generation as shown in figure 4. For energies lower than 100 mJ, the sharpening of the front edge of the pulse due to ionization is combined with the transverse modification of the structure of the laser pulse guided in the capillary; the use of the non-Gaussian distribution of figure 6 at the entrance thus induces a larger wavelength shift. This can be seen by comparison with figure 3(a) where the wavelength shift obtained for an initially Gaussian pulse in transverse direction is almost zero at 70 mm, whereas in figure 7 it is of the order of 7 nm for 50 mJ.

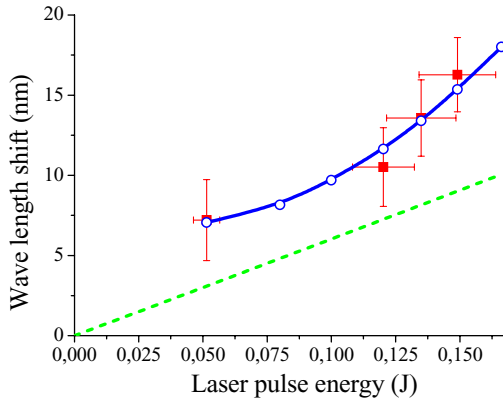


Figure 7. Wavelength shift measured in the experiment (squares with error bars) and obtained in the modeling (line with circles) as functions of the laser pulse energy for a 70 mm-long capillary filled with hydrogen gas at a pressure of 40 mbar. The dashed line is the analytical prediction (12).

The agreement between modeled and measured red shifts observed in figure 7 is supported by the agreement achieved for the transmitted laser pulse spectra shown in figure 8 for laser pulse energies 50, 120 and 150 mJ measured for different shots (black and gray solid lines in figures 8(a) and (c)) and obtained in full-scale modeling (dashed lines). The blue solid line in figure 8(b) shows a spectrum averaged over four shots. This shows that not only the pulse broadening but also the growth of the amplitude of the modulations can be reproduced by the simulations when the energy is increased.

The wavelength shifts as functions of pressure for different lengths of a capillary are shown in figure 9 at a laser pulse energy 120 mJ. For short, 12 mm-long capillaries the measured, modeled and analytically predicted shifts are close to zero as the ionization blue shift roughly cancels the wakefield red shift as can be seen for 20 mbar in figure 1(a). For longer capillaries, when wakefield generation has a substantial effect on the transmitted laser spectra, the measured and modeled dependences shown in figures 9(b)–(d) closely follow analytical predictions up to a pressure of the order of 25 mbar, which corresponds to the value determined by the linear resonant condition for the wakefield generation, $\omega_p \tau = 2$, for the Gaussian time envelope (10).

For higher pressures, in excess of 40 mbar and for capillaries longer than 50 mm, the measured and modeled red shifts grow with increasing pressure as opposed to the drop in the analytical behavior caused by the departure from the resonance between the laser pulse length and plasma wavelength (see figure 9, dashed lines). An increase of the wakefield generation and corresponding red wavelength shift for pressures higher than that determined by the linear resonant condition is caused by nonlinear laser pulse shortening. For monomode laser pulse propagation and 70 mm capillary length, this process is illustrated in figure 4(a) for a hydrogen pressure of 40 mbar. For the radial distribution of figure 6 and for higher pressure, the propagation in the capillary is multi-mode, leading to a more important pulse shortening as shown in figure 10 for the capillary length 71 mm and pressure 60 mbar (see also [24]). However, it should be noted that even for this strong nonlinear modification of the laser pulse,

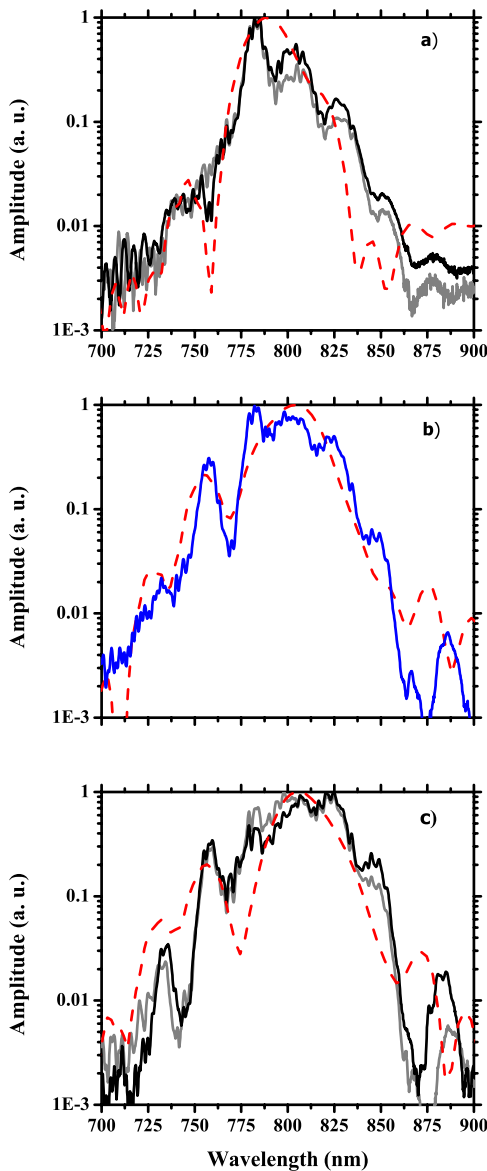


Figure 8. Laser pulse spectra for pulse energies 50 (a), 120 (b) and 150 mJ (c) measured in the experiment (solid lines are for different shots in (a) and (c) and the average of 4 shots is shown in (b)) and obtained in simulations (dashed lines). Parameters are indicated in the text.

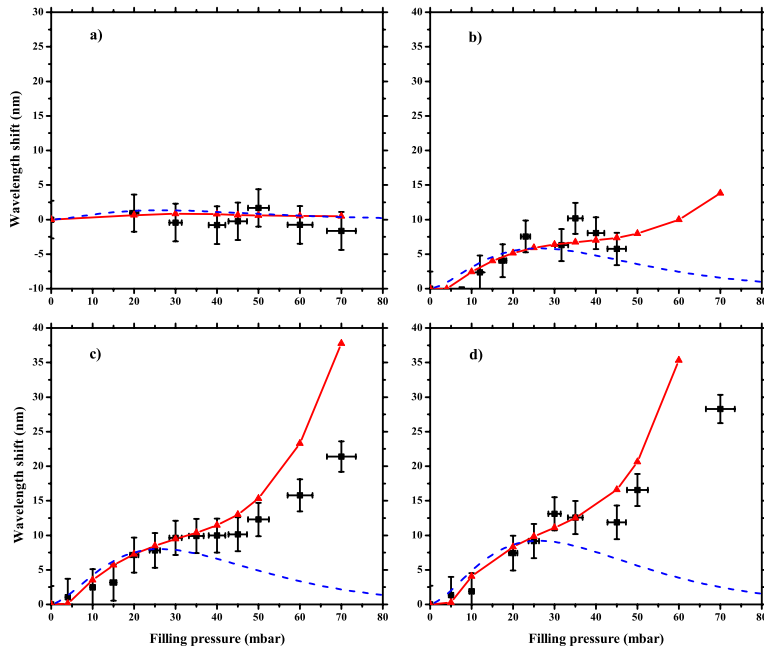


Figure 9. Wavelength shifts as functions of pressure at a laser pulse energy of 120 mJ for different lengths of capillary $L_{\text{cap}} = 12$ (a); 50 (b); 71 (c) and 81 mm (d). Squares with error bars are experimentally measured values, solid lines are the results of modeling and dashed lines are for analytical prediction (12).

the wakefield generated along the capillary tube is very regular as can be seen in figure 10(c), where the radial distribution of the wakefield potential as a function of the local time in the co-moving frame (moving with the speed of light) is shown by the color map. The zero of the local time corresponds to the time when the laser pulse maximum reaches the capillary entrance, see figure 10(a). The increasing deviations of the modeled red shift from the one measured as the pressure and the capillary length are increased (see figure 9) are attributed to the asymmetry of the focal spot in the experiment, whereas cylindrical symmetry, assumed in the model, leads to more pronounced nonlinear effects.

Figure 11 shows the wavelength shifts as functions of the length of the capillary filled with hydrogen gas, measured in the experiment and obtained in the modeling for pressures of 20 and 40 mbar and a laser pulse energy of 120 mJ. The wavelength shift grows linear as a function of length for the 20 mbar case, in agreement with analytical prediction (12). The fit of experimental data by simulation results demonstrates that the plasma wave is excited over a length as long as 8 cm. As the pressure is increased, the nonlinear laser pulse evolution is amplified with the propagation length leading to larger plasma wave amplitude.

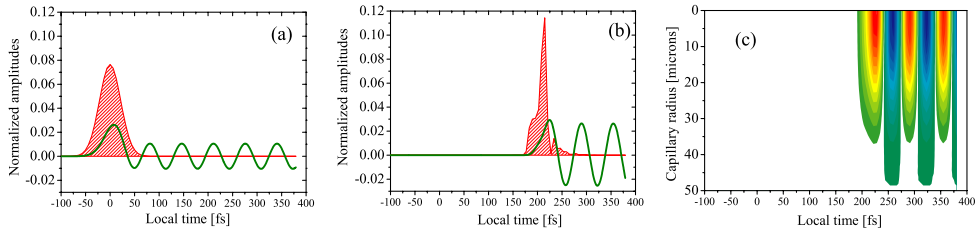


Figure 10. Normalized laser pulse intensity (the hatched area) and wakefield potential (the solid line) on the axis at the entrance (a) and after propagation in a capillary of length 71 mm (b), as functions of the local time; radial distribution of the wakefield potential in time (c). Parameters of modeling correspond to figure 9(c) at pressure 60 mbar.

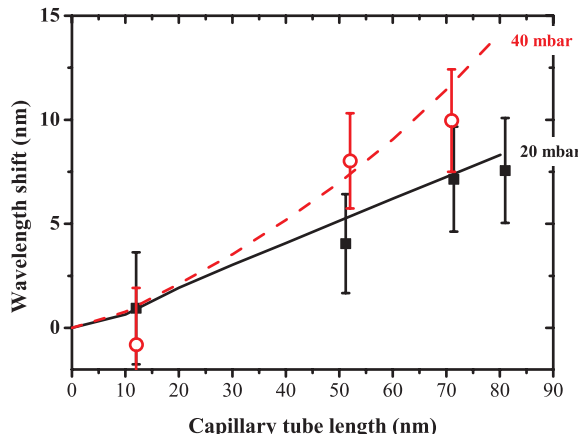


Figure 11. Wavelength shifts as functions of the length of capillary filled with 20 mbar of hydrogen gas measured in the experiment (solid squares with error bars) and obtained in the modelling (solid line); open circles with error bars and dashed line are for a pressure of 40 mbar. Laser pulse energy is 120 mJ.

6. Conclusion

Analytical predictions of the laser pulse frequency red shift based on the general approach of the frequency momentum theory formulated without any restrictions on the radiation intensity and geometry were used to analyze the wakefield generated by a short intense laser pulse propagating in a gas-filled capillary tube. The full-scale self-consistent modeling completely confirms the results obtained analytically in the following conditions: monomode propagation of the laser pulse, in a moderately nonlinear regime, with intensities much higher than the threshold value for the OFI of hydrogen filling the capillary, and gas pressures lower than the value determined by the linear resonant condition for wakefield generation. For higher pressures and laser pulse energies, modeling results exhibit nonlinear pulse shortening, enhanced wakefield

generation and frequency red shift closely fitting experimental results. Even for intensities much higher than the threshold value for the OFI of filling gas, ionization-induced refraction can substantially modify the laser pulse, and the influence of ionization is more pronounced for higher pressures and lower pulse energies.

The agreement between modeled and measured red shifts observed as functions of pulse energy, pressure of hydrogen gas filling the capillary and capillary length is supported by the agreement achieved for the transmitted laser pulse spectra obtained in simulations and experiment. The value of the longitudinal accelerating field in the plasma obtained from the simulation is in the range $1\text{--}10 \text{ GV m}^{-1}$. The average product of gradient and length achieved in this experiment is of the order of 0.4 GV at a pressure of 50 mbar; it could be increased to several GV by extending the length and diameter of the capillary tube with higher laser energy.

In conclusion, the outgoing spectra of driving laser pulses measured after propagation in gas-filled capillaries supported by relevant modeling can provide detailed information on laser pulse dynamics and on the main characteristics of the accelerating fields excited in the wake of the laser pulses over the long distances necessary for efficient acceleration of electrons to high energies.

Acknowledgments

This work was supported in part by the Programs on fundamental research of the Russian Academy of Sciences, by the Russian Foundation for Basic Research—CNRS PICS program (grant 07-02-92160), and by the European Community—New and Emerging Science and Technology Activity under the FP6 ‘Structuring the European Research Area’ programme (project EuroLEAP, contract 028514). This work was also supported by the Marie Curie Early Stage Training Site MAXLAS (MEST-CT-2005-020356), the Swedish Research Council and the Knut and Alice Wallenberg Foundation.

References

- [1] Tajima T and Dawson J 1979 *Phys. Rev. Lett.* **43** 267
- [2] Gorbonov L M and Kirsanov V I 1987 *Sov. Phys.—JETP* **66** 290
- [3] Esarey E, Sprangle P, Krall J and Ting A 1996 *IEEE Trans. Plasma Sci.* **24** 252
- [4] Marques J R *et al* 1996 *Phys. Rev. Lett.* **76** 3566
Siders C W *et al* 1996 *Phys. Rev. Lett.* **76** 3570
- [5] Le Blanc S P, Gaul E W, Matlis N H, Rundquist A and Downer M C 2000 *Opt. Lett.* **25** 764
- [6] Dias J M, Silva L O and Mendonca J T 1998 *Phys. Rev. ST Accel. Beams* **1** 031301
- [7] Wilks S C, Dawson J M, Mori W B, Katsouleas T and Jones M E 1989 *Phys. Rev. Lett.* **62** 2600
Esarey E, Ting A and Sprangle P 1990 *Phys. Rev.* **42** 3526–31
- [8] Andreev N E, Chegotov M V, Cros B, Mora P and Vieux G 2006 *Phys. Plasmas* **13** 053109
- [9] Andreev N E, Fortov V E and Chegotov M V 2003 Spectral analysis of the ultrafast processes by the interaction of short laser pulses with matter *Physics of Extreme States of Matter* ed V E Fortov *et al* (Chernogolovka: Institute of Problems of Chemical Physics RAS) p 11
Chetogov M V 2004 *Proc. Scientific Session of Moscow Institute of Engineering Physics* MIFI-2004 p 163
- [10] Andreev N E and Chegotov M V 2005 *J. Exp. Theor. Phys.* **101** 56–63
- [11] Murphy C D *et al* 2006 *Phys. Plasmas* **13** 033108
- [12] Wojda F *et al* 2009 *Phys. Rev.* **80** 066403

- [13] Chegotov M V 2002 *Tech. Phys.* **47** 1002
Chegotov M V 2003 *Quantum Electron.* **33** 370–6
- [14] Andreev N E, Nishida Y and Yugami N 2002 *Phys. Rev. E* **65** 056407
Andreev N E, Cros B, Gorbunov L M, Matthieussent G, Mora P and Ramazashvili R R 2002 *Phys. Plasmas* **9** 3999–4009
- [15] Leemans W, Siders C W, Esarey E, Andreev N, Shvets G and Mori W B 1996 *IEEE Trans. Plasma Sci.* **24** 331
- [16] Dorchies F *et al* 1999 *Phys. Rev. Lett.* **82** 4655
Courtois C, Couairon A, Cros B, Marque's J R and Matthieussent G 2001 *Phys. Plasmas* **8** 3445
Cros B, Courtois C, Matthieussent G, Di Bernardo A, Batani D, Andreev N and Kuznetsov S 2002 *Phys. Rev. E* **65** 026405
- [17] Andreev N E, Chegotov M V and Veisman M E 2000 *IEEE Trans. Plasma Sci.* **28** 1098
Andreev N E, Veisman M E, Cadjan M G and Chegotov M V 2000 *Plasma Phys. Rep.* **26** 947
- [18] Sprangle P, Esarey E and Ting A 1990 *Phys. Rev. Lett.* **64** 2011
- [19] Kandidov V P, Kosareva O G and Shlenov S A 1994 *Quantum Electron.* **24** 971
- [20] Ammosov M V, Delone N B and Krainov V P 1986 *Sov. Phys.—JETP* **64** 1191
Delone N B and Krainov V P 1998 *Phys.—Usp.* **41** 469
Delone N B and Krainov V P 1998 *Usp. Fiz. Nauk* **168** 531
- [21] Andreev N E, Chegotov M V and Pogosova A A 2003 *J. Exp. Theor. Phys.* **96** 885
- [22] Esarey E, Schroeder C B, Shadwick B A, Wurtele J S and Leemans W P 2000 *Phys. Rev. Lett.* **84** 3081
Hubbard R F, Sprangle P and Hafizi B 2000 *IEEE Trans. Plasma Sci.* **28** 1122
- [23] Andreev N E, Kuznetsov S V, Pogosova A A, Steinhauer L C and Kimura W D 2003 *Phys. Rev. ST Accel. Beams* **6** 041301
Kimura W D *et al* 2005 *IEEE Trans. Plasma Sci.* **33** 3–7
- [24] Skobelev S A, Kulagin D I, Stepanov A N, Kim A V, Sergeev A M and Andreev N E 2009 *JETP Lett.* **89** 540–6

PAPER IV

Laser-plasma electron acceleration in dielectric capillary tubes

G. Genoud, K. Cassou, F. Wojda, H. E. Ferrari, C. Kamperidis, M. Burza, A. Persson, J. Uhlig, S. Kneip, S.P.D. Mangles, A. Lifschitz, B. Cros and C.-G. Wahlström.

Appl. Phys. B, in Press, DOI: 10.1007/s00340-011-4639-4 (2011).

Laser-plasma electron acceleration in dielectric capillary tubes

G. Genoud · K. Cassou · F. Wojda · H.E. Ferrari · C. Kamperidis · M. Burza ·
 A. Persson · J. Uhlig · S. Kneip · S.P.D. Mangles · A. Lifschitz · B. Cros ·
 C.-G. Wahlström

Received: 25 January 2011 / Revised version: 19 April 2011
 © The Author(s) 2011. This article is published with open access at Springerlink.com

Abstract Electron beams and betatron X-ray radiation generated by laser wakefield acceleration in long plasma targets are studied. The targets consist of hydrogen filled dielectric capillary tubes of diameter 150 to 200 microns and length 6 to 20 mm. Electron beams are observed for peak laser intensities as low as $5 \times 10^{17} \text{ W/cm}^2$. It is found that the capillary collects energy outside the main peak of the focal spot and contributes to keep the beam self-focused over a distance longer than in a gas jet of similar density. This enables the pulse to evolve enough to reach the threshold for wavebreaking, and thus trap and accelerate electrons. No electrons were observed for capillaries of large diameter (250 µm), confirming that the capillary influences the interaction and does not have the same behaviour as a gas cell. Finally, X-rays are used as a diagnostic of the interaction

and, in particular, to estimate the position of the electrons trapping point inside the capillary.

1 Introduction

When an intense femtosecond laser pulse interacts with gas, a plasma is formed and the ponderomotive force of the pulse generates a large amplitude plasma wave. This wave can break, trap, and accelerate electrons. The acceleration field can be more than a thousand times higher than those achieved in accelerators based on conventional technology. Laser plasma wakefield accelerators are thus a promising alternative to conventional accelerators, especially because of their compactness and short pulse duration. Quasi-monoenergetic beams of electrons, of hundreds of MeV kinetic energy, have been produced in several experiments [1–5]. The laser pulse can also be externally guided, for example by using either a plasma channel created by a discharge inside a capillary [6] or a dielectric capillary tube. In this article, we discuss the use of gas-filled dielectric capillary tubes to assist guiding and thereby enable wave breaking and self-trapping of electrons at lower laser intensities than required with gas jets, which also have a homogeneous transverse gas profile.

Even when the intensity at the entrance of the plasma is below the threshold for wave-braking and electron trapping, it can be reached through the non-linear evolution of the pulse, undergoing self-focusing and pulse compression. In the experiment reported here, electron beams were observed with peak laser intensities as low as $I = (5 \pm 2) \times 10^{17} \text{ W/cm}^2$ (corresponding to a normalized pulse amplitude $a_0 = 0.5$) for a plasma electron density of the order of 10^{18} cm^{-3} . With such a low intensity, the evolution of

G. Genoud · C. Kamperidis · M. Burza · A. Persson ·
 C.-G. Wahlström (✉)
 Department of Physics, Lund University, P.O. Box 118, 22100
 Lund, Sweden
 e-mail: claes-goran.wahlstrom@fysik.lth.se
 Fax: +46-46-2224250

K. Cassou · F. Wojda · H.E. Ferrari · A. Lifschitz · B. Cros
 Laboratoire Physique Gaz et Plasmas (UMR 8578), Université
 Paris-Sud 11, 91405 Orsay Cedex, France

H.E. Ferrari
 CONICET, Buenos Aires, Argentina

J. Uhlig
 Department of Chemical Physics, Lund University, P.O. Box 124,
 22100 Lund, Sweden

S. Kneip · S.P.D. Mangles
 Blackett Laboratory, Imperial College London, London,
 SW7 2BZ, UK

the laser pulse would not be sufficient over the length typical for a gas jet experiment (a few mm). However, capillary tubes longer than 6 mm provide a distance of interaction long enough to achieve electron trapping and acceleration.

The inside walls of the capillary tubes are smooth at the laser wavelength and the laser pulse is guided by Fresnel reflection on the walls. Ultrashort intense laser pulses propagate using eigenmodes of the capillary tubes [7]. For a Gaussian distribution of energy at the entrance of the capillary, with a waist matched to the capillary radius, more than 98% of the incident energy can be transferred into the fundamental capillary mode, inducing quasi-perfect monomode guiding [8]. This can produce linear plasma waves over several centimetres [9] which could be used as an accelerating structure for injected electrons. The electron density in this type of capillary can be arbitrarily low which is an advantage, as the dephasing length can then be made equal or longer than the capillary tube. Dephasing occurs at the point where the electrons outrun the plasma wave and start decelerating. The dephasing length is given by $L_d = (\omega_0/\omega_p)^2 \lambda_p$, where ω_0 is the laser frequency, $\omega_p = (n_e e^2 / \epsilon_0 m_e)^{1/2}$ the plasma frequency of a plasma of electron density n_e and λ_p the corresponding plasma wavelength. e and m_e are the charge and mass of an electron, respectively. However, when the capillary diameter is too large to match the focal spot, the propagation is not monomode, as higher order modes are then also excited. In the experiment reported here, the focal spot size was deliberately chosen significantly smaller than the tube diameter to allow higher order modes to be excited. This resulted in a regime where external guiding, non-linear pulse evolution and self trapping take place inside the tube.

X-rays can be produced within a wakefield accelerator through a process called betatron oscillations [10]. Transverse fields can cause electrons within the wakefield to oscillate transversely to their acceleration direction and produce X-rays, which have great potential as novel ultra-short radiation sources. Moreover, their observation provides insight into the laser-plasma interaction itself, because their production is directly linked to the trapping and acceleration of electrons. For large amplitude oscillations of electrons, the radiation emitted close to the axis can be shown [11] to have a synchrotron-like spectrum, which is a broadband spectral distribution peaked close to the critical energy $E_c = 3/2\hbar K \gamma^2 \omega_\beta$, with $\gamma m_e c^2$ the electron energy [12]. The betatron frequency $\omega_\beta = \omega_p / \sqrt{2\gamma}$ and the betatron strength parameter $K = \gamma r_\beta \omega_\beta / c$ describe the trajectory of an electron oscillating with an amplitude r_β .

2 Experiment

2.1 Experimental arrangement

The experiment was performed using the 10 Hz multi-terawatt Ti:sapphire laser system at the Lund Laser Centre,

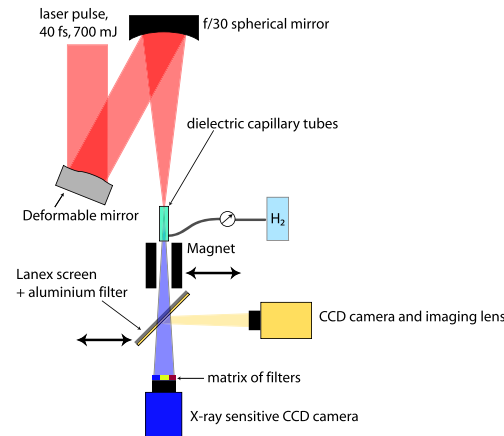


Fig. 1 Schematic view of the experimental setup

which delivered 0.7 J within a focal spot of 50 μm size (radius of the first minimum of an Airy-like pattern) in 40 fs (FWHM) pulse duration at $\lambda_0 = 795 \text{ nm}$ centre wavelength. A schematic view of the experimental arrangement is presented in Fig. 1. The laser pulses were loosely focused at the entrance of dielectric capillary tubes, using a spherical mirror in combination with a deformable mirror, to correct aberrations of the phase front in the focal plane. Glass capillary tubes with inner diameter ranging from $d = 150 \mu\text{m}$ to 250 μm and length varying between 6 mm and 20 mm were aligned along the optical axis. Hydrogen gas was filled into the tubes through two thin ($\sim 300 \mu\text{m}$) slits located 2.5 mm from each end of the tubes. An electro-magnetic valve controlled the pressure in a reservoir which in turn controlled the flow of gas into the capillary tube. Gas densities inside the capillary corresponding to electron densities in the range $5 \times 10^{17} - 1.5 \times 10^{19} \text{ cm}^{-3}$, were achieved and characterized by off-line interferometric measurement. Each capillary tube could be used for a large number of laser shots (~ 100 shots in the same capillary), as long as the focused laser beam remained well centered at the capillary entrance. Pointing variations due to thermal drifts and mechanical vibrations were therefore minimized or actively compensated for [13]. The laser pulse was guided in the capillary in the multi-mode regime [7], ionizing the gas and producing a wake. Figure 2 illustrates how the capillary guides the laser beam in vacuum. In (a), the focal spot at the entrance of the capillary tube is shown. In (b), the mode pattern at the exit of the capillary tube shows that the laser pulse was guided in the multi-mode regime. The transmission within the capillary diameter is 70% (capillary of 20 mm long and 200 μm diameter). The symmetry of this multi-mode structure at the exit of the capillary tube is the criterion used for the alignment of the tube on the laser axis.

Laser-plasma electron acceleration in dielectric capillary tubes

Electrons from the plasma were trapped, accelerated and then detected on a phosphor screen (Kodak Lanex), placed 59 cm after the laser focus, imaged by a CCD camera. A permanent magnet ($B = 0.7$ T, length 100 mm) could be moved into position between the capillary exit and the phosphor screen to deflect the electrons and thereby allow their energy distribution to be measured. Electrons with energy below 40 MeV did not reach the phosphor screen and were thus not detected. Far-field profiles of the X-rays, generated due to betatron oscillations inside the capillary, were recorded by a 16 bit CCD X-ray camera placed on the laser axis. X-rays and electron spectra were recorded simultaneously when the electron beam was deflected from the axis by the magnet. A matrix of metallic filters was placed over the chip of the camera in order to block laser and visible light and to provide a low resolution measurement of the X-ray spectrum. The camera, an Andor 434-BN CCD chip with 1024×1024 pixels of $13\text{ }\mu\text{m}$ size, was placed 89 cm away from the source, corresponding to a chip collection angle of $15 \times 15\text{ mrad}^2$.

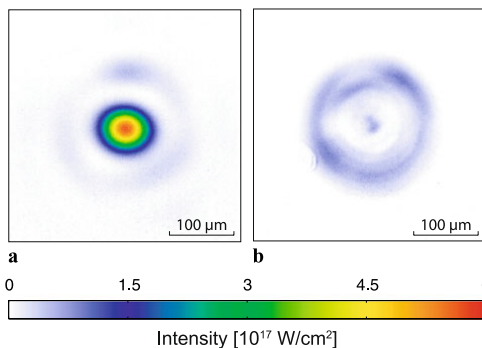
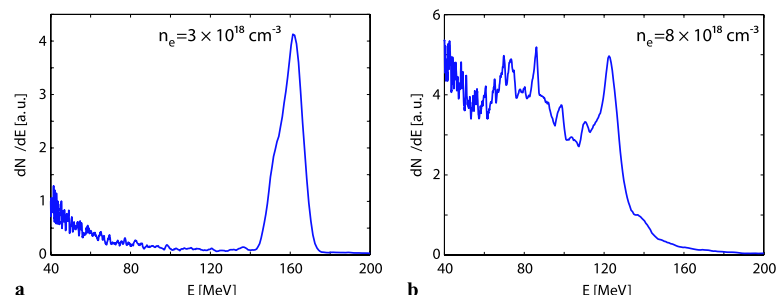


Fig. 2 Transmission trough a capillary tube of 20 mm long and 200 μm diameter in vacuum. In (a) the focal spot at the entrance of the capillary tube and (b) the multi-mode pattern at the exit of the capillary tube. The transmission within the capillary diameter is 70%

Fig. 3 Experimental electron spectra. In (a) a peaked spectrum and in (b) a broad spectrum with multiple peaks, with a total charge above 40 MeV of 2.3 pC and 7.7 pC, respectively



2.2 Electrons

Electron beams, with charge varying in the range 1–100 pC, were observed. The quality of the beam was found to depend very sensitively on the plasma electron density. Individual shots showed peaks with energies up to 170 MeV, with energy spreads as low as 7% and divergence as low as 4 mrad FWHM. At optimum plasma density, monoenergetic features were observed, as illustrated in Fig. 3(a) for $n_e = 3 \times 10^{18}\text{ cm}^{-3}$, a capillary length of 20.5 mm and a diameter of 200 μm . At higher densities, trapping occurs at more than one point leading to broad electron spectra, occasionally with multiple peaks as shown in Fig. 3(b) for $n_e = 8 \times 10^{18}\text{ cm}^{-3}$ in a capillary 11 mm long and of 200 μm diameter. Both spectra were recorded at a peak laser intensity of $6 \times 10^{17}\text{ W/cm}^2$.

The influence of the plasma electron density, laser intensity and capillary parameters, such as diameter and length, are presented in Fig. 4. In (a), the charge above 40 MeV is plotted as a function of the plasma electron density for different capillary diameters, and laser intensities. The capillary length was kept fixed (20.5 mm) and the diameter varied: 180 μm (circles), 200 μm (squares, diamonds) and 250 μm (triangles). The laser intensity was $6 \times 10^{17}\text{ W/cm}^2$ except for the data represented by squares, where the laser intensity was $5 \times 10^{17}\text{ W/cm}^2$. Figure 4(a) shows that for each capillary diameter and laser intensity, there is a narrow range of electron density for which accelerated electrons are produced. In this regime of acceleration, the plasma electron density is a crucial parameter for the trapping and acceleration process. This is also observed in simulations where changes in diameter and intensity significantly change the pulse evolution, as discussed by Ferrari et al. in [14]. In order to fully understand this very complex interaction and, in particular, how the different parameters influence the value of the optimum density, further modelling and systematic studies are required. Here, we merely demonstrate this sensitivity. Finally, for capillaries of 250 μm , diameter no electrons were observed over the entire range of electron densities explored. This suggests that for such large diameter

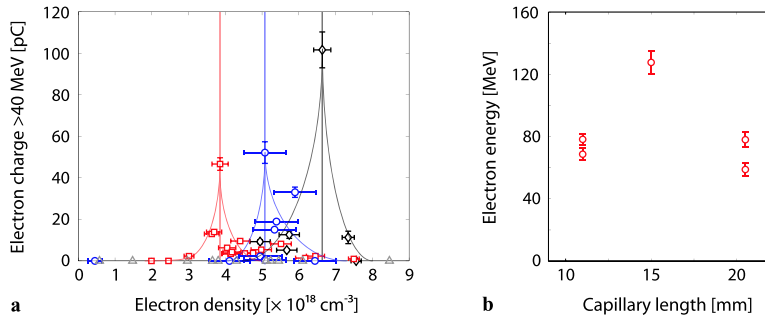


Fig. 4 Influence of the electron density, the laser intensity and the capillary parameters (diameter and length) on the electron beams. In (a) the charge above 40 MeV as function of electron density is shown for different capillary diameters: 180 μm (blue circles), 200 μm (red squares, black diamonds) and 250 μm (grey triangles) for a laser intensity of $6 \times 10^{17} \text{ W/cm}^2$ except for the points represented by the squares

where the laser intensity was $5 \times 10^{17} \text{ W/cm}^2$. Each point corresponds to one laser shot. The graph shows complete data sets and therefore also illustrates the shot to shot fluctuations. The lines are drawn to guide the eye. The peak electron energy is plotted as function of the capillary length in (b) for $n_e = 5 \times 10^{18} \text{ cm}^{-3}$. The effect of dephasing is clearly visible

the capillary acted mainly as a windowless gas cell: the reflection from the wall are not sufficient to contribute significantly to the pulse evolution. In Fig. 3(b), the peak energy as a function of the capillary length is shown at a fixed electron density of $5 \times 10^{18} \text{ cm}^{-3}$ for a capillary diameter of 180 μm and laser intensity of $6 \times 10^{17} \text{ W/cm}^2$. The onset of dephasing is observed as the peak energy decreases for the longest capillaries. At this density the theoretical dephasing length is $L_d = 5 \text{ mm}$. As it is seen in the simulations (see, for example Fig. 8), for the values of densities and power considered, self-focusing is a slow process: it takes 6.4 mm in this example for a_0 to reach an adequate value for electron injection and trapping. Adding the evolution distance to the dephasing length gives a value of the order of what we observe in the experiment. Thus, the maximum electron energy can be reached inside the capillary. Alternatively, pump depletion can also contribute to limit the maximum energy. From simulations (Fig. 6 of [14]), it is estimated that 40% of the laser energy is depleted after 11 mm, where self-focusing stops.

2.3 X-rays

The production of betatron X-rays is directly linked to the trapping and acceleration of electrons. The far-field distribution of X-ray beams were recorded and gave additional insight into the interaction itself. The number of X-ray photons obtained strongly depends on the charge of the electron beam, and thus also on the plasma electron density. We obtained up to $\sim 5 \times 10^4$ photons/mrad² over the range 1–10 keV, which is comparable to the results in [10].

Figure 5(a) and (b) show far-field distributions of the X-ray beam for two slightly different electron densities,

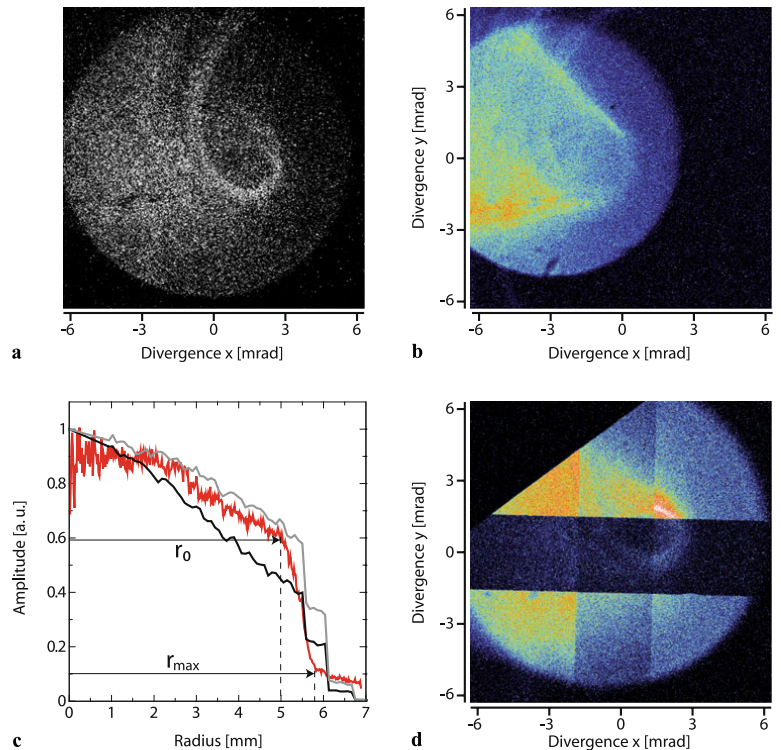
$n_e = 5.3 \times 10^{18} \text{ cm}^{-3}$ and $n_e = 5.9 \times 10^{18} \text{ cm}^{-3}$, respectively. Both were produced in a capillary 20 mm long and of 180 μm diameter and recorded using a uniform filter (6 μm mylar and 3 μm Al) in front of the CCD chip. Figure 5(c) shows a radial profile, averaged over angles (red curve) of the image of Fig. 5(a), as well as line-outs in two transverse directions (black and grey curves) of a simulated X-ray beam, from simulations discussed in the next section, with $n_e = 5 \times 10^{18} \text{ cm}^{-3}$, a capillary diameter of 150 μm and a length of 20 mm for an X-ray photon energy of 1 keV. Figure 5(d) shows the X-ray beam distribution produced in a capillary tube of length 20 mm and diameter 200 μm , $n_e = 7 \times 10^{18} \text{ cm}^{-3}$, and a different set of filters (a base of 6 μm mylar and 3 μm Al, with a 3 μm thick vertical stripe of Al and a 3 μm thick horizontal stripe of Sn). Assuming a synchrotron-like spectrum, using the tabulated transmission data of the filters and known CCD sensitivity, an estimate of the critical energy $E_c = 1.3 \text{ keV}$ was deduced using a least-squares method [15].

The shape of the edge of the beam on the images of Fig. 5 shows that the wall of the capillary in the output plane casts a shadow, indicating that the source of the X-rays is inside the tube. The shadow of the wall is observed also on the simulation results and its size is similar to the experimental data. From the different images in Fig. 5, it is clearly observed that the divergence of the X-ray beam varies, which can be related to a different geometry (different capillary tubes) or a different position of the X-ray source along the capillary axis, due for example to a different electron density.

Sources situated at different points along the axis of the capillary produce circular beams of different radii on the detector, as illustrated in Fig. 6. The points closest to the entrance of the tube, situated on the left in Fig. 6, will therefore produce the smallest beam and the point closest to the exit

Laser-plasma electron acceleration in dielectric capillary tubes

Fig. 5 Far-field distribution of the X-ray beam for two different densities in (a) and (b). In (d) the absorption in additional stripes of metallic foils placed in front of the detector are visible and are used to make a rough estimate of the X-ray spectrum. In (c), radial average profile of (a) (red curve), horizontal (black curve) and vertical (grey curve) line-outs of a simulated X-ray beam profile are shown



of the tube produces the largest one. This means that the radius, r_0 , where the signal starts to decrease corresponds to emission from the point producing the smallest beam, i.e. the point closest to the entrance of the capillary. As shown in Fig. 5(c), r_0 can be obtained from the X-ray image and then using simple geometry, the position of the start of the X-ray emission can be estimated. Assuming that X-rays are not reflected by the capillary walls, the distance on axis between the start of the X-ray source and the exit of the capillary, L_X , can be written as $L_X = L / [(r_0/r_{\text{cap}}) - 1]$ where L is the distance between the capillary output and the CCD camera, and r_{cap} the capillary tube radius. For example in the case of Fig. 5(a), $r_0 = 5$ mm, and the distance from the capillary entrance $L_{\text{cap}} - L_X$ to the beginning of the X-ray emission is then estimated as 4.6 mm.

The shape of the edge of the beam is also an indicator of the extend of the X-ray source, or of the existence of multiple sources. The radius r_{\max} corresponds to emission from the point producing the largest beam, i.e. the point closest to the exit of the capillary. Using the same calculation as previously, it is possible to estimate where the X-ray emission stops. For the case in Fig. 5(c), we find $r_{\max} = 5.8$ mm and the position of the end of the source is then estimated to be

6.8 mm from the capillary entrance. The source therefore extends from 4.6 to 6.8 mm after the entrance of the capillary. However, this is only a lower limit for the extend of the source as the detector is not perfect and the signal drops below the noise level. According to [16–19], the transverse source size is expected to be of the order of a few microns which would result in a radius difference of about ~ 0.2 mm on the detector. This has been neglected as the radius difference due to the longitudinal source size is much larger.

As the electrons start emitting X-rays as soon as they are trapped, the position of the X-ray source can be used to determine the trapping position. However, due to the filters in front of the CCD camera, only X-rays above 500 eV were detected and only the point where the electrons have been sufficiently accelerated to produce X-rays above 500 eV can be determined. Figure 7 shows the dependence of the position of the onset of the first X-ray emission, determined from the X-ray beam diameter, on the electron density for different capillaries and laser intensities. We observe that for most of the capillaries the X-ray emission starts at a shorter distance when the density is increased. The capillary diameter, as well as the laser intensity, also influences the result, confirming that the whole acceleration process is very sensitive

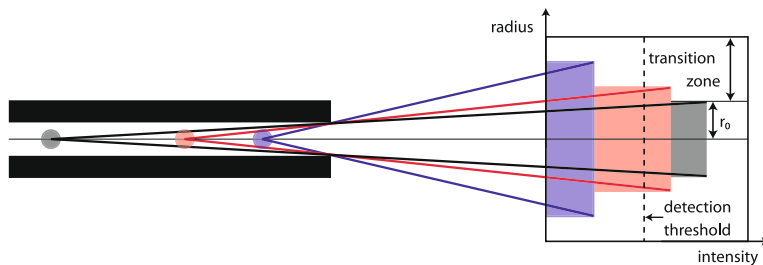


Fig. 6 Schematic explanation of the interpretation of the far-field intensity profiles images of the X-ray beams. The longitudinal spread of the X-ray emission inside the capillary tube is represented as different point sources. Depending on the position of the source, the beams outside of the capillary obtain different divergence. The points closest

to the entrance in the tube, situated on the left of the figure, produce the smallest radius on the detector. By measuring r_0 , it is possible to estimate the start of the X-ray emission and therefore the trapping point of the electrons

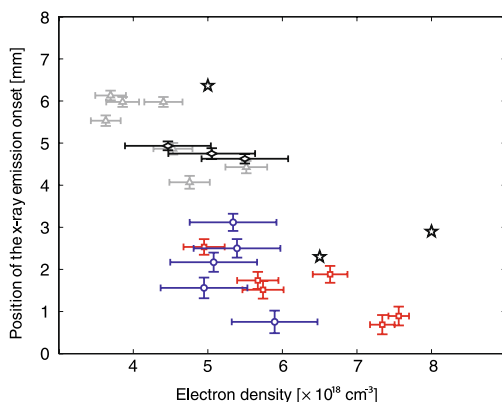


Fig. 7 The diameter of the X-ray image can be used to determine the position of the onset of the first X-ray emission relative to the laser focus inside the capillary. This is done for different capillaries as a function of electron density: a capillary of 20 mm length and 200 μm diameter (grey triangles, red squares), a capillary of 20 mm length and 180 μm diameter (blue circles), a capillary of 15 mm length and 180 μm diameter (black diamonds) for a laser intensity of $6 \times 10^{17} \text{ W/cm}^2$ except for the points represented by the triangles and the diamonds where the laser intensity was $5 \times 10^{17} \text{ W/cm}^2$. Each point corresponds to one laser shot. The stars correspond to the trapping points obtained from the simulations described in the next section

to these parameters. This is consistent with the observations of the electron beam, as shown in Fig. 4(a). The points represented by stars in Fig. 7 correspond to the trapping position obtained from the simulations described in the next section. A trend similar to the experimental one is observed.

Superimposed over a more-or-less uniform background, the far-field beam profiles in Fig. 5(a) and (b) show spatial features, which suggest particular trajectories of the electrons [18]. A “spiral-like” feature is observed in the images for many different shots and for different capillaries. As-

suming that specular reflections of X-rays from the inside walls are negligible, the spiral shapes might be understood as the X-ray emission characteristics of electrons along a spiral-like trajectory [20]. Features similar to the observed ones correspond to an oscillation amplitude of the order of $\sim 0.1 \mu\text{m}$, which is about one order of magnitude smaller than the ones mentioned in [18, 19]. This much smaller oscillation amplitude might be due to the particular interaction in the capillary tube, as the experiments reporting larger amplitudes were all performed in gas jets.

3 Simulations and discussion

Simulations were carried out in order to better understand the interaction processes [14] for the low laser intensity and low electron density used in the experiment, where one would not expect trapping and acceleration of electrons to occur and consequently no betatron X-rays to be produced. Particle-in-cell (PIC) simulations were performed using the electromagnetic code CALDER-CIRC [21]. To model the propagation of the laser pulse along the capillary tube, a dielectric boundary condition was added to the code. Detailed results of these simulations are presented in [14]. Additional simulations results are shown in this section. They were performed for a 35 fs laser pulse with a radial intensity profile fitting the θ -averaged experimental profile, and a peak normalized laser amplitude of 0.6. The focal plane was located at the capillary entrance. The capillary diameter was 150 μm , its length 20 m. A ramp of 400 μm increased the electron density from 0 to n_e , with n_e being the electron density inside the capillary. Simulations were carried out for three different electron densities $n_e = 5, 6.5$ and $8 \times 10^{18} \text{ cm}^{-3}$.

An example of results is shown in Fig. 8 for $n_e = 5 \times 10^{18} \text{ cm}^{-3}$. The solid black curve shows the evolution of the normalized laser amplitude along the axis of the

Laser-plasma electron acceleration in dielectric capillary tubes

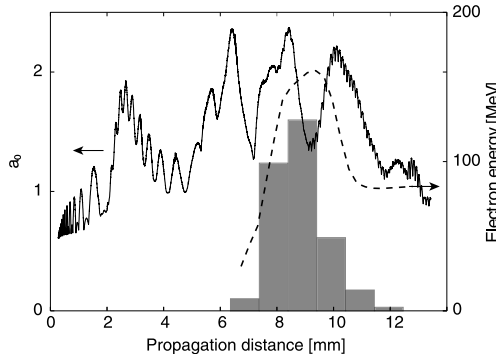


Fig. 8 Simulation of the interaction in the capillary tube using the PIC code CALDER-CIRC. The solid black curve shows the evolution of the laser intensity along the capillary length. The dashed line shows the energy of the first electron bunch. The corresponding X-ray emission is shown by the grey bars, with the total X-ray energy plotted in arbitrary units. The maximum of the X-ray emission coincides with the maximum energy of the electrons

capillary tube. The beam undergoes a slow process of self-focusing, reaching a maximum amplitude of $a_0 = 2.5$ after a propagation of 6.4 mm (i.e. the intensity has increased by a factor 17). This relatively modest amplitude is nevertheless large enough to produce self-injection of electrons, mainly into the first bucket of the wakefield, even at such low density. The capillary confines the energy surrounding the main peak of the focal spot and contributes to maintaining the beam self-focused 2–3 mm longer than without the capillary. The simulations show that the evolution of the laser intensity depends strongly on capillary diameter, initial laser intensity, and electron density, as the mode propagation is quite sensitive to these parameters. This is consistent with our experimental observations, as shown in Figs. 4(a) and 7, where the optimum density and the position of the trapping point depend strongly on these parameters.

After trapping, the electron bunch is accelerated by the plasma wave in the capillary. Simulations show that the electrons reach dephasing, as illustrated by the dashed line in Fig. 8 showing the energy of the first electron bunch. This is also consistent with the experimental electron data (see Fig. 4(b)). At this low density, the dephasing length is ~ 5 mm but dephasing is still reached inside the capillary. The extracted electron bunch therefore presents a wide energy spectrum, similar to the experimental spectrum shown in Fig. 3(b). In some cases, the peaks in the simulated electron spectra are more pronounced, but the quasi-monoenergetic features observed experimentally, such as the one shown in Fig. 3(a), are not reproduced in the simulations. Mono-energetic spectra could result from a strongly asymmetric self-injection of electrons, originated in beam asym-

metry and eventually associated hosing. Further studies taking into account asymmetrical features are needed to test these hypotheses.

The X-ray spectra generated by accelerated electrons, obtained in the simulations, are found to be synchrotron-like, with a critical energy of about 1 keV in fair agreement with experimental data. The total X-ray energy (integrated from 0 to 10 keV) is also calculated and shown by the grey bars in Fig. 8. It is clearly seen that most of the X-rays are generated in the region where electrons reach their maximum energy. The emitted power scales with γ^4 [11] and, therefore, the X-ray emission is maximum when the electrons have their maximum energy. The spatial profile is calculated with the assumption that the X-rays are absorbed at the capillary wall. The simulated results are very close to the experimental ones, as seen for example in Fig. 5(c). In the simulations, the radius of the X-ray beam is also found to vary as a function of the electron density. This agrees with our explanation that the diameter of the X-ray beam on the detector gives us an indication about the position of the trapping point. For $n_e = 8 \times 10^{18} \text{ cm}^{-3}$, the simulations shows that the electrons are trapped early (~ 3 mm) and the divergence of the X-ray beam is 9.4 mrad. For $n_e = 5 \times 10^{18} \text{ cm}^{-3}$, electrons are trapped later (~ 7 mm), and the divergence of the X-ray beam is therefore much bigger (13.6 mrad). The trapping position estimated from the simulation results fairly agree with the experimental determination.

4 Conclusion

Experimental data show that inside dielectric capillaries trapping and acceleration of electrons is possible at lower laser intensities than in gas jets, where in both cases the laser pulse interacts with a neutral gas homogeneous in the transverse direction. It was found that the capillary confines energy located outside the main peak in the focal plane and contributes to the beam self-focusing over longer distances, thus allowing the pulse to evolve enough to reach the threshold for trapping and acceleration of electrons. The interaction was found to depend strongly, and in a complex way, on parameters such as plasma electron density, capillary diameter, and laser intensity. This has been investigated experimentally, both by observing the accelerated electron beam directly and by analysing betatron X-ray radiation as an additional diagnostic of the interaction. Simulations are in good agreement with experimental results. The work presented here shows that the interaction in a capillary tube is different from the interaction in more conventional targets, such as gas jets. This suggests that this kind of structures has interesting properties for electron acceleration. In order to explore the potential of these novel targets for electron acceleration, further studies are required.

Acknowledgements We acknowledge the support of the European Community—NEST Activity under the FP6 Structuring the European Research Area programme (project EuroLEAP, contract 028514), Marie Curie Early Stage Training Site MAXLAS (MEST-CT-2005-020356), the Lund University X-ray Center (LUXC), the Swedish Research Council (including the Linné grant to the LLC), the Knut and Alice Wallenberg Foundation, the RTRA Triangle de la Physique, and the French Agence Nationale de la Recherche. We also thank the referees for their constructive comments.

Open Access This article is distributed under the terms of the Creative Commons Attribution Noncommercial License which permits any noncommercial use, distribution, and reproduction in any medium, provided the original author(s) and source are credited.

References

1. S.P.D. Mangles, C.D. Murphy, Z. Najmudin, A.G.R. Thomas, J.L. Collier, A.E. Dangor, E.J. Divall, P.S. Foster, J.G. Gallacher, C.J. Hooker, D.A. Jaroszynski, A.J. Langley, W.B. Mori, P.A. Norreys, F.S. Tsung, R. Viskup, B.R. Walton, K. Krushelnick, *Nature* (London) **431**, 535 (2004)
2. C.G.R. Geddes, Cs. Toth, J. van Tilborg, E. Esarey, C.B. Schroeder, D. Bruhwiler, C. Nieter, J. Cary, W.P. Leemans, *Nature* (London) **431**, 538 (2004)
3. J. Faure, Y. Glinec, A. Pukhov, S. Kiselev, S. Gordienko, E. Lefebvre, J.-P. Rousseau, F. Burgby, V. Malka, *Nature* (London) **431**, 541 (2004)
4. S.P.D. Mangles, A.G.R. Thomas, M.C. Kaluza, O. Lundh, F. Lindau, A. Persson, F.S. Tsung, Z. Najmudin, W.B. Mori, C.-G. Wahlström, K. Krushelnick, *Phys. Rev. Lett.* **96**, 215001 (2006)
5. J. Osterhoff, A. Popp, Zs. Major, B. Marx, T.P. Rowlands-Rees, M. Fuchs, M. Geissler, R. Hörllein, B. Hidding, S. Becker, E.A. Peralta, U. Schramm, F. Grüner, D. Habs, F. Krausz, S.M. Hooker, S. Karsch, *Phys. Rev. Lett.* **101**, 085002 (2008)
6. W.P. Leemans, B. Nagler, A.J. Gonsalves, Cs. Tóth, K. Nakamura, C.G.R. Geddes, E. Esarey, C.B. Schroeder, S.M. Hooker, *Nat. Phys.* **2**, 696 (2006)
7. B. Cros, C. Courtois, G. Matthieu, A. Di Bernardo, D. Batani, N. Andreev, S. Kuznetsov, *Phys. Rev. E* **65**, 026405 (2002)
8. F. Dorches, J.R. Marquès, B. Cros, G. Matthieu, C. Courtois, T. Vélikorousov, P. Audebert, J.P. Geindre, S. Rebibo, G. Hamiaux, F. Amirani, *Phys. Rev. Lett.* **82**, 4655 (1999)
9. F. Wojda, K. Cassou, G. Genoud, M. Burza, Y. Glinec, O. Lundh, A. Persson, G. Vieux, E. Brunetti, R.P. Shanks, D. Jaroszynski, N.E. Andreev, C.-G. Wahlström, B. Cros, *Phys. Rev. E* **80**, 066403 (2009)
10. A. Rousse, K.T. Phuoc, R. Shah, A. Pukhov, E. Lefebvre, V. Malka, S. Kiselev, F. Burgby, J.-P. Rousseau, D. Umstadter, D. Hulin, *Phys. Rev. Lett.* **93**, 135005 (2004)
11. E. Esarey, B. Shadwick, P. Catravas, W. Leemans, *Phys. Rev. E* **65**, 056505 (2002)
12. J.D. Jackson, in *Classical Electrodynamics*, 3rd edn. (Wiley, New York, 1975), Chap. 14
13. G. Genoud, M. Burza, A. Persson, F. Wojda, C.-G. Wahlström, *Rev. Sci. Instrum.* **82**, 033102 (2011)
14. H.E. Ferrari, A.F. Lifschitz, B. Cros, *Plasma Phys. Control. Fusion* **53**, 014005 (2010)
15. S. Kneip, S.R. Nagel, C. Bellei, N. Bourgeois, A.E. Dangor, A. Gopal, R. Heathcote, S.P.D. Mangles, J.R. Marquès, A. Maksimchuk, P.M. Nilson, K.T. Phuoc, S. Reed, M. Tzoufras, F.S. Tsung, L. Willingale, W.B. Mori, A. Rousse, K. Krushelnick, Z. Najmudin, *Phys. Rev. Lett.* **100**, 105006 (2008)
16. S. Kneip, C. McGuffey, J.L. Martins, S.F. Martins, C. Bellei, V. Chvykov, F. Dollar, R. Fonseca, C. Huntington, G. Kalintchenko, A. Maksimchuk, S.P.D. Mangles, T. Matsuoka, S.R. Nagel, C.A.J. Palmer, J. Schreiber, K.T. Phuoc, A.G.R. Thomas, V. Yanovsky, L.O. Silva, K. Krushelnick, Z. Najmudin, *Nat. Phys.* **6**, 980 (2010)
17. R.C. Shah, F. Albert, K.T. Phuoc, O. Shevchenko, D. Boschetto, A. Pukhov, S. Kiselev, F. Burgby, J.-P. Rousseau, A. Rousse, *Phys. Rev. E* **74**, 045401 (2006)
18. K.T. Phuoc, S. Corde, R. Shah, F. Albert, R. Fitour, J.-P. Rousseau, F. Burgby, B. Mercier, A. Rousse, *Phys. Rev. Lett.* **97**, 225002 (2006)
19. S.P.D. Mangles, G. Genoud, S. Kneip, M. Burza, K. Cassou, B. Cros, N.P. Dover, C. Kamperidis, Z. Najmudin, A. Persson, J. Schreiber, F. Wojda, C.-G. Wahlström, *Appl. Phys. Lett.* **95**, 181106 (2009)
20. K. Ta Phuoc, S. Corde, R. Fitour, R. Shah, F. Albert, J.-P. Rousseau, F. Burgby, A. Rousse, V. Seredov, A. Pukhov, *Phys. Plasmas* **15**, 073106 (2008)
21. A.F. Lifschitz, X. Davoine, E. Lefebvre, J. Faure, C. Rechatin, V. Malka, *J. Comput. Phys.* **228**, 1803 (2009)

PAPER V

Controlling the spectrum of x-rays generated in a laser-plasma accelerator by tailoring the laser wavefront

S. P. D. Mangles, G. Genoud, S. Kneip, M. Burza, K. Cassou, B. Cros, N. P. Dover, C. Kamperidis, Z. Najmudin, A. Persson, J. Schreiber, F. Wojda and C.-G. Wahlström.

Appl. Phys. Lett. **95**, 181106 (2009).

Controlling the spectrum of x-rays generated in a laser-plasma accelerator by tailoring the laser wavefront

S. P. D. Mangles,^{1,a)} G. Genoud,² S. Kneip,¹ M. Burza,² K. Cassou,³ B. Cros,³ N. P. Dover,¹ C. Kamperidis,² Z. Najmudin,¹ A. Persson,² J. Schreiber,¹ F. Wojda,³ and C.-G. Wahlström²

¹Blackett Laboratory, Imperial College London, London SW7 2AZ, United Kingdom

²Department of Physics, Lund University, P.O. Box 118, S-22100 Lund, Sweden

³Laboratoire de Physique des Gaz et des Plasmas, Centre National de la Recherche Scientifique, Université Paris XI, 91405 Orsay, France

(Received 1 September 2009; accepted 13 October 2009; published online 4 November 2009)

By tailoring the wavefront of the laser pulse used in a laser-wakefield accelerator, we show that the properties of the x-rays produced due to the electron beam's betatron oscillations in the plasma can be controlled. By creating a wavefront with coma, we find that the critical energy of the synchrotronlike x-ray spectrum can be significantly increased. The coma does not substantially change the energy of the electron beam, but does increase its divergence and produces an energy-dependent exit angle, indicating that changes in the x-ray spectrum are due to an increase in the electron beam's oscillation amplitude within the wakefield. © 2009 American Institute of Physics. [doi:10.1063/1.3258022]

The use of intense laser pulses to excite plasma waves with a relativistic phase velocity is a possible route to the development of compact particle accelerators. Using this laser-wakefield acceleration technique, experiments have produced quasimonoenergetic 0.1 to 1 GeV electron beams in distances on the order of 1 cm.^{1–3} Such compact particle sources have a clear potential as a source of x-rays. The plasma waves produced in current generation experiments not only have a strong accelerating field but also have strong focusing fields. These focusing fields can cause electrons within the wakefield to oscillate transverse to their acceleration direction, in “betatron orbits.” This motion generates x-ray radiation which can have properties, in particular peak brightness, similar to those achievable with conventional “3rd generation” light sources.⁴ This is, in part, due to the ultrashort-pulse nature of these x-ray sources, which are thought to be at least as short as the laser pulse involved in the interaction,⁵ i.e., on the order of tens of femtoseconds. Such x-ray sources could be used for a wide range of studies into the structure of matter. The ultrashort duration of the x-ray pulse and the possible femtosecond synchronization with other photon and particle sources driven by the same laser offer significant benefits.

Studies to date have concentrated on characterizing the properties of this x-ray source in terms of the spectrum, angular distribution, source size, and its ultrashort nature.^{4–7} In this letter we demonstrate an ability to control the spectral properties of the betatron x-ray source by controlling the laser wavefront.

In Ref. 8, a correlation between the energy of the electron beam and the angle at which it exited the plasma was attributed to betatron oscillations caused by off-axis injection of the electrons. It was hypothesized that this was caused by an aberration in the focal spot. However, in that study, no direct control of the excitation of the betatron motion was attempted, nor was the effect on x-ray production measured.

In this work we use a deformable mirror to tailor the laser wavefront and show that the x-ray spectrum can be changed significantly, in particular we show that a coma wavefront produces more high-energy photons than a flat wavefront. This change in the photon spectrum is due to an increase in the strength of the plasma wiggler, a direct result of off-axis injection.

In the blow-out regime relativistic electrons with energy $\gamma m_e c^2$ undergo transverse (or betatron) oscillations at the betatron frequency $\omega_\beta = \omega_p / \sqrt{2\gamma}$, with a wavenumber $k_\beta = \omega_\beta/c$ (where $\omega_p = \sqrt{n_e e^2/m_e \epsilon_0}$ is the plasma frequency of a plasma of electron density n_e). The wiggler (or betatron) strength parameter for an electron oscillating with an amplitude r_β is $K = \gamma k_\beta r_\beta$. For sufficiently large oscillations ($K > 1$) the radiation is broadband and well characterized by a synchrotronlike spectrum,^{4,9} i.e., close to the axis ($\theta=0$) the spectrum takes the form of $d^2I/(dEd\Omega)_{\theta=0} \propto \xi^2 \mathcal{K}_{2/3}^2(\xi/2)$, where $\mathcal{K}_{2/3}(x)$ is a modified bessel function of order 2/3 and $\xi = E/E_c$. The shape of this spectrum is characterized by a single parameter, the critical energy E_c . The on-axis spectrum is broadband and peaked close to E_c , with approximately half the energy radiated below E_c (note the present definition of E_c is different to that used in Refs. 7 and 9 but consistent with Refs. 4, 6, and 10). For fixed γ and n_e , the critical energy is directly proportional to the oscillation amplitude. $E_c = \frac{3}{4} \hbar \gamma^2 \omega_p^2 r_\beta / c$. Thus increasing the oscillation amplitude of the electrons within the wakefield is expected to have a significant effect on the x-ray photon spectrum.

The experiment was performed using the multi-terawatt laser at the Lund Laser Centre, which provided 0.6 J energy pulses on target with a full width at half maximum (FWHM) duration of 45 ± 5 fs at a central wavelength of 800 nm. The laser was focused onto the edge of a 2 mm supersonic helium gas jet using an f/9 off-axis parabolic mirror. The plasma density was held constant at $1.5 \times 10^{19} \text{ cm}^{-3}$, at which the laser pulse length is approximately 1.5 times the wavelength of the relativistic plasma wave $\lambda_p = 2\pi c/\omega_p = 9 \mu\text{m}$.

^{a)}Electronic mail: stuart.mangles@imperial.ac.uk.

The laser wavefront was measured using a wavefront sensor (Phasics SID4). A 32 actuator deformable mirror (Night N Adaptive Optics DM2-65-32), placed before the focusing optic was used to correct for wavefront errors present in the laser system, defining our flat wavefront. The deformable mirror could be adjusted to tailor the wavefront. The wavefront discussed here is coma, defined on a unit circle by the Zernike polynomial $Z(r, \theta) = \sqrt{8C} (3r^3 - 2r)\cos \theta$ for horizontal coma. (where C is the rms. amplitude of the coma in units of the laser wavelength λ).

The intensity distribution of the focal spot was recorded on a 12 bit charge coupled device (CCD) camera using a microscope objective. The flat wavefront setting produced a focal spot with a $1/e^2$ intensity radius, or waist, of $w_0 = 12 \pm 1 \mu\text{m}$. 42% of the pulse energy was within the FWHM. This corresponds to a peak intensity of $4.0 \times 10^{18} \text{ W cm}^{-2}$ or a normalized vector potential of $a_0 = 1.4$, where $a_0 = eA_0/(m_e c) = eE_0/(m_e \omega_0 c)$ (A_0 and E_0 are the amplitude of the vector potential and electric field of the laser and ω_0 is the laser frequency). For $C = 0.175\lambda$ horizontal coma the peak intensity reduced to $2.1 \times 10^{18} \text{ W cm}^{-2}$, or a normalized vector potential of $a_0 = 1$. The energy contained within the FWHM reduced to 25%. Horizontal coma elongates the focal spot in the horizontal (x) direction, but it does not do so symmetrically. For $C = 0.175\lambda$ and $x < 0$ the waist is close to the flat wavefront case with $w_{x<0} = 13 \pm 1 \mu\text{m}$. However, for $x > 0$ the waist is significantly increased to $w_{x>0} = 18 \pm 1 \mu\text{m}$. Horizontal coma leaves the vertical (y) beam waist unaffected.

To diagnose the effect of coma on the electron beam profile a scintillator screen (Kodak Lanex regular) was placed in the beam path and imaged onto a 12 bit CCD camera. A permanent magnet ($B = 0.7 \text{ T}$, length 100 mm) could be moved into position between the gas jet and the scintillator screen to sweep the electrons away from the laser axis. The magnetic field dispersed the electrons in the vertical direction, the vertical (y) position of the electron beam on the scintillator screen is then a function of the beam energy (E) so that, taking into account the nonlinear dispersion dy/dE and the response of the lanex to high-energy electrons¹¹ the electron energy spectrum dN/dE can be calculated.

X-rays generated by betatron oscillations in the wake were recorded by an x-ray sensitive 16 bit CCD camera (Andor 434-BN). The CCD chip had 1024×1024 pixels and was placed on the laser axis. The chip collection angle corresponded to $20 \times 20 \text{ mrad}^2$. The x-rays were only recorded when the magnet was in position to prevent the electron beam striking the CCD chip. An array of filters (Al, Zn, Ni, and Fe) were placed directly in front of the CCD chip. Using the known transmission of x-rays¹² through the filters, and the CCD sensitivity, we find the critical energy E_c which best describes the x-ray photon spectrum using a least-squares method.⁷

The variation in E_c with coma amplitude is shown in Fig. 1(a). For the flat wavefront we observed $E_c = 1.5 \pm 0.5 \text{ keV}$. As the coma amplitude increases, a clear shift in the x-ray spectrum toward higher photon energies is observed, reaching $E_c = 4.0 \pm 1.5 \text{ keV}$ for 0.175λ coma. The electron spectra shows a constant mean electron energy of $\langle \gamma \rangle = 144 \pm 7$ for all the coma settings, implying that the change in E_c is due to a change in the oscillation amplitude,

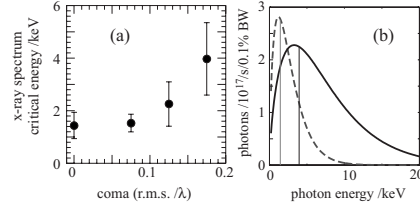


FIG. 1. (a) Variation in the observed x-ray spectrum critical photon energy, E_c with the amplitude of coma. For larger coma no x-rays were observed. (b) best-fit synchrotron spectra for a flat wavefront (dashed line) and 0.175λ amplitude coma (solid line). The curves take into account the expected change in beam divergence and assume the duration of the x-rays is that of the laser pulse. The vertical lines indicate the position of E_c .

r_β . We calculate that the oscillation amplitude increases from $r_\beta = 1.0 \pm 0.4 \mu\text{m}$ to $r_\beta = 3 \pm 1 \mu\text{m}$ corresponding to an increase in the wiggle strength parameter from $K = 5 \pm 2$ to $K = 17 \pm 6$. The largest oscillation amplitudes are slightly less than the radius of the wakefield (approximately $\lambda_p/2 = 4.5 \mu\text{m}$) and indicate that almost the whole width of the plasma channel is being used for radiation generation. Oscillations larger than this would not be supported and may indicate why, when larger amplitude coma wavefronts were used, no electrons or x-rays were observed.

Integrating the signal recorded on the CCD and taking into account the expected photon beam divergence, $\theta \approx K/\gamma$, we estimate that as the coma is increased the number of photons remains approximately constant at $(3 \pm 1) \times 10^7$ photons per shot. The energy in the x-ray beam therefore increases, as expected for an increase in K . Two x-ray spectra are shown in Fig. 1(b). While the peak intensity is reduced for the case of 0.175λ coma, there is significantly more intensity at the higher photon energies.

The source of the change in the x-ray spectrum can be elucidated by examining the effect of coma on the electron beam. Figure 2 shows the variation in the electron beam profile and energy spectrum with the amplitude of coma. The electron beam profile images (each representing an average

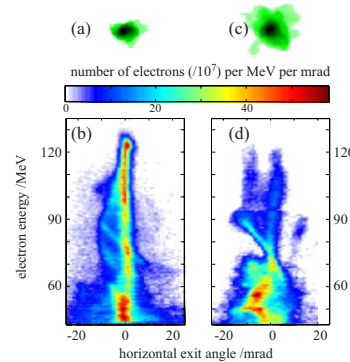


FIG. 2. (Color online) Effect of coma on the electron beam. [(a) and (b)] Flat wavefront, [(c) and (d)] coma = 0.175λ . (a) and (c) show the electron beam profile (average from several shots), (b) and (d) show the electron energy spectrum (from a single shot). The vertical axis is a linear energy scale and the horizontal axis is the exit angle in the nondispersion plane.

of five shots) show that the electron beam divergence increases with the amplitude of coma from ≈ 10 mrad (FWHM) for the flat wavefront to ≈ 20 mrad for 0.175λ coma. The images of the electron energy spectrum (each from a single shot) show the electron energy spectrum dN/dE as a function of the horizontal angle at which the beam exits the plasma. For shots with the flat wavefront and $n_e = 1.5 \times 10^{19} \text{ cm}^{-3}$ the electron spectrum is broadband, extending in energy to ≈ 120 MeV. For the flat wavefront the electrons have an approximately constant exit angle, indicating a small betatron amplitude. With coma we observe an energy-dependent exit angle, indicating a large betatron oscillation amplitude. This occurs because, for broad energy-spread beams, an electron's energy can be mapped to its phase within the plasma wave. Different energy electrons will therefore be at a different phase of their betatron orbit as they exit the plasma, resulting in an oscillatory dependence of the exit angle with energy, as observed.

The electron beam diagnostics show that, by tailoring the wavefront to create an asymmetric focal spot, the wake dynamics are sufficiently perturbed so as to increase the amplitude of the betatron oscillations. This is likely due to the promotion of off-axis injection due to the generation of an asymmetric wakefield by the asymmetric focal spot. Images of self-scattered radiation show that a long wavelength hosing of the channel sometimes occurred; the likelihood of observing this hosing increased with coma. However, the hosing wavelength was significantly longer than the plasma wavelength so would not produce an energy-dependent exit angle, and no correlation between the amplitude of the hosing and x-ray spectrum was observed.

By tailoring the laser wavefront to produce an asymmetric focal spot we have demonstrated an ability to change the energy spectrum of the x-ray photons from a laser-plasma wiggler; increasing the number of high-energy ($E \geq 5$ keV) photons without the need to increase the laser power or electron beam energy. This offers an alternative route to higher energy laser-based x-ray sources without the significant cost of petawatt laser facilities. On some shots we observe that the effect of the coma on the electron beam divergence is

predominantly in the plane of the laser asymmetry. If this effect can be controlled then it also offers a mechanism for producing polarized x-rays with a laser-plasma wiggler.

We acknowledge support from The Royal Society, the Marie Curie Early Stage Training Site MAXLAS (Grant No. MEST-CT-205-02936), the Swedish Research Council, and the EuroLEAP network.

- ¹W. P. Leemans, B. Nagler, A. J. Gonsalves, C. Toth, K. Nakamura, C. G. Geddes, E. Esarey, C. B. Schroeder, and S. M. Hooker, *Nat. Phys.*, **2**, 696 (2006).
- ²S. Karsch, J. Osterhoff, A. Popp, T. P. Rowlands-Rees, Z. Major, M. Fuchs, B. Marx, R. Horlein, K. Schmid, L. Veisz, S. Becker, U. Schramm, B. Hidding, G. Pretzler, D. Habs, F. Gruner, F. Krausz, and S. M. Hooker, *New. J. Phys.*, **9**, 415 (2007).
- ³S. Kneip, S. R. Nagel, S. F. Martins, S. P. D. Mangles, C. Bellei, O. Chekhlov, R. J. Clarke, N. Delerue, E. J. Divall, G. Doucas, K. Ertel, F. Fiuzza, R. Fonseca, P. Foster, S. J. Hawkes, C. J. Hooker, K. Krushelnick, W. B. Mori, C. A. J. Palmer, K. Ta Phuoc, P. P. Rajeev, J. Schreiber, M. J. V. Streeter, D. Urner, J. Viera, L. O. Silva, and Z. Najmudin, *Phys. Rev. Lett.*, **103**, 035002 (2009).
- ⁴A. Rousse, K. T. Phuoc, R. Shah, R. Fitour, and F. Albert, *Eur. Phys. J. D*, **45**, 391 (2007).
- ⁵K. T. Phuoc, R. Fitour, A. Tafzi, T. Garl, N. Artemiev, R. Shah, F. Albert, D. Boschetto, A. Rousse, D. E. Kim, A. Pukhov, V. Seredov, and I. Kostyukov, *Phys. Plasmas*, **14**, 080701 (2007).
- ⁶A. Rousse, K. T. Phuoc, R. Shah, A. Pukhov, E. Lefebvre, V. Malka, S. Kiselev, F. Burgy, J. P. Rousseau, and D. Umstadter, *Phys. Rev. Lett.*, **93**, 135005 (2004).
- ⁷S. Kneip, S. R. Nagel, C. Bellei, N. Bourgeois, A. E. Dangor, A. Gopal, R. Heathcote, S. P. D. Mangles, J. R. Marques, A. Maksimchuk, P. M. Nilson, K. Ta Phuoc, S. Reed, M. Tsoufras, F. S. Tsung, L. Willingale, W. B. Mori, A. Rousse, K. Krushelnick, and Z. Najmudin, *Phys. Rev. Lett.*, **100**, 105006 (2008).
- ⁸Y. Glinec, J. Faure, A. Lifschitz, J. M. Vieira, R. A. Fonseca, L. O. Silva, and V. Malka, *Europhys. Lett.*, **81**, 64001 (2008).
- ⁹E. Esarey, B. A. Shadwick, P. Catravas, and W. P. Leemans, *Phys. Rev. E*, **65**, 056505 (2002).
- ¹⁰J. D. Jackson, *Classical Electrodynamics* 3rd ed. (Wiley, New York, 1999).
- ¹¹Y. Glinec, J. Faure, A. Guennie-Tafo, V. Malka, H. Monard, J. P. Larbre, V. De Waele, J. L. Marignier, and M. Mostafavi, *Rev. Sci. Instrum.*, **77**, 103301 (2006).
- ¹²J. Hubbell and S. Seltzer, N.I.S.T., Gaithersburg, MD, <http://physics.nist.gov/xamdi>, 2004.

PAPER VII

**Evolution of energy spectrum from
laser-accelerated protons with a 100 fs intense
prepulse**

Y. Glinec, G. Genoud, O. Lundh, A. Persson and C.-G. Wahlström.
Appl. Phys. B **93**, 317 (2008).

Evolution of energy spectrum from laser-accelerated protons with a 100 fs intense prepulse

Y. Glinec · G. Genoud · O. Lundh · A. Persson ·
C.-G. Wahlström

Received: 18 June 2008 / Published online: 23 August 2008
© Springer-Verlag 2008

Abstract A parametric study is reported where a femtosecond prepulse is used to change the target properties before the interaction with a multi-terawatt laser pulse which accelerates protons from a foil target. The proton spectrum as function of the prepulse delay and intensity, up to 1.5 ns and up to $3 \times 10^{16} \text{ W/cm}^2$, respectively, shows a global decrease of the maximum proton energy with delay and intensity. However, under appropriate conditions, it is found that the maximum proton energy increases by more than 10% and that the spectral shape changes.

PACS 41.75.Ak · 41.75.Jv · 52.35.-g · 52.38.Kd

1 Introduction

The interaction of an intense laser, focused to relativistic intensities (above 10^{18} W/cm^2), with a thin-foil target (a few μm) can be used to accelerate protons to multi-MeV energies. Among the different parameters that influence the interaction, the intensity level of the Amplified Spontaneous Emission (ASE) pedestal is one of the most critical. It modifies the target before the interaction with the main pulse, thus limiting the minimum thickness of the foil that can be used and therefore the maximum proton energy [1–5]. The influence of a preplasma on the maximum energy has been studied in different geometries: at the front side by the ASE pedestal [3], by an external pulse either at the front [6, 7],

or at the back side [1, 8] of the target. In these studies, for fixed target material and thickness, the maximum ion energy tends to decrease as the gradient scale length of the preplasma increases. This supports the idea that the cleaner the laser pulse, the better the acceleration [5]. However, it has also been reported that a soft prepulse can lead to a small increase of the maximum proton energy [6–8]. It has been attributed to an enhanced heating of the plasma due to resonant absorption at the front [9] or to the breaking of the ion plasma wave in the density gradient at the back of the foil [10].

The increase of the maximum energy is important for applications such as proton oncology [11, 12]. Because the scaling with laser intensity show a rather slow increase of the maximum proton energy [13], it is important to optimize the efficiency by properly designing the interaction in terms of laser and target parameters. This experimental study gives a more detailed overview of the effect of a short prepulse on the acceleration of protons. Data from many shots have been acquired with an independent variation of the prepulse delay and its intensity while keeping other parameters constant, which bridges the gap left by previous studies carried out under specific conditions: (i) with a 400 fs prepulse at a delay of 50 ps on 1.8 μm -thick targets [6], (ii) with a 55 fs prepulse at a fixed delay of 9 ns [7], and (iii) using a 350 fs prepulse on the rear-side of 25 μm -thick targets and ps delays [8].

The previous experiments have showed that a prepulse with different characteristics can enhance the maximum energy of the protons but they did not clearly point out for which set of parameters this is happening. In this article we are presenting a parametric study which defines the region where this increase is possible.

Y. Glinec · G. Genoud · O. Lundh · A. Persson ·
C.-G. Wahlström (✉)
Department of Physics, Lund University, P.O. Box 118,
22100 Lund, Sweden
e-mail: claes-goran.wahlstrom@fysik.lth.se
Fax: +46-46-2224250

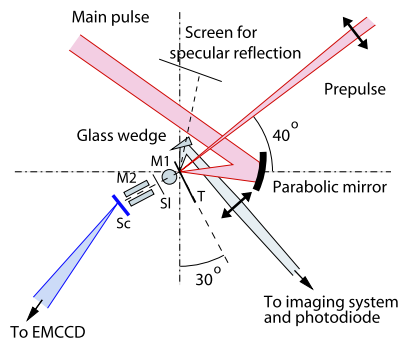


Fig. 1 Experimental setup. Details are given in the text. (T) Target, (M1) weak-field magnet, (SI) Slit, (M2) Spectrometer magnet, (Sc) Scintillator

2 Experimental method

The experiment is performed using the 10 Hz multi-terawatt laser at the Lund Laser Centre (LLC). It is a Ti:sapphire system based on the Chirped Pulse Amplification (CPA) scheme and operating at 800 nm, delivering for this experiment 0.7 ± 0.1 J of laser energy on the target in 50 fs at Full Width at Half Maximum (FWHM). As shown on Fig. 1, the laser beam is focused using an $f/3$ off-axis parabolic mirror to a 5 μm FWHM spot, yielding an inferred peak intensity exceeding $6 \times 10^{19} \text{ W/cm}^2$. In the focal plane, 3 μm thick aluminium foils are positioned for p-polarized irradiation at 30° angle of incidence.

The temporal profile of the main pulse, on the ps timescale, is also shown in Fig. 1. Thanks to the addition of a preamplifier and a saturable absorber in the laser system [14], the contrast ratio at 100 ps (the ratio between the peak intensity of the laser and the intensity 100 ps earlier) is better than 10^9 . The prepulse is extracted from the main beam before compression, sent to a separate compressor, and focused on target at an incidence angle of 10° using an $f/25$ doublet lens to a large focal spot of diameter 28 μm (FWHM). The initial energy of the prepulse (25 mJ) is filtered using calibrated neutral densities corresponding to an adjustable peak intensity on target of $0-2.5 \times 10^{16} \text{ W/cm}^2$ for a pulse duration of 100 fs. The prepulse intensity level is shown in Fig. 2. The arrival time of this pulse is controlled by a translation stage and can be varied between 0 and 1.5 ns.

The detection system is an ion spectrometer [15] consisting of a 50 mm-long magnetic field of effective value 0.7 T, a BC-400 scintillating screen from Saint-Gobain, and a 44 μm -wide and a 10 mm-thick iron slit, the back of which is placed at 55 mm from the interaction point (giving a proton energy resolution of ± 0.4 MeV at 10 MeV). The light

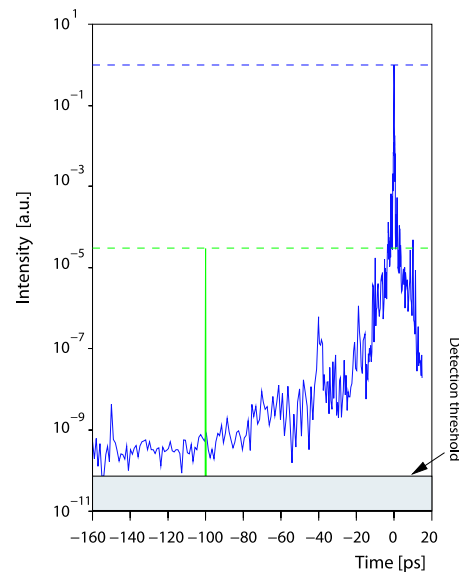


Fig. 2 Temporal intensity profile from third order autocorrelator and relative intensity level of the adjustable prepulse (illustrated for the case of $5 \times 10^{14} \text{ W/cm}^2$)

emitted by the scintillator is collected by a lens in a solid angle 4 msr and detected by an Electron Multiplying Charge Coupled Device camera (EMCCD). A 70 nm spectrally-wide band-pass filter centered at 450 nm is used to transmit the light emitted by the scintillator and an additional weak magnetic field is applied between the target and the slit. This magnetic field peaks at 120 mT and deflects electrons to prevent the charging of the slit, which could affect the measurement of the ion spectrum. A 60 μm thick aluminium filter covers the scintillator to stop any other ions but protons. This gives a lower proton cutoff of 2.5 MeV. Despite the sensitivity of our detection to other particles (X-rays, electrons), a tremendous asset of this system is its speed, which makes an optimization of the signal possible in “real-time.”

The shot-to-shot positioning of the target is guided by imaging the reflexion from a colinear HeNe beam on the target with a magnification factor of 15. This gives an accuracy of $\pm 5 \mu\text{m}$ and allows monitoring the overlap of the two beams. Every 6–7 shots (every 30 min), the alignment of the two beams is checked, and the laser energy is measured. If any variation is observed, the shots are rejected from the analysis. The final data comprises a total of 121 shots.

3 Experimental results

Figure 3 shows the variation in maximum proton energy for delays ranging from 100 fs to 1.5 ns and prepulse intensity

levels ranging from 2×10^{13} to $2.5 \times 10^{16} \text{ W/cm}^2$. The variation in maximum energy is compared to reference shots taken during the sequence of shots. This reduces the error

due to any day-to-day variations of the laser alignment and intensity. On the reference shots, the average maximum energy is 7.3 MeV.

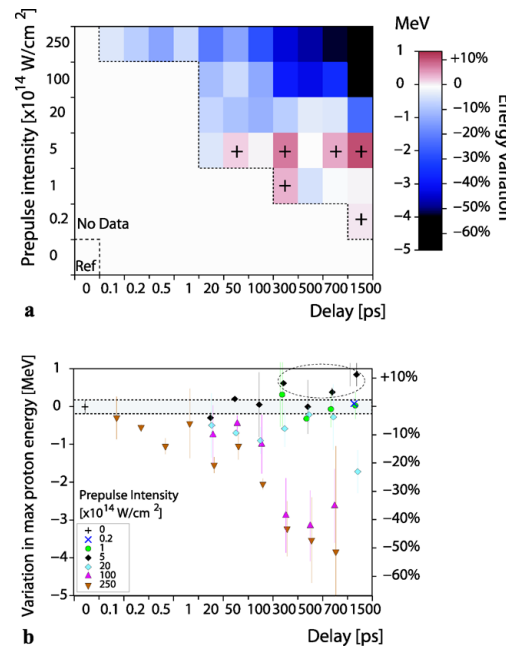


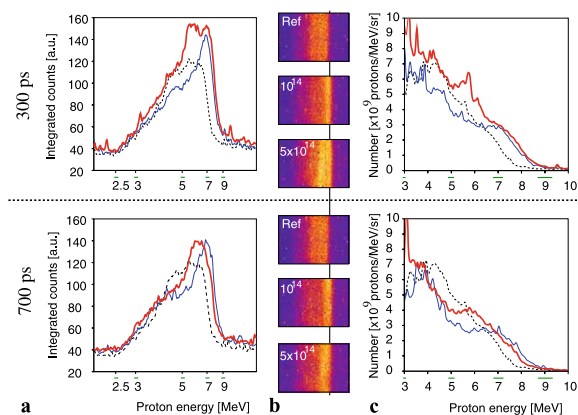
Fig. 3 Variation of maximum proton energy vs prepulse delay and intensity. (a) Overview of the evolution of the maximum proton energy, (b) contains error bars for the same dataset (121 shots). The ellipse contains data points for which the maximum energy increases with the prepulse. The error bars correspond to ± 1 standard deviation of the fluctuations. Data points have been slightly shifted sideways to avoid overlap of the errorbars. Axes representing delay and intensities are not linear. The reference energy is 7.3 MeV

At short delays (below 20 ps), an intense prepulse is required to exceed the ASE intensity level of the main pulse shown in Fig. 1. A prepulse intensity of $3 \times 10^{16} \text{ W/cm}^2$ leads to a decrease of the maximum proton energy already after 20 ps. On this timescale, only the front of the target is affected and essentially only the electron density profile. For a prepulse intensity above $5 \times 10^{14} \text{ W/cm}^2$ and delay above 100 ps, the maximum proton energy tends to decrease with an increase of any of these two parameters. At moderate prepulse intensities (around $1\text{--}5 \times 10^{14} \text{ W/cm}^2$), we observe an increase of the maximum proton energy (identified by "+" marks).

The energy gain reported in Fig. 3a is rather small (about 10%). Error bars, defined as the standard deviation of fluctuations, are shown in Fig. 3b for the same data. It turns out that there are several data points at $5 \times 10^{14} \text{ W/cm}^2$ which are significantly above the fluctuations (at 300, 700, and 1500 ps). Moreover, these points correspond to averaged data (10 shots in total) obtained during 3 different days, and the same trend appeared every time. During scans at a given delay, the prepulse intensity was varied nonmonotonically, thus preventing any correlation between maximum energy and time (such as the evolution of laser parameters during the day). On the other hand, the size of the error bars does not allow us to confirm the results presented in [6] at 50 ps, but this difference might also arise from different ASE levels and the fact that thinner foils were used in [6].

In addition to these observations of the evolution of the maximum energy, we also see an effect of the prepulse on the shape of the spectrum, as shown in Fig. 4. These shots were taken at a delay of 300 and 700 ps, respectively, and belong to the same series of shots. Column (a) contains the lineouts of the raw signal obtained on the EMCCD, on

Fig. 4 (a) Lineouts of proton spectra for different prepulse intensities at a delay of 300 and 700 ps. (b) Corresponding raw images with a vertical line to guide the eye. (c) Spectra obtained after deconvolution by the dispersion and the dose deposition. (Dashed line) no prepulse, (thin, blue) prepulse intensity of 10^{14} W/cm^2 , (thick, red) prepulse intensity of $5 \times 10^{14} \text{ W/cm}^2$. Horizontal bars below the horizontal axis represent the resolution of the detector



a nonlinear energy scale, which clearly shows the shift to higher proton energies with a prepulse. On this scale, one can also see a relative increase of the high-energy population and a relative decrease of the low-energy population at 700 ps. Column (c) shows the corresponding spectra, on a linear energy scale, after deconvolution of the dispersion and taking into account the dose deposited by protons after the aluminium filter. The calibration of the optical system was done by a simultaneous measurement of a proton spectrum on a piece of CR39 (nuclear track detector) and the scintillator, by covering one half of the proton spectrum by the CR39.

4 Conclusion and outlook

We confirm in this article that a prepulse does not only produce negative effects but can also increase the maximum energy of the protons under certain conditions (right delay and intensity). We also found for which set of parameters this increase is observed. However, the next step would be to explain why this increase is occurring for these specific parameters. As an outlook, we present in the following some ideas that should be studied in future experiments to explain our observations.

With our experimental parameters, the shock breaks out through the foil after some hundreds ps. The enhancement of the proton energy is observed in the same timescale. This implies that effects occurring both at the front and at the back of the foil may be involved. For this reason, it is very difficult to give a clear explanation for our observation without further investigation. By using thicker targets, thereby excluding back side effects, this could be sorted out.

On the front side, the preplasma triggers an expansion of the target which can improve the resonant absorption of the laser at an oblique incidence in p-polarisation. This effect competes with the effective increase of the target thickness while the plasma expands into vacuum [9]. Other effects could also influence the interaction, for example, self-focusing, refraction, or instabilities. Nonlinear effects, such as relativistic transparency or hole boring, can make the laser pulse penetrate deeper. It makes it difficult to predict the exact absorption rate, but this interplay was shown by Maksimchuk et al. [6] to enhance temporarily the maximum ion energy for an irradiance between 10^{14} – 10^{15} W/cm². On the rear side, the heating by hot electrons or X-rays and the arrival of the shockwave launched by the prepulse will also trigger an expansion. The breaking of the ion wave can temporarily increase the ion population at high energy and affect the interaction [8].

The reader should also be aware of the fact that the spectrum is recorded only along the target normal: any energy-dependent variation of the divergence or the direction of the

proton beam can affect the shape of the spectrum along the line of sight. An energy-dependent skew in the proton beam direction has been previously reported, which came from the deformation of the target foil induced by the ASE prepulse on the ns timescale [16]. Recently, Carroll et al. have observed an evolution of the spatial profile of the proton beam with a ns prepulse also on the Vulcan laser system at the Rutherford Appleton Laboratory [17]. In the present experiment, at the front side, the main pulse interacts with a large 1D-like density profile, but on the back, the typical proton source size is less than 20 μm [18], which is only slightly smaller than the FWHM of the prepulse, and influence on the divergence of the proton beam might still exist.

An increase of the electron temperature at the front side can contribute to the increase of the maximum proton energy, but it is unlikely to reduce the population of protons at low energy, shown in Fig. 4. The observed change in the shape of the spectrum might be a signature of the breaking of the ion wave (Landau damping) as shown in Fig. 13 in [10] or from transverse effects on the angular distribution of the proton beam (an increase of the divergence for protons with low energy would decrease the collection efficiency in this spectral range). A more detailed description would require extensive numerical studies which are beyond the scope of this study.

In conclusion, we report on an experimental parametric study which gives new results on the effect of a prepulse on proton acceleration. We used a short (100 fs), intense and independent prepulse with variable intensity and delay with respect to the main pulse. Under moderate irradiation ($\sim 10^{14}$ W/cm²), we observe an increase of the maximum proton energy and a variation in the shape of the proton spectrum, measured along the target normal. Various mechanisms such as an increased absorption, the breaking of the ion wave, and transverse effects are discussed as possible contributions to the observed features.

Acknowledgements The authors acknowledge the financial support from the Swedish Research Council and the Knut and Alice Wallenberg Foundation. This research was supported by the Marie Curie Early Stage Training Site MAXLAS (MEST-CT-2005-020356) within the 6th European Community Framework Programme.

References

1. A.J. Mackinnon, M. Borghesi, S. Hatchett, M.H. Key, P.K. Patel, H. Campbell, A. Schiavi, R. Snavely, S.C. Wilks, O. Willi, Phys. Lett. **88**, 215006 (2002)
2. I. Spencer, K.W.D. Ledingham, P. McKenna, T. McCanny, R.P. Singha, P.S. Foster, D. Neely, A.J. Langley, E.J. Divall, C.J. Hooker, R.J. Clarke, P.A. Norreys, E.L. Clark, K. Krushelnick, J.R. Davies, Phys. Phys. E **67**, 046402 (2002)
3. M. Kaluza, J. Schreiber, M.I.K. Santala, G.D. Tsakiris, K. Eidmann, J.M. ter Vehn, K.J. Witte, Phys. Phys. Lett. **93**, 045003 (2004)

4. D. Neely, P. Foster, A. Robinson, F. Lindau, O. Lundh, A. Persson, C.-G. Wahlström, P. McKenna, *Appl. Phys. Lett.* **89**, 021502 (2006)
5. T. Cecchetti, A. Levy, H. Popescu, F. Reau, P. D'Oliveira, P. Monot, J.P. Geindre, E. Lefebvre, P. Martin, *Phys. Rev. Lett.* **99**, 185002 (2007)
6. A. Maksimchuk, S. Gu, K. Flippo, D. Umstadter, V.Y. Bychenkov, *Rev. Phys. Lett.* **84**, 4108 (2000)
7. A. Yogo, H. Daido, A. Fukumi, Z. Li, K. Ogura, A. Sagisaka, A.S. Pirozhkov, S. Nakamura, Y. Iwashita, T. Shirai, A. Noda, Y. Oishi, T. Nayuki, T. Fujii, K. Nemoto, I.W. Choi, J.H. Sung, D.-K. Ko, J. Lee, M. Kaneda, A. Itoh, *Phys. Plasmas* **14**, 043104 (2007)
8. J. Fuchs, C.A. Cecchetti, M. Borghesi, T. Grismayer, E. d'Humières, P. Antici, S. Atzeni, P. Mora, A. Pipahl, L. Romagnani, A. Schiavi, Y. Sentoku, T. Toncian, P. Audebert, O. Willi, *Phys. Rev. Lett.* **99**, 015002 (2007)
9. Y. Sentoku, V. Bychenkov, K. Flippo, A. Maksimchuk, K. Mima, G. Mourou, Z. Sheng, D. Umstadter, *Appl. Phys. B* **74**, 207 (2002)
10. T. Grismayer, P. Mora, *Phys. Plasmas* **13**, 032103 (2006)
11. S. Bulanov, V.S. Khoroshkov, *Plasma Phys. Rep.* **28**, 453 (2002)
12. V. Malka, S. Fritzler, E. Lefebvre, E. d'Humières, R. Ferrand, G. Grillon, C. Albaret, S. Meyroneinc, J.P. Chambaret, A. Antonetti, D. Hulin, *Med. Phys.* **31**, 1587 (2004)
13. T. Esirkepov, M. Yamagiwa, T. Tajima, *Phys. Rev. Lett.* **96**, 105001 (2006)
14. Y. Glinec, A. Persson, M. Glimtoft, E. Pourtal, C. Homann, O. Lundh, C.-G. Wahlström, (2008 in preparation)
15. P.S. Foster, M. Steeter, D. Carroll, F. Lindau, O. Lundh, A. Persson, C.-G. Wahlstrom, P. McKenna, B. Dromey, M. Zepf, D. Neely, (2008 in preparation)
16. F. Lindau, O. Lundh, A. Persson, P. McKenna, K. Osvald, D. Batani, C.-G. Wahlström, *Phys. Rev. Lett.* **95**, 175002 (2005)
17. D.C. Carroll, P. McKenna, O. Lundh, F. Lindau, C.-G. Wahlström, S. Bandyopadhyay, D. Pepler, D. Neely, S. Kar, P.T. Simpson, K. Markey, M. Zepf, C. Bellei, R.G. Evans, R. Redaelli, D. Batani, M.H. Xu, Y.T. Li, *Phys. Rev. E* **176**, 065401 (2007)
18. O. Lundh, Y. Glinec, C. Homann, F. Lindau, A. Persson, C.-G. Wahlström, D.C. Carroll, P. McKenna, *Appl. Phys. Lett.* **92**, 011504 (2008)

PAPER VIII

Hollow microspheres as targets for staged laser-driven proton acceleration

M. Burza, A. Gonoskov, G. Genoud, A Persson, K. Svensson, M. Quinn, P. McKenna, M. Marklund and C.-G. Wahlström.

New J. Phys. **13**, 013030 (2011).

New Journal of Physics

The open-access journal for physics

Hollow microspheres as targets for staged laser-driven proton acceleration

M Burza^{1,5}, A Gonoskov^{2,3}, G Genoud¹, A Persson¹, K Svensson¹, M Quinn⁴, P McKenna⁴, M Marklund² and C-G Wahlström¹

¹ Department of Physics, Lund University, PO Box 118, SE-221 00 Lund, Sweden

² Department of Physics, Umeå University, SE-901 87 Umeå, Sweden

³ Institute of Applied Physics, Russian Academy of Sciences,

46 Ulyanov Street, Nizhny Novgorod 603950, Russia

⁴ SUPA Department of Physics, University of Strathclyde, Glasgow, G4 0NG, UK

E-mail: matthias.burza@fysik.lth.se

New Journal of Physics **13** (2011) 013030 (14pp)

Received 21 July 2010

Published 21 January 2011

Online at <http://www.njp.org/>

doi:10.1088/1367-2630/13/1/013030

Abstract. A coated hollow core microsphere is introduced as a novel target in ultra-intense laser–matter interaction experiments. In particular, it facilitates staged laser-driven proton acceleration by combining conventional target normal sheath acceleration (TNSA), power recycling of hot laterally spreading electrons and staging in a very simple and cheap target geometry. During TNSA of protons from one area of the sphere surface, laterally spreading hot electrons form a charge wave. Due to the spherical geometry, this wave refocuses on the opposite side of the sphere, where an opening has been laser micromachined. This leads to a strong transient charge separation field being set up there, which can post-accelerate those TNSA protons passing through the hole at the right time. Experimentally, the feasibility of using such targets is demonstrated. A redistribution is encountered in the experimental proton energy spectra, as predicted by particle-in-cell simulations and attributed to transient fields set up by oscillating currents on the sphere surface.

⁵ Author to whom any correspondence should be addressed.

Contents

1. Introduction	2
2. Experiment	4
2.1. Target preparation	4
2.2. Experimental setup	4
2.3. Experimental measurements and results	6
3. Simulations	8
3.1. Simulation results	9
4. Discussion and outlook	10
5. Conclusions	12
Acknowledgments	12
References	13

1. Introduction

Laser-driven ion acceleration is an area of research that currently attracts significant scientific interest. The ion beams produced in these experiments have several attractive characteristics, such as very low transverse emittance and small virtual source size [1] together with a short pulse duration (at the source). Proposed applications of this possibly compact ion beam source include ion radiotherapy for cancer treatment [2, 3], isotope production for medical imaging techniques [4], proton radiography of inertial fusion plasmas [5] and implementation as injectors for future ion accelerators.

In a typical experiment, a high-power laser pulse of short duration, \leq ps, is focused on the surface of a thin foil to an intensity exceeding 10^{19} W cm $^{-2}$. The laser interacts with target electrons and a population of hot electrons with a Maxwellian temperature of typically a few MeV is generated. A large fraction of these electrons traverse the target and build up exceptionally high electrostatic fields, \sim TV m $^{-1}$, at the rear surface of the foil, in a direction normal to the target surface. Atoms on the target surface are rapidly field ionized and accelerated. This is referred to as target normal sheath acceleration (TNSA) [6]. Because of the presence of hydrocarbon and water vapour on the surfaces of the foils (in typical vacuum conditions \sim 10 $^{-5}$ mbar), protons are the dominating ion species. Due to their high charge-to-mass ratio, protons are more efficiently accelerated than heavier ions.

The acceleration of protons behind the target foil is very rapid, due to the high field strength. However, this field is present during a short time only, limiting the maximum energy reached by the protons. The energy spectra of these proton beams exhibit a longitudinal emittance comparable to that of conventional accelerators, with a quasi-exponential shape and a distinct cut-off energy [6]. The divergence of the proton beam is typically \sim 30° half-angle. Significant theoretical and experimental efforts have been devoted to the exploration of a means of boosting the maximum proton energy without the use of increasingly larger laser systems [7, 8].

Practical limitations in laser size and costs, laser materials and repetition rate are necessitating alternative or modified laser acceleration schemes and targets in order to further increase the peak proton energy. It has been found that the maximum proton energy and laser-to-ion energy conversion is enhanced by the use of ultra-thin targets in combination with laser pulses of high temporal contrast [9]. Staging, i.e. combining two or more accelerator stages in series,

may be one way to post-accelerate a selected portion of the protons accelerated in a preceding TNSA stage and thus raise the maximum proton energy and reduce the energy spread [10]. In parallel, extensive studies on controlling beam parameters such as collimation and means to produce quasi-monoenergetic energy distributions have been carried out [11, 12]. In particular, mass-limited targets can be used to reduce the energy spread of the protons [13]–[15]. Curved target foils [16], electrostatic charging of specially shaped targets [17] and separate focusing cylinders [18] enable spatial shaping of the proton beam.

In addition, experiments and numerical modelling have shown that while part of the hot electron distribution is passing through the target foil, a significant part is also spreading laterally along the target. McKenna *et al* [19] found that, when these electrons reach the target edges, after a time determined by the geometrical size of the target and the lateral electron transport velocity, they establish quasi-static electric fields, similar to the one produced behind the target during TNSA, resulting in ion acceleration from the edges. Normally, this mechanism just represents a loss of absorbed laser energy, which is converted to hot electrons but not contributing to the quasi-static sheath built up at the target rear side. In a recent study [15], however, using very small diameter targets, the refluxing of transversely spreading electrons was found to enhance and smooth the sheath field for TNSA from the rear surface.

In this paper, we discuss the use of hollow microspheres, as novel targets for laser acceleration of protons. With this target, several of the above features are combined, which may facilitate improved laser-to-proton efficiency, eventually leading to increased proton energy and reduced divergence. Lateral electron transport is here utilized to set up a post-acceleration field for staged acceleration.

The basic idea behind our approach is to use hollow microspheres with diameters of about 10–50 μm and sub-micrometer wall thickness. In each sphere a small circular opening is made. We refer to the position of this opening as the ‘north pole’ (see figure 1). A short pulse laser irradiates the sphere at the ‘south pole’, where TNSA takes place. The primary proton direction will be along the z -axis, defined as the axis from the south pole passing through the north pole of the sphere. The spherical surface, with TNSA taking place from the concave side, results in a collimated or even converging proton beam. Therefore, all the protons can be made to pass through the opening at the north pole. In addition—and this is the key point—electrons leaving the laser focus laterally in any direction along the sphere surface will be guided on different longitudes over the sphere and eventually reach the edge of the opening at the north pole simultaneously after some given time. A very strong quasi-static electric field is then formed in the opening, along the z -axis. This quasi-static field will post-accelerate protons passing through the opening at the correct time.

In our approach to test this idea, theoretical and experimental studies go hand in hand:

To test the experimental feasibility, we perform experiments, at the Lund High Power Laser Facility, with commercially available hollow microspheres of 50 μm diameter.⁶ The walls of these spheres are made of glass with a thickness of 0.5–1 μm and coated with a \sim 50 nm silver layer (see the inset of figure 1), which facilitates the optical alignment and guiding of electrons along the sphere surface. Openings of different sizes are laser micromachined. We present these experiments in section 2, including target preparation, fixation and alignment in the experimental setup together with first results.

⁶ Such spheres are very low weight and low cost objects. They weigh only some tens of ng each and cost \sim 1 USD for 10^5 Ag-coated spheres. The manufacturing of the hole at the north pole, however, is part of the local target preparation and not included in the price.

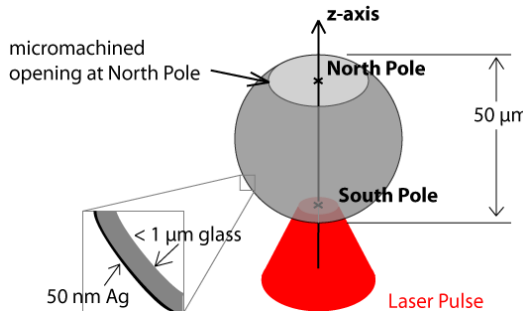


Figure 1. A glass hollow microsphere, with an ~ 50 nm silver coating on its $\leq 1 \mu\text{m}$ thick wall, is struck by a laser pulse at the ‘south pole’. TNSA protons are emitted through a circular opening at the ‘north pole’ and post-accelerated.

In parallel, we perform particle-in-cell (PIC) simulations of hollow conducting spheres with openings, irradiated by short laser pulses. These simulations, presented in section 3, qualitatively describe the dynamics involved.

We discuss the outlook and prospects for further experiments in section 4 and present the conclusions in section 5.

2. Experiment

2.1. Target preparation

Isolated spheres are suspended into a nylon mesh grid, where both the front and back sides of each sphere are accessible for further processing. Openings in the spheres are made with a confocal microscope-based laser micromachining setup. In a two-step process the silver coating is ablated in a well-defined region on the sphere surface, followed by ablation of the glass substrate. This is done with a lateral resolution of about $2 \mu\text{m}$ utilizing a femtosecond laser system running at 10 Hz repetition rate. Real-time target observation and a high numerical aperture in the setup facilitate both high drilling accuracy and control in the transverse direction, while at the same time preventing the TNSA surface inside the sphere from being damaged in the process.

Afterwards, the target, which is still fixed in the nylon mesh, is mounted in a holder. This also accommodates a gold mesh, placed close to the sphere’s north pole, to extract information about proton trajectories, as will be discussed later.

2.2. Experimental setup

The Lund multi-terrawatt laser, which is a Ti : sapphire system based on chirped pulse amplification (CPA), is used for this experiment. In this experiment, it is tuned to 850 mJ pulse energy at 805 nm centre wavelength with a typical pulse duration of 42 fs FWHM. Due to the sub-micron thickness of the sphere walls and the thin silver coating on them, an amplified spontaneous emission (ASE) contrast better than 10^8 some tens of picoseconds prior to the pulse peak is desirable.

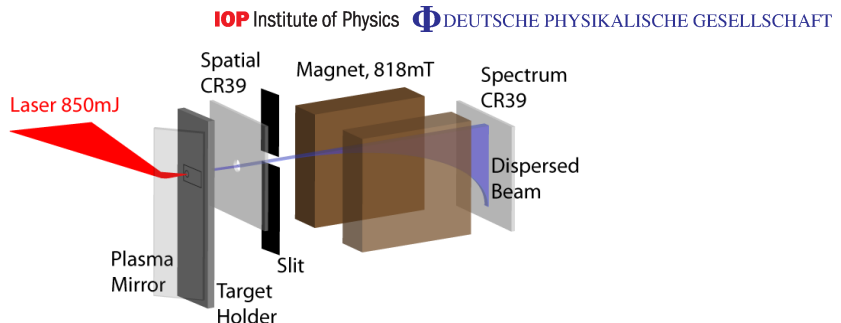


Figure 2. The laser pulse (red) is impinging on the PM at Brewster's angle, which reflects the pulse onto the target at normal incidence. After some centimetres of free passage the resulting particle beam (blue) reaches a CR-39 detector plate, which has the function of providing a lateral image of the beam profile and at the same time enabling a fraction of the beam to enter the slit of a subsequent permanent magnet spectrometer. After traversing the field, a vertically dispersed spectrum is recorded on a second CR-39 plate.

To optimize contrast on a very fast timescale, the convergent, horizontally polarized laser pulse hits a dielectric plasma mirror (PM) at Brewster's angle (3.0 ± 0.2 mm) prior to the primary focus. At this location, the PM is operating at $(8.5 \pm 1.1) \times 10^{15} \text{ W cm}^{-2}$ spatially averaged peak intensity over the beam diameter (I_{centre}/e^2). When activated, it deflects the laser beam onto the target, at normal incidence (see figure 2).

Plasma mirror characteristics have been investigated by many groups (see e.g. [20]–[22]). A PM assembly, similar to the one applied in the present experiment, was utilized by Neely *et al* [9], using the Lund laser system. In that experiment, proton beams from Al foil targets as thin as 20 nm were observed. Our experiment relates to that one as the very thin silver coating on our target surface is of comparable thickness. Ray tracing, taking a 22 nm FWHM broad Gaussian spectrum and a p-polarized converging beam into account, predicts a contrast increase by a factor of 100 in our experiment (assuming a maximum reflectivity $\sim 50\%$ from the PM [22]).

Together with a third-order autocorrelation contrast measurement, 2 ps prior to the main pulse, a contrast better than 10^6 on the target can be guaranteed for an intact rear TNSA surface during the first phase of acceleration. This contrast is due to non-perfect compression in the CPA chain and should not be mistaken for the ASE contrast, encountered on a longer picosecond timescale prior to the main pulse, which is of the order 10^{11} on the target.

The infrared (IR) pulse is focused by an $f/3$ off-axis parabolic mirror (OAP) down to a $4.4 \mu\text{m}$ spot diameter (intensity FWHM), containing 39% of the total energy and reaching a peak intensity of $\sim 3 \times 10^{19} \text{ W cm}^{-2}$. Target positioning is accomplished by a confocal imaging system: an expanded HeNe laser beam is superimposed with the IR and a confocal reflection from the silver-coated target surface is imaged, utilizing the OAP as an objective.

The detector system for protons, designed to simultaneously provide a spatial beam profile and a spectrum, is depicted in figure 2. It consists of a primary CR-39 plate at some centimetres distance from the target, which is utilized to characterize the transverse spatial beam profile. This plate is covered by a $6 \mu\text{m}$ Al foil, which stops protons below 0.5 MeV [23]. At its centre,

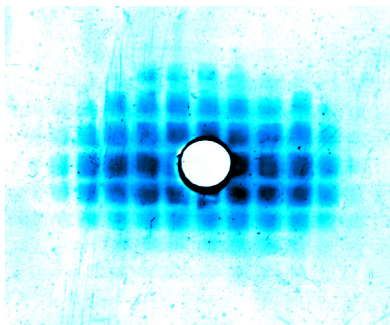


Figure 3. Proton beam profile on a CR-39 plate showing a magnified Au mesh image, recorded (24 ± 0.5) mm distance from the target.

a ~ 4 mm diameter hole enables protons close to the target normal axis to continue to the momentum dispersive part of the detector and access an $88 \mu\text{m}$ wide entrance slit of a permanent magnet spectrometer, where they traverse a 51 mm long and 818 mT strong effective field. The vertically dispersed proton spectrum is then recorded by a second CR-39 plate with an accuracy of ± 0.2 MeV at 4 MeV proton energy. By this arrangement, spectra can be correlated to the lateral position within the particle beam.

2.3. Experimental measurements and results

After optimization of the PM working distance with the help of proton beams originating from flat 400 nm thick Al foil targets, shots were taken on machined and unmachined microspheres as well as on $0.9 \mu\text{m}$ thick Mylar foil targets.

Several shots were taken on machined microspheres with holes of typically $18 \mu\text{m}$ diameter. An example of a proton beam imprint originating from such a sphere on the spatial CR-39 plate, covered by $6 \mu\text{m}$ Al and located at (24.0 ± 0.5) mm distance from the target, can be seen in figure 3.

One can see a slightly oval beam profile. This slight asymmetry can be attributed either to a non-uniform Ag coating on the sphere's south pole or to grazing incidence of the laser energy around the z -axis due to the curved sphere surface: at a given latitude, the linear polarization of the laser pulse will be incident as p- or s-polarization on the spherical surface, depending on the azimuthal angle. Polarization effects will also facilitate different strengths of the surface currents, depending on the longitude where electrons propagate around the sphere [24].

One can further see the imprint of the earlier mentioned Au mesh on the spatial proton beam image, which is introduced into the proton beam path close to the target. This rectangularly shaped $4 \mu\text{m}$ thick mesh features squared holes with a nominal aperture of $11 \times 11 \mu\text{m}^2$ and a lateral wire width of $5 \mu\text{m}$. It is fixed at $(165 \pm 2) \mu\text{m}$ distance from the rim of the opening of the microsphere. The motivation to introduce this mesh is twofold: firstly, it verifies that protons contributing to the signal on the spatial CR-39 plate are not due to edge emission at the north pole, which would have resulted in a distinctively different shadow image. Secondly, thanks to this mesh the protons can be shown to come from a virtual source located $(54 \pm 12) \mu\text{m}$ from the inner sphere TNSA surface, i.e. very close to the opening. This estimate is valid for the majority

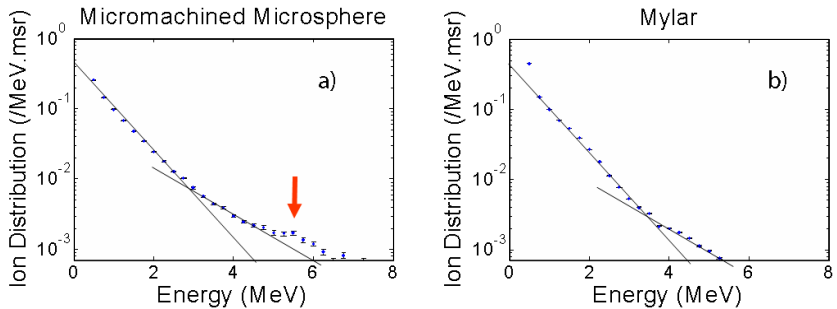


Figure 4. Normalized proton spectra from a microsphere target (a) and a Mylar plane foil (b). The red arrow in (a) indicates a region of constant yield in contrast to the strictly decreasing number density from plane foil TNSA experiments, such as the one depicted in (b); black lines are a dual-temperature guide to the eye.

of particles traversing the opening at late times, where we expect the surface oscillations to have vanished. In order to visualize the effects of a transient field emanating from the rim of the microsphere opening, one would have to filter this image to the appropriate energy. However, as will be discussed later, with our present experimental parameters, we expect only the fastest particles to be affected by these fields, so a filtered signal would become very weak.

By neglecting Coulomb repulsion between protons in the beam, and tracing proton trajectories further back, one can make a rough estimate about the proton emission surface. We find that proton emission seems to occur from a solid angle covering $\approx 140\pi$ msr of the inner shell, measured from the centre of the sphere. This compares to a focal spot, covering $\approx 8\pi$ msr (intensity FWHM), and is consistent with previous observations of the TNSA surface source area being considerably larger than the laser focus [25, 26]. The virtual proton source in a flat foil TNSA experiment [27] was pinpointed to several hundreds of microns distance before the target front side, i.e. the laser-irradiated side. A spherical target, such as the one used for isochoric heating [28, 29], combines ballistic proton propagation with target curvature and an altered electron distribution. A particle focus near the north pole is consistent with these findings.

To further verify that the protons are indeed emitted from the sphere interior, we irradiate closed hollow microspheres that have not gone through the laser micromachining stage. Lacking hydrogenic contaminations, such as water vapour, on the interior surface of the sphere, TNSA of protons is not expected to occur there. Indeed no protons with energies sufficient to be recorded by our diagnostics ($E_{\text{proton}} > 0.8$ MeV) are observed. In addition, lacking the opening and retaining the silver coating, return currents will prevent the formation of a strong edge field at the north pole. This will be further discussed in section 3.1.

Spectra from sphere targets with openings between 18 and $20\ \mu\text{m}$ were taken and a typical spectrum can be seen in figure 4(a). A clear high-energy ‘cut off’ is not visible in the data, and values above 8 MeV are ignored to ensure that the data presented here are at least one order of magnitude above the noise level. Reference shots are taken on flat $0.9\ \mu\text{m}$ thick Mylar foil targets. A typical proton spectrum can be seen in figure 4(b). Even though the laser absorption

and particle yield are expected to be different as compared to the silver-coated glass surface of the microspheres (~ 30 times higher particle number), those shots provide reference spectra, enabling the identification of special features in the microsphere spectra.

All microsphere spectra from the experimental study look very similar, but with an integrated particle yield varying by a factor of 4, which is twice as much as for the Mylar targets. There are indeed features present that could possibly be attributed to a secondary field interaction and a post-acceleration by a secondary field at the sphere opening, which is still prevailing during arrival of the fastest protons. In all microsphere spectra, there is a slight modification of particle yield between 5.5 and 6.5 MeV, where the counts per energy bin remain nearly constant (figure 4(a), red arrow) as compared to the strictly decreasing dual exponential decay observed from the flat foil targets, shot under the same experimental conditions (figure 4(b)). (Likewise, previous experiments carried out with various planar targets using the Lund laser system [30] have resulted in spectra very similar to the ones presented here for Mylar foils.) The plateau in the microsphere spectra can be understood in terms of a spectral redistribution of the order of 1 MeV of proton energies as a result of a secondary field interaction near the opening. Looking at the experiment the other way around, we can regard the protons as a probe for intracavity fields as well. A two-temperature curve fit provides comparable temperatures for low energies for both the targets ((0.6 ± 0.1) MeV and (0.5 ± 0.3) MeV for spheres and Mylar, respectively) but larger values for the high-energy component from the microsphere spectra ((2.0 ± 0.1) MeV) as compared to the foil spectra ((1.6 ± 0.3) MeV).

In the following section, we will discuss the modelling of the present experiment, giving insights into the dynamic processes of hot electron transport on the sphere surface and motivate the observed spectral features. Beyond that, we will consider a means to enhance the post-acceleration mechanism.

3. Simulations

To improve our understanding of the underlying dynamic processes, we have carried out a number of numerical experiments with the parallel PIC code Extreme Laser–Matter Interaction Simulator (ELMIS), developed by the SimLight group [31]. ELMIS is a relativistic code, which uses a parallel fast Fourier transform (FFT) technique to solve Maxwell's equations.

The processes involved in the setup are essentially of two-dimensional (2D) nature. Thus, we perform 2D simulations in order to retain the appropriate space and time scales while still not compromising the physical outcome. However, the 2D nature restricts the interpretation of these results to a qualitative level as scaling laws behave differently in 2D as compared to 3D space.

In the simulations a linearly polarized TEM00 laser pulse (where electric field lies in the plane of simulation) with $\tau_l = 50$ fs duration (Gaussian profile, FWHM) and a total energy of 1 J is focused to a $10\text{ }\mu\text{m}$ spot on the target surface. The laser field reaches a maximum field strength equal to $\sim 3.5 a_{\text{rel}}$, where $a_{\text{rel}} = 2\pi mc^2/(e\lambda) \approx 3.2 \times 10^{12} \text{ V m}^{-1}$, e and m are the electron charge and mass, respectively, c is the speed of light and $\lambda = 1\text{ }\mu\text{m}$ is the laser wavelength. This corresponds to a maximum intensity of $2 \times 10^{19} \text{ W cm}^{-2}$. The target consists of a hollow metal sphere with $D_S = 32\text{ }\mu\text{m}$ diameter and a $10\text{ }\mu\text{m}$ opening. It has a $0.5\text{ }\mu\text{m}$ thick wall, which in our 2D PIC simulation was considered as a (cylindrical) overdense plasma with the electron density of $50 n_{\text{crit}}$ and an Au^{6+} ion density of $50 n_{\text{crit}}/6$, where $n_{\text{crit}} = \pi mc^2/(\lambda^2 e^2) \approx 1.1 \times 10^{21} \text{ cm}^{-3}$ is the critical density for $\lambda = 1\text{ }\mu\text{m}$.

To simulate TNSA, we consider a 100 nm contaminant layer of protons and electrons with a density $10n_{\text{crit}}$, covering the internal surface of the target. The simulation is done for a box size of $64 \mu\text{m} \times 64 \mu\text{m}$ (4096×4096 cells) with absorbing boundaries for the fields and accumulating boundaries for the particles. The initial plasma temperature is set to 16 keV, and the cell size is 15.625 nm, which is approximately 4 times the Debye length for the considered plasma. In the simulation, 100 virtual particles per cell are used for the electrons and Au^{6+} ions and 20 particles per cell are used for the protons; the total number of virtual particles is 4×10^7 . The time steps are set to $(2\pi/\omega_p)/16 \approx 3 \times 10^{-17}$ s, where $\omega_p = (4\pi e^2 50n_{\text{crit}}/m)^{1/2}$ is the plasma frequency. The duration limit of the simulation is set to when the leading protons in the accelerating bunch reach the simulation box boundary.

3.1. Simulation results

As the laser pulse reaches the target at the south pole it is reflected from the outer overdense plasma surface, initiating electron heating. This time is set to $t = 0$ in the simulation. Subsequently, protons undergo TNSA from the internal surface and move towards the north pole. A part of the heated electrons leave the plasma, thereby producing an electric field retaining part of the electrons to the target surface. Those trapped hot electrons move along the plasma layer, recirculating near the wall and conserving their momentum in the direction along the surface. Eventually they will arrive at the edge of the sphere opening, where they will leave and return to the plasma layer, thus setting up a charge separation field. This process, albeit for a flat target, was discussed and experimentally observed by McKenna *et al* [19]. Due to the relativistic intensity of the laser pulse, the electrons move with a speed close to c , thus forming a bunch size comparable to the longitudinal extension of the laser pulse ($c\tau_l = 15 \mu\text{m}$). This bunch does not effectively carry any charges due to cold return currents within the plasma. However, due to the absence of a return current at the edges, the bunch produces a charge separation field. The simulation shows that this wave is then reflected from the opening at the north pole and heads back to the south pole, where it refocuses, passes through (collisionlessly) and continues moving towards the opening at the north pole again.

The dynamics are illustrated in figure 5(a), where the radial electric field at $3 \mu\text{m}$ distance from the sphere surface is plotted over time and latitude angle (180° corresponds to the south pole, while 0° represents the north pole). Figure 5(b) depicts the electric field component E_z along the z -axis, using red and blue colours. The evolution of the proton density along the z -axis is visualized by the grey distributions, in equidistant frames. In both pictures, one can identify large charge separation fields, set up at the rim due to the absence of a return current.

One can identify certain frames where the field becomes large, alternatingly at the north and the south pole. The periodicity can be estimated as $T_d \approx \pi D_S/v_e$, where v_e is the velocity of the surface dipole wave. From our simulations we obtain $T_d \approx 380$ fs, corresponding to a frequency of 2.64 THz and an electron wave velocity of $v_e \approx 0.9 c$.

When the surface dipole wave reaches the opening it produces electric field maxima at the north pole at times t_1 , t_2 , t_3 (see labels in figure 5(b)), which can be utilized for proton post-acceleration, i.e. staging. Those maxima exist only during relatively short periods. Thus, the timing of the proton bunch and the electron dipole wave is important. In order to have an effective post-acceleration, one would like protons to be pre-accelerated by the TNSA mechanism in such a way that they traverse the vicinity of the north pole when a maximum in accelerating field is present, resulting in a redistribution of the proton energy spectrum.

10

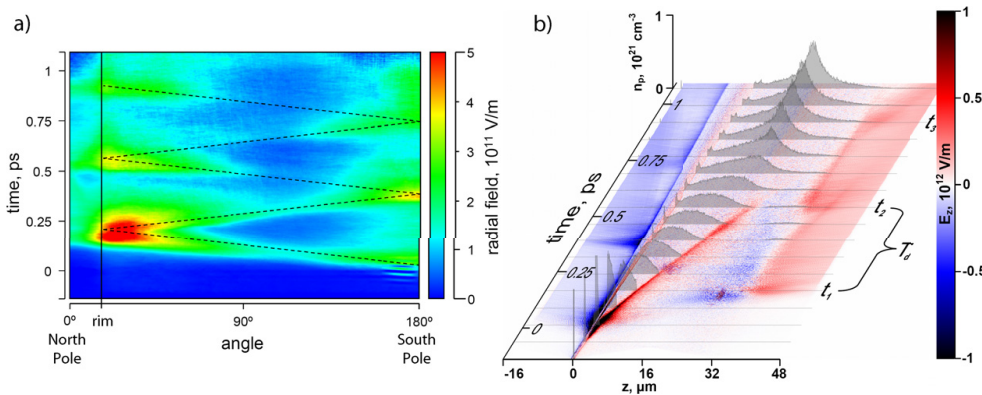
IOP Institute of Physics Φ DEUTSCHE PHYSIKALISCHE GESELLSCHAFT

Figure 5. (a) Radial electric field strength, encountered at $3 \mu\text{m}$ distance from the surface as a function of time. (b) Electric field component E_z along the z -axis; grey plots depict the proton density evolution along the z -axis in equidistant frames.

It should be noted that the surface dipole wave oscillation amplitude decays, which implies that fewer oscillations prior to the proton passage provide a stronger post-acceleration. Additionally to the maxima, a weaker quasi-constant accelerating background field occurs at the opening from t_1 onwards, showing no significant decay on this timescale. Post-acceleration by this background field, which occurs due to a charge up of the sphere during laser irradiation, does not require an accurate timing for the proton passage. However, it provides smaller field strengths as compared to the surface dipole wave oscillations. The effect from both contributions can be seen in figure 6 in the upper marked region, labelled the ‘post-acceleration stage’, where the evolution of the proton energy distribution is displayed as a function of time. (Note that, due to the limited number of particles, modulations in these spatially integrated spectral distributions manifest themselves as lines that could easily be misinterpreted as trajectories.)

The final state of this simulation is summarized in figure 7 together with the emission angle–energy distribution in the inset, taking all protons into account. From this figure it can be seen that the considered geometry provides additional energy of several MeV for a part of the protons that form a bunch with a small divergence of about 8° half-angle.

4. Discussion and outlook

In the present simulation, a fraction of the protons, with kinetic energies around 9 MeV, reach the opening at time t_3 and pass through a spike in the accelerating field of the post-acceleration stage. However, the acceleration exerted on the protons by this field is relatively small. In 2D simulations, the charge increase due to refocusing of electron trajectories at the north pole is not fully reproduced. Even though qualitatively correct, the simulations are therefore expected to underestimate the field effects.

However, a larger fraction of the particles could be post-accelerated if the relative timing between the surface dipole wave and the proton arrival could be controlled. This could be done

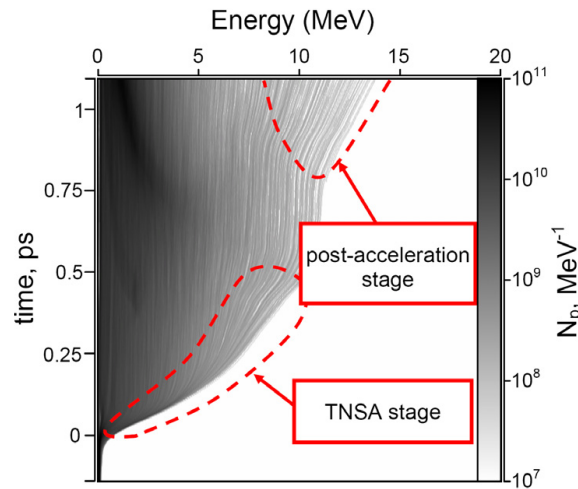


Figure 6. Spatially integrated proton energy distribution along the z -axis with colour-coded number density and its evolution in time.

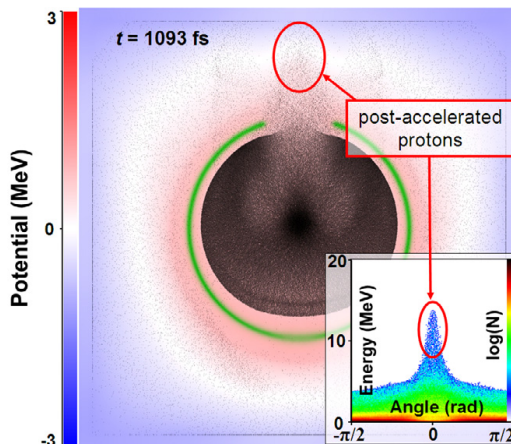


Figure 7. The final instant of the simulation and the corresponding angle–energy distribution of the protons.

either by making use of smaller spheres or oblate spheroidal targets to compensate for their different propagation velocities or by simply increasing the proton temperature in the TNSA stage as they are still moving non-relativistically. In the latter case, an energy of 9 MeV is sufficient for protons to reach the north pole at time t_3 , while 37 MeV would be required for a passage at t_2 and GeV energies for t_1 . TNSA acceleration to the GeV regime is not feasible, but 37 MeV should be within reach of short-pulse laser systems at intensities below $I_{\text{laser}} = 10^{21} \text{ W cm}^{-2}$ [32, 33]. In addition, one might be able to reduce the velocity of the surface electron wave by surrounding the sphere with an appropriate dielectric.

With spheroids the advantages of spheres are conserved, but the relative distance for protons and electrons to propagate can be varied. Simulations with oblate spheroidal surfaces, performed as for the spherical targets above, show both stronger acceleration and a narrower collimation of the protons. Experimentally, however, such targets are not as easily available as spheres.

In the experiment, we irradiated the target at normal incidence to obtain maximum symmetry and facilitate direct comparison with our simulations. However, it is well known that by irradiating the target with p-polarized light at an angle, the efficiency of coupling laser energy to the plasma increases. This should, in our case, enhance both TNSA at the south pole and drive a significantly stronger transverse electron current along the target surface [24]. An extension of both simulation and experimental geometry to allow for non-normal incidence irradiation will be a topic for further study.

Finally, we would like to point out that our target has additional interesting features. One of them is an intermediate particle focus slightly outside the spatial boundaries of the target. This could be used for experiments in fundamental physics that require high proton flux, inherently synchronized with a high-power laser beam line. Additionally, as the microsphere acts as a cavity for electron surface dipole waves, it could provide an efficient means to produce THz radiation with high-intensity lasers. In such an experiment almost all the incident laser energy can be absorbed by irradiating the sphere through the opening at the north pole, launching an electron surface wave from the inside.

5. Conclusions

We have introduced a new scheme for staged laser-driven proton acceleration, using hollow microspheres as targets. On the one side of a microsphere, protons are accelerated by TNSA from the concave inner surface of the sphere. Laser-heated electrons that are spreading transversely in the target, as a charge wave, are refocused on the opposite side of the sphere, where they produce a strong but transient charge separation field in an opening located there. Protons passing through the opening at the correct time can thus be post-accelerated. We have done 2D PIC simulations that confirm that this process indeed occurs and that the electrons spread over the sphere as a charge wave. This wave was found to oscillate back and forth over the sphere while decaying in amplitude, forming charge separation fields in the opening at regular intervals. These simulations also show that protons arriving at the correct time, i.e. those protons that have the right kinetic energy, are post-accelerated. Experimentally we have demonstrated the technical feasibility of preparing and irradiating this type of target. In addition, the preliminary results show some signatures of post-acceleration, although the timing between the electron charge wave and the TNSA protons was far from optimal in this first experiment. Further work with improved relative timing is needed for fully exploring the potential of this new scheme and target geometry.

Acknowledgments

We acknowledge support from the Swedish Research Council (including contract no. 2007-4422 and the Linnaeus grant to the Lund Laser Centre), the Marie Curie Early Stage Training Site MAXLAS (MEST-CT-2005-020356) within the 6th European Framework Programme, the Knut and Alice Wallenberg Foundation, the Swedish National Infrastructure for Computing (SNIC)

and the EPSRC (grant no. EP/E048668/1). This research was further partially supported by the European Research Council under contract no. 204059-QPQV. We also thank D C Carroll for processing the CR-39 plates.

References

- [1] Cowan T E *et al* 2004 Ultralow emittance, multi-MeV proton beams from a laser virtual-cathode plasma accelerator *Phys. Rev. Lett.* **92** 204801
- [2] Malka V *et al* 2004 Practicability of protontherapy using compact laser systems *Med. Phys.* **31** 1587
- [3] Linz U *et al* 2007 What will it take for laser driven proton accelerators to be applied to tumor therapy? *Phys. Rev. ST Accel. Beams* **10** 094801
- [4] Spencer I *et al* 2001 Laser generation of proton beams for the production of short-lived positron emitting radioisotopes *Nucl. Inst. Methods Phys. Res. B* **183** 449
- [5] Mackinnon A J *et al* 2006 Proton radiography of a laser-driven implosions *Phys. Rev. Lett.* **97** 045001
- [6] Wilks S C *et al* 2001 Energetic proton generation in ultra-intense laser-solid interactions *Phys. Plasmas* **8** 542
- [7] Glinec Y *et al* 2008 Evolution of energy spectrum from laser-accelerated protons with a 100 fs intense prepulse *Appl. Phys. B* **93** 317
- [8] McKenna P *et al* 2008 Effects of front surface plasma expansion on proton acceleration in ultraintense laser irradiation of foil targets *Laser Part. Beams* **26** 591
- [9] Neely D *et al* 2006 Enhanced proton beams from ultra thin targets driven by high contrast pulses *Appl. Phys. Lett.* **89** 021502
- [10] Jaeckel O *et al* 2009 Staged laser ion acceleration *Proc. Conf. on Lasers and Electro-Optics 2009 and 2009 Conf. on Quantum Electronics and Laser Science (CLEO/QELS 2009)* (Baltimore, MD, 2–4 June 2009) pp 1–2
- [11] Allen M *et al* 2003 Proton spectra from ultraintense laser-plasma interaction with thin foils: experiments, theory and simulation *Phys. Plasmas* **10** 3283
- [12] Brantov A V *et al* 2006 Quasi-mono-energetic ion acceleration from a homogeneous composite target by an intense laser pulse *Phys. Plasmas* **13** 122705
- [13] Schwoerer H *et al* 2006 Laser-plasma acceleration of quasi-monoenergetic protons from microstructured targets *Nature* **439** 445
- [14] Sokollik T *et al* 2009 Directional laser-driven ion acceleration from microspheres *Phys. Rev. Lett.* **103** 135003
- [15] Buffetchoux S *et al* 2010 Hot electrons transverse refluxing in ultraintense laser-solid interactions *Phys. Rev. Lett.* **105** 015005
- [16] Roth M *et al* 2002 Energetic ions generated by laser pulses: a detailed study on target properties *Phys. Rev. ST Accel. Beams* **5** 061301
- [17] Kar S *et al* 2008 Dynamic control of laser-produced proton beams *Phys. Rev. Lett.* **100** 105004
- [18] Toncić T *et al* 2006 Ultrafast laser-driven microlens to focus and energy-select mega-electron volt protons *Science* **312** 410
- [19] McKenna P *et al* 2007 Lateral electron transport in high-intensity laser-irradiated foils diagnosed by ion emission *Phys. Rev. Lett.* **98** 145001
- [20] Dromey B *et al* 2004 The plasma mirror—a subpicosecond optical switch for ultra high power lasers *Rev. Sci. Instrum.* **75** 3
- [21] Doumy G *et al* 2004 Complete characterization of a plasma mirror for the production of high-contrast ultraintense laser pulses *Phys. Rev. E* **69** 026402
- [22] Ziener Ch *et al* 2003 Specular reflectivity of plasma mirrors as a function of intensity, pulse duration and angle of incidence *J. Appl. Phys.* **93** 768

- [23] National Institute of Science and Technology *PSTAR Database* <http://www.physics.nist.gov/PhysRefData/Star/Text/PSTAR.html>
- [24] Psikal J *et al* 2010 Lateral hot electron transport and ion acceleration in femtosecond laser pulse interaction with thin foils *Phys. Plasmas* **17** 013102
- [25] Roth M *et al* 2002 The generation of high-quality, intense ion beams by ultra-intense lasers *Plasma Phys. Control. Fusion* **44** 99
- [26] Schreiber J *et al* 2004 Source-size measurements and charge distributions of ions accelerated from thin foils irradiated by high-intensity laser pulses *Appl. Phys. B* **79** 1041
- [27] Borghesi M *et al* 2004 Multi-MeV proton source investigations in ultraintense laser–foil interactions *Phys. Rev. Lett.* **92** 055003
- [28] Roth M *et al* 2005 Laser accelerated ions in ICF research prospects and experiments *Plasma Phys. Control. Fusion* **47** B841
- [29] Patel P K *et al* 2003 Isochoric heating of solid-density matter with an ultrafast proton beam *Phys. Rev. Lett.* **91** 125004-1
- [30] McKenna P *et al* 2006 High-intensity laser-driven proton acceleration: influence of pulse contrast *Phil. Trans. R. Soc. A* **364** 711
- [31] <http://www.ipfran.ru/english/structure/lab334/simlight.html>
- [32] Fuchs J *et al* 2006 Laser-driven proton scaling laws and new paths towards energy increase *Nat. Phys.* **2** 48
- [33] Zeil K *et al* 2010 The scaling of proton energies in ultrashort pulse laser plasma acceleration *New J. Phys.* **12** 045015